2012-08-09

Novel Iron Catalyst and Fixed-Bed Reactor Model for the Fischer-Tropsch Synthesis

Kyle Martin Brunner
Brigham Young University - Provo

Novel Iron Catalyst and Fixed-Bed Reactor Model for the Fischer-Tropsch Synthesis

Kyle M. Brunner

A dissertation submitted to the faculty of
Brigham Young University
in partial fulfillment of the requirements for the degree of

Doctor of Philosophy

William C. Hecker, Chair
Calvin H. Bartholomew
Brian F. Woodfield
Larry L. Baxter
Thomas A. Knotts

Department of Chemical Engineering

Brigham Young University

December 2012

ABSTRACT

Novel Iron Catalyst and Fixed-Bed Reactor Model
for the Fischer-Tropsch Synthesis

Kyle M. Brunner
Department of Chemical Engineering, BYU
Doctor of Philosophy

This work investigates a novel iron Fischer-Tropsch (FT) catalyst preparation and describes the development of a trickle fixed-bed recycle reactor model (TFBRRM) for the FT synthesis applicable to both iron and cobalt catalysts. The iron catalyst preparation was developed using a novel solvent deficient precipitation reaction. Fifteen Fe/Cu/K/SiO_2 catalysts were prepared to investigate key preparation variables including timing of promoter addition, washing or not washing after precipitation, and drying temperature. Adding promoters to starting materials before precipitation (1S) gives more uniform promoter distributions which gives higher water-gas shift activity and lower methane selectivity. Unwashed catalysts have smaller average pore and crystallite diameters (3.9–10.8 nm versus 15.3–29.5 nm) and 30% smaller pore volumes, but 65% higher rates of reaction than washed catalysts. Catalysts dried first at 100 °C have up to 50% smaller average pore and crystallite diameters, but 10–20% higher rates of reaction than catalysts dried first at 60 °C. Overall, 1S catalysts, left unwashed, and dried first at 100 °C are best suited in activity, selectivity, and stability for wax production from hydrogen-deficient feed stocks such as coal, biomass, or municipal waste. The activity of the most active catalyst of this study is greater than or equal to the activities of two of three catalysts reported in the literature.

This dissertation describes in detail the TFBRRM, reports its validation, and presents results of varying fundamental, theoretically-based parameters (e.g. effective diffusivity, Prandtl number, friction factor, etc.) as well as physical process parameters (i.e. recycle ratio, pressure, flow rate, tube diameter, cooling temperature, and pellet diameter and shape). For example, the model predicts that decreasing effective diffusivity from $7.1 \cdot 10^{-9}$ to $2.8 \cdot 10^{-9}$ m^2/s results in a lower maximum temperature (from 523 to 518 K) and a longer required bed length to achieve 60% conversion of CO (from 5.7 to 8.5 m). Using the Tallmadge equation to estimate friction losses as recommended by the author results in a pressure drop 40% smaller than using the Ergun equation. Validation of the model was accomplished by matching published full-scale plant data from the SASOL Arge reactors.

Keywords: Fischer-Tropsch, catalyst preparation, reactor modeling, iron catalyst, solvent-deficient precipitation

ACKNOWLEDGMENTS

I have enjoyed Dr. Hecker's mentoring, encouragement, and friendship. Thank you for your patient guidance.

For their support and assistance, I thank the committee, especially Dr. Bartholomew and Dr. Baxter. Many hours were spent helping me design experiments, analyze data, and calculate statistics.

Much of the experimental and modeling work was performed by the students of the BYU catalysis lab, including catalyst preparation, characterization, and testing and numerous parametric studies. Many thanks to Grant Harper, Brad Chandler, Luke Harrison, Kamyar Keyvanloo, and others who spent many days and nights operating the test reactor. Special thanks to Luke for his work on the friction factor correlation.

I owe my greatest debt of gratitude to my wife, Jenny. You have worked at least as hard or harder than I these past few years especially in raising Eliza, Lily, and Anabeth. May our future adventures be as richly filled with memories as this one has been.

TABLE OF CONTENTS

LIST OF TABLES

LIST OF FIGURES

0.1 Nomenclature

a	fitted constant for $(\alpha\beta)_l$
a_k	catalyst activity
A	kinetic pre-exponential factor
A_{cs}	cross sectional area of a tube
b	fitted constant for $(\alpha\beta)_l$
B	constant in rate equation
c_p	specific heat capacity
C_A	concentration of species A
d_c	crystallite diameter
d_i	inner diameter (hollow cylinder)
d_p	diameter of the pellet
d_{pore}	average pore diameter
d_t	diameter of the tube
D	diffusivity
D_k	Knudsen diffusivity
$Disp$	dispersion
E_A	activation energy
f_k	friction factor
F_A	molar flow rate of species A
F_A^0	initial molar flow rate of species A
g	gravitational constant
G	superficial mass velocity
h_{wall}	effective heat transfer coefficient at the wall
k	kinetic constant
k_{int}	intrinsic rate constant
K_{Lam}	fitted constant for the laminar term of friction factor equation
K_{Turb}	fitted constant for the turbulent term of friction factor equation
L	liquid volumetric flow rate
L_{bed}	bed length
L_{p_e}	effective diffusion length
m	power on numerator CO partial pressure
M	molecular weight (g/cm^3)
M_W	Weisz modulus
n	power on numerator H_2 partial pressure
n_A	carbon number of species A
n_{tubes}	number of tubes in the FBR
n_o	carbon number of representative olefin species
n_p	carbon number of representative paraffin species
n_{ro}	effective reaction order for Thiele modulus calculation
P	pressure
P_{in}	pressure at reactor inlet

P_i	partial pressure of species i
PA	GC peak area
Pr	Prandtl number
q_r	heat flux
r	tube radius
$-r_{CO}$	intrinsic rate of consumption of CO
r_d	rate of deactivation
R	ideal gas constant
Re	Reynolds number
RF	molar response factor (PA/mol) of GC calibration
RFm	mass response factor (PA/mass) of GC calibration
RR	recycle to outlet ratio
RSD	relative standard deviation
s_N	sample standard deviation
S	selectivity
t	time
T	temperature
T_{avg}	average axial bed temperature
T_{bed}	local bed temperature
T_{max}	maximum bed temperature
T_R	radial temperature at maximum radius
T_{wall}	temperature of the tube wall
u	superficial fluid velocity
U	overall heat transfer coefficient
V_{pore}	specific pore volume (mL/g)
$\bar{V}$	specific volume (cm^3/mol)
W_{cat}	mass of catalyst
x_i'	predicted value, used with $\Delta P/L_{bed}$ in Equation 7.6
x_i	measured value, used with $\Delta P/L_{bed}$ in Equation 7.6
X_A	conversion of species A
z	axial distance in reactor
z_{1-6}	powers on the denominator terms in the rate equation

Greek Letters

$(\alpha\beta)$	dynamic thermal conductivity coefficient
δ_{GW}	pressure drop of gas in a packed tube
$\Delta H_{rxn\|T^0}$	heat of reaction at reactor feed temperature
ΔP	pressure drop in reactor tubes
ε_b	void fraction of the bed
ε_l	dynamic liquid holdup
ε_p	pellet porosity (assumed to be 0.40–0.45)
ε_w	void fraction adjusted for the static liquid holdup
ϕ	Thiele modulus
ϕ_p	pellet sphericity

η	overall effectiveness factor
λ	thermal conductivity
λ_{er}	effective radial thermal conductivity
λ_{er}^{g}	dynamic contribution of gas to thermal conductivity
λ_{er}^{l}	dynamic contribution of liquid to thermal conductivity
λ_{er}^{s}	static contribution to thermal conductivity
μ	viscosity
ρ	density
ρ_b	bed density
ρ_p	pellet density
σ	molecular diameter (Angstrom)
τ	tortuosity (assumed to be 3.5)

Subscripts

a	property of solute in diffusivity calculations
b	property of solvent in diffusivity calculations
e	indicates an effective property (effective diameter, effective diffusivity, etc.)
g	property of the gas
l	property of the liquid
s	property of the solid

CHAPTER 1. INTRODUCTION

1.1 Overview

Demand for liquid fuel sources combined with political unrest in some of the regions of the world most abundant in oil and natural gas and the recent natural gas boom from hydraulic fracturing have pushed global and domestic energy policies to focus on domestic production and sustainability. This push for domestic supplies of fuel provides opportunities for innovation in industry to develop and improve alternative liquid fuel sources including natural gas, biomass, and coal. Processes which convert natural gas, biomass, or coal to liquid fuels are referred to as natural gas to liquids (GTL), biomass to liquids (BTL), or coal to liquids (CTL). The Fischer-Tropsch (FT) Synthesis (FTS) is one commercially proven process for producing hydrocarbon products from carbon monoxide and hydrogen (syngas) and is a key step in GTL, BTL, and CTL projects.

1.1.1 State of the Fischer-Tropsch Industry

Franz Fischer and Hans Tropsch developed the process that bears their names during the 1920's. Nazi Germany commercialized the process to support the war effort and obtained a peak production of 4.1 Mbbl/y (11,500 bbl/d) [1]. After World War II, South Africa Coal and Oil (SASOL) continued commercialization and development of the FTS and continues production of synthetic fuels to the present. At various times in the past, usually accompanying high oil prices, massive government programs and many industrial players have explored FTS development. These include SASOL, Exxon Mobil, Shell, Synfuels China, and a number of smaller players. Current world FTS production is about 410,000 bbl/d, mostly from facilities built and operated by SASOL, Shell, and Synfuels China. Several projects have been announced or are under construction in China, South Africa, Germany, Qatar, Malaysia, Nigeria, and the United States amounting to an additional 260,000 bbl/d of potential capacity, though the completion of these projects will depend

on complex economic variables. The Fischer-Tropsch industry is well established and will continue to be an important alternative fuel source.

FTS is carried out in fixed-bed (FB), fluidized-bed, or slurry bubble column (SBC) reactors and is catalyzed by either iron or cobalt. Choice of reactor and catalyst depends on the availability and source of the syngas feed as well as the desired product slate (e.g. chemicals, gasoline, diesel, or jet fuel). The choice of feedstock is determined in large part by the availability of local resources. Biomass is most widely available as it is not concentrated in deposits the way coal and natural gas are; however, biomass also contains the lowest energy density so that BTL processes are generally limited to smaller scale operation as the cost of transporting feedstock quickly becomes prohibitive. GTL and CTL processes are typically located near natural gas and coal sources. Cobalt catalysts are generally used with hydrogen-rich syngas derived from natural gas while iron catalysts are used with hydrogen-lean syngas derived from biomass and coal because of iron's water-gas shift (WGS) activity. The WGS reaction can significantly reduce the stoichiometric ratio of required H_2 to CO for FTS in exchange for making CO_2. FB reactors and SBC reactors are used when heavier liquid and wax products are desired while fluidized-bed reactors have mainly been used to produce gasoline and olefins.

1.1.2 Reactors and Catalysts

Commercial reactors for FTS include fixed-bed (FB), fluidized-bed, and slurry-bubble column (SBC) reactors. The merits of each type of reactor with respect to economy of scale, product slate, and feed stock have been discussed by others [2, 3]. Fixed-bed (FB) reactors allow for high through-puts and relatively easy maintenance while avoiding the difficult wax-catalyst separation problem in slurry-bubble column (SBC) applications. FB reactors have the advantage of well-established design and operating procedures and are easily scaled up. The front of a FB reactor behaves as a guard bed against upstream upsets that may introduce catalyst poisons. Given their simplicity and scalability, FB reactors are the preferred choice for smaller-scale applications such as BTL and are also used for larger CTL and GTL applications [4, 5]. To improve temperature control, prolong catalyst life, and optimize conversion, effluent gas is typically recycled in these reactors. FB reactors for FTS are often operated in a trickle-flow regime, defined as the condition in which the mass flux of the liquid and gas are approximately equal. The bed entrance does not

operate within trickle flow conditions unless some of the liquid product is recycled. Liquid recycle presents the additional challenge of evenly distributing the liquid to each tube.

Both iron and cobalt catalysts are currently used in commercial FB and SBC FT reactors. Sasol uses iron catalysts in its Arge FB and fluidized bed SAS reactors in South Africa and cobalt catalysts in its SBC reactors at its Qatar-based joint venture. Shell uses cobalt catalysts in its FB reactors at Bintulu, Malaysia and in its Pearl GTL facility in Qatar. Synfuels China uses iron catalysts in its FB and SBC reactors located in Inner Mongolia.

Cobalt catalyzed FTS produces mainly normal paraffins while the product slate for iron also includes significant amounts of olefins, oxygenates (e.g. valuable, high molecular weight alcohols), and a large fraction of CO_2. FTS products are inherently free of sulfur and heavy metals that typically accompany crude oil all the way through the production process and into the fuel tank. As a clean fuel source free of these contaminants, FTS products are sold at a premium. In addition, environmental regulations mandate that transportation fuels incorporate oxygen containing compounds to encourage more complete combustion. The health concerns surrounding MTBE and other additives have increasingly favored long chain alcohols and paraffinic oxygenates, which are produced on iron FT catalysts, as the preferred source of oxygenates in fuel. New iron catalysts can increase the selectivity of these oxygenates alongside the fuel products. A significant amount of work continues in developing new iron and cobalt FT catalysts.

1.1.3 Computer Models

Reactor design, construction, and operation can be among the most significant costs in building and running a chemical facility. Optimum design and efficient operation of reactors can be realized through the use of accurate, well-crafted computer models. For FB reactors, 1-D models are less robust since they ignore radial gradients of temperature and concentration, but they are easily formulated and run on computationally simple platforms while giving results that are suitable for preliminary reactor design and optimization. 2-D models give more realistic estimates of radial gradients and overall performance, but require more time and experience to develop and run. Models may reflect assumptions that bulk and intra-particle conditions are the same (homogeneous), that bulk and intra-particle conditions are different (heterogeneous), or a combination of both (pseudo-homogeneous or pseudo-heterogeneous).

Several groups have produced computational reactor models for FTS in FB reactors [6–13]; however, few models are flexible enough to model FTS on both iron and cobalt. In addition, little work has been done to model recycle and none of the models include generally-applicable, theoretically-based, industrially-relevant kinetic models for iron and cobalt. A model that addresses these issues could help to further reduce the barriers to entry into the FT industry and spur further investment and development.

This work focuses on the preparation, characterization, and kinetics of novel iron FT catalysts and on the development of a trickle fixed-bed recycle reactor model for the FTS.

1.2 Literature Review

1.2.1 Iron Catalyst Preparation

Catalyst preparation is a complex process intended to produce desirable chemical, physical, and catalytic properties in the final catalyst by choice of materials (i.e. metal, precursor, promoter, and support) and by manipulation of preparation variables and conditions (e.g. precipitation pH and temperature, washing, drying and calcination temperatures, and reduction environment and temperature) [1]. Promoters are added to catalysts to enhance their physical, chemical, and catalytic properties such as reduction temperature, rate of reaction, selectivity, or catalyst life. Supporting a catalyst on an oxide matrix (e.g. alumina, silica, ceria, or titania) requires extra preparation time and steps, but is desirable when the precursor is expensive (as is the case for cobalt or precious metal catalysts) or when structural enhancements (e.g. surface area, pore volume, or pore diameter) increase the dispersion, selectivity, or stability of the catalyst. Preparation variables largely determine the crystallite size, dispersion of the catalyst, and the pore and surface structure. After preparation, iron catalysts require pretreatment in order to create an iron carbide which is the active phase for FTS. Commercial iron FT catalysts at Sasol and at Synfuels China (currently the only commercial scale facilities using iron catalysts) are unsupported, precipitated catalysts promoted with copper (or zinc in the case of Synfuels), potassium, and silica. This study focuses on catalysts containing these promoters.

Precipitated Catalysts

Good, extensive and detailed reviews of precipitated catalysts have been published [1, 10]. A more brief summary follows.

Near the end of WWII and following, Ruhrchemie developed the first commercial iron catalyst used (and later modified) by Sasol [14]. Preparation involved pouring a near boiling solution of iron and copper nitrates (5 g Cu per 100 g Fe) into a hot solution of sodium carbonate while controlling pH around 6. After extensive washing in hot water to remove sodium, the precipitate was slurried and impregnated with potassium silicate (25 g SiO_2 per 100 g Fe) to improve thermal stability. Potassium was removed by adding nitric acid until the desired amount of potassium remained (5 g K per 100 g Fe). The effects of preparation methods such as the precipitation order (acid into base or vice versa), final pH, temperature, viscosity of solvent at drying time, calcination temperature, and reduction temperature and environment (H_2 only or H_2 + CO) were known but not necessarily understood. Commercial catalysts used at Sasol and at Synfuels China are modifications of the Ruhrchemie catalyst. Although other methods and formulations have been developed, the fact that the Ruhrchemie preparation is still used in modified forms speaks to the robust nature and activity of these catalysts.

Improvements on the Ruhrchemie catalyst have been developed both by academic and industrial interests. Industrial players are understandably reluctant to share details of their most successful catalysts; however, a wealth of knowledge and experience in iron catalyst preparation is available, in part due to the age of the industry (Sasol's FB reactors have seen 60 years of operation). Early work by Sasol showed 1) lower reduction temperature with increasing Cu content, 2) increased thermal stability and pore structure with increasing SiO_2 content, and 3) increased wax selectivity with increasing K content [14].

Later, Texas A&M studies spanning more than 10 years resulted in a continuous coprecipitation method to carefully control pH and temperature, resulting in highly active, selective, and stable catalysts for both FB and slurry reactor applications [15–22] which are among the most active iron catalysts reported in the literature. Studies showed that K inhibits reducibility, increases WGS and iron FTS activity, and increases selectivity to olefins and heavy hydrocarbons. It was suggested that at higher K loadings, the apparent decrease in activity may be due to increased diffusion effects from pores filled with heavier molecular weight hydrocarbons. Increasing SiO_2

loading increased stability, but decreased reducibility, activity, and selectivity possibly due to lowering effectiveness of Cu and K loadings as SiO_2 interacts with and neutralizes the effects of Cu and K. Cu increases reducibility and promotes WGS activity.

Studies at U. C. Berkeley focused on promoter effects (K, Zn, Cu, and Ru) and on the effects of solvent viscosity on surface structure and promoter dispersion [23]. The goal was to increase the density of CO binding sites thus making Fe catalysts of comparable activity to Co catalysts. Promoters increased site density by encouraging smaller nucleation sites during reductions and reaction. Replacing water in precursor pores with low surface tension alcohols resulted in larger surface areas. Catalysts prepared by this method were of comparable activity to a low activity Co catalyst and had lower selectivities to CH_4.

Work at the Chinese Academy of Science Institute of Coal Chemistry and by Synfuels, China not only explored the effects of other metal promoters such as Mn but also produced highly active, stable and selective catalysts from sulfur-containing precursors which traditionally have been avoided due to the strong poisoning behavior of sulfur [24, 25].

New advances in iron catalyst preparation continue to increase the fundamental understanding and knowledge of promoter-promoter interactions, surface structure-activity effects, and mechanistic reaction pathways. Good discussions of these topics are found in Chapter 6 of Bartholomew and Farrauto [1] and Chapter 7 of Steynberg and Dry [10].

Solvent Deficient Precipitation

Co-precipitation of aqueous solutions of precursors has been the principle preparation method for iron FT catalysts in the past; however, recent breakthroughs in solvent deficient precipitation of transition metal oxide nanoparticles provide exciting new possibilities for simpler, more uniform, and faster catalyst preparation methods. The BYU Chemistry Department and Cosmas, Inc. have published papers, given presentations, and submitted a patent on transition metal oxide nanoparticle preparation [26–32]. Nanoparticle size distributions are tight and can be controlled over several orders of magnitude (1–10,000 nm) by simple factors such as adding water during reaction, washing after reaction, and calcining at different temperatures. Successful synthesis of nanoparticle oxides has been achieved on over 20 different transition metals, rare earth metals, and groups I, II, and III of the periodic table including Ti, Al, Zr, Ni, Cu, Fe, Co, and La which are

all common catalyst or support materials. The Cosmas solvent deficient precipitation method has never been used for catalyst preparation prior to the work presented in this dissertation.

1.2.2 Fixed Bed Reactor Modeling

Based on available literature, it appears that Atwood and Bennett [6] published the first 1-D FB reactor model for the FTS. While they reported experimental data for both a CCI nitrided fused iron catalyst and a Harshaw precipitated cobalt-silica catalyst, their single species, 1-D homogeneous reactor simulation was based only on the iron catalyst and assumed first-order kinetics with respect to CO in calculating an effectiveness factor to account for pore diffusion resistance. More recently, Wang et al. [7] developed a 1-D heterogeneous reactor model with a highly detailed kinetics model that required 14 kinetic parameters and predicted individual species including paraffins, olefins, and carbon dioxide produced on an active Fe-Cu-K catalyst. In addition, the reactor model included a more comprehensive pellet model [33] based on a modified SRK equation of state correlation specific for gas-liquid equilibrium in FTS [34]. Model validation was performed using pilot plant data developed internally. Nevertheless, this model is not general. Because it was developed for a specific catalyst, modification to suit another catalyst would require obtaining extensive experimental activity and selectivity data for the new catalyst. Rahimpour and Elekaei [8] developed and validated a combined FB/fluidized-bed reactor model with the reactors in series using pilot plant data from the Research Institute of Petroleum Industry (RIPI). Data were obtained in FB and membrane-assisted fluidized-bed reactors. The FB reactor portion of the model appeared to agree with the data better than the fluidized-bed reactor model did. Guettel and Turek [9] developed a model with kinetics specifically for their cobalt catalyst, but they neglected the static liquid holdup and thereby underestimated the pressure drop in the reactor. No model validation was provided. Additional 1-D models are described by Steynberg and Dry [10].

2-D models by Bub and Baerns [11], Jess and Kern [12], Jess et al. [13], Liu et al. [35], Marvast et al. [36] each have their own merits; however, like the 1-D models most were not validated against real data and may have been developed for a specific catalyst (not general). Only the model by Jess and Kern is discussed here because of its use in comparing simulation results with results from the reactor model developed by this work. The model was described in two publications which separately emphasized FTS for a nitrogen-rich syngas [13] and a comparison of

FTS behavior and modeling on iron and cobalt catalysts [12]. These publications mention both a pseudo-homogeneous two-dimensional fixed-bed reactor model and pseudo-homogeneous one-dimensional fixed-bed model. The authors of the later publication claim that it is the only study at the time of its publication that includes reactor modeling of the FTS on both iron and cobalt catalysts. The model assumes hydrogen diffusion limits the pore diffusion, a questionable assumption since rates of both viscous and Knudsen diffusion are more rapid than those for carbon monoxide by a factor of $\sqrt{28/2} = 3.7$. Model predictions were compared with lab scale reactor data and with data reported for commercial processes, but no in-depth validation against commercial reactor performance was given.

Analysis and Current Work

Although a great deal of progress has been made in modeling FB reactors for FTS, currently available computer models lack several features that would make them more generally applicable and useful; namely, 1) the ability to model FTS on both iron and cobalt catalysts, 2) the flexibility to input different kinetic expressions, and 3) the ability to model recycle. The first two features are necessary for adapting the model to specific applications while the third is required in order to reflect industrial reactor performance. In addition, most previous models fail to address the effects of 1) liquid product on heat transfer and pressure drop; 2) choice of effective diffusivity and reaction order on Thiele modulus; and 3) pellet geometry on heat transfer, pressure drop, and pore diffusion limitations. Also, few of the previous models were validated against real data.

This study involved development of a computational model for a 1-D trickle-fixed-bed reactor model which addresses these needs, is applicable to both cobalt and iron catalysts, and accounts for gas and liquid recycle. Included with the model are a selection of kinetic models for both iron and cobalt catalysts and the ability to easily input a wide variety of Langmuir-Hinshelwood (LH), Eley-Rideal (ER), and power law kinetic models. While the model is 1-D, a correlation is used to account for radial thermal conductivity and heat transfer [37]. Traditional pressure drop calculations for a packed column were modified with a correlation [38] to account for trickle-flow conditions. The model was validated by matching published full-scale plant data from the SASOL Arge reactors. This dissertation presents results of varying fundamental theoretically-based parameters (i.e. effective diffusivity, Prandtl number, friction factor, etc.) and of varying process

parameters (i.e. recycle ratio, pressure, feed flow rate, tube diameter, cooling temperature, and catalyst pellet size and shape).

1.2.3 Packed Bed Friction Factor Correlations

Pressure drop in a packed bed can be estimated using a friction factor correlation. Ergun [39] proposed the classical friction factor correlation still commonly used. Tallmadge [40] showed that the Ergun correlation departs from experimental data when $Re/(1-\varepsilon_b) > 500$, added a correction to the turbulent term, and validated his correlation over five orders of magnitude in *Re*. Mehta and Hawley [41] demonstrated lack of fit in the Ergun correlation for laminar flow regimes in packed tubes in which the ratio of tube diameter to pellet diameter is less than 15 (high pellet-wall interaction region) and proposed a correction to account for void spaces in the bed. Liu et al. [42] proposed a different pellet-wall correction that improved the accuracy of the Ergun equation in laminar flow regimes over the accuracy of the Mehta-Hawley correlation. Only the Tallmadge correlation materially changed the form of the original Ergun equation and then only by adding a *Re* dependence to the turbulent term and refitting the coefficients. The other two studies retained the original Ergun coefficients. None of these correlations addresses high *Re* flow in high pellet-wall interaction regimes. This dissertation proposes a friction factor correlation that combines the corrections in the Tallmadge equation with the correction in the Liu equation.

1.3 Objectives and Approach

The objective of this work was to increase scientific knowledge and improve present technology for the FTS in two focus areas: 1) iron catalyst preparation and 2) computational FB reactor model development. To accomplish this objective, the following tasks were undertaken and represent the principle accomplishments of this work.

1. Prepare, characterize, and test novel iron FT catalysts prepared using the solvent-deficient precipitation.
    (a) Identify and explore key oxide and precursor preparation variables (washing, drying, and promoter addition steps).

(b) Prepare 8 catalysts using a 2^3 factorial design of experiments to determine the effects of preparation variables.

(c) Prepare an additional 4 catalysts to determine the effect of the order of the preparation variables (washing and drying steps).

(d) Characterize the 12 prepared catalysts.

(e) Collect activity data on the 12 catalysts under industrially relevant differential conditions in a FBR and determine the two most optimal catalysts.

(f) Prepare and characterize larger batches of the two optimal catalysts as needed.

(g) Compare activities, selectivities, and product distributions of prepared catalysts with the activities and selectivities of state of the art and industrial catalysts as reported in literature.

(h) Collect kinetic data as functions of temperature and partial pressures of CO and H_2 under differential conditions in a FBR and fit power-law kinetic constants and orders of reaction to the data for one of the optimal catalysts.

2. Develop and validate an advanced trickle FB recycle reactor model for the FTS.

(a) Include both gas and liquid recycle in the model.

(b) Explore several friction factor equations for applicability to FT conditions.

(c) Identify and include industrially relevant rate laws for Co and Fe catalysts from literature.

(d) Include an effective radial thermal conductivity term to more accurately model bed temperature.

(e) Validate the reactor model against full-scale plant data and compare the performance of the reactor model to other 1-D FT FBR models in literature.

(f) Explore the sensitivity of the model to theoretical and physical design parameters.

3. Develop an improved friction factor correlation for single phase packed bed systems.

(a) Collect pressure drop data found in literature.

(b) Combine correlations for high *Re* flow and for high pellet-wall interaction regions into a single correlation.

(c) Refit laminar and turbulent parameters of the correlation to the pressure drop data set.

1.4 Original Contribution

Original contributions from this work include:

1. Applying the novel solvent-deficient precipitation method to catalyst preparation in general and particularly to iron FT catalyst preparation. Prior to this work, the solvent-deficient precipitation method was only applied to making metal oxide nanoparticles. Based to a large extent on the work reported in this dissertation, a patent was filed covering iron and cobalt FT catalyst preparation using this new method [43].

   (a) Characterizing the novel catalysts including collecting activity data.

   (b) Estimating kinetic parameters from the kinetic data for the novel catalysts.

2. Continuing and substantially advancing development and implementation of a 1-D fixed-bed reactor model for the FTS originally begun by Professor Calvin Bartholomew.

   (a) Applying averaged properties calculations to the Prandtl number calculation for use in a FB FTS reactor model.

   (b) Using the diffusivity of CO as the characteristic diffusivity for diffusion calculations instead of the diffusivity of H_2. Other published models have assumed a characteristic diffusivity consistent with H_2.

   (c) Writing the model code in highly accessible Visual Basic Applications with a user-friendly interface.

3. Combining the improvements to the Ergun equation proposed by Tallmadge (Reynold's number dependence on the turbulent term) and by Liu, et al. (catalyst-tube wall effects) into a single equation and estimating model parameters from a combined data set gleaned from three pressure drop studies in literature.

Creating a catalyst using the Cosmas solvent deficient precipitation method is the author's own work; however, several individuals contributed to his knowledge of the process. Genesis for the idea was a weekly advisory meeting with two committee members (WCH and CHB) in which the author was made aware of the new precipitation method and its potential for a much simpler catalyst preparation method. The author met a few times with Stacey Smith and other students in the BYU Chemistry Department involved in the development of the new materials and discussed properties of the synthesized oxide materials for iron and for copper. At that time, some bi-metallic oxides had been successfully synthesized; however, to the author's knowledge, no attempt had been made at coprecipitating iron and copper catalysts by this method. The author also learned in these discussions that particle size was affected by the presence of water during and after precipitation. The author drew upon his knowledge of other catalyst preparation methods in literature to determine the materials and devise a way to incorporate the desired promoters into the metal oxides, specifically by substituting a potassium bicarbonate for an equivalent portion of the stipulated ammonium bicarbonate and by using a silica (Cab-O-Sil) that was free of alkali metals or hetero atoms. Mixing these promoter materials in with the starting materials or with the metal oxide products had not been tried before according to Ms. Smith. The remainder of the preparation procedure involving washing, drying, calcining, and reducing catalyst materials was developed from the author's knowledge of these processes in the BYU Catalysis Lab and from literature.

1.5 Organization of the Dissertation

The dissertation is comprised of 8 chapters. Chapter 1 contains background information on the FTS, catalyst preparation, and reactor modeling. Included in Chapter 1 is a review of the pertinent literature on catalyst preparation and reactor modeling. Chapter 2 describes the apparatus and experimental methods used in catalyst preparation and testing. Chapter 3 reports and discusses the results of catalyst characterization experiments. Chapter 4 reports and discusses the results of activity and kinetic experiments and compares the performance of catalysts prepared in this study to some of the best published catalysts from industry and academia. Chapter 5 describes the computerized trickle FB recycle reactor model and reports a validation of the model against the Sasol full-scale Arge iron FT FBR. Model results for what is known about the Shell Bintulu Co

FB reactor are also given along with comparisons between this model and other FT FBR models in literature. Chapter 6 reports and discusses the results of parametric studies showing the effects of varying process parameters on model predictions. Chapter 7 describes the proposed friction factor correlation for packed beds and compares its prediction of pressure drop data to predictions of other friction factor correlations for packed beds. Chapter 8 summarizes conclusions drawn in earlier chapters and identifies possible areas for future work.

Section 1.2.2 and all of Chapter 5 except Section 5.8 reprint material published in a peer-reviewed journal available from `www.degruyter.com/view/j/ijcre` [44].

CHAPTER 2. EXPERIMENTAL METHODS AND APPARATUS

2.1 Catalyst Preparation

2.1.1 Preliminary Experiments for Variable Identification

The Cosmas solvent deficient precipitation (SDP) produces metal oxide nanomaterials [26] which can be used as supports, oxide catalysts, or catalyst precursors. To find the pertinent variables in producing the ideal nanomaterial precursor, a series of preliminary experiments (GWL, GWLa, GUL, GULa, GULb, 1ULa, and 1WLa) were performed. Preliminary experiments involved preparing mixed Fe and Cu oxide nanomaterials by co-precipitation of iron and copper nitrate salts with ammonium bicarbonate in a solvent deficient environment. After precipitation, the damp precipitate was either washed or not washed. Silica was added to some of the catalysts either before or after the precipitation step.

Preparation variables for catalyst preparation studies were chosen based on anticipated results and on the results of the preliminary experiments. Adding promoters before the SDP reaction was expected to result in more uniform distributions of promoters, so timing of promoter addition was chosen as one variable. Results presented in Section 3.1 and Table 3.1 show a significant increase in surface area and pore volume after calcination for washed catalysts over unwashed catalysts regardless of silica content; thus, washing or not washing the precursor was chosen as the second preparation variable. Finally, it is well known that drying rate (controlled by drying temperature) can affect the distribution of soluble components (e.g. K and SiO_2) when solvent is present [1]; therefore, drying temperature (which influences drying rate) was chosen as the third preparation variable. These three preparation variables, 1) timing of promoter addition, 2) washing, and 3) drying temperature, were considered in developing the design of experiments. It was anticipated that washing may remove some or all of any added promoter (e.g. K), but this concern

was mitigated by use of a factorial design which included washed catalysts with K addition after the washing step resulting in full K loadings (see Section 2.1.2).

An important consideration in the future manufacturing of this catalyst is the large amount of NH_4NO_3 (roughly 50% of the total mass) produced as a byproduct of the SDP reaction. NH_4NO_3 is a valuable commodity and its recovery for sale is desirable. Washing is the most efficient method of separating the NH_4NO_3 from the catalyst precursor; however, as mentioned above, washing apparently leads to increased surface area and pore volume after calcination. This increase suggests a structural change rather than a simple removal of byproduct. As such, consideration was given to the possibility that catalyst structural properties may largely be determined only after completely drying the catalyst. If so, then washing the catalyst after complete drying would remove the NH_4NO_3 without adverse effects to catalyst performance.

Other variables that may affect catalyst properties but which were not included in the design of experiments include, but are not limited to, calcination temperature, solvent viscosity, temperature of reactants during precipitation, and pH of solution at the time of reaction.

2.1.2 Design of Experiments

Based on the results of the preliminary experiments and on the considerations described above, a 2^3 factorial design of experiments was used to investigate the effects of the three preparation variables identified in the previous section, namely 1) timing of promoter addition, 2) not washing or washing the precursor, and 3) drying temperature. Two levels of each of these variables were chosen and each level is represented by a single alphanumeric character. The eight catalysts of the factorial design are designated by the three characters representing the variable levels throughout this dissertation. The eight catalysts are listed with their variable levels in Table 2.1. Levels for promoter addition timing were 1 Step (designated by a 1) in which potassium and silica promoters were added to the salts before precipitation and the catalysts were created in a single step, and 2 Steps (designated by a 2) in which potassium and silica promoters were added in a separate step after precipitation and washing if applicable. The levels for washing were unwashed (U) or washed (W) immediately following precipitation. Levels for initial drying temperature were high (H) temperature (100 °C) and low (L) temperature (60 °C overnight, followed by 100 °C). The six alphanumeric characters for catalyst designation represent the levels of the promoter addition (1

or 2), washing (U or W), and drying steps (L or H). For example, 1UH designates a catalyst prepared in 1 Step (with potassium and silica added to salts before precipitation), left unwashed after precipitation, and dried at the high drying temperature (100 °C); 2WL denotes a catalyst prepared in 2 Steps (with potassium and silica added after precipitation and washing), washed directly after precipitation, and dried first at the low drying temperature (60 °C) followed by drying at 100 °C.

Table 2.1: 2^3 factorial design of experiments to explore three key preparation variables.

Catalyst ID	Promoter Addition	Washing Step	Drying T (°C)
1UH	1 Step[a]	Unwashed	100
1UL	1 Step	Unwashed	60/100[b]
1WH	1 Step	Washed	100
1WL	1 Step	Washed	60/100
2UH	2 Step[c]	Unwashed	100
2UL	2 Step	Unwashed	60/100
2WH	2 Step	Washed	120[d]
2WL	2 Step	Washed	60/100

[a]added to salts prior to precipitation
[b]initial/final temperature
[c]added after precipitation or washing
[d]unintentionally higher than 100 °C

In addition to the 8 catalysts from the 2^3 factorial experiments, a 2^2 factorial design of experiments (4 additional catalysts) was used to investigate the effects of the timing of promoter addition and initial drying temperature on catalysts that were dried completely following precipitation which were then washed (D) and finally dried again after washing. The purpose was to demonstrate whether the catalysts could be washed without adverse affects to catalyst properties. Levels of these variables were the same as for the 2^3 factorial experiments and designations followed the same convention, except that the washing designation for these catalysts is D e.g. 1DH denotes a catalyst prepared in 1 Step (with promoters added to the salts before precipitation), dried at the high drying temperature immediately after precipitation, and then washed and dried again at the high temperature. Table 2.2 gives the catalyst designations and variable levels for this design.

Table 2.2: 2^2 factorial design of experiments for four additional catalysts dried completely before washing.

Catalyst ID	Promoter Addition	Drying T (°C)
1DH	1 Step[a]	100
1DL	1 Step	60/100[b]
2DH	2 Step[c]	100
2DL	2 Step	60/100

[a]prior to precipitation
[b]initial/final temperature
[c]after washing

2.1.3 Catalyst Synthesis

The 12 catalysts of the experimental design were prepared in either 1 Step or 2 Step preparations (six catalysts each) with target compositions designated as 100 Fe/5 Cu/4 K/16 SiO_2 which indicates relative mass values of each component.

1 Step Preparation

In the 1 Step preparation, the silica promoter was added to the iron and copper salts (acid) and the potassium promoter was added to the ammonium bicarbonate (base) before combining and mixing all components in the SDP of the precursor. A large amount of precursor (359 g total mass equivalent to 30 g_{Fe}) was precipitated in a single large batch to eliminate possible variations in catalyst properties and behavior that may result from several smaller batches. The large batch of precursor was divided into six separate catalysts as illustrated by Figure 2.1.

The specifics for this preparation are given here. Before beginning the precipitation, 4.822 g fumed SiO_2 (Cab-O-Sil) were added to 217.005 g $Fe(NO_3)_3 \cdot 9\,H_2O$ and 5.485 g $Cu(NO_3)_2 \cdot 2.5H_2O$ and mixed well with a pestle in a large glass bowl. In a separate container, 3.071 g $KHCO_3$ were mixed with 128.989 g NH_4HCO_3 following which the bicarbonate mixture was added to the metal salt mixture. The combined mixture of powders was vigorously mixed with the pestle during which waters of hydration were released. Mixing continued until precipitation of Fe and Cu hy-

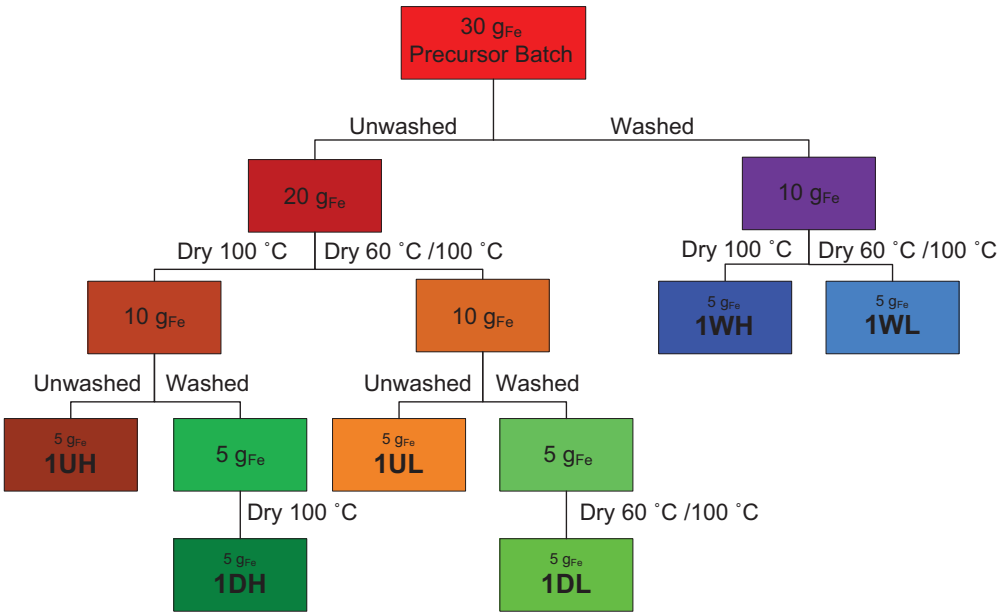

Figure 2.1: Schematic showing the division of the single 1 Step preparation of precursor into six separate catalysts.

droxides was complete as indicated by cessation of CO_2 release as bubbles according to the Cosmas SDP. Reaction and mixing was complete within about 20 minutes. One third of the precursor was placed unwashed in an oven and dried at 100 °C for 16–48 hours (third level, left hand branch of Figure 2.1). Another third of the precursor was placed unwashed in another oven and dried first at 60 °C for 16–48 hours followed by 100 °C for 16–48 hours (third level, middle branch of Figure 2.1). The remaining third was washed five times with 100 mL of deionized water and then split into two (second and third levels, right hand branch of Figure 2.1). One portion was placed in the first oven to be dried with the first third of precursor and was designated 1WH. The remaining portion was placed in the second oven to be dried with the second third of precursor and was designated 1WL. The five washes were retained for elemental analysis. The third of the precursor that was unwashed and dried initially at high temperature was split into two with one portion designated 1UH and the other portion washed five times with 100 mL of deionized water and then dried again and designated 1DH (fourth and fifth levels, left hand branch of Figure 2.1). The remaining third precursor that was unwashed and dried initially at low temperature was also split into two with one portion designated 1UL and the remaining portion also washed five times with 100 mL of deionized water and and then dried again and designated 1DL (fourth and fifth levels, middle

branch of Figure 2.1). Only the first (of five) washes of 1DH and 1DL were retained for elemental analysis. Secondary drying conditions were the same as the primary drying conditions for 1DH (100 °C for 16–48 h) and 1DL (60 °C followed by 100 °C for 16–48 h each temperature), except that 1DL was initially put in a 100 °C oven for 2–3 hours before being removed and placed into a 60 °C oven overnight to continue the prescribed drying procedure. All drying was done in a circulating air oven or a furnace with flowing air. After drying, the precursors were pelletized, crushed, and sieved to $-30/+60$ mesh. For the remainder of this chapter and in subsequent chapters, the four 1 Step catalysts of the 2^3 factorial design are referred to collectively as 1S catalysts and the two 1 Step catalysts of the 2^2 factorial design are referred to as 1D catalysts.

2 Step Preparations

For the 2 Step preparations, each of the six catalyst precursors was prepared in separate batches (10 g_{Fe}). The masses of starting materials for each preparation are given in Table 2.3. In each preparation, the metal salts were precipitated according to the SDP method. The promoters and enough water to make a thick clay were added to the damp precipitate before drying. For 2UH and 2UL, the promoters were added immediately after complete precipitation and before drying. For 2WH and 2WL, the promoters were added immediately after washing. For 2DH and 2DL, the promoters were added after washing and before the final drying step. 2WH was dried at 120 °C instead of 100 °C, but all other precursors were dried at 100 °C for 16–48 hours or at 60 °C for 16–48 hours followed by 100 °C as designated. As with the 1 Step precursors, the dried precursors were pelletized, crushed and sieved to $-30/+60$ mesh. In the following sections and subsequent chapters, the four 2 Step catalysts of the 2^3 factorial design are referred to collectively as 2S catalysts and the two 2 Step catalysts of the 2^2 factorial design are referred to as 2D catalysts.

Repeat Preparations

Besides the 12 catalysts already described, three repeat catalysts were prepared in the BYU lab and one repeat catalyst was prepared by Cosmas, Inc. The repeat catalysts are designated by a small letter "a" after the preparation method (e.g. 1UHa is a repeat of 1UH) and are listed in Table 2.4 along with two other catalysts described later in this section. One repeat catalyst was

Table 2.3: Masses of starting materials for 2 Step catalyst preparations. All numbers are grams of specified moiety.

Catalyst	$Fe(NO_3)_3$[a]	$Cu(NO_3)_2$[b]	$KHCO_3$	SiO_2	NH_4HCO_3
2UH	72.492	1.836	1.077	1.611	43.799
2UL	72.335	1.836	1.029	1.606	43.731
2WH[c]	72.357	1.841	1.025	1.604	43.717
2WL	72.360	1.829	1.065	1.595	43.737
2DH	72.383	1.814	1.043	1.613	43.738
2DL	72.365	1.854	1.032	1.605	43.725

[a] $Fe(NO_3)_3 \cdot 9\,H_2O$
[b] $Cu(NO_3)_2 \cdot 2 \cdot 5\,H_2O$
[c] dried at 120 °C

prepared according to the 1UH preparation in a 30 g_{Fe} batch (the same size as the 1 Step batch) and designated 1UHa. Two other repeat catalysts were actually preliminary experiments (see Table 3.1) similar to 1UL and 1WL in preparation except that the higher drying temperature was 120 °C, not 100 °C, in both cases. These two catalysts were designated 1ULa and 1WLa and were 11 g_{Fe} batches each. Comparisons of 1UH with 1UHa and of 1UL and 1ULa are discussed in Section 4.6.

Table 2.4: Repeat and conventional coprecipitation catalyst preparations.

Catalyst ID	Precip. Method[a]	Promoter Addition[b]	Washing Step	Drying T (°C)[c]	Batch (g_{Fe})[d]
1UHa	SDP	1 Step	Unwashed	100	30
1ULa	SDP	1 Step	Unwashed	60/120	11
1ULC[e]	SDP	1 Step	Unwashed	60/120	>37
1WLa	SDP	1 Step	Washed	60/120	11
P1	Conv.	2 Step	Washed	60/120	11
P2	Conv.	2 Step	Washed	60/120	5.5

[a] Solvent deficient precipitation (SDP) or conventional (Conv.)
[b] 1 Step: prior to SDP, 2 Step: after SDP or washing
[c] Initial temperature/final temperature, where applicable
[d] Effective batch size based on mass of iron basis
[e] Prepared by Cosmas, Inc.

Cosmas, Inc. (Provo, UT) prepared a large amount of catalyst (> 52 g_{Fe}) using the 1ULa preparation (dried ultimately at 120 °C) and it is designated 1ULC with the capital "C" indicating it was prepared by Cosmas, Inc. The Cosmas preparation was purchased by International Composting Corporation (ICC, Victoria, BC) and sent to Emerging Fuels Technology (EFT, Tulsa, OK) for testing. Cosmas, Inc. and ICC have consented to share the results of the tests on 1ULC in this dissertation.

Conventional Precipitation Preparations

Besides the 16 catalysts described above, two additional catalysts were prepared using conventional co-precipitation based loosely on a published method [22] for a total of 18 prepared catalysts. The two conventional co-precipitation catalysts were designated P1 and P2. Both catalysts were prepared with the same general procedure except that P2 was half the batch size of P1, and P2 was cooled in an ice bath immediately after precipitation. The precipitation reaction was done in a potassium acetate/acetic acid buffer solution to help minimize pH swing. To make the buffer solution, acetic acid was added to 100 mL of a 1.75 mol/L aqueous solution of potassium acetate until the pH was 6.0. An aqueous solution of the desired amounts of iron and copper nitrate salts (2.0 mol/L Fe) was prepared and put into a burrette. A second burrette was filled with 4.0 mol/L KOH. Both solutions were dripped simultaneously and slowly into the heated buffer solution which was stirred continuously. Control of pH ($5.8 <$pH< 6.2) was effected by controlling the relative drip rate of the two solutions. Temperature was controlled in the range of 78 °C$< T <$ 82 °C by a heated water bath and by adjusting the total flow rate of the two solutions. After precipitation, P1 was cooled to ambient temperature whereas P2 was cooled to ice water temperature. After cooling, the solutions were filtered and washed 2–5 times with deionized water. It was assumed that 100% of the K from the buffer solution was removed by washing. P1 formed a fine colloidal suspension during washing and became extremely difficult to filter. The precipitate was left in the wash for 48 hours without any observable changes, but then was successfully filtered after cooling in an ice bath presumably due to changes in properties of the suspension with temperature. After the catalyst had been washed, a 0.4 g/mL solution containing the desired amount of silica in the form of K_2SiO_3 was added to the precipitate. The moderately basic pH of the solution dropped at a moderate rate and settled slowly over a period of about 30 minutes due to interactions of the silica

with the iron precursor after which the pH was lowered to between 6.3 and 6.6 by adding 0.1 mol/L HNO_3 drop wise. The solution was stirred for 4 hours and then filtered and washed again as above to remove K. The precipitate was dried overnight at 60 °C and then crushed and sieved to smaller than 30 mesh. The desired amount of potassium was added in the form of $KHCO_3$ dissolved in water by incipient wetness. After potassium impregnation, the catalyst was dried again at 60 °C overnight.

2.1.4 Bulk Calcination, Reduction, and Passivation

Precursors for all SDP catalysts above were bulk calcined (20–50 g material) at 300 °C in flowing air for 6–16 hours. The temperature program was based on temperature programmed oxidation (TPO) measurements of representative samples of the catalysts in a thermo-gravimetric analyzer (TGA). Temperature was ramped from ambient temperature to 90 °C at 3 °C/min, soaked for 1 hour, then ramped to 190 °C at 0.5–3 °C/min followed by ramping to 210 °C at 0.1–1 °C/min, soaked for 4 hours, and finally ramped to 300 °C at 0.5 °C/min for the final soak at 300 °C for 6–10 h. In the case of 1UHa (30 g_{Fe}), the precursor was calcined in three separate batches because of volume constraints in the reactor tube following which the three calcined batches were thoroughly mixed together.

Calcined precursors were reduced at 300 °C in 10% H_2/He at a GHSV of $> 2,000$. The temperature program was based on temperature programmed reduction (TPR) measurements of representative samples in a TGA. A heating rate of 0.5 °C/min up to 250 °C was followed by a 1 hour soak before continuing to 300 °C for a 10 hour soak. Following the 10 hour soak, the composition was switched to 100% H_2 for an additional 6 hour soak at 300 °C. The catalyst was then cooled in He to less than 30 °C. The reduced catalyst was carefully passivated by first exposing it to flowing air in helium ($< 1\%$) followed by gradually increasing concentrations of air in helium so that the wall of the metal reactor tube in contact with the bed was always less than 37 °C.

The four 2S and two 2D catalysts were bulk reduced immediately following bulk calcination. In each case the procedures described above were followed; however, between the end of the calcination procedure and the beginning of the reduction procedure, the catalysts were cooled to less than 190 °C (not ambient) and the reactor was not opened between procedures. For all other

catalysts, the calcination and reduction steps involved complete removal and repacking of catalyst between procedures.

Three samples of each of the 17 catalysts prepared at BYU were retained for characterization: after drying, after calcining, and after reducing. For the four 2S and two 2D catalysts that were reduced immediately following calcination, calcined samples were obtained by calcining small portions of the dry samples in crucibles in a lab furnace with flowing air according to the temperature program described above.

Calcination and reduction of conventional precipitation catalysts was as follows. Temperature programs were based on TPO and TPR measurements of representative catalyst samples in a TGA. After drying, the catalysts were calcined at 300 °C for 6 hours following 1 hour soaks at 270 °C, 150 °C, and 50 °C. The calcined catalysts were bulk reduced up to 300 °C by ramping temperature at 0.5 °C/min to 300 °C with 1 hour soaks at 70 °C and 250 °C and a final 16 h soak at 300 °C. During reduction, the gas composition was 10% H_2/He except for the last 6 h at the end of the final soak when the composition was changed to 100% H_2. Following reduction, the catalysts were carefully passivated in gradually increasing concentrations of air in helium so that the temperature of the catalyst bed did not appear to increase more than 10 °C.

2.2 Characterization Instruments and Procedures

The 12 factorial catalysts (Tables 2.1 and 2.2) and 5 other catalysts (Table 2.4) prepared at BYU were characterized using a variety of tools and techniques.

2.2.1 BET

Surface area (*SA*), pore volume (V_{pore}), and pore size distribution (PSD) were calculated from nitrogen isotherm data measured using a Micromeritics TriStar 3000 BET analyzer. Sample sizes were typically 0.3–0.5 g. Average pore diameter and PSD were calculated using methods proposed by Gregg and Sing [45] and modified to fit a log-normal PSD [46–49]. Calculations using this new method were automated in a VBA program for MS Excel written by the author. The program code is given in Appendix E.

2.2.2 TGA

Temperature programmed oxidation (TPO), temperature programmed reduction (TPR), isothermal oxygen titration and CO chemisorption were performed on 10–40 mg samples in a Mettler Toledo TGA/DSC 1 equipped with an automated GC 200 gas controller. Gas flow rates of H_2, CO, and O_2 (or air depending on the source) were set by rotameters, but gas switching during all experiments was controlled by the GC 200 controller and the TGA software.

TPO experiments were used to design temperature programs for bulk calcination. The rate of mass loss during a constant temperature ramp of 3 °C/min from ambient temperature to 700 °C in 100 mL/min of 70–80% air/He was analyzed to determine appropriate temperature ramps and soaks for controlling byproduct decomposition at low rates.

TPR experiments were used to determine temperature programs for bulk reduction. Again, the rate of mass loss during a straight temperature ramp of 3 °C/min from ambient temperature to 700 °C in 100 mL/min 10% H_2/He was analyzed to determine appropriate temperature ramps and soaks for reduction to proceed at an acceptable rate without producing high partial pressures of H_2O.

Isothermal oxygen titration experiments were used to determine the extent of reduction (EOR) to Fe metal following reduction. EOR was calculated from O_2 uptake during oxidation at 400 °C after re-reduction of previously passivated catalyst for 6 hours at 300 °C in 10% H_2/He. An example calculation for EOR is given in Appendix E.

Gravimetric carbon monoxide adsorption was used as a relative measurement of chemisorption site density. CO uptake was measured at 25 °C in 10% CO/He following re-reduction of passivated catalysts at 300 °C for 6 hours in 10% H_2/He and a 1 hour purge in 100% He at 290 °C.

2.2.3 Hydrogen Chemisorption

Dispersion and crystallite diameters of reduced catalysts were calculated from hydrogen chemisorption uptake measurements. Hydrogen was chemisorbed on reduced catalysts in a flow-through adsorption system using procedures and equipment developed in the BYU catalysis lab [50]. Passivated catalysts were re-reduced at 300 °C in 100% H_2 for 6 hours followed by purging in Ar at 280 °C to remove residual H_2 from the reduction. Hydrogen was adsorbed at 100 °C

before purging at dry ice/acetone temperatures (77 K) to remove physisorbed molecules. Finally, hydrogen was desorbed during a temperature ramp up to 600 °C. Dispersion (*Disp*) and average crystallite diameter (d_c) estimates were calculated from the hydrogen uptake and extent of reduction data using Equations 2.1 and 2.2, respectively [1].

$$Disp = 1.12 \times \frac{\text{H}_2 \text{ Uptake}}{\text{EOR} \times \text{Weight Loading}} \tag{2.1}$$

$$d_c = \frac{123}{Disp} \tag{2.2}$$

Crystallite diameter (d_c) is in nm when H_2 uptake is in μmol/g, EOR is the fraction of Fe in the metallic state, and weight loading is the mass percent of Fe in the catalyst. Example calculations for *Disp* and d_c and representative hydrogen uptake scans are given in Appendix E.

2.2.4 ICP

To confirm the elemental content of prepared catalysts, digested catalysts and catalyst washes were analyzed in a Perkin Elmer Optima 2000 DV ICP analyzer. Catalyst samples (20–45 mg) were digested in hydrofluoric acid, dried, and then dissolved in 10 mL 3% nitric acid. 0.5–1 mL of digested sample was diluted with 20–40 mL of 3% nitric acid, giving final analyte concentrations of about 100 mg_{cat}/L. Samples of catalyst washes (3–5 mL) were diluted with 15 mL of 3% nitric acid before analysis. Analyte wavelengths were 238.2 nm (Fe), 327.4 nm (Cu), and 766.5 nm (K). Instrument calibration and operation were performed by the BYU Chemistry Department.

2.2.5 XRD

Crystalline phases of catalysts after drying, calcining, reducing, and carbiding (a result of FB FTS testing) were identified using Xray diffraction (XRD) patterns in order to understand phase changes at each of these steps and to estimate crystallite diameters. XRD patterns were collected using a PANalytical X'Pert Pro diffractometer with a Cu source and a Ge monochromator tuned to the Cu-Kα1 wavelength ($\lambda = 1.540598$ Å). Samples were scanned from 20 to 90°2θ using a step size of 0.016° at scan rates between 100 and 400 s/step. Diffraction patterns were compared

to standard patterns in the ICDD (International Center for Diffraction Data) database. Average crystallite size (d_c) is related to the X-ray wavelength (λ), half-intensity line broadening (β_{XRD}), and angle (θ) by Scherrer's equation (Equation 2.3).

$$d_c = \frac{0.9 * \lambda}{\beta_{XRD} \cos\theta} \tag{2.3}$$

2.2.6 Electron Microprobe

To determine the uniformity of promoter distributions at the micron level, macro elemental distributions of Fe, Cu, K, and Si in 50–400 μm catalyst agglomerates were imaged using a Cameca SX50 electron microprobe at 15 kV and 20–30 nA.

2.2.7 TEM

Confirmation of the presence of crystallite diameters estimated from other techniques was attempted with TEM imaging. Crystallites and agglomerates were imaged on a FEI TF30 TEM operating at 300 keV or on a FEI TF20 Ultra-twin TEM/STEM operating at 200 keV. Between 2 and 16 qualitative images each of 1UH and 2UH before and after FTS (for a total of 36 images) were recorded. The total image count included bright field, dark field and diffraction pattern (d-ring spacing) images. Since an estimate of crystallite diameter by TEM was not part of the scope of this work, the number of imaged crystallites was inadequate for a representative statistical estimate of crystallite diameters.

2.3 Activity Test Equipment and Procedures

Catalyst activity, selectivity, and stability are the ultimate catalyst characterization metrics. Activity data at four or five temperatures were obtained in a fixed-bed (FB) reactor (FBR) for each catalyst to determine catalyst performance. Minimal product distribution data were obtained during reaction including CO_2, CH_4 and C_2H_6 selectivities. System constraints did not allow for online determination of larger hydrocarbon species, moreover detailed product analysis of reaction products at each set of reactor conditions was beyond the scope of this work. Some indication of

stability was obtained on catalyst runs lasting longer than 200 h with the longest FB run accumulating more than 800 h of data. The following sections detail the equipment and procedures for collecting these data.

2.3.1 FBR Description

Catalyst activity was measured under differential conditions (low conversion) in a fixed-bed reactor system containing two reactor beds in parallel. A flow diagram of the reactor system is shown in Figure 2.2. Using a purification system not shown in Figure 2.2, He, CO (containing a 12% Ar tracer), and H_2 flowed from their respective cylinders through absorbents described by Critchfield [51] to remove low level impurities such as iron carbonyls, hydrogen sulfide, oxygen, water, etc. The only modifications to the gas purification trains Critchfield described were the removal of the All G Pur traps which were no longer effective. Individual gas flow rates, and thereby total feed gas composition, were controlled by mass flow controllers (Brooks 5850E). The feed gas was then split three ways with one part going to a bypass line controlled by a back pressure regulator (Grove Valve and Regulator Co. S-91XW typically set to 340 psig) and two lines with mass flow controllers (Brooks 5850E) that fed the two downflow reactors. From the reactors, gas and liquid effluent flowed through the reactor beds to the hot traps at 90–110 °C followed by cold traps at ice water temperature. Gases leaving the cold traps flowed through back pressure regulators (one for each reactor, Grove Valve and Regulator Co. S-91XW typically set to 300 psig) to valves which allowed the gases to flow to the sample loop of the GC or to the vent. If allowed to flow to the GC, each gas flowed through a temperature controlled automated sample valve and sample loop of an Agilent 6890 GC and then to the vent. Both reactors were encased in the same three zone tube furnace. Furnace temperatures were controlled by three Omega controllers. Reactor bed temperatures were measured by thermocouples in contact with the bed. The hot and cold traps are used to nominally collect liquid wax products (C_{20+}) and condensables (C_5–C_{20} hydrocarbons, oxygenates, and water), respectively.

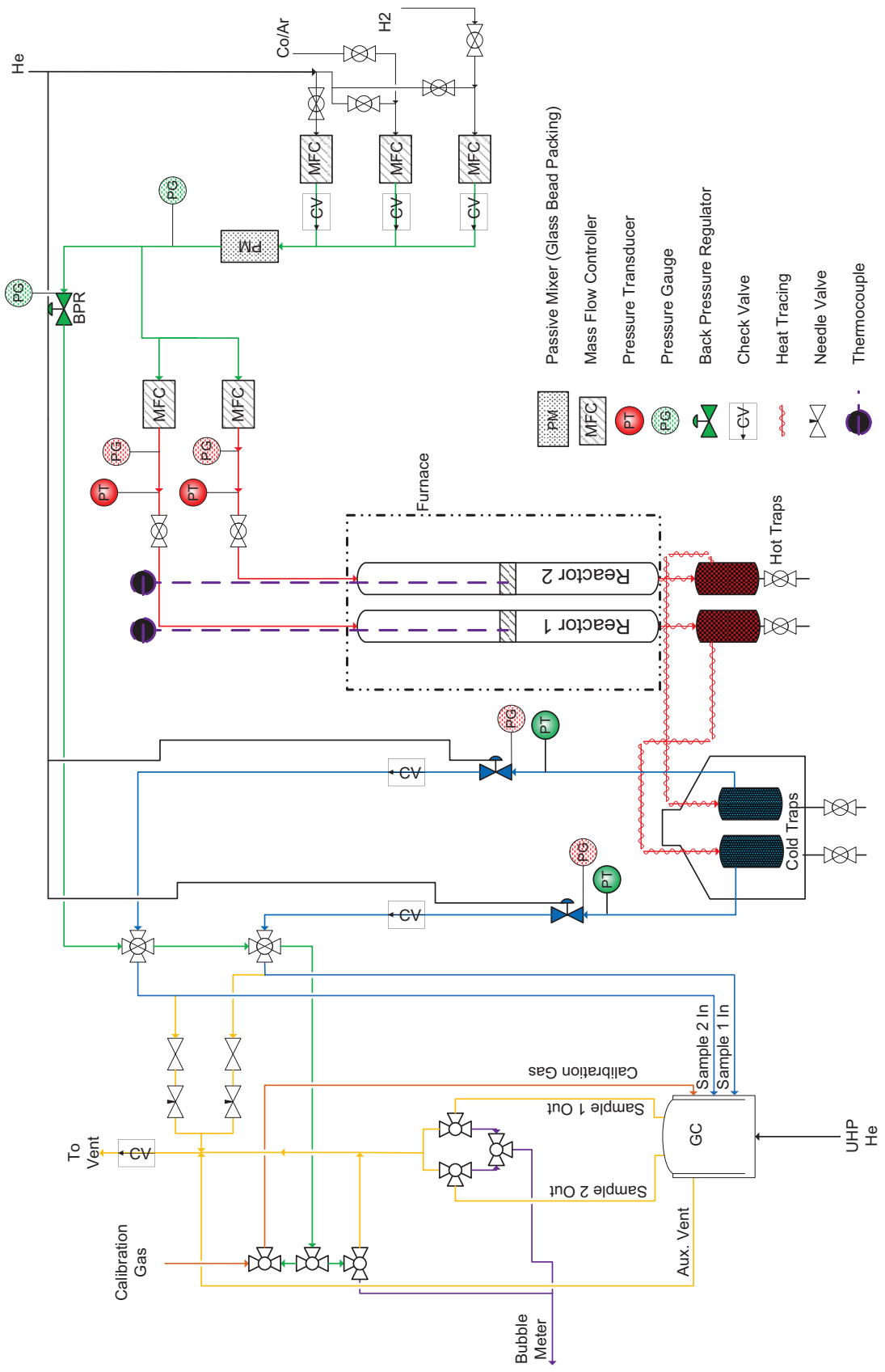

Figure 2.2: Process flow diagram of dual channel fixed bed reactor system.

2.3.2 FBR Loading and Catalyst Recovery

Catalysts were loaded into reactors as follows. Passivated catalysts were sieved to $-30/+60$ mesh to remove fines likely to escape the catalyst bed. The reactor tubes, which were $3/8$ inch OD (9.5 mm OD), were fit with a ring slightly smaller than the inner diameter and then slightly crimped to hold the ring in place. A metal frit or piece of stainless steel mesh (100 mesh) was placed on top of the ring to provide structural support for the bed and help prevent catalyst loss. Just enough quartz wool was placed over the mesh to prevent catalyst loss where irregularities in the shape of the frit or mesh may have left small gaps near the edges of the tube wall for catalyst to fall through. The catalyst was diluted with quartz sand ($-50/+70$ mesh) to avoid hot spots within the bed and to encourage plug flow behavior. Catalyst (0.25–0.5 g) was thoroughly mixed with sand (1 g) and then charged to the reactor. Quartz wool was placed on top of the catalyst bed to prevent the possibility of catalyst fines traveling back up the reactor in the unlikely event of a pressure upset. After reaction, the entire catalyst bed assembly excluding the ring was removed from the tube and separated. The tube was cleaned with hot water, toluene, and acetone as needed to remove residual wax and catalyst particles. Spent catalyst samples were retained to study physical changes as a result of carbidization.

After FB testing, catalysts were recovered and separated from the wax and quartz sand. Wax removal was accomplished in four toluene extractions. The bed solids were placed in a conical vial and heated in a 90 °C water bath. For each extraction, 2–4 mL toluene was added to the vial (surface level was about 2 inches above the solids) and the contents were vigorously stirred every 2 minutes. After 8–10 minutes, the catalyst was allowed to settle for 1 minute and then the toluene above the catalyst was removed by pipette. After four extractions, the catalyst was dried in a hood over night. Following wax extraction, the catalyst was separated from the quartz sand by magnet. The affinity of the catalyst for the magnetic field varied from sample to sample, but all samples achieved a high degree of separation with the magnet. Separated catalysts were stored in vials in a desiccator until characterized by BET and XRD.

2.3.3 Hot and Cold Trap Product Collection

Products collected in the hot and cold traps were recovered after partial shutdown of the reaction system. To do so, the reactant feed valves were closed, the furnace was turned off, and the reactors were allowed to cool to ambient temperature while the hot and cold traps were kept at their respective temperatures. The reactors and associated lines were depressurized and purged with He to remove H_2 and CO and then repressurized to provide a driving force for product removal. Cold and hot trap products were recovered and stored in separate jars for each catalyst (four different product samples for each FB run). Products were collected at ambient conditions while the respective traps remained at their operating temperatures (0 °C and 110 °C, respectively). During product collection in both traps, regardless of the care of the operator, a burst of fine mist was emitted near the end of product collection which dissipated quickly and which likely contained light hydrocarbon products and water vapor. The mist was probably a result of flashing the contents from conditions in the traps to ambient conditions.

2.3.4 Rate and Selectivity Calculations

GC chromatograms and associated data give gas compositions from which values for the rate of reaction and selectivity were calculated according to the following relationships. Assuming differential reactor conditions, the reactor performance equation is reduced to Equation 2.4.

$$\frac{W_{cat}}{F_{CO}^0} = \frac{X_{CO}}{-r_{CO}} \tag{2.4}$$

The mass of catalyst (W_{cat}) and inlet molar CO flow rate (F_{CO}^0) were known or measured directly, so the calculation of rate depended only on the determination of CO conversion. The CO conversion was calculated from GC measurements of the unreacted feed and the reactor effluent. Use of an internal inert tracer, such as the Ar that was premixed in the CO cylinders for FB tests in this research, simplified this calculation greatly since conversion is independent of all factors other than GC peak area (PA) as shown by Equation 2.5 and derived in Appendix A.

$$X_{CO} = 1 - \frac{PA_{CO}}{PA_{\mathrm{Ar}}} \frac{PA_{\mathrm{Ar}}^0}{PA_{CO}^0} \tag{2.5}$$

It follows from Equation 2.4 that calculation of rate is also independent of GC calibration. In contrast, calculation of selectivity (S) is dependent on the calibrated GC molar response factors (RF) of each species which appear in Equation 2.6.

$$S_A = \frac{n_A}{X_{CO}} \frac{PA_A}{PA_{\mathrm{Ar}}} \frac{PA^0_{\mathrm{Ar}}}{PA^0_{CO}} \frac{RF_{CO}}{RF_A} \tag{2.6}$$

Multiplication by the carbon number of the species (n_A) makes S_A the fraction of the reacted moles of C converted to species A. Derivations and example calculations for X_{CO}, $-r_{CO}$, and S_A are given in Appendix A.

2.3.5 Activation Procedure

All catalysts tested in the BYU dual channel FBR system (all catalysts but 1ULC) were activated in syngas (CO and H_2) following in-situ reduction in H_2 as shown in Table 2.5 and described below. The parallel FB reactors are designated R1 and R2. Table 2.5 is intended to show system conditions during catalyst activation and not to compare catalyst performance. First, passivated catalysts were re-reduced in 10% H_2/He at 300 °C for 10 hours followed by 100% H_2 for 6 hours (except 2UL, 2WH, and 1ULa which remained at 10% H_2/He for 16 hours) at a SV of at least $2,000\ \mathrm{h}^{-1}$. After reduction, furnace temperature was reduced to 240 °C or less and reactants were introduced at the desired composition (30% H_2/30% CO/4% Ar/36% He by volume). Bed temperature was increased over several hours to the activation temperature ($T_{<50h}$).

Starting with FB Run 6 and for all subsequent runs, flow rates in each reactor were decreased to produce a targeted CO conversion of 20–50%. The higher conversions on Runs 9 and 10 were the peak conversions during a period lasting up to several hours due to overshooting conversion targets, but the majority of the conversion during the activation period for these catalysts was below the 50% upper target. Conversion during activation was intentionally higher to speed up the time required to carbide the catalyst, fill the pores with wax, and achieve steady state activity.

Activation was considered complete only after the ratio of standard deviation to GC peak area was less than 0.02 for effluent values of H_2, CO, and Ar. For earlier runs (1–5), a specific activation procedure was not defined which may have led to some short term instability in activity. This short term instability is illustrated by Figures 2.3 and 2.4 which show an Arrhenius plot of

Table 2.5: Reactor setup and catalyst activation conditions for ten dual FB Reactor tests. The two reactors are designated R1 and R2. GC designations indicate the single channel B instrument, or the dual channel F instrument. Runs are listed in chronological order.

Run	R1	R2	GC	Mass R1 (g)	Mass R2 (g)	T_{PR}[a] °C	T_{gas}[b] °C	$T_{<50h}$[c] °C	R1 X_{CO}[d]	R2 X_{CO}[d]
1	1WLa	P2	B	0.500	0.500	25	207	235	0.09	0.15
2	1ULa	P1	B	0.499	0.501	25	250	263	0.46	0.28
3	2UL	2WH	B	0.513	0.516	240	240	240	0.16	0.14
4	2DL	2DH	B	0.513	0.506	25	25	240	NA	0.46
5	2UH[e]	2WL	B	0.251	0.256	25	25	240	0.10	0.06
6	1UH	1WH	B	0.250	0.251	240	240	250	0.45	0.35
7	1UL	1WL	F	0.250	0.251	230	230	250	0.36	0.39
8	1DH	1DL	Both[f]	0.251	0.250	230	230	242	0.24	0.17
9	1UH[e]	1UHa	F	0.511	0.501	230	230	245	0.58	0.78
10	2UH	2UH	F	0.251	0.250	210	240	250	0.60	0.54

[a]Post-reduction (PR) furnace temperature
[b]Temperature at time of reaction gas introduction
[c]Peak sustained temperature during first 50 hours of reaction (activation)
[d]Highest sustained conversion in first 50 hours of activation
[e]Not included in kinetic data sets for parameter estimation.
[f]Both GC instruments were used due to TCD failure on GC F

kinetic data and a plot of reaction rate normalized to 250 °C as a function of time on stream, respectively, for 1WL (FB Run 7). Data points on Figure 2.3 before 150 h show similar slope to the data after; however, the activity after 150 h has clearly decreased. The later set of data shows no further activity decline as illustrated by the tight cluster of repeat data points at 240 °C ($1/T = 1.95 \cdot 10^{-3}$ K^{-1}) from measurements taken 32 h apart.

Figure 2.4 shows rate data during startup normalized to 250 °C and $P_{H_2} = P_{CO} = 6.21$ atm using $E_A = 79{,}000$ J/mol and power law partial pressure dependencies of 0.6 and -0.05, respectively. Actual temperatures ranged from 220 °C to 250 °C. Bed temperature was increased from 230 °C to 250 °C between 14 and 22 h. From 35 to 60 h, flow rate in the reactor was lowered to give higher conversion which resulted in lower observed rates due to internal mass transfer limitations. The data in this period were normalized using a calculated effectiveness factor of 0.8 which is discussed in Section 2.7.2. Rate appears to peak after 140 h. Data from other studies have shown a characteristic activation period for iron catalysts including an initial activity increase sometimes

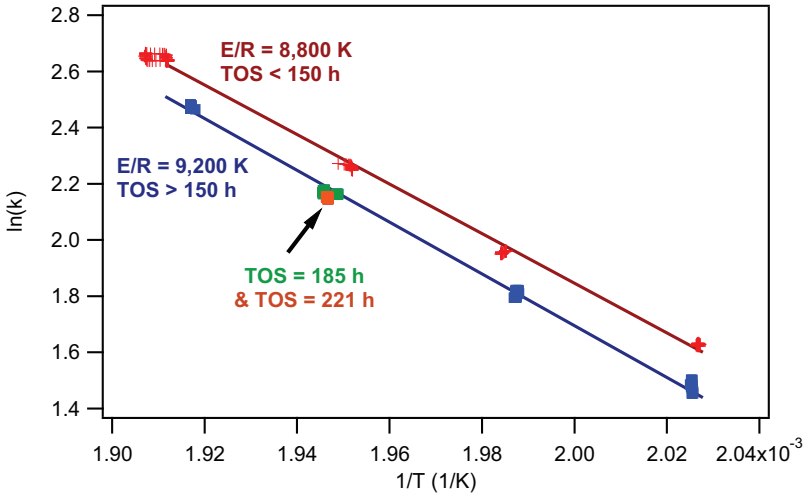

Figure 2.3: Arrhenius plot of kinetic data for 1WL. Rate constant was calculated with $m = -0.05$ and $n = 0.6$.

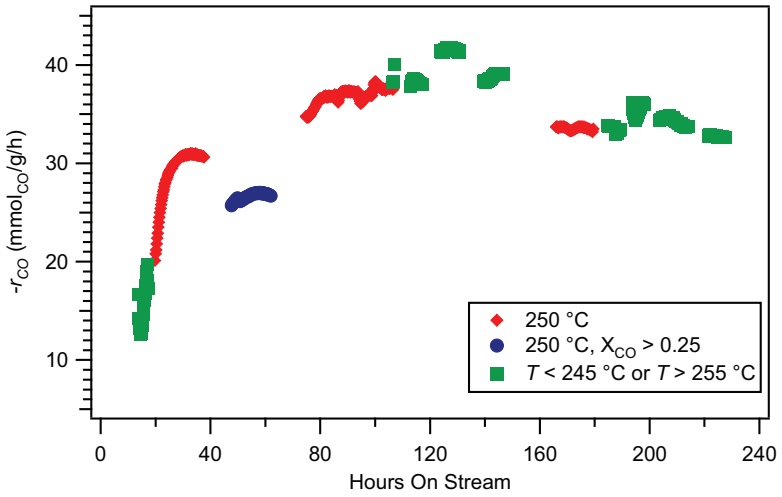

Figure 2.4: Rate data normalized to 250 °C and $P_{CO} = P_{H_2} = 6.21$ atm as a function of time on stream for 1WL.

followed by a decline and changing selectivity over a period of up to 150 h [16, 20, 21, 52, 53]. The increase is attributed to more complete reduction and carbidization of the catalyst in the presence of CO and the decline may be caused by pores filling with wax products which increase diffusion resistance or by deactivation through carbon deposition. As such, data reported in this dissertation within the initial 150 h window were carefully screened and compared to subsequent data before including them in kinetic data sets for parameter estimation.

2.4 Gas Chromatography

Two different Agilent 6890 GC instruments were connected to the FB reactor at different times during the period covering the testing of the 17 catalysts. Both instruments were equipped with two columns and two detectors. Plumbing diagrams for the two instruments and example chromatograms are included in Appendix A.

2.4.1 GC Instrumentation and Operation

The instrument originally connected to the FB was designated GC B and had one packed column connected to a thermal conductivity detector (TCD) and one capillary column connected to a flame ionization detector (FID). Selection of which reactor was sampled by the GC was by three manual 3-way valves which allowed for continuous flow of both reactor effluent streams whether to the GC or to the vent. Injection ports allowed for manual sample loading on each column, but an automated 12-port valve also allowed for continuous simultaneous online sampling from two separate sources (see Figure A.1). This instrument was originally equipped with a 10-port valve for simultaneous sampling of a single source to two columns, but after the first three FB runs of this study, the 10-port valve was replaced with the 12-port valve. The valve temperature was maintained by the GC valve box at 150 °C.

The second instrument had two packed columns and two TCD detectors for simultaneous analysis of the two separate reactor effluent streams and was designated GC F. Two automated 10-port sampling valves, one for each column, were plumbed to operate like 6-port valves and allowed for simultaneous loading of two separate samples to the two columns (see Figures A.2 to A.4). The temperature of the valves and sample loops was maintained at 50 °C in an attached auxiliary oven built by Wasson ECE Instrumentation. Manual injections were not possible on GC F.

The three packed columns in both instruments were made by Supelco and were 4.6 m long stainless steel tubes with a $1/8$ inch tube diameter and packed with $-60/+80$ mesh Carboxen 1000. The packed columns separated H_2, Ar, CO, CH_4, CO_2, C_2H_6, and C_2H_4 for analysis by the TCDs.

The automated pneumatic sampling valves on the GCs allowed for online sampling of the effluent gas. Each 10-port valve of GC F was plumbed with one 1 mL sample loop and the

12-port valve of GC B was plumbed with two 1 mL sample loops. Sample loop pressures on both instruments were controlled by separate back pressure regulators for each loop. Sample loop pressure was set to 15–17 psig depending on the FB run and was held constant throughout the FB run.

The GC temperature program for the first two FB runs in this study was as follows. The initial oven temperature was 50 °C and was held for 5 min. The temperature was increased at 20 °C/min to 225 °C and held for 6.5 min for a total run time of 21 min.

For subsequent FB runs, it was found that increasing the initial GC oven temperature and ramp rate could significantly decrease the run time for each GC injection from 21 min to less than 15 min without compromising the peak integrity of the calibrated species. The initial oven temperature was held at 115 °C for 2.5 min then ramped to 250 °C at 25 °C/min and held for 2.0–7.3 min, depending on the FB run. The range of times for the final hold at 250 °C was due to operator confusion about the true elution time of C_{2+} species (12 min for GC B and 14 min for GC F). Hold times shorter than 5.1 min on GC B (13 min total time) and 7.3 min on GC F (15.2 min total time) caused C_{2+} species of a prior GC injection to elute with the uncondensable species of a subsequent injection. This behavior is discussed in more detail in Appendix A.5. Despite this behavior, the retention time and separation of C_2H_6 from other calibrated species were known for every run because of the use of a calibration standard mixture.

2.4.2 GC Calibration

TCD responses (peak areas) for H_2, Ar, CO, CO_2, CH_4, and C_2H_6 were calibrated by varying the sample loop pressure (total number of moles sampled) while holding temperature constant and sampling a custom gas standard mixture containing these gases prepared and certified by Airgas. C_2H_4 peak areas were not calibrated with a gas standard because the high reactivity of C_2H_4 requires specially constructed, low pressure cylinders which would significantly increase the cost of the gas standard mixture used for calibration. Molar responses for C_2H_4 were estimated by comparing published relative response factors (compared to benzene = 100) for CH_4 (36), C_2H_4 (48), and C_2H_6 (51) to calibrated responses for CH_4 and C_2H_6 [54]. An example calibration curve and analysis are given in Appendix A.

Experimental techniques for catalyst preparation and testing were much less developed For FB Runs 1 and 2 which may have led to less certain results. For example, the GC calibration method for these two runs did not make use of varying the sample loop pressure as described above but relied on a less determinate method of adjusting total flow rates. This would not affect the determination of reaction rates or conversions, but may have affected the quantification of products. Selectivity values for FB Runs 1 and 2 (1ULa, 1WLa, P1, and P2) presented in this dissertation use relative response factors derived from a GC calibration using the sample loop pressure method described above. Relative molar response factors (compared to 1 for Ar) were 0.0608 (H_2), 0.894 (CO), 1.15 (CO_2), 0.727 (CH_4), 1.15 (C_2H_4), and 1.22 (C_2H_6).

2.4.3 Hot and Cold Trap Product Analysis

Liquid and wax products (cold trap and hot trap, respectively) from only 1UHa (FB Run 9) and 2UH (FB Run 10) were analyzed further. Liquid products from the cold trap included an aqueous and an organic (oil) phase which were separated using a pipette. Wax products were dissolved in CH_2CL_2 or hexanes. The solid waxes did not completely dissolve in either solvent until the solution was heated just prior to injection in GC B. The sample vial was heated with the lid in place on the metal plate surrounding the heated (300 °C internal) injection port. After cooling, solid waxes reappeared. Chromatograms of wax products appeared to be unaffected by the choice of solvent particularly since wax products contain very little amounts of light products in the solvent range.

Liquid samples (aqueous, organic, and dissolved wax) were quantified by FID (300 mL/min air, 50 mL/min H_2, 300 °C) in GC B. 2 μL of sample were injected into the injection port in split mode for separation in a Supelco SP-2100 phase capillary column (30 m long, 0.25 mm ID, 0.25 μm film thickness) and detection by FID. A split of 100 : 1 was used for injections of the organic phase samples and a split of of 20 : 1 was used for injections of the aqueous and dissolved wax samples. For each injection, the oven was held at 50 °C for 10 min then ramped at 2.5 °C/min up to 250 °C and held for up to 150 min. Runs were truncated when it was apparent that the sample had completely eluted before the allotted time. It was assumed that all hydrocarbons had a relative mass response factor of 1 and that all oxygenated species had relative mass response factors of

0.85 except for CH_3OH (0.23), C_2H_5OH (0.46), C_3H_7OH (0.60), C_4H_9OH (0.66), and $C_5H_{11}OH$ (0.71).

For FID peak area data, the mass fraction of each species is calculated by dividing the GC peak area (PA) of each species by its mass response factor (RFm). The quotient for each species is then divided by the sum of all quotients for a chromatogram as given by Equation 2.7.

$$\text{Mass Fraction} = \frac{PA_A/RFm_A}{\sum_{i=1}^{n} PA_i/RFm_i} \tag{2.7}$$

Peak identification was achieved by a combination of comparison to chromatograms of injected standards, comparison to GCMS chromatograms, and by analogy to retention times of smaller members of of the same functional group series. Peak identification in this manner was possible because chromatograms of FT products show a characteristic repeating pattern of peaks as described and discussed by others [55]. Figure 2.5 shows the repeating peak pattern of FT products in a portion of a chromatogram of the wax products of 2UH. The full chromatogram is given in Appendix A. Although not all of the peaks were specifically labeled, all of the major peaks were identified as described below. It was assumed that all of the minor peaks preceding the major hydrocarbon groups were branched alkanes or alkenes of the same carbon number as the primary alkane of the group. In reality, a small number of those peaks correspond to oxygenated species including branched alcohols and acids.

For GCMS chromatograms, liquid samples were injected into the injection port of an Agilent 7890 GCMS under the same injection conditions and oven program as for GC B described above, except that the final oven temperature was 300 °C. The 7890 GCMS was equipped with an HP-5 column (30 m long, 0.32 mm ID, 0.25 μm film thickness) and a 5975C MS with electron impact ionization and quadrupole detector. GCMS peaks were identified by comparing ion fragmentation patterns to the NIST database. Chromatograms of the same samples on the 7890 GCMS and on GC B were sufficiently similar to afford analogous identification. Example chromatograms are given in Appendix A.

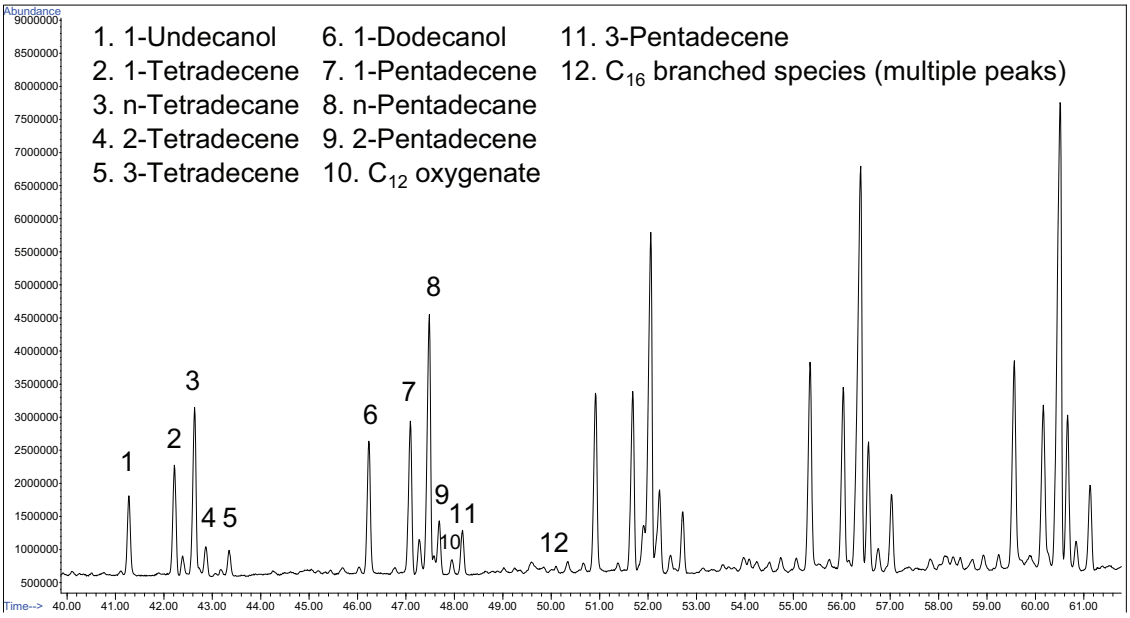

Figure 2.5: Repeating GC peak pattern of FT products around the C_{14}–C_{18} hydrocarbon groups of a wax sample from 2UH. This is a portion of the full chromatogram shown in Appendix A. All of the major peaks were identified by GCMS even though only the first two hydrocarbon groups are specifically labeled.

2.5 Reactor and GC TCD Consistency

The behavior of the two parallel FB reactors and the responses of the two different detectors on GC F were investigated to ensure that the data collected on these apparatus were consistent. Two 0.25 g samples of 2UH were run simultaneously in the two FB reactors at the same temperatures (in the same furnace), pressures, and feed compositions. Gas composition exiting each reactor was monitored by the corresponding detector on GC F: reactor 1 with detector A and reactor 2 with detector B. Figure 2.6 shows an Arrhenius plot of the rate data from the reactors. The data from the two reactors and detectors agree very well indicating good consistency in data collection from the two detectors and very similar reactor performance.

2.6 Procedures for Temperature Variation Experiments

To obtain rate and activity data, reactor flow rates were adjusted to achieve differential conditions and temperature was changed to obtain data at no less than four temperatures. Flow rates in each reactor were chosen in an attempt to limit CO and H_2 conversions to 23% or less at

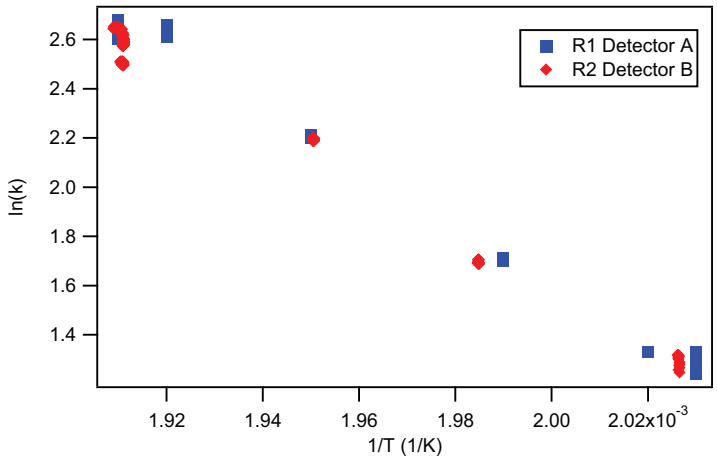

Figure 2.6: Arrhenius plot of rate data for two samples of 2UH run simultaneously in the two FB reactors.

250 °C. Each catalyst was tested at a minimum of four temperatures between 220 °C and 260 °C with repeat measurements of at least one temperature. For some runs and for 250 °C and higher temperatures, maintaining conversions below 23% was not strictly adhered to or may not have been possible due to limitations on mass flow controllers. The error in assuming differential conditions instead of using integral reactor analysis was less than 1% of the rate constant value for the highest measured reaction rate (93 mmol/g/h) with the highest conversion (0.607) at the highest temperature (277 °C) for any catalyst in this study which was from FB Run 2 on 1ULa. This calculation is provided in Appendix B using data from Appendix C. Temperature progression during tests was non-consecutive.

2.6.1 Steady State Conditions

Progress of the reaction was monitored by GC analysis of reactants and gaseous products. Online GC analysis provided continuous conversion and productivity data; however, only steady state subsets of the data were used for kinetic parameter estimation and comparison between catalysts. The ratio of the standard deviation of peak area to the average peak area was monitored with time for the effluent values of each species. The condition for steady state was when this ratio was less than 0.02 for the effluent values of species in the feed (H_2, CO, and Ar) and less than 0.05 for quantified product species (CO_2, CH_4, and C_2H_6). The collection of these steady state subsets of

data for each catalyst make up a kinetic data set. Data at temperatures over 250 °C and higher conversions were included in kinetic data sets only if the data appeared to be free of deactivation and pore diffusion effects on an Arrhenius plot. Kinetic data sets were used for parameter estimation and catalyst comparisons. Calculations for deriving values for rate and selectivity from GC data are given in Section 2.3.4 and Appendix A.

2.6.2 Step Change Time Lag

Each change in temperature created a transient period in the data collection due to changing rate of reaction with temperature and changing gas composition in the hot and cold traps with changing extent of reaction. Figure 2.7 shows a typical transient period in the peak area of CO as a result of changing reactor temperature. Changes in reaction rate were probably relatively fast, but steady-state GC data were observed only after between 2 and 12 h due to large dead volumes in the hot and cold traps. The amount of time over which transient data were observed was a function of flow rate and the difference between previous and subsequent gas compositions due to X_{CO}.

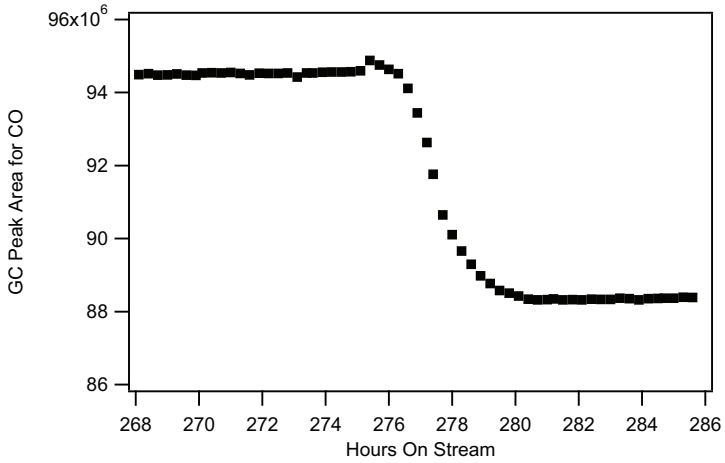

Figure 2.7: Typical transient period in CO peak area caused by changing reactor temperature from 220 °C to 240 °C for R1 of FB Run 10 (2UH) with a feed flow rate of 135 mmol/h.

2.6.3 Activation Energy and Pre-Exponential Factor Estimation

To estimate activation energies and pre-exponential factors, several quantities were calculated from the kinetic data sets. Experimental rates of reaction were calculated using Equations 2.4 and 2.5. FB runs which produced the temperature kinetic data sets were run with similar inlet concentrations of CO and H_2, but since the X_{CO} varied somewhat, the average P_{CO} and P_{H2} varied slightly.

To determine values of the rate constant, it was assumed that the rate followed a simple power law equation. In reality, the kinetic orders change with temperature and partial pressure. A more rigorous full kinetic study would collect data and fit kinetic parameters for a Langmuir-Hinshelwood type rate expression which accounts for shifting orders of reaction, but that is beyond the scope of this work. Since this work is only concerned with comparing relative activities of catalysts, a power-law model is adequate.

The dependencies on the partial pressures of CO and H_2 were assumed to be consistent with the dependencies proposed by Eliason [56] as in Equation 2.8.

$$-r_{CO} = kP_{CO}^{-0.05}P_{H_2}^{0.6} \tag{2.8}$$

Eliason developed his rate expression for an unsupported, potassium promoted iron catalyst (100 g iron to 0.9 g potassium) which was wash-coated onto a monolith. The Arrhenius law (Equation 2.9) provided a relationship between rate constant (k), and the activation energy (E_A) and pre-exponential factor (A).

$$k = Ae^{-E_A/RT} \tag{2.9}$$

Rate constant was calculated from measured quantities using Equation 2.10.

$$k = \frac{-r_{CO}}{P_{CO}^{-0.05}P_{H_2}^{0.6}} \tag{2.10}$$

Partial pressures (P_{CO} and P_{H_2}) were calculated from the averages of the mole fractions of CO and H_2 at the inlet and outlet of the reactor and from the total pressure of the reactor. With all other values known or calculated, values of E_A and A were regressed by non-linear least squares

minimization of the kinetic data sets described above using the nlstools package of the R Project statistical computation software [57, 58].

Since the pre-exponential factor and activation energy are highly correlated parameters, traditional confidence intervals are misleading in expressing the confidence ranges of these parameters. Instead, approximate joint 95% confidence regions were calculated for each set of fitted parameters and plotted on charts like Figure 2.8. Confidence regions were calculated using the nlsConfRegion function of the nlstools package. Rather than outlining a continuous region, Figure 2.8 shows 1,000 randomly generated points which fall within the 95% confidence region and which allow the reader to visualize the whole region. The R script used for estimating the parameters and the confidence regions for all 17 catalysts is given in Appendix B.

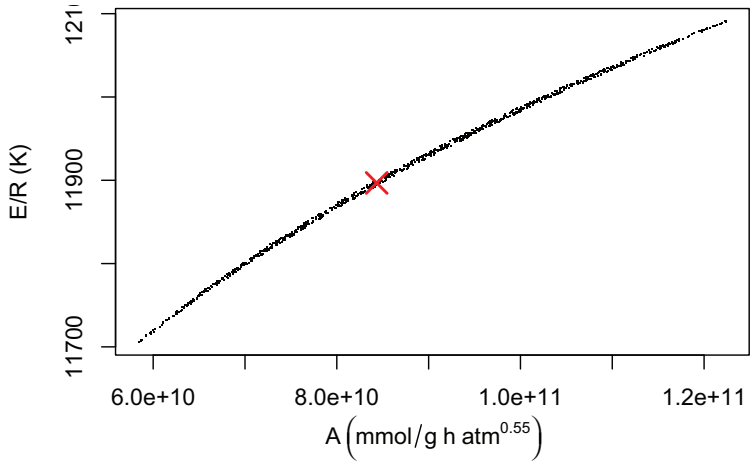

Figure 2.8: Example of an approximate joint 95% confidence region for estimated values of E/R and A for 1UH. The least-squares best estimate of the parameters is indicated by a red X.

2.6.4 FB Runs Excluded From Kinetic Analysis

Data of Run 5 (see Table 2.5) showed exceptionally high values of activity for 2UH. Run 10 confirmed the high activity of 2UH even though the measured rate of reaction was lower (21%) than measured in Run 5. The difference is probably due to the issue of initially high, but unsettled activity described earlier (see Section 2.3.5) since Run 5 was conducted for only 108 h. In addition, analyzed rate data of Run 10 over 539 h demonstrate a constant, linear decrease in activity with

time indicating slow deactivation which may have been observed for 2UH in Run 5 had it been run for a longer period of time. Given the likelihood of higher quality data from Run 10, they were used to characterize and estimate parameters for 2UH reported in the charts and tables that follow. The temperature kinetic data for 2UH of Run 10 (except for one additional point at 528 h) were obtained within a period of 107 h (from 206 to 313 h on stream). The estimated total decline in activity from 206 to 313 h was less than 6%. Given the low rate of deactivation, the data for 2UH were not corrected for deactivation in estimating activation energy and pre-exponential factors for comparison with other catalysts; however, the partial pressure data were corrected for deactivation as part of the analysis described in Sections 2.7.2 to 2.7.4 and 4.7. Data from Run 5 for 2UH are reported only in Appendix C. Run 5 for 2WL was not repeated as the observed activity was significantly lower than other catalysts, nevertheless, rate and characterization data were reported for this catalyst.

Some repeat FB runs gave much lower activity than the initial runs. Specifically, 1UH of Run 9 and a repeat of Run 8 for 1DH and 1DL (not shown in Table 2.5) resulted in significantly lower measured rates of reaction than in Runs 6 and 8. The sample of 1UH for Run 9 may have been contaminated as it was left exposed to the atmosphere for more than a day after it was weighed out before it was loaded into the reactor. In addition to possible contamination, the catalyst may have dropped from the bed into the hot trap during reaction despite careful packing. The sample of 1UHa for the same run was loaded immediately into the reactor after weighing and was not left exposed to air as 1UH was. The data for the repeat of FB Run 8 are not shown in Table 2.5; there may have been a malfunction or a poor calibration of the H_2 mass flow controller and it is possible that the catalyst may have been lost from the bed into the hot trap. These data (1UH of Run 9 and the repeat of Run 8) were not included in parameter estimation data and selectivity data, are not reported in subsequent tables or figures, and are not discussed further in this dissertation.

2.7 Procedures for Partial Pressure Variation Experiments

Besides rate versus temperature experiments, experiments to determine the dependence of rate on partial pressures of CO and H_2 were performed on 2UH (FB Run 10). The goal was to

estimate the kinetic orders of reaction for the rate model given in Equation 2.11 for 2UH.

$$-r_{CO} = kP_{CO}^{m}P_{H_2}^{n} \tag{2.11}$$

2.7.1 Optimal Design of Experiments

A D-optimal design of experiments [59] was used in which the powers m and n were assumed to be -0.05 and 0.6, respectively consistent with Equation 2.8. The purpose of a D-optimal design is to collect data at conditions which will minimize the error of the estimated parameters. Optimal design analysis indicated that the two levels of P_{CO} should be as high and as low as practical and that $P_{H_2}^{low} = 0.19P_{H_2}^{high}$. Levels of P_{CO} and P_{H_2} were chosen in consideration of limitations of the mass flow controllers and of avoiding extreme conditions ($H_2/CO < 0.7$) thought to induce deactivation. Mass flow controller limitations meant that minimum reactant partial pressure for H_2 was greater than the optimal design indicated (4.5 atm compared to 2.2 atm) and that the maximum partial pressure for CO was only 7.7 atm. The experimental design, levels of partial pressures, and randomized run order are given in Table 2.6. Each condition was replicated for a total of eight runs and the run order was randomized.

Table 2.6: Optimal design of partial pressure variation experiments and run order.

Condition	Order	P_{CO} (atm)	P_{H_2} (atm)	H_2/CO
1	1,6	7.7	5.6	0.74
2	2,4	6.1	4.5	0.73
3	3,7	5.7	11.5	2.03
4	5,8	2.9	5.8	2.02

2.7.2 Pore Diffusion Calculations

Pore diffusion is the transportation of reactants through catalyst pores to the active catalyst surface. In the FTS, the catalyst pores quickly fill with liquid and wax products which can

impede the transport of the reactants and thereby limit the observed rate of reaction. Since intrinsic rate data are required for meaningful kinetic parameter estimation, pore diffusional resistance must be minimized. Pore diffusion resistance can be reduced by decreasing both particle size and temperature.

Diffusion effects are estimated by an effectiveness factor (η) which is the ratio of the observed to intrinsic rate of reaction. Effectiveness factor is calculated from the Thiele modulus (ϕ) or Weisz modulus (M_W) using Equations 2.12–2.14 [60].

$$M_W = L_{p_e}^2 * \frac{m+1}{2} * \frac{-r_{CO} * \rho_b}{D_e * P_{CO}} * R * T \tag{2.12}$$

$$M_W = \phi^2 * \eta \tag{2.13}$$

$$\eta = \frac{1}{\phi} * \left(\frac{1}{tanh(3*\phi)} - \frac{1}{3*\phi} \right) \tag{2.14}$$

Calculations of η and ϕ are iterative. Note that the observed reaction rate (not intrinsic) is used in calculations of M_W. Equation 2.14 is specifically for spherical particles. The effective diffusion length (L_{p_e}) for spherical particles is $1/6$ of the particle diameter. A more in depth discussion of the effective diffusivity (D_e) and how it is calculated is given in Section 5.4. Pore diffusion effects are important when $\eta < 0.93$ or $\phi > 0.40$.

Pore diffusion was neglected for all kinetic temperature experiments because calculations for 1UHa, the most active catalyst in this study, showed $\eta > 0.94$ for $T \leq 250\,^{\circ}$C and $\eta = 0.91$ ($\phi = 0.41$) for $T = 260\,^{\circ}$C which is just within the lower limit of significant pore diffusion resistance. It was assumed that less active catalysts would have smaller pore diffusion resistance at similar T, P_{CO}, and P_{H2}.

Pore diffusion calculations were applied to the kinetic data set for the partial pressure study of 2UH described in Sections 2.7 and 4.7. Pore diffusion calculations were also applied to the high X_{CO} portions of the data shown in charts of rate or rate constant.

2.7.3 Deactivation Model

Deactivation was modeled in order to better estimate intrinsic kinetic parameters. This analysis was used exclusively with the results of the partial pressure kinetic experiments on 2UH

to correct for observed deactivation in the kinetic data described in Section 4.7.1. Furthermore, this treatment was only applied to data from R2 of FB Run 10. This analysis was not applied to other catalysts, though it is generally applicable to the study of deactivation.

A full deactivation study is beyond the scope of this work. Such a study would ideally make use of a Langmuir-Hinshelwood rate model and would capture the temperature dependence of the deactivation rate as in Equations 2.15 and 2.16.

$$-r_{CO} = f(C,T)a_k = \frac{kP_{CO}^{0.5}P_{H_2}^{0.75}}{\left(1+k_1P_{CO}^{0.5}P_{H_2}^{0.25}\right)^2}\cdot a_k \tag{2.15}$$

$$-\frac{da_k}{dt} = k_d = A_d e^{-E_d/RT} \tag{2.16}$$

Equation 2.15 was developed from elementary steps of the carbide mechanism for iron FTS [61]. The two equations above would be solved simultaneously on a large enough collection of data to give good statistical estimates of the fitted parameters. Eliason [56] concluded that for a more rigorous study Equation 2.16 should also be a Langmuir-Hinshelwood form as opposed to the simple form shown above which assumes zero order in P_{CO} and P_{H_2}.

Since FB Run 10 was not intended to collect deactivation or even extensive kinetic data and since most of the data were collected at a single temperature which appeared to have a constant linear decline in activity, a simpler approach was used. The rate of deactivation (r_d) is defined in Equation 2.17 as the time rate of change of activity (a_k).

$$r_d = -\frac{da_k}{dt} \tag{2.17}$$

The value of r_d is calculated from measured quantities using the following derivation. Assuming r_d is constant and integrating Equation 2.17 yields Equation 2.18.

$$a_k(t) = a_k(0) - r_d t \tag{2.18}$$

Activity is defined as the ratio of the intrinsic reaction rate ($r_{CO}(t)$) at any time (t) to the initial intrinsic reaction rate ($r_{CO}(0)$) for a constant set of conditions (i.e. T, P_{CO}, and P_{H2}). By this

definition, initial activity ($a_k(0)$) is 1. Assuming that the rate is a power law equation and that dependencies on P_{CO} and P_{H2} are constant yields (Equation 2.19).

$$a_k(t) = \frac{-r_{CO}(t)}{-r_{CO}(0)} = \frac{k(t)}{k(0)} \tag{2.19}$$

Rearranging for $k(t)$ and substituting Equation 2.18 for $a_k(t)$ produces Equation 2.20.

$$k(t) = a_k k(0) = k(0) - r_d k(0) t \tag{2.20}$$

Equation 2.20 is linear in t based on the initial assumption of constant r_d with the intercept equal to $k(0)$ and the slope equal to $-r_d k(0)$. Values of k are calculated from observed rate ($-r_{CO,obs}$) and measured partial pressures by Equation 2.21 which also accounts for pore diffusion resistance.

$$k(t) = \left(\frac{1}{\eta}\right) \frac{-r_{CO,obs}}{P_{CO}^m P_{H_2}^n} \tag{2.21}$$

Once the intercept and slope are known, calculating r_d requires simple algebra.

Combining Equation 2.20 with Equation 2.11 and accounting for pore diffusion resistance gives Equation 2.22.

$$-r_{CO}(t) = \eta a_k(t) k(0) P_{CO}^m P_{H_2}^n \tag{2.22}$$

The Arrhenius law relates k to E_A and A (Equation 2.10) and $a_k(t)$ is expanded by Equation 2.18 in Equation 2.23.

$$-r_{CO}(t) = \eta\,(1 - r_d t) A e^{-E_A/RT} P_{CO}^m P_{H_2}^n \tag{2.23}$$

Estimates of the true values of A, E_A, m, n, r_d, and η can be solved simultaneously in an iterative calculation.

For this study which was meant to produce a simple correction for slow deactivation, deactivation was estimated from data taken at $T = 250$ °C and $P_{CO} \approx P_{H2} \approx 6.2$ atm. To obtain the largest possible representative subset of steady state data at a single temperature for 2UH, the kinetic data at temperatures other then 250 °C and for the partial pressure experiments were excluded leaving only the data at 250 °C at the initial partial pressure conditions. This subset of data

was combined with data from the first 200 h on stream which included some high conversion data ($0.25 < X_{CO} < 0.54$) to make a deactivation data set.

2.7.4 Algorithm for Parameter Estimation from Deactivation Data

The analysis presented below was applied specifically to data from R2 of FB Run 10 on 2UH and to no other catalyst or FB run in this study. The deactivation data set included all steady state data at 250 °C from R2 of FB Run 10 for which $P_{CO} \approx P_{H_2} \approx 6.2$ atm, including the high X_{CO} data before 200 h. The reaction conditions and kinetic data sets are given in Section 4.7.1. The results of using this algorithm for parameter estimation on 2UH data are given in Section 4.7.2.

The algorithm is shown in Figure 2.9 and is described as follows. First, an estimate of the CO partial pressure dependence (m) in Equation 2.22 is used to calculate new estimates of η from Equations 2.12–2.14 for each data point in the kinetic and deactivation data sets. Then, values of $k(t)$ are calculated from Equation 2.21 for the deactivation data set with minor adjustments for temperature variations (via E_A). Next, estimates of r_d and $k(0)$ are regressed according to Equation 2.20 and a_k is calculated from Equation 2.19. Finally, the new values of η and a_k are input to the rate equation and new values of A, E_A, m, and n are regressed according to Equation 2.22 from the kinetic data set using a non-linear least squares method. The process is repeated until values of A, E_A, m, n, r_d, and $k(0)$ converge to an acceptable tolerance. For the R2 data of FB Run 10 on 2UH and using the nlstools package of the R Statistical Computation Software [57, 58], values of these 6 variables converge to 4 significant figures within 6 iterations.

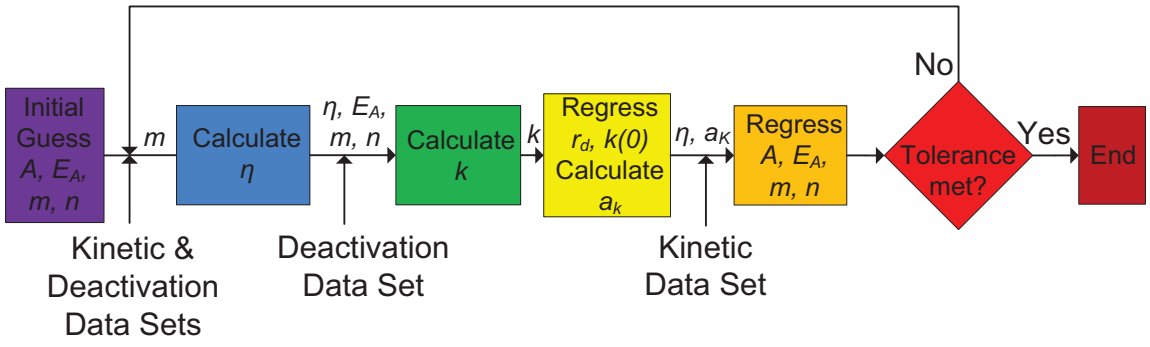

Figure 2.9: Algorithm for simultaneously estimating parameters from data that include deactivation.

2.8 Off-site Catalyst Testing of 1ULC

As mentioned previously, the 1ULC catalyst was prepared and tested by commercial collaborators. The calcined catalyst was bulk reduced in several batches using BYU Catalysis Lab equipment and procedures described earlier. In preparation for testing, 10 mL of catalyst (1.06 g_{cat}/mL) sieved between 80 and 120 mesh were charged to a single FB reactor tube. The passivated catalyst was re-reduced in situ in 10% H_2/He with $SV = 300$ h^{-1}. The temperature was ramped at 0.5 °C/min from ambient to 260 °C with a 1 h soak at 110 °C and a 2 h soak at 190 °C. Temperature was held at 300 °C for 8 h and then H_2 content was increased to 100% ($SV = 2,000$ h^{-1}) for an additional 8 h soak.

Following in situ reduction, the catalyst was activated in syngas. First, the temperature was reduced to 210 °C in H_2. Over several minutes, CO was added to give a H_2/CO of 1.0. Next, pressure was gradually increased to 20 atm and flow was increased to give $SV = 3,000$ h^{-1}. Finally, temperature was gradually increased over several hours up to 260 °C and flow rate was adjusted over several hours to allow conversion of CO to increase to between 65% and 70% and reach steady state for 10 h.

After activation, the reactor temperature was decreased to 230 °C for steady state data and product acquisition. The feed composition was adjusted to 50% N_2, 30% H_2, and 20% CO ($H_2/CO = 1.5$). CO conversion was maintained below 60%. Steady state data were collected at 28.5 atm, 23.2 atm, 18.3 atm, and 12.4 atm absolute pressure. Liquid products and wax products were collected at the latter three pressures. Total time on stream was more than 867 h.

Preliminary gas, liquid, and wax product analysis data were provided along with conversion and rate data by the testing facility (EFT). The product distribution was later analyzed at BYU to give total mass compositions of the products and to calculate an Anderson-Schultz-Flory propagation probability term.

CHAPTER 3. RESULTS AND DISCUSSION OF CHARACTERIZATION EXPERIMENTS

After preparation, the 12 catalysts of the factorial experiments and the 5 repeat and other preparations were subject to the characterization techniques described in Chapter 2 and the results are reported in the following sections. Before reporting these results, pertinent results of the preliminary experiments are presented and discussed. These preliminary experiments definitively identified several key preparation variables from which the catalyst preparation method and factorial experiments were developed.

3.1 Preliminary Experiments

Several preliminary experiments helped to identify preparation variables involved in the solvent-deficient preparation method. The first experiments were performed to become familiar with the solvent-deficient precipitation reaction and stoichiometry. The precipitation reaction producing the iron precursor is given in Equations 3.1 and 3.2.

$$Fe(NO_3)_3 \cdot 9\,H_2O + 3\,NH_4HCO_3 \longrightarrow Fe(OH)_3 + 3\,NH_4NO_3 + 9\,H_2O + 3\,CO_2 \tag{3.1}$$

$$Fe(OH)_3 \longrightarrow FeOOH \cdot H_2O \tag{3.2}$$

The $Fe(OH)_3$ quickly converts to $FeOOH \cdot H_2O$. XRD spectra of the iron oxide precursors after drying show broad peaks consistent with 2-line ferrihydrite [27, 29] , an amorphous hydrated iron oxyhydroxide with particle sizes between 2 and 4 nm. No official structure or formula has been assigned to ferrihydrite, but it may be represented by $Fe_5HO_8 \cdot 4\,H_2O$, $Fe_2O_3 \cdot 2\,FeOOH \cdot 2.6H_2O$, or $5\,Fe_2O_3 \cdot 9\,H_2O$ which are stoichiometrically identical to $FeOOH \cdot 0.4H_2O$ [62]. Unwashed precursors also show strong (highly crystalline) NH_4NO_3 XRD peaks.

Subsequent experiments focused on adding promoters and the effect of the washing step on the precursor. Table 3.1 reports surface areas of several preliminary metal oxide preparations after calcination at 300 °C for 5 hours (materials were first dried at 60 °C followed by drying at 120 °C). Four of these experiments were not considered full catalyst preparations and are designated by a G followed by U or W as appropriate and by an L (since all of these preparations were dried first at 60 °C). Subsequent iterations of similar preparations are denoted by a small letter "a" or "b". Comparing washed to unwashed oxides (GUL to GWL, GULa to GWLa, and 1ULa to 1WLa) reveals a 65–100% increase in BET surface area and a 45–50% increase in pore volume when the precursor is washed. Washing removes the NH_4NO_3 byproduct which accounts for up to 50% of the precursor mass after precipitation.

Table 3.1: Preliminary Fe and Cu oxide preparations using solvent deficient precipitation. BET data are given for calcined samples.

ID	Fe pbm[b]	Cu pbm	K[a] pbm	SiO_2[a] pbm	Unwashed/ Washed	BET SA (m^2/g)	Pore Vol. (mL/g)
GWL	100	5.1			W	56	0.31
GUL[c]	100	5.0			U	28	0.07
GULa	100	5.0		16.6_A	U	168	0.18
GULb	100	5.4		16.2_B	U	169	0.17
GWLa	100	5.0	4.0_A	15.8_B	W	280	0.31
1ULa	100	5.0	4.0_B	16.0_B	U	161	0.19
1WLa	100	5.0	4.0_B	15.4_B	W	262	0.28

[a]Subscripts denote K and/or SiO_2 added Before (with salts) or After precipitation (and washing if applicable)
[b]pbm = nominal parts by mass equal to g per 100 g Fe
[c]GUL and GULa were precipitated in a single batch

In the presence of water and with the byproduct removed, the precipitated metal crystallites are free to reorganize themselves. After calcination at 300 °C, XRD spectra show two very different patterns for the unwashed and washed catalysts. Unwashed catalysts give spectra consistent with Fe_2O_3 mixed with some ferrihydrite while spectra of washed catalysts show only 2-line ferrihydrite. Immediately after precipitation, the liquid product of the reaction is nearly saturated with NH_4NO_3 and may interfere with particle-particle interactions of the crystallites. The presence

of Fe_2O_3 after calcination for unwashed catalysts may be caused by more facile transformation of uncoordinated ferrihydrite particles to Fe_2O_3. Alternatively, the decomposition of NH_4NO_3 may catalyze the transformation. In either case, there is a structural difference between washed and unwashed catalysts, that of the washed catalysts resulting from some form of reorganization.

Adding SiO_2 enhances surface and pore characteristics. Comparing surface areas of catalysts with and without SiO_2 (GWL to GWLa and 1WLa; GUL to GULa, GULb, and 1ULa) shows that adding SiO_2 increases surface area by more than 300% (4–6 fold increase). Comparing pore volumes for these same groups of catalysts shows that adding SiO_2 does not improve pore volumes for washed catalysts, but does increase pore volumes in unwashed catalysts by 150%. The fine 2 and 4 nm crystallites that are the product of the precipitation reaction have inherently high surface areas and pore volumes. As an example of the most amorphous and porous iron oxide nanostructure, the surface area of ferrihydrite is 225–350 m^2/g and the pore volume is 0.39–0.54 cm^3/g after drying up to 100 °C [63, 64]. Ferrihydrite surface areas and pore volumes are known to decrease when higher calcination temperatures are used which lead to dehydration and pore collapse. The inherent high surface area and porosity of the oxide combined with the relatively small loading of SiO_2 suggests that rather than adding surface area and pore volume, the SiO_2 preserves some of the original pore structure through the calcination process which is consistent with the findings of others [16]. The presence of even small amounts of SiO_2 delays the bulk transition of ferrihydrite to hematite (from 340°C to 740°C, depending on loading) [64]. With the removal of the byproduct by washing, more of the oxide pore structure is open and available for SiO_2 impregnation. For unwashed catalysts in which the SiO_2 is added after reaction, the SiO_2 easily fills large voids between particles in agglomerates, but must diffuse through pores filled with a nearly saturated solution of the NH_4NO_3 byproduct in order to penetrate through the entire structure. As seen in the unwashed catalysts (GULa, GULb, and 1ULa), there is no apparent difference between adding the SiO_2 before or after precipitation, suggesting that the SiO_2 is quickly and effectively attracted to the iron hydroxide structure.

In short, preliminary catalysts show a number of significant findings. The product of the solvent-deficient precipitation is ferrihydrite. Washing increases surface areas and pore volumes of the precursor significantly. Unwashed precursors readily convert to Fe_2O_3 during calcination at 300 °C while washed precursors retain the ferrihydrite structure. Adding SiO_2 increases surface

area by more than 300% for all precursors and increases pore volumes of unwashed precursors by 150%.

3.2 Composition

The remainder of this chapter focuses on the twelve catalysts of the factorial experiments. The twelve catalysts are referred to in groups of four, namely 1S for the four 1 Step catalysts of the 2^3 factorial design, 2S for the four 2 Step catalysts of the 2^3 factorial design, and D for the four catalysts of the 2^2 factorial design (see Tables 2.1 and 2.2). The repeat preparations are occasionally discussed in order to emphasize specific trends observed in the other preparations, but data for all catalysts are presented in tables when available.

Catalyst elemental compositions determined by ICP analysis are shown in Table 3.2 and are in good agreement with nominal compositions, except for the washed catalysts of the 1 Step preparation. Washed 1S and 1D catalysts show almost complete loss (92% by mass) of K as expected after a significant amount of washing. ICP analysis of Si content in all cases was unreliable due to the formation of volatile SiF_4 during digestion and therefore are not reported. For 1UH, 1UL, and all 2S and 2D catalysts, nominal SiO_2 content should be accurate since these catalysts were either not washed, or else washed prior to the addition of SiO_2 and losses of Fe precursor to equipment or washing during preparation were small (estimated $< 5\%$).

ICP analysis of the seven retained washes (five washes for 1W catalysts and 1 wash each for 1DH and 1DL) confirms the presence in the washes of nearly all of the K and the absence of SiO_2 (Table 3.3). Since the potassium concentrations in the first washes are too high for quantification, they must account for more than the 24.6% loss from the second wash. That suggests a minimum potassium mass loss for 1WH and 1WL of 70%. The actual mass loss of K in the first washes is likely 47%, giving a total loss of 92% as estimated from analysis of the digested catalysts. By contrast, the mass of Si lost to washing is less than 0.1% in every case. Fumed SiO_2 is insoluble in water, but it will disperse in clusters in water and is a well known thickening agent. Anchored to the hydroxide precursor and in the absence of hydrofluoric acid, the SiO_2 in the catalyst does not re-disperse during washing and the SiO_2 in washes does not form volatile compounds, thus ICP measurements of the washes show that the nominal SiO_2 content of the catalysts should reflect actual content.

Table 3.2: Nominal and measured elemental compositions of prepared catalysts.

Catalyst	Nominal composition pbm[c]	ICP composition[a] pbm	Fe Content[b] mass%
1UH	100Fe/5.0Cu/4.0K/16.0SiO_2	100Fe/5.1Cu/3.6K	66.3
1UL	100Fe/5.0Cu/4.0K/16.0SiO_2	100Fe/4.8Cu/3.7K	72.1
1WH	100Fe/5.0Cu/4.0K/16.0SiO_2	100Fe/4.9Cu/0.3K	62.1
1WL	100Fe/5.0Cu/4.0K/16.0SiO_2	100Fe/5.1Cu/0.3K	70.2
2UH	100Fe/5.0Cu/4.2K/16.1SiO_2	100Fe/4.1Cu/3.6K	68.0
2UL	100Fe/5.0Cu/4.0K/16.0SiO_2	100Fe/5.5Cu/4.2K	62.8
2WH	100Fe/5.0Cu/4.0K/16.1SiO_2	100Fe/5.3Cu/5.2K	65.1
2WL	100Fe/5.0Cu/4.2K/16.0SiO_2	100Fe/5.1Cu/5.0K	72.8
1DH	100Fe/5.0Cu/4.0K/16.0SiO_2	100Fe/5.6Cu/0.4K	62.2
1DL	100Fe/5.0Cu/4.0K/16.0SiO_2	100Fe/5.3Cu/0.4K	58.4
2DH	100Fe/5.0Cu/4.1K/16.1SiO_2	100Fe/5.2Cu/4.6K	68.3
2DL	100Fe/5.1Cu/4.0K/16.1SiO_2	100Fe/5.3Cu/5.1K	67.6[d]
1UHa	100Fe/5.0Cu/4.0K/16.1SiO_2	100Fe/5.1Cu/4.2K	64.9
1ULa	100Fe/5.0Cu/4.0K/16.0SiO_2	100Fe/5.4Cu/3.9K	66.5
1WLa	100Fe/5.0Cu/4.0K/15.4SiO_2	100Fe/5.4Cu/1.1K	62.8

[a]SiO_2 not quantified by ICP
[b]after reduction and passivation
[c]parts by mass equal to g per 100 g_{Fe}
[d]assumes ICP measurement of 2DL is 30% too high

Table 3.3: Loss of promoters (mass%) to washing as determined by ICP.

	1WH and 1WL					1DH	1DL
Ele.	Wash 1	Wash 2	Wash 3	Wash 4	Wash 5	Wash 1	Wash 1
Fe	0.0	0.0	0.0	0.0	0.0	0.0	0.0
Cu	0.53	0.12	0.05	0.01	0.005	0.56	1.25
K	-sat-[a]	24.6	11.2	7.1	2.5	-sat-	-sat-
Si	0.01	0.03	0.04	0.07	0.08	0.03	0.05

[a]saturated detector signal

3.3 Promoter Distribution

With the elemental composition of the catalyst established, the question of elemental distribution is now addressed. Figures 3.1 to 3.4 are microprobe images of 1UH, 1WH, 2UH, and 2WH and show Fe, Cu, K, and SiO_2 for each catalyst at the micron scale. They indicate differences in elemental distributions between 1S and 2S catalysts and between U and W catalysts. Since Fe constitutes 60%–66% of these passivated catalysts, images of the other elements are compared to images of Fe to show contrasts in distributions.

Figure 3.1 shows a microprobe image of a 320 μm agglomerate of 1UH. Figures 3.1(b) to 3.1(d) show uniform intensities and give the same details of cracks and boundaries as Figure 3.1(a). This indicates that the Cu, K, and Si distributions are uniform and that the promoters are in intimate association with Fe. Images of 1UL are similar to images of 1UH.

Figure 3.2 shows uniform intensities of Fe, Cu, K, and SiO_2 in a 160 μm agglomerate of 1WH. Figure 3.2(d) exhibits strong intensities and shows the same details of the agglomerate structure as Figure 3.2(a) suggesting uniform distribution and contact of SiO_2 with Fe. The weak signal of Figure 3.2(c) is indicative of the low K content of 1WH. Images of 1WL are similar to 1WH.

A 50 μm view of an agglomerate of 2UH (Figure 3.3) shows a marked difference in elemental distributions of K and Si compared to 1UH and 1WH. While Figures 3.3(a) and 3.3(b) show uniform distributions of Fe and Cu, Figures 3.3(c) and 3.3(d) show preferential distributions of K and Si along particle boundaries. The center of the agglomerate shows almost no signal for K and Si, but since the signals lack sharp and well defined edges, it appears that the promoters are distributed within outer structures and spaces and beginning to penetrate inward with the much smaller K^+ ions penetrating farther than the large clusters of SiO_2. This observation is supported by the fact that water was not added to 2UH during promoter addition as the precursor appeared moist enough to completely dissolve the $KHCO_3$ and SiO_2. The minimal amount of moisture distributed the promoters between particles, but the pores, already filled with a nearly saturated solution of NH_4NO_3 byproduct, presented some diffusional resistance for the promoters and prevented full penetration and uniform dispersion of the promoters.

A 50 μm view of an agglomerate of 2WH (Figure 3.4) shows much better penetration of K and Si into the particles than does Figure 3.3. The K signal in Figure 3.4(c) appears to reflect

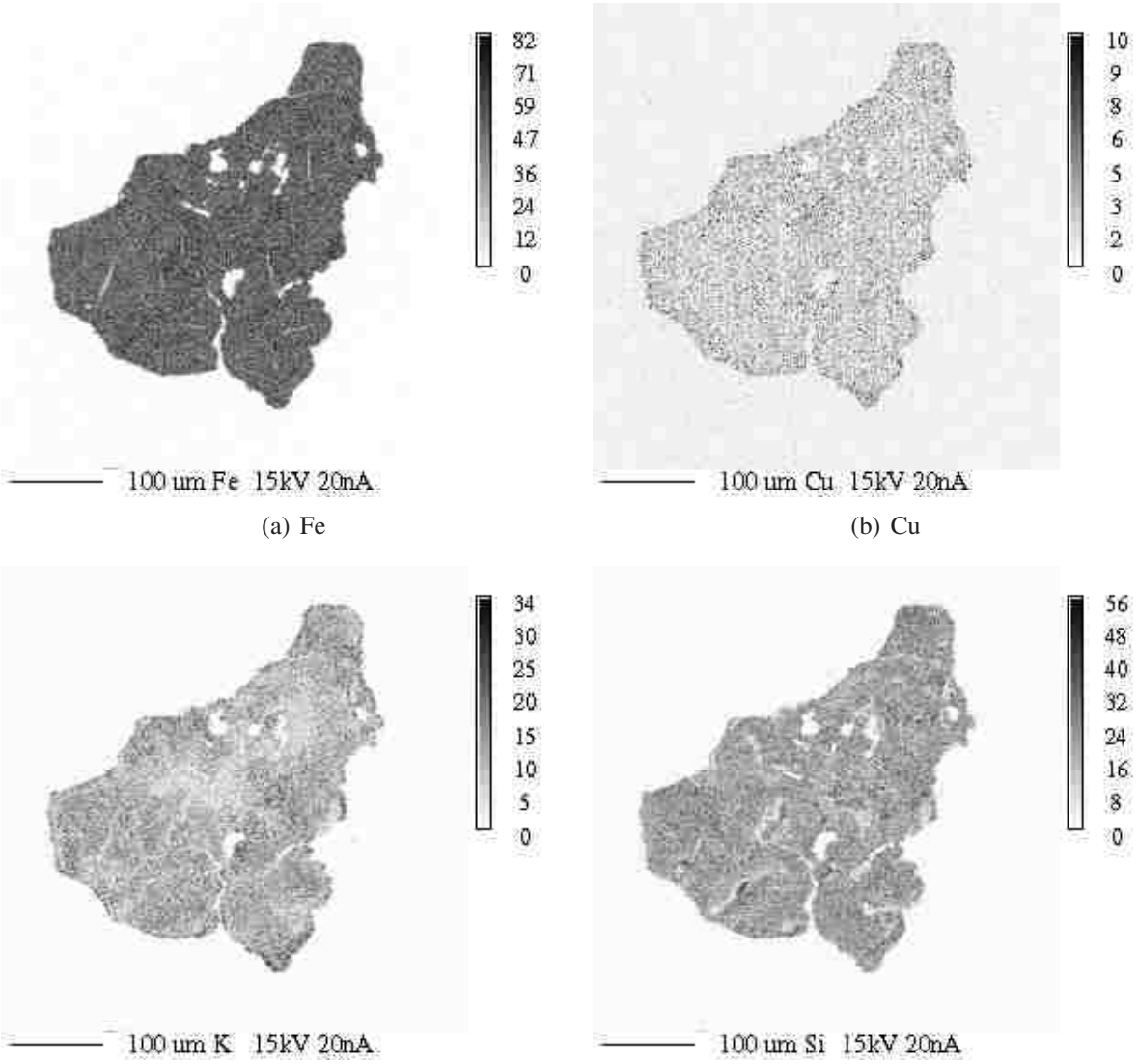

(a) Fe (b) Cu

(c) K (d) Si

Figure 3.1: Electron microprobe images of an agglomerate of 1UH showing distributions of Fe, Cu, K, and Si.

the structure shown by the Fe signal in Figure 3.4(a) and shows no preferential accumulation at particle boundaries. The very center of the agglomerate shows some decrease, but not complete absence of signal. The Si signal in Figure 3.4(d) clearly shows the structure and defects observed in Figure 3.4(a). The signal within the agglomerate is uniform despite the fact that the outside edges of the particle show well defined edges and stronger signal. Strong signal is also shown in spaces devoid of Fe signal between closely spaced particles. This is explained in part by the washing process and method of promoter addition. For 2WH, promoters were first dissolved in a

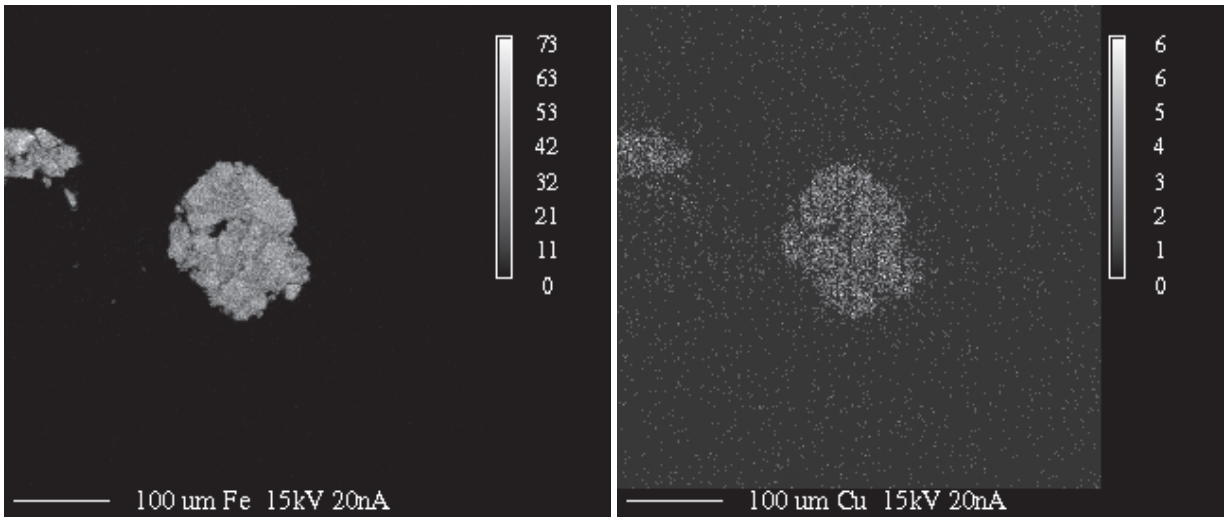

(a) Fe (b) Cu

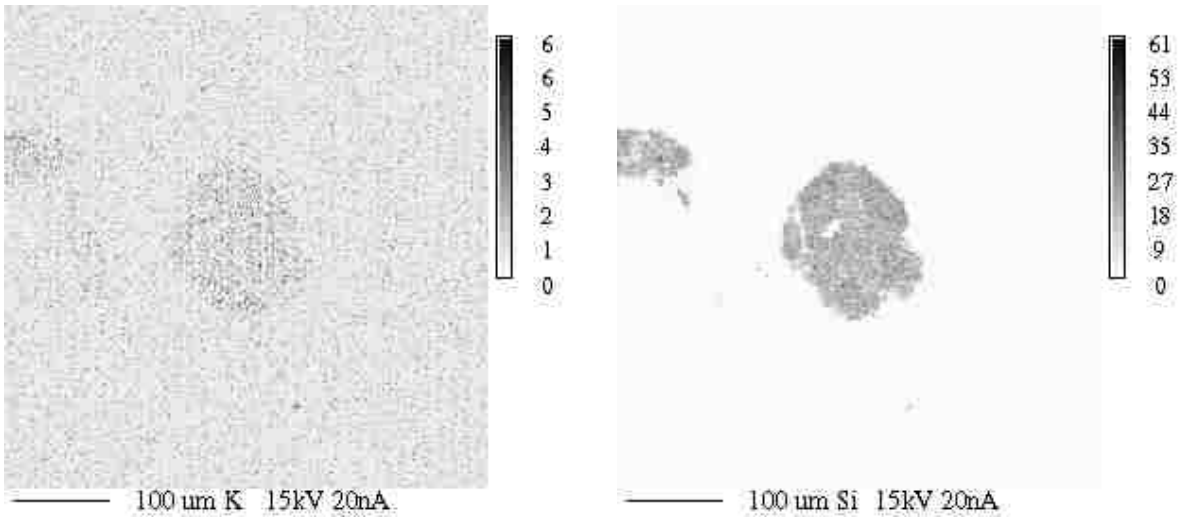

(c) K (d) Si

Figure 3.2: Electron microprobe images of an agglomerate of 1WH showing distributions of Fe, Cu, K, and Si.

minimal amount of water and then added to the precursor. Vacuum filtration following washing leaves the precursor relatively dry and the solution containing the promoters is readily absorbed into the pores, but there is still a bias to accumulate on the outer edges of the particle, especially for SiO_2.

From this analysis, it is clear that the promoters in 1S preparations are more uniformly distributed than in 2S preparations. While the byproduct is present in both 1UH and 2UH, the uniform distribution of potassium and silica promoters in 1UH shows that the promoters are intimately

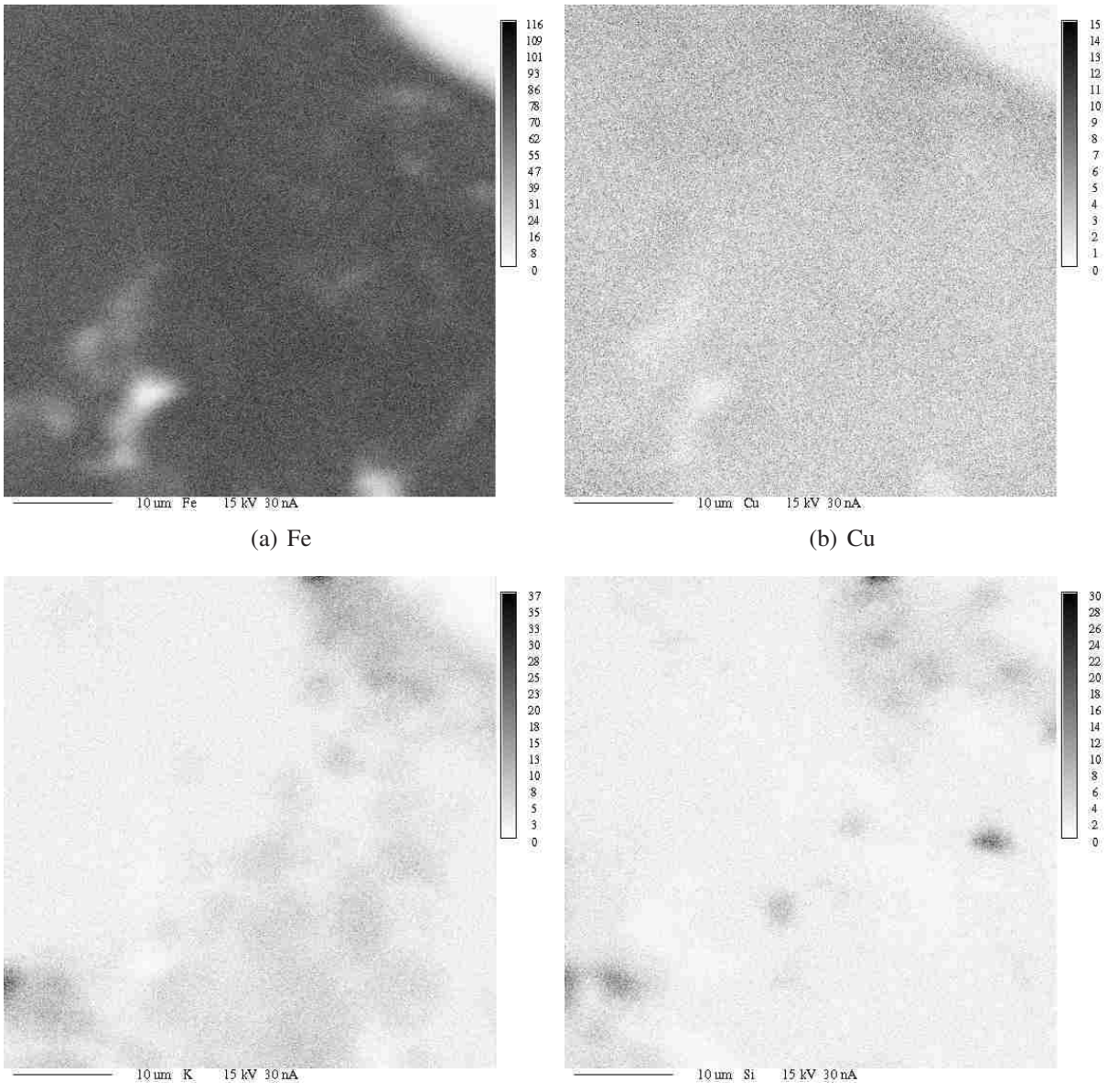

(a) Fe (b) Cu

(c) K (d) Si

Figure 3.3: Electron microprobe images of an agglomerate of 2UH showing distributions of Fe, Cu, K, and Si.

mixed with the Fe and their distribution is unaffected by diffusion through concentrated solutions of the byproduct as opposed to 2UH in which the diffusion hinders full penetration of particles by the promoters. Promoter distribution in 2WH is uniform within particles (despite higher concentrations on the outside edges of particles) due to removing the byproduct (by washing) and much of the water (by vacuum) so that the solution of promoters is readily absorbed into pores while in

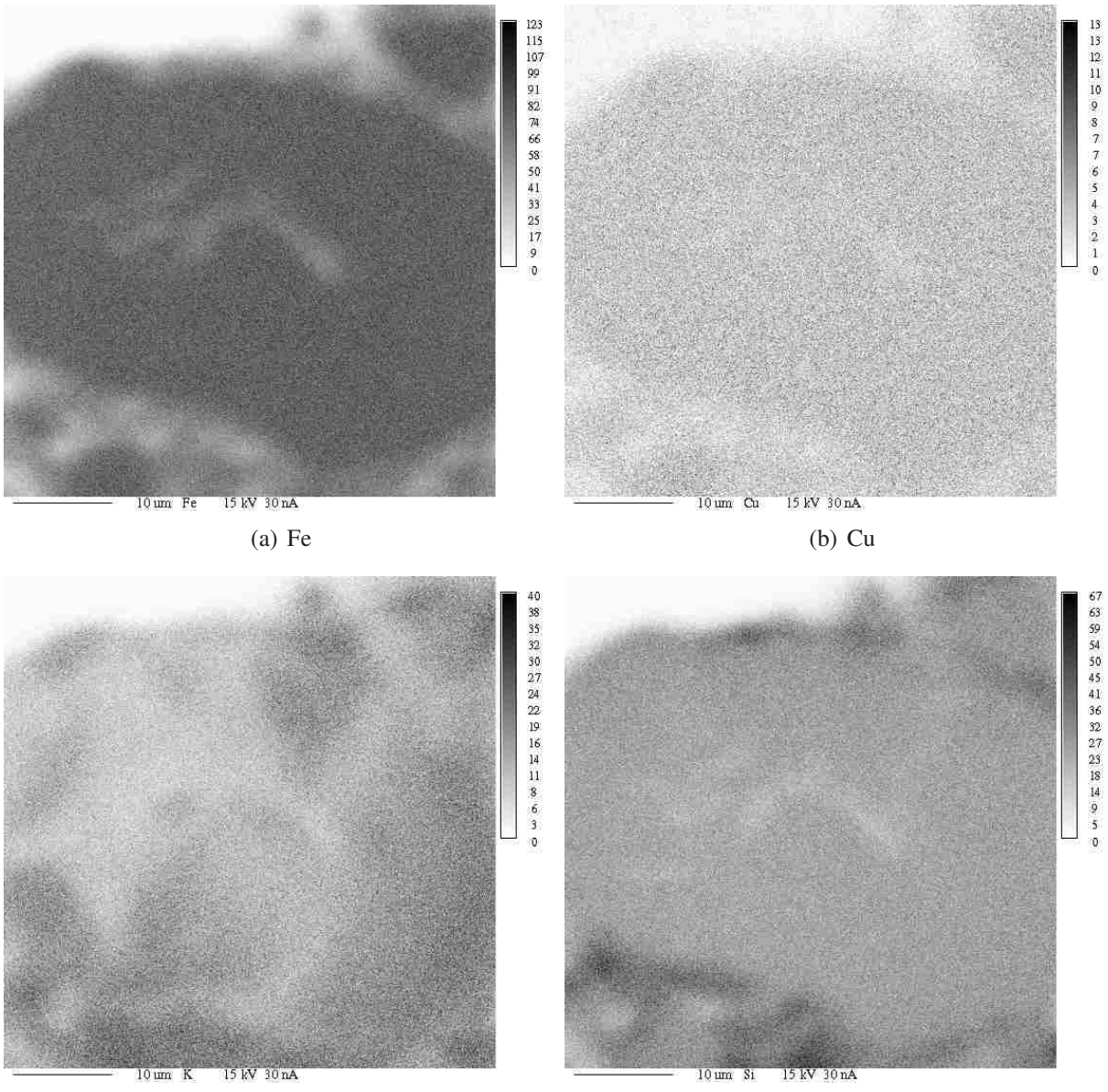

(a) Fe (b) Cu

(c) K (d) Si

Figure 3.4: Electron microprobe images of an agglomerate of 2WH showing distributions of Fe, Cu, K, and Si.

2UH the promoters are more concentrated near particle boundaries. These differences in promoter distributions affect other characteristics of the catalyst discussed below.

3.4 Reducibility

Reduction of iron catalysts follows a progression of oxidation states ($Fe_2O_3 \longrightarrow Fe_3O_4 \longrightarrow FeO \longrightarrow Fe$). The nature of iron catalysts and the chosen promoters do not give discreet reduction peaks corresponding to each of these oxidation state transformations. Instead, there is a continuum of iron sites that allow complete reduction to the metal at some sites at temperatures as low as 250 °C [21]. Despite this continuum of sites, the first peak from TPR analysis is commonly thought of as the reduction peak representing $Fe_2O_3 \longrightarrow Fe_3O_4$ and the broader second peak represents the complete reduction to metal.

The discussion of the results of TPR experiments is divided into the respective factorial experiments with 1S and 2S catalysts for the 2^3 factorial experiments, and D catalysts for the 2^2 factorial experiments.

3.4.1 TPR of 1S and 2S Catalysts

Mass loss rate curves during TPR for 1S and 2S catalysts are shown in Figures 3.5 and 3.6, respectively. In general, these curves show an initial, more narrow peak corresponding to the reduction of Fe_2O_3 to Fe_3O_4 (and FeO) and a second more broad peak corresponding to the reduction of Fe_3O_4 to Fe metal. A small shoulder (more apparent on 1UH, 1UL, 2UH, and 2WH) starting between 150 °C and 180 °C corresponds to the reduction of CuO to Cu metal and begins the onset of the initial Fe_2O_3 reduction peak.

The mass loss rate curves of the 1S catalysts (Figure 3.5) show multi-modal initial peaks which have peak temperatures of 210–250 °C. Integration of the peaks of 1S and 2S catalysts gives a second peak area of between 0.15 and 0.20 for all eight catalysts. Integration of the first peaks, however, gives larger peak areas of 0.18 and 0.22 for 1UH and 1UL, respectively, and smaller areas of 0.07–0.10 for the other catalysts. The multi modal peaks of 1S catalysts and the larger areas of 1UH and 1UL might be caused by decomposition of residual NH_4NO_3 (decomposition temperature is 210 °C), transformation of residual ferrihydrite to Fe_2O_3, and/or dehydration associated with ferrihydrite transformation. The presence of NH_4NO_3 after calcination at 300 °C is highly unlikely; however, the possibility of persistent NH_4NO_3 whether by incomplete calcination or by a false temperature reading in the furnace is entertained to explain the multimodal peaks of

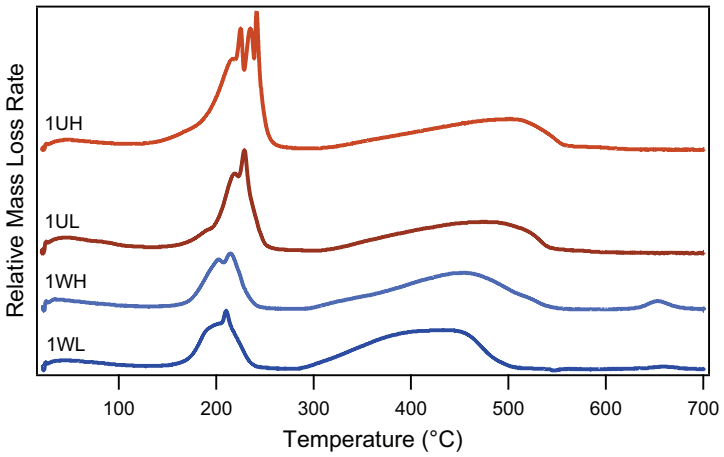

Figure 3.5: Mass loss rate during reduction with constant temperature ramp of 3 °C/min to 700 °C of calcined 1S catalysts.

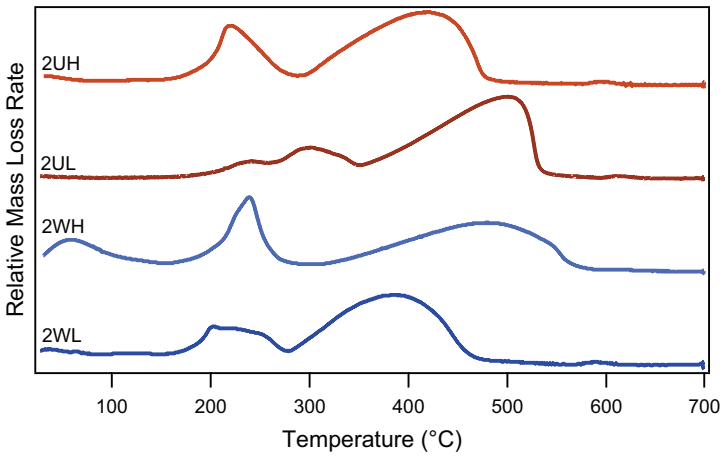

Figure 3.6: Mass loss rate during reduction with constant temperature ramp of 3 °C/min to 700 °C of calcined 2S catalysts.

the 1S catalysts. Alternatively, a small layer of NH_4NO_3 may have deposited on the catalysts upon recombining from decomposition gases during cooling if the air flow during calcination was not adequate to remove the decomposition gases. Recombined NH_4NO_3 was observed on the furnace door after cool down. It is noteworthy that only the unwashed catalysts have unusually high first peak areas, supporting the possibility that a small portion of the NH_4NO_3 persisted after calcination and then decomposed during reduction. It is also interesting to note that for 6 of the 8 catalysts (all but 1UH and 1UL) the first to second peak area ratios are between 1 : 1.7 and 1 : 3.1 (average of 1 : 2.3).

The 1WH curve is very similar to the 1WL curve and both show bimodal initial peaks giving maximum rates at about 210 °C. Onset of secondary peaks occurs at about 290 °C with maximum rates between 420 °C and 460 °C and complete reduction by 510–545 °C. The unwashed catalysts peaks are broader and shifted higher by 10 °C for 1UL and 20 °C for 1UH than the washed catalysts. Unwashed catalysts give maximum rates for the secondary peaks between 480 °C and 500 °C and complete reduction by 545–560 °C. Higher temperatures for unwashed catalysts indicate more difficult reduction. The unwashed catalysts also have higher K content than the washed catalysts as determined by ICP. Higher reduction temperatures and higher K loadings agree with prior work which shows that increasing potassium content inhibits reduction [18].

The mass loss rate profiles of the 2S catalysts (Figure 3.6) appear to be single peaks as opposed to the multi-modal peaks of the 1S catalysts. The profile for 2UH appears to be similar to 2WL with the maximum rate of the initial peak between 200 °C and 210 °C. The onset of the second peak is between 280 °C and 290 °C with maximum rates between 390 °C and 410 °C and nearly complete reduction by 500 °C (460 °C for 2WL). The 2WH profiles shows that the maximum rate of the initial peak and the onset of the second peak are shifted higher by 10 °C and the maximum rate of the second peak is shifted higher by 50 °C with nearly complete reduction by 580 °C. The second peak of 2WH is also much more broad (spanning 290 °C) than second peaks of the other 2S catalysts, but is similar to second peaks of 1S catalysts. The profile for 2UL is very different from the others. The first peak appears to be a very delayed Cu reduction peak (around 210 °C) followed by a delayed Fe_2O_3 peak (around 300 °C). The onset of the second peak occurs around 350 °C with a maximum rate at 500 °C and nearly complete reduction by 530 °C.

Since Cu promotes reduction and the Cu in the 2S catalysts was coprecipitated with Fe and since these catalysts were all promoted with equal levels of K and Si, the differences in profiles are likely due to the degree of integration of the promoters into the precursor structure. For instance, microprobe images of 2UH and 2WH (Figures 3.3 and 3.4) discussed previously show poor distributions of K and Si in 2UH compared to 2WH. Both K and SiO_2 make reduction more difficult as K potentially blocks nucleation sites and SiO_2 interacts with Cu, blocking the reduction benefits of Cu [18]. More complete and uniform distributions of K and SiO_2 in 2WH could explain the higher reduction temperatures and broader second peak compared with 2UH. The 2WL profile is very similar to 2UH. For 2WL, the promoters were added directly without first dissolving them in

water and therefore may not have been as well mixed similar to the case of 2UH. The promoters may not have been sufficiently mobilized to penetrate the precursor particles as was the case in 2UH, which explains the similarity of these reduction profiles. In the case of 2UL, promoters were dissolved in water prior to their addition to the catalyst. Recall that for all 2S catalysts, sufficient water was used to make a thick paste with the precursor (see Section 2.1.3) and it may be that there was sufficient water contact and time to allow for good mixing and incorporation of promoters and for SiO_2 to form bonds with Cu and Fe. Interactions between copper, SiO_2, and the hydroxide precursor could explain the delayed reduction of Cu and consequently of the Fe_2O_3 peak; however, the delay of these peaks continues to stand out against all other 1S and 2S catalysts.

3.4.2 TPR of D catalysts

Reduction profiles of the dried and then washed catalysts (Figure 3.7) show characteristics of both the 1S and 2S profiles already described. All four catalysts show onset of the first peak between 150 °C and 180 °C with maximum rates of the initial peaks at 210 °C. Secondary peaks of 2DH and 2DL begin around 280 °C with maximum rates at between 380 °C and 400 °C and nearly complete reductions by 450 °C, consistent with 2UH and 2WL and suggesting poor integration of K and SiO_2 promoters. Broad secondary peaks for 1DH and 1DL begin at about 250 °C with maximum rates between 420 °C and 480 °C and nearly complete reductions between 510 °C and 550 °C, suggesting good incorporation of SiO_2.

Since the SiO_2 in all 1S and 1D catalysts was present during precipitation, the more intimate mixing and contact time may have afforded more interactions with Cu and Fe causing the broad second peak also seen in 1UH, 1UL, 1WH, and 1WL. The narrowness of the initial peaks for 1DH and 1DL are indicative of the absence of K. The third peaks on 1DH and 1DL at 650 °C may represent the transition of lingering ferrihydrite structures to oxide (as mentioned in Section 3.1) and immediately to iron metal. Smaller peaks appear on reduction profiles of 1WH and 1WL at about 650 °C and on profiles of 2UH, 2UL, 2WL, 2DH and 2DL around 600 °C.

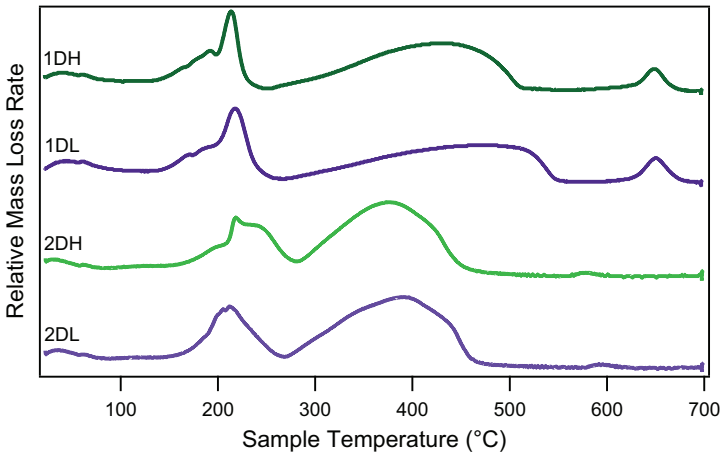

Figure 3.7: Mass loss rate during reduction with constant temperature ramp of 3 °C/min to 700 °C of calcined D catalysts.

3.4.3 Summary of TPR Analysis

The shape and breadth of TPR peaks is heavily influenced by promoter content and distribution. Well-dispersed potassium and silica delay and broaden the TPR peaks by interfering with nucleation sites and interacting with Cu, respectively. All 1S, and 1D catalysts as well as 2UL and 2WH show broad TPR peaks suggesting good distributions of promoters while 2UH, 2WL, and the 2D catalysts show more narrow peaks suggesting less effective distributions of promoters.

3.5 Surface Area and Pore Properties

3.5.1 Surface Area

BET data for reduced and passivated catalysts are summarized in Table 3.4. Surface areas for the four 1S catalysts are 37.2–55.6 m^2/g while surface areas for the four 2S catalysts are 23.6–65.7 m^2/g. For all 1S, 2S, D and repeat catalysts, surface area follows the same order of progression with WL<UH<UL<WH. It is noteworthy that the pattern is consistent across so many different batches and repeat preparations, though the reason is not immediately apparent. A study in the literature on the effect of SiO_2 loading on precipitated iron catalyst surface area reported catalysts with no SiO_2 having reduced surface areas of 10 m^2/g or less (after reduction in H_2) while catalysts with 8 or 24 parts SiO_2 per 100 parts Fe have surface areas of 98 m^2/g and 150 m^2/g (after reduction

in CO), respectively [18]. If reduction in CO rather than H_2 gives larger surface areas by a factor of 2–3 as it appears to do, then the surface areas of 1S and 2S catalysts are between reported surface areas for precipitated catalysts containing 8 and 24 parts SiO_2, as expected. Notable exceptions are 2UH, 2WL, 2DH, and 2DL all of which have surface areas less than 40 m^2/g. These are also the catalysts pointed out in Section 3.4 as having the most facile reduction profiles possibly as a result of poor dispersion and penetration of SiO_2 and K promoters despite having promoter loadings equal to 2UL, 2WH, 1UH, and 1UL. These low surface area values support the previous supposition that the distribution of SiO_2 in these catalysts is not uniform.

Table 3.4: Surface areas, pore volumes, and pore size distributions of reduced and passivated catalysts from BET data.

catalyst	SA[a] m^2/g	V_{pore}[b] mL/g	d_{pore} nm	range[c] nm	V_{pore}[d] %
1UH	45.6	0.14	10.3	6.3–17.4	92.9
1UL	51.7	0.13	8.1	4.2–15.5	94.8
1WH	55.6	0.24	15.5	8.7–28.0	89.4
1WL	37.2	0.24	34.2	16.1–70.7	82.5
2UH	36.8	0.14	8.7	5.0–15.3	60.8
2UL	54.7	0.15	13.1	4.0–43.0	96.1
2WH[e]	65.7	0.13	5.5	1.2–12.8	69.5
2WL	23.6	0.20	46.1	16.6–127.8	89.4
1DH	65.8	0.20	9.1	4.6–17.6	90.9
1DL	73.8	0.17	7.0	3.9–12.4	88.0
2DH	24.2	0.23	49.1	15.7–153.4	98.9
2DL	34.9	0.21	46.8	10.0–219.6	88.1
1UHa	49.5	0.16	14.9	6.3–35.1	92.9
1ULa[e]	68.5	0.13	5.5	3.3–9.2	78.2
1WLa[e]	82.9	0.14	5.5	4.0–7.4	85.3

[a] 95% confidence interval = ± 2.1 m^2
[b] 95% confidence interval = ± 0.01 mL/g
[c] ± 2 standard deviations of log normal avg. d_{pore}
[d] percent of total volume in range
[e] dried at 120 °C instead of 100 °C

3.5.2 Pore Volume

Pore volumes of all reduced 1S, 2S, D, and repeat catalysts are 0.13–0.24 mL/g with washed catalysts giving larger pore volumes (0.17–0.24 mL/g compared with 0.13–0.17 mL/g) in every case (consistent with pore volume trends in Section 3.1) except 2WH (0.13 mL/g) and 1WLa (0.14 mL/g). Both 2WH and 1WLa are washed catalysts dried ultimately at 120 °C and are the only washed catalysts in Table 3.4 dried at that temperature. Drying at 120 °C appears to affect catalyst pore structure in an unexpected way and is discussed in more detail in Section 3.5.4. The smaller pore volumes of the unwashed catalysts again suggest a different precursor structure than found in the structure of the washed catalysts. The four catalysts with the smallest surface areas are 2UH, 2WL, 2DH, and 2DL which may have potentially poor distributions of SiO_2 as discussed above. Of those, the three washed catalysts (2WL, 2DH, and 2DL) have large pore volumes (0.20–0.23 mL/g). Large pore volumes combined with small surface areas indicate large pore diameters such as the spaces between particles in an agglomerate which is where the SiO_2 would accumulate if it were poorly distributed as shown in the microprobe image of 2UH (Figure 3.3) or if it were preferentially deposited on the outside of the particle as shown in the image of 2WH (Figure 3.4).

3.5.3 Pore Size Distribution and Agglomeration Theory

Pore diameters for the fifteen prepared catalysts follow log-normal distributions with average pore diameters between 5.5 and 49.1 nm (see Table 3.4). Trends observed in PSDs of 1S and 2S catalysts are discussed first followed by trends for D catalysts. Repeat catalyst PSDs are discussed in Section 3.5.4. Figure 3.8 shows pore size distributions (PSD) for 1S catalysts. Ranges of diameters are given in Table 3.4 and represent four standard deviations of the volume weighted average of the natural log of pore diameter, spanning 11.1, 11.3, 19.3, and 54.6 nm for 1UH, 1UL, 1WH, and 1WL, respectively. Average diameters (and diameter ranges) for 1UH and 1UL are very similar (10.3 nm and 8.1 nm, respectively) while 1WH is 50–100% larger (15.5 nm) and 1WL is 220–320% larger (34.2 nm). Thus, for the 1S preparation, unwashed catalysts have smaller pores and narrower distributions of pores.

From the 1WH and 1WL data, drying temperature has a combined effect with the presence of water such that lower drying temperatures correspond to larger pores (and larger particles).

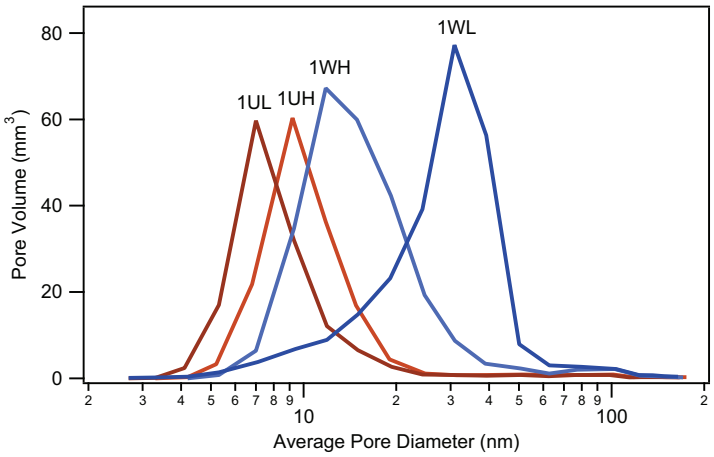

Figure 3.8: Pore size distributions of 1S catalysts after reduction and passivation.

PSDs from BET measurements of the four 1S catalysts after calcination are nearly identical and show only pores smaller than 9 nm with averages between 2 nm and 4 nm. Since all of the 1S catalyst pore structures are nearly identical after calcination, differences after reduction would not be expected; however, as seen in Figure 3.8 there are significant differences. These differences after reduction could be due to the extent that the structures after drying lend themselves to particle growth (sintering) and to reduction, i.e. degree of crystallinity and contact between particles. It has been reported that the degree of crystallinity of ferrihydrite increases as a function of temperature and time in the presence of water [65]. One theory of agglomeration states that linkages between molecules of water on the surfaces of smaller particles cause the particles to agglomerate. When the water is driven off, the ordered linkages lend themselves to phase transition from ferrihydrite to Fe_2O_3 as larger agglomerates [66]. Thus, pore size (which is related to particle size) increases with time and temperature in the presence of water. The lower drying temperature for 1WL may have driven water off slowly enough and provided enough energy to increase the rate of agglomeration sufficiently to create larger linked agglomerates. The higher drying temperature of 1WH afforded the creation of some linkages (more so than in 1UH or 1UL), but drove the water off too quickly to create the extensive linking in the larger agglomerates of 1WL. Figure 3.9 illustrates the process of agglomeration.

In contrast with 1WH and 1WL, 1UH and 1UL show little or no effect of drying temperature on PSD. As noted earlier (Equations 3.1 and 3.2), the products of reaction provide 10

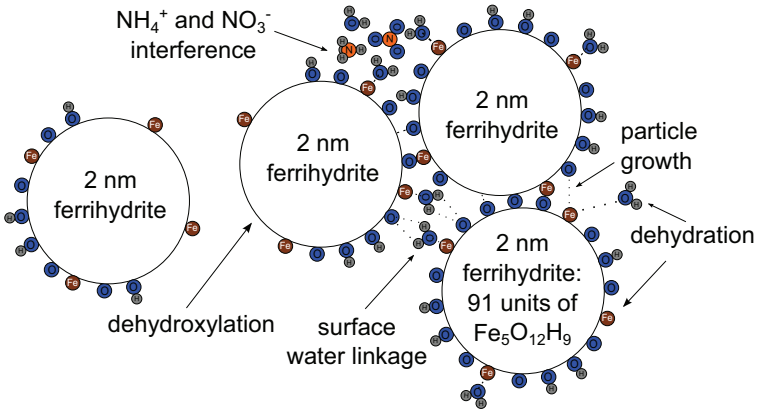

Figure 3.9: Illustration of agglomerate formation from ferrihydrite precursor particles. Large circles represent cross sections of 2 nm spheres of ferrihydrite while smaller circles represent 1.5 Å atomic cross sections.

molecules of H_2O for every atom of Fe in the preparation. This is more than adequate for hydration and coordination of the precursor, yet the PSDs of 1UH and 1UL are almost identical. Even though there is plenty of water present, the water is nearly saturated with byproduct NH_4NO_3. To the original agglomeration theory, this work adds that the byproduct may interfere with the weak water linkages between particles, making it difficult for larger agglomerates to form. Once dry, the particles are no longer free to form linkages and agglomerate, resulting in more narrow PSDs and smaller average diameters.

PSDs for the four 2S catalysts are shown in Figure 3.10. The PSD for 2UH shows a bimodal distribution with the first average pore size at 8.7 nm and the four standard deviation range spanning 10.3 nm representing only 60.8% of the total pore volume as given in Table 3.4. The second average pore size at 34.6 nm has a four standard deviation range from 12.5 nm to 99.1 nm and accounts for 38.2% of the pore volume. The PSD for 2UL is fit as a single peak, even though it has a slight shoulder representing a second peak, giving a volume weighted average diameter of 13.1 nm and a range spanning 39.0 nm. The average pore diameter of 2WL is 46.1 nm and the range spans 111.2 nm. Since 2WH was dried at 120 °C, its PSD is discussed below under that heading.

All three 2S PSDs described above cover much broader ranges of diameters than their 1S counter parts. Like 1WL for 1S catalysts, 2WL has the largest average pore diameter and PSD of 2S catalysts. In contrast to the 1U catalysts, the PSDs for 2UH and 2UL are quite broad. The primary

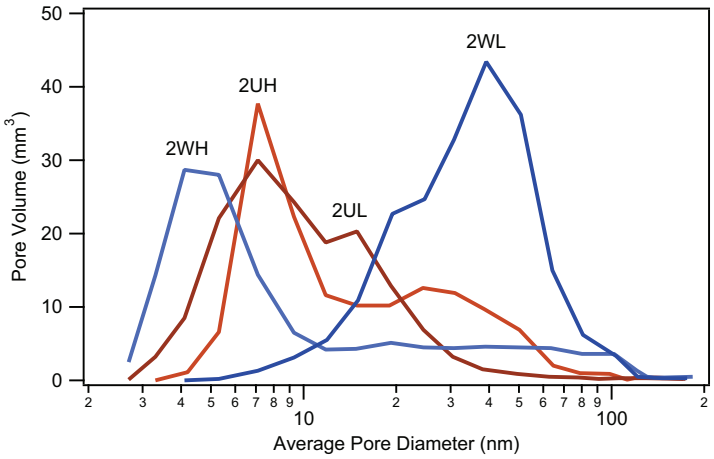

Figure 3.10: Pore size distributions of 2S catalysts after reduction and passivation.

PSD for 2UH is in the expected narrow range and of smaller average diameter for an unwashed catalyst as explained above, but the secondary PSD is much larger. This secondary range may be the result of adding precursors in a second step. The PSDs *after calcination* for all 2S catalysts have bimodal distributions with 50–75% of the pore volume in pores less than 9 nm. The balance of the pore volume for all of these catalysts spans the pore sizes described above. This shows that while the primary PSDs increased with reduction, the secondary PSDs for these catalysts did not. This behavior is expected if the secondary PSDs are filled with and supported by SiO_2 which was added in the second preparation step as has been suggested (Section 3.3). For 2UL to which more than an adequate amount of water was added during promoter addition, the extra water may have diluted the byproduct enough so that it did not interfere with the formation of linkages between particles leading to a larger PSD than 1UL and the primary PSD of 2UH.

PSDs for the four D catalysts are shown in Figure 3.11. The PSDs for 1DL and 1DH are very similar to 1UH and 1UL despite having been washed after drying while PSDs for 2DH and 2DL are similar to 2WL. The fact that 1DH and 1DL have PSDs similar to the 1UH and 1UL suggests that their pore structures were fixed after the first drying. It may be that the SiO_2 which was well dispersed in 1DH and 1DL provided a rigid structure after drying that prevented the particles from re-dispersing and forming new linkages which would otherwise lead to larger pores and particle sizes. In contrast, 2DH and 2DL both have very large average pore diameters and

broad distributions. In the absence of SiO_2 after the first drying, the precursor particles were free to reorganize and form new linkages leading to larger pores.

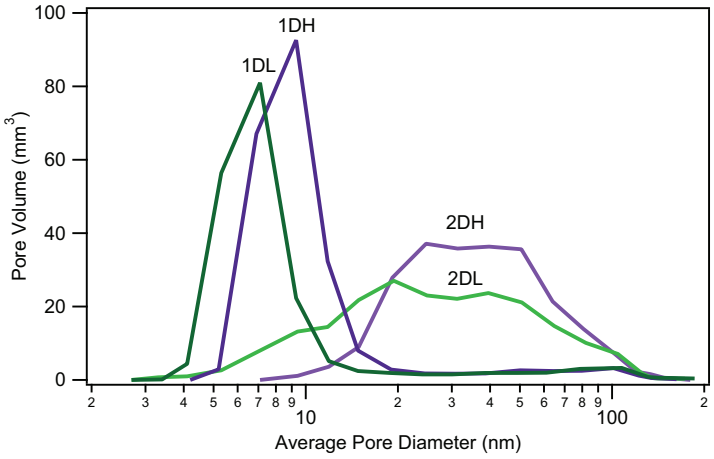

Figure 3.11: Pore size distributions after reduction and passivation of catalysts that were dried before washing.

To recap, agglomeration of very small crystallites and particles (2–4 nm) is heavily influenced by inter-particle interactions due to the high surface energies of the small primary particles and is directly related to pore diameter. In particular, surface bound water forms linkages which result in particle growth. The presence of NH_4NO_3 interferes with these linkages leading to the smaller average particle diameters which in turn give the smaller average pore diameters of the 1U, 2U, and 1D catalysts. Washing removes the NH_4NO_3 and allows more linkages to form as shown by the large pore diameters of 1WL, 2WL, and the 2D catalysts. Drying at higher temperatures destroys some of the linkages and results in the intermediate average pore diameter of 1WH.

3.5.4 Drying at a Higher Temperature

As mentioned in Sections 2.1.3, 3.5.2 and 3.5.3, 2WH, 1ULa, 1ULC, and 1WLa were dried at 120 °C. Figure 3.12 shows PSDs for these catalysts. Except for 1ULC, these catalysts have smaller average pore diameters and narrower PSDs than all other catalysts. With other catalysts dried at the lower temperature, linkages formed between particles produced larger pore sizes and broad PSDs after reduction, but for catalysts dried at 120 °C, any linkages that may have formed

appear to have been destroyed. This suggests that at 120 °C an energy barrier is surpassed which does more than simply dehydrate inter-particle linkages. One DSC/TGA study on ferrihydrite shows an endothermic transformation around 105–125 °C and also suggests that the surface of the ferrihydrite particles are covered in hydroxide groups [63]. Others show that drying at 130 °C results in partially dehydroxylating the ferrihydrite [62]. These two observations may be related meaning that the endothermic transformation may actually be a removal of the surface hydroxides. A particle undergoing partial dehydroxylation would lose its surface hydroxides at lower temperatures than its interior hydroxides, leaving an oxide surface with a protected oxyhydroxide core. Surface hydroxides are the likely structures to form linkages with surface water between particles. As described above, slowly dehydrating the linked structures leads to larger agglomerates that grow into single particles of Fe_2O_3. At 120 °C, the water linkages may dehydrate at the same time that the surface hydroxides decompose which would destroy any linkages between particles and result in smaller pore diameters and very narrow PSDs.

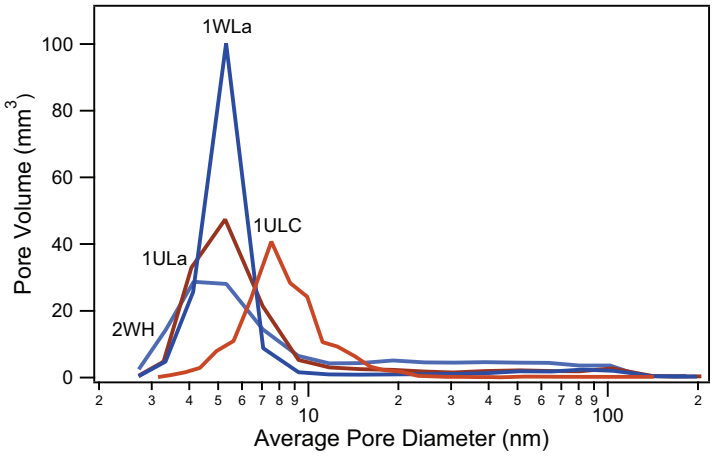

Figure 3.12: Pore size distributions after reduction and passivation of catalysts dried at 120 °C. 1ULC is a repeat preparation by Cosmas, Inc. described in Section 2.1.3 and Table 2.4.

3.6 Chemisorption and Extent of Reduction

Dispersion, crystallite diameter, and particle diameter were investigated by H_2 and CO chemisorption, TPR and oxygen titration, XRD, and TEM. H_2 and CO uptake, extent of reduction

(EOR), dispersions, and crystallite diameters for reduced and passivated catalysts are given in Table 3.5.

Table 3.5: H_2 and CO uptakes, extents of reduction, dispersions, and crystallite diameters of catalysts after re-reduction in H_2 at 300 °C for 6 hours.

	uptake[a]					crystallite diameter		
catalyst	H_2[b] μmol/g	CO[c] μmol/g	H_2/CO %	EOR %	Disp. nm	H_2[a] nm	Fe[d] nm	Fe_3O_4[d,e]
1UH	159	583	3.7	21.5	12.5	9.8	19.7	20.5
1UL	146	893	6.1	15.5	14.8	8.3	19.8	22.6
1WH	203	746	3.7	46.1	8.0	15.3	26.3	15.2
1WL	131	675	5.2	50.6	4.2	29.5	36.4	21.2
2UH[f]	158	145	0.92	9.3	31.1	3.9		24.5
2UL	118	264	2.2	12.1	17.4	7.1	17.8	6.6
2WH	164	242	1.5	14.8	19.0	6.5	18.3	16.4
2WL	61	166	2.7	14.2	6.7	18.5	35.0	16.2
1DH	200	858	4.3	41.4	8.7	14.1		
1DL	272	1272	4.7	30.4	17.2	7.2		
2DH	101	160	1.6	24.6	6.7	18.3	31.7	21.0
2DL	126	128	1.0	37.6[g]	5.6[g]	22.1[g]	35.1	16.2
1UHa	192	459	2.4	29.2	11.4	10.8		
1ULa	195	716	3.7	17.9	18.2	6.8		
1WHa	269	881	3.3	25.8	18.6	6.6		

[a]after re-reduction for 6 h at 300 °C
[b]95% confidence interval = ±25%
[c]95% confidence interval = ±23%
[d]from XRD peak broadening
[e]Fe_3O_4 indistinguishable from FeO
[f]2UH showed 26.8 nm Fe_2O_3, but no Fe
[g]assumes ICP measurement on 2DL is 30% too high

Hydrogen chemisorption measurements are 131–272 μmol_{H_2}/g for 1S and 1D catalysts and 61–164 μmol_{H_2}/g for 2S and 2D catalysts. Uptakes are larger for H catalysts than for L catalysts, except for 1DH and 2DH. EOR are 15.5–50.6% for 1S and 1D catalysts and 9.3–37.6% for 2S and 2D catalysts with W>U. Dispersions are 4.2–17.2% for 1S and 1D catalysts and 5.6–31.1% for 2S catalysts.

The much higher EOR for the four 1S catalysts are reflected in Figures 3.5 to 3.7 which show nearly equal divisions of area under the mass loss rate curves for the first and second reduction peaks. In contrast, the four 2S catalysts show roughly $2/3$ of the area under the more difficult second peak.

Ratios of CO to H_2 chemisorption for the four 1S catalysts are 3.7–6.1 with unwashed catalysts both lower than washed catalysts. The ratio for a monolayer of linearly adsorbed CO molecules per site (e.g. for a planar site) is 2. The much larger ratios for the 1S catalysts indicate several possibilities including: (1) the H_2 chemisorption was underestimated (unlikely), (2) the re-reduction temperatures in the two apparatus were different (though not likely more than 10 °C), (3) the CO source was contaminated with air (not supported by uptake curves), (4) CO spilled over to partially reduced sites , and (5) multiple CO molecules adsorption on a single site.

Ratios for the four 2S catalysts are 0.9–2.7 which are much closer to expected values. Chemisorption ratios less than 2 could indicate bridged bonding or dissociative adsorption which occurs when binding energy is high such as in defect sites. Ratios greater than 2 result from adsorption of more than one molecule per adsorption site such as gem dicarbonyl configurations or even higher stoichiometries and are characteristic of rough, low-coordination surfaces containing many edges and corners. Ratios for 2UL and 2WL are more than 2 and ratios for 1UL and 1WL are greater than 5, suggesting that drying at lower temperature produces more edges after reduction. 2UH and 2WH have ratios less than 2 while 1UH and 1WH have nearly equal ratios of 3.7. Lower ratios for catalysts dried at higher temperature may indicate a larger ratio of defect sites to edge sites. Interestingly, washing the catalyst does not have as much effect on the chemisorption ratio as it does on PSD, indicating that washing the catalyst does not greatly affect the ratio of edge and defect sites to adsorption sites on the particle surfaces. These observations can be explained by the agglomeration theory discussed in Section 3.5.3 and illustrated in Figure 3.9. More rapid dehydration of particle linkages would lead to imperfect particle-particle couplings and larger numbers of defect sites on the surface, independent of whether the catalyst was washed or not. Slower dehydration could lead to greater numbers of merged particles, producing more edges than defects. One step catalysts produce more edges and defects than two step catalysts probably as a result of the intimate mixing of SiO_2 with the precursor and its consequential influence on particle surface texture.

3.7 Phases in Reduced and Passivated Catalysts

Crystalline phases in catalysts following reduction and passivation are identified using XRD. Only 1S and 2S catalysts are discussed since 2D catalysts did show and 1D and repeat catalysts were expected to show similar XRD patters after after reduction and calcination. XRD patterns were not collected for the 1D and repeat catalysts. All spectra are smoothed, curve subtracted, and normalized to the largest peak height. Standard spectra for Fe, FeO, Fe_3O_4, and Fe_2O_3 are normalized to half the peak height of catalyst spectra. Only crystalline portions of samples give XRD spectra and the most crystalline structures (largest particles) give the highest and sharpest peaks. Smaller crystals give broader and less intense peaks to the point that crystallites smaller than 2 nm are not detectable. The XRD data in this dissertation are qualitative only and do not indicate relative phase abundance. Quantitative estimates of phase abundance are not directly related to peak height or area and require instrument specific calibrations for response and broadening characteristics which were not performed. Peak broadening in conjunction with Scherrer's equation does give estimates of crystallite diameters as reported in Table 3.5 and discussed in Section 3.8.

XRD spectra of the four 1S catalysts are shown in Figure 3.13. Peaks at $2\theta = 44.4$, 64.8, and 82.1 are characteristic of Fe while peaks at 29.9, 35.2, 42.9, 53.4, 56.9, 62.4, and 74.0 are characteristic of Fe_3O_4 and FeO which are indistinguishable from each other and referred to only as Fe_3O_4 in following discussions. Fe and Fe_3O_4 account for every peak in these four spectra. The principle peak height for Fe at $2\theta = 44.4$ is three times larger than the principle peak for Fe_3O_4 at $2\theta = 35.2$, except for 1WH in which Fe is 1.5 times larger. While the data do not directly represent relative phase abundance, they do indicate the most crystalline phase present. The crystalline structures of these catalysts are predominantly Fe metal which shows that passivation successfully protects larger particles from re-oxidation and that reduction causes the particles to become more ordered (crystalline). The EOR for these catalysts are 15.5–50.6% before passivation, illustrating that peak intensities cannot be used as proxies to quantitatively estimate the fraction of Fe present after passivation.

Figure 3.14 shows XRD spectra of the four 2S catalysts after passivation. Except for 2UH, these spectra show mainly Fe peaks and very small peaks for Fe_3O_4. 2UH shows primarily Fe_3O_4 with very small peaks for Fe_2O_3. EOR for for these catalysts are 9.3–14.1% before passivation, so

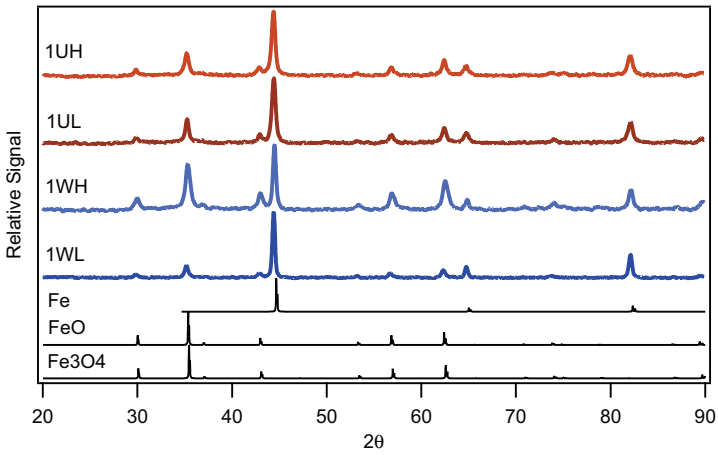

Figure 3.13: XRD spectra of reduced/passivated 1S catalysts.

phases other than Fe and some Fe_3O_4 are not crystalline enough to give strong peaks. The reason for the lack of a metal peak for 2UH may be that the temperature during passivation increased more than initially thought and recorded or because of exposure to air over time while being stored in a lidded jar inside a desiccator. It is interesting that the largest peaks for catalysts other than 2UH correspond to Fe since these catalysts were all bulk reduced and passivated six months prior to XRD analysis and the EOR of these catalysts were 9.3–14.8%.

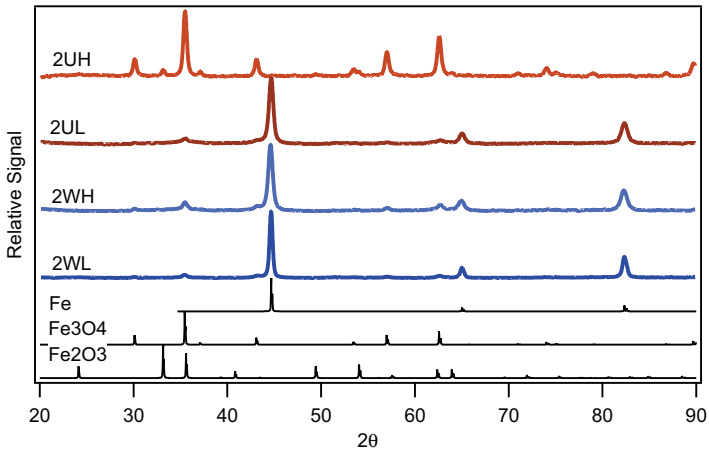

Figure 3.14: XRD spectra of reduced/passivated 2S catalysts.

3.8 Dispersion and Particle Size

Dispersion and average crystallite diameters of iron particles are estimated from chemisorption measurements using Equations 2.1 and 2.2, respectively. Diameters estimated from chemisorption follow the trends for pore diameter and PSD and particle size is attributed to the agglomeration theory discussed in Section 3.5.3. Estimated average crystallite diameters for 1UH, 1UL, and 1WH agree amazingly well with their average pore diameters (within $\pm$0.8 nm) while 1WL is within 5 nm (14%) of its average pore diameter (see Figure 3.15). Estimated diameters for 2UH, 2UL, and 2WL are roughly half of their pore diameters while the crystallite diameter for 2WH is within 1 nm (20%) of its pore diameter.

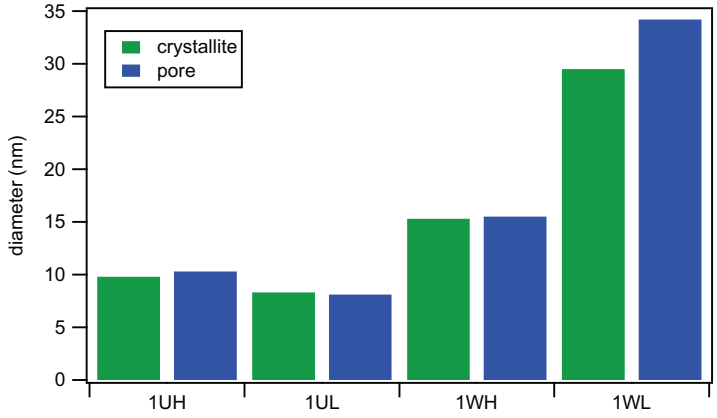

Figure 3.15: Comparison of average pore diameters from BET with average Fe crystallite diameters calculated from H_2 uptake for 1S catalysts.

Diameters from XRD data for Fe crystals in the passivated catalysts are larger than the diameters calculated from H_2 chemisorption. Diameters for Fe_3O_4 crystals are also larger than chemisorption diameters, except for 1WH, 1WL, 2UL, and 2WL. Based on PSD, EOR, and chemisorption, the XRD diameters are larger than the chemically active crystallites.

TEM images of catalysts confirm the presence of crystallites with particle diameters equal to those estimated from chemisorption and XRD analysis. Figures 3.16 and 3.17 are TEM images of 300 nm agglomerates of 1UH and 1WH, respectively. Figure 3.16 shows fine grains (5–10 nm) clumped together in 20–30 nm agglomerates, some of which have begun to merge into continuous

particles, but which retain textures of the fine grains. This confirms the chemisorption crystallite diameter estimate of 9.8 nm for 1UH and also the 20 nm diameter XRD estimates of Fe and Fe_3O_4 crystals.

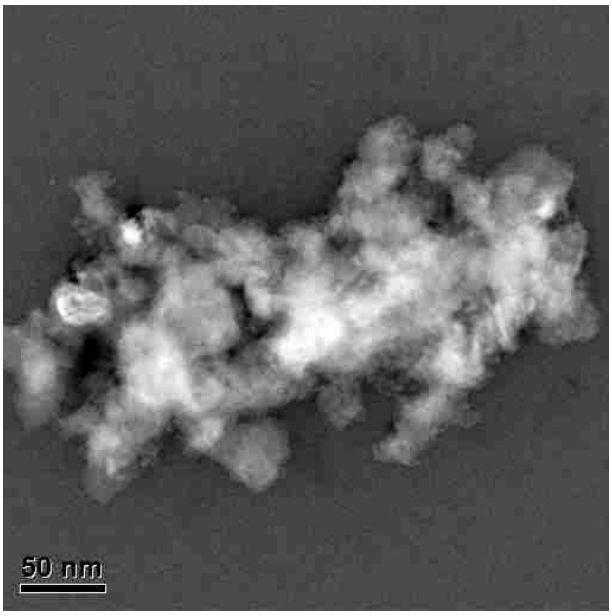

Figure 3.16: TEM of 1UH.

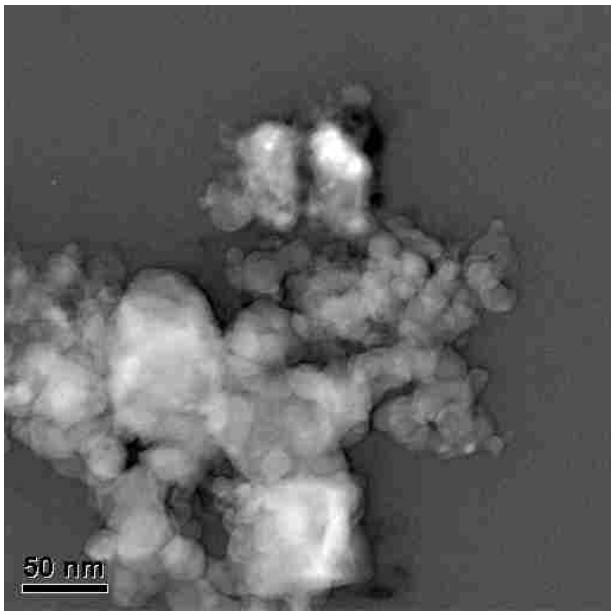

Figure 3.17: TEM of 1WH.

The TEM image of 1WH (Figure 3.17) shows much coarser single grains 10–30 nm in size. In contrast with 1UH, these larger particles appear to be continuous without smaller constituent pieces or textures. This also confirms the chemisorption diameter estimate of 15.3 nm as well as the XRD estimates of Fe (26.3 nm) and Fe_3O_4 (14.1 nm) crystallite diameters.

These TEM images cannot confirm the agglomeration theory, but do corroborate it by not showing any findings contrary to it for either 1UH or 1WH.

3.9 Structural Differences After Carbidization

A well known theory is that the active phase for FTS is neither Fe metal nor an oxide but an iron carbide. Carbiding the catalyst changes the crystallite and pore structures of the catalyst and is a result of the FTS. The following characteristics are observed on the eight 1S and 2S catalysts following FTS in the FBR for 125–600 hours.

BET surface areas are 7–28 m^2/g (down from 23.6–65.7 m^2/g) and pore volumes are 0.05–0.24 mL/g (down from 0.13–0.24 mL/g) as shown in Table 3.6. All catalysts show significant loss of surface area which is likely due to incomplete wax removal. The two 1W catalysts both of which have pore sizes greater than 15 nm and 2UH show more than 80% recovery of pore volume, suggesting more complete removal of wax. In contrast, 2WL recovered only 40% of its pore volume despite its relatively large average pore size. 1WH and 1WL show larger average pore sizes and PSD after FTS than before. Section 3.5.3 discusses the bimodal PSD of 2UH after reduction and passivation. The average pore diameter and PSD for 2UH after FTS appear much closer to the second peak of the reduced PSD range (34.6 nm and 12.5–99.1 nm). Other catalysts show smaller pore volumes, suggesting at least partial filling by wax, supported by smaller average pore sizes and slightly smaller PSD than after reduction.

Table 3.6: Surface areas, pore volumes, and primary pore size distributions of prepared catalysts pre- and post-reaction.

catalyst	TOS h	SA m^2/g	V_{pore} mL/g	d_{pore} nm	range[a] nm
1UH	521	46 / 8	0.14 / 0.05	10.3 / 7.4	6.3–17.4 / 3.8–15.2
1UL	324	52 / 18	0.13 / 0.06	8.1 / 7.5	4.2–15.5 / 5.0–11.4
1WH	521	56 / 29	0.24 / 0.20	15.5 / 23.8	8.7–28.0 / 12.3–48.6
1WL	324	37 / 28	0.24 / 0.24	34.2 / 38.9	16.1–70.7 / 22.9–68.0
2UH	559	37 / 20	0.14 / 0.12	8.7 / 26.4	5.0–15.3 / 7.0–79
2UL	125	55 / 19	0.15 / 0.09	13.1 / 11.9	4.0–43.0 / 5.6–37.3
2WH	125	66 / 17	0.13 / 0.07	5.5 / 6.7	1.2–12.8 / 3.6–12.1
2WL	124	24 / 7	0.20 / 0.08	46.1 / 49.9	16.6–127.8 / 16.3–147

[a] ± 2 standard deviations of log normal avg. pore diameter

XRD spectra of 1S and 2S catalysts after reaction show Fe_2C, Fe_5C_2, and Fe_3O_4 (Figures 3.18 and 3.19). The tallest and broadest peak for all catalysts (except 1WH) corresponds to Fe_2C, which may be a candidate for the active phase of the catalyst. 1UH, 1WL, 2UH, and 2UL (which are the most active catalysts) show the least signal (or none at all) for Fe_3O_4 and Fe_5C_2. 1UL, 1WH, 2WH and 2WL have strong Fe_5C_2 peaks while 1UL and 1WH also show peaks for Fe_3O_4. As stated previously, these results do not prove which phase is active (or which is most

active) for FTS; however, it is interesting that the most active catalysts show the weakest signal for Fe_3O_4 and Fe_5C_2 and the strongest signal for Fe_2C.

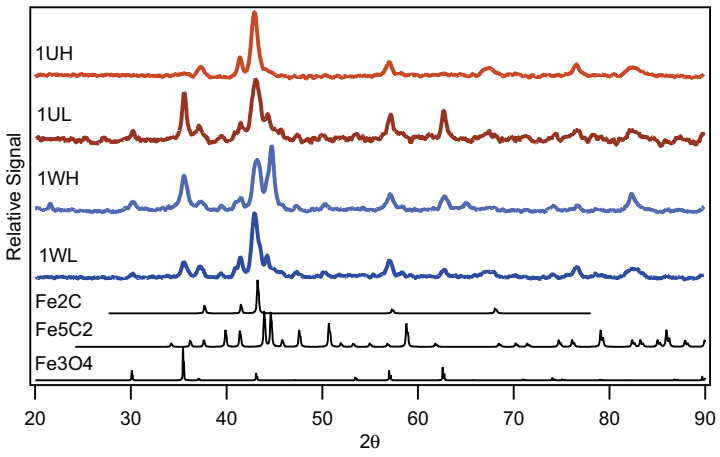

Figure 3.18: XRD spectra of 1S catalysts after 228–521 h of FTS.

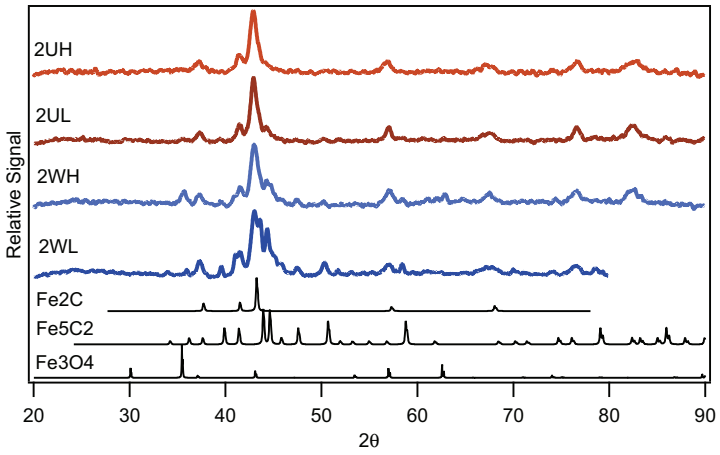

Figure 3.19: XRD spectra of 2S catalysts after 120–355 h of FTS.

Crystallite diameters calculated from peak broadening are given in Table 3.7. Peak broadening calculations were not performed for 2WL. Estimated Fe_2C crystallite diameters are smaller (10.2–14.8 nm) than XRD estimates of the Fe and Fe_3O_4 crystallites before reaction (after reduction) given in Table 3.5 (15.2–36.4 nm) excepting the post reduction oxide of 2UL. Estimated Fe_5C_2 and Fe_3O_4 crystallite diameters after carbiding are 10.1–22.1 nm. Estimated diameters after

carbiding lie within the range of H_2 chemisorption and XRD diameter estimates (3.9–36.4 nm) after reduction. Smaller crystallite diameters suggest increased dispersion despite the loss of surface area and pore volume noted above. Thus, the loss in surface area and pore volume is likely due to incomplete wax removal and not to sintering.

Table 3.7: Crystallite diameters by phase after 125–559 h of FTS calculated from XRD peak broadening.

	crystallite diameter		
catalyst	Fe_3O_4 nm	Fe_5C_2 nm	Fe_2C nm
1UH			13.6
1UL	22.1	18.2	11.3
1WH	11.8	18.6	10.2
1WL	17.4	21.3	14.7
2UH			10.3
2UL		16.4	14.8
2WH	10.1	11.8	13.5

TEM images of 1UH and 1WH after carbiding show particles within the respective ranges given in Table 3.7 (Figures 3.20 and 3.21). Both images show outlines around individual particles which could be removed locally by concentrating the beam and which are likely layers of residual wax. The ranges of particle sizes observed in TEM images of the reduced catalysts are also present in the carbided catalysts.

Overall, the conversion of the reduced catalyst to the carbide appears to decrease crystallite diameter (increase dispersion). Loss of surface area and pore volume is likely due to persistent wax. Also, it appears that Fe_2C particles are smaller and on the order of the crystallite diameters calculated from H_2 chemisorption after reduction and may correlate with activity.

3.10 Efficacy of Wax Extraction

A previous BYU study used Soxhlet extraction with toluene as the solvent to remove wax from spent catalyst [67]. Extraction was performed at 120 °C which is higher than the boiling point

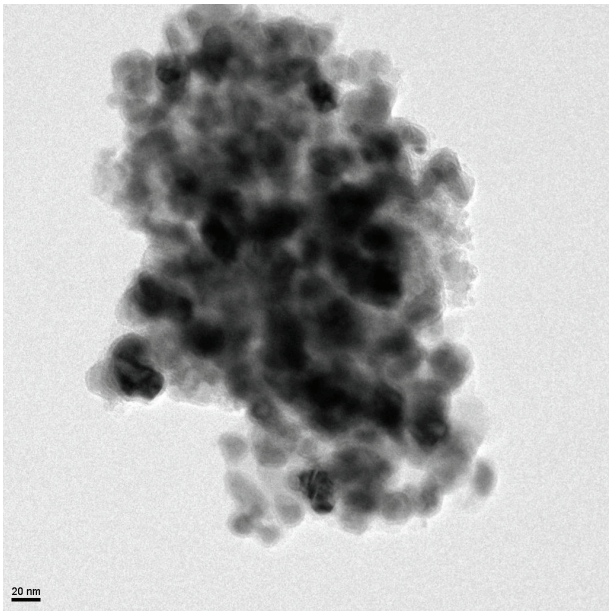

Figure 3.20: Bright field TEM image of an agglomerate of 1UH after 521 h of FTS.

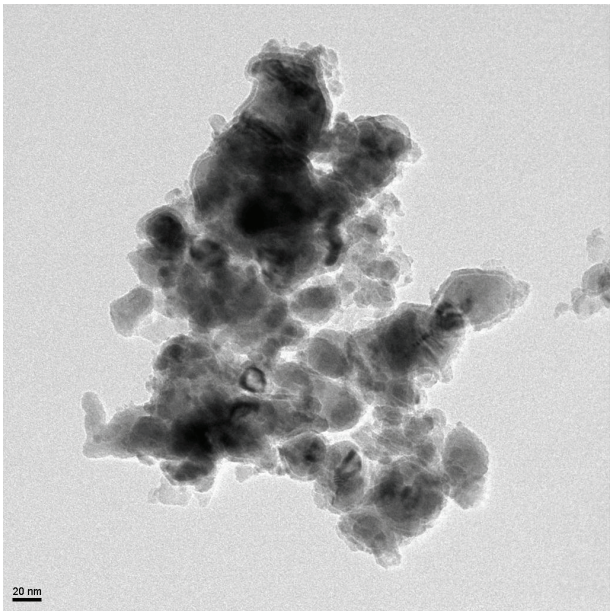

Figure 3.21: Bright field TEM image of an agglomerate of 1WH after 521 h of FTS.

of toluene (110 °C). The extracted catalyst was dried at 80 °C in air over night. The study indicated that Soxhlet extraction and drying resulted in nearly complete loss of surface carbide as measured by temperature programmed surface reaction possibly as a result of oxidation during the extraction process. Although surface reaction was not performed on spent catalysts of this study, the above discussion of XRD phases on the spent catalyst shows that extraction by toluene at more mild conditions (80 °C) and subsequent exposure to air did not result in loss of the bulk carbide phase. The wax extraction did successfully remove the peaks associated with wax from XRD spectra; however, TEM images on carbided catalysts after wax extraction show persistent wax film around crystallites. There was also no correlation between the amount of oxide present in the catalyst after extraction and the apparent recovery of pore volume and surface area as evidenced by 2UH which had one of the highest pore volume and surface area recoveries, but showed no oxide peak by XRD. More complete removal of wax may be accomplished by larger numbers of consecutive extractions by toluene as described in Section 2.3.2 without apparent changes to catalyst phases; however, more investigative work on surface phases using temperature programmed surface reaction is required to determine whether the surface carbide species remain intact. It has also been

reported that mild H_2 treatment will remove wax without oxidation and breakdown of the carbide species [67]. Such a study is beyond the scope of this work.

CHAPTER 4. RESULTS AND DISCUSSION OF ACTIVITY EXPERIMENTS

The ultimate characterization of a catalyst must reveal its performance in activity, selectivity, and stability; the catalyst must be tested in the reactor. To be meaningful, the reactor test should be descriptive enough in data and methods to allow researchers who will never personally handle the catalyst to compare with confidence results across different studies from different laboratories using different methods. To this end, the following data and analysis are given.

4.1 Reaction Conditions for Temperature Experiments

Reactant composition, reactant flow rates, and total pressure were mainly invariant within each fixed-bed run while temperature was varied. Once compositions and flow rates were set, they were not changed in most runs with the exception of the partial pressure experiments of Run 10. Reactor pressure was controlled by back pressure regulators set to 300 psig (21 atm) which were monitored and reset when the set pressure dropped by about 10 psi (about every 6–12 hours). Table 4.1 gives the flow rates, catalyst masses, and time on stream for the kinetic data portions of each FB run, not including the startup period. Flow rates for the partial pressure kinetic study are not given here, but are given in Table 4.11. FB runs are presented in chronological order. For runs with ranges of flow rates, see Appendix C in which specific averaged conditions including full conversion, rate, and selectivity data at each steady state subset of data are given for each catalyst. Similar data for the partial pressure experiments of FB Run 10 are given in Table 4.11.

The listed times on stream include the last data point in the kinetic data sets for each catalyst except for 2UH of Run 5 and 1UH of Run 9 which were not included in kinetic data sets. Actual times on stream for Runs 8 and 10 are longer than are shown, but the excluded data show distinctly lower activity at later times. For a fair comparison with the other catalysts and catalyst runs, those data are not included in the estimation of activation energy (E_A) and pre-exponential factor (A) for those catalysts.

Table 4.1: Reactant flow rates, catalyst masses, and times on stream for temperature experiments. Fixed-bed runs are presented in chronological order.

Cat.	Run	Rctr	Mass (g)	F_{H2} mmol/h	F_{CO} mmol/h	F_{Ar}[a] mmol/h	F_{He} mmol/h	TOS h
1WLa	1	1	0.500	39.6	40.8	5.5	41.7	356
P2	1	2	0.500	86.1	88.6	11.9	90.7	268
1ULa	2	1	0.499	74.6	76.5	10.7	78.8	308
P1	2	2	0.501	73.3	75.2	10.6	77.4	312
2UL	3	1	0.513	69.4	68.6	9.1	75.9	109
2WH	3	2	0.516	57.2	56.5	7.5	62.6	117
2DL	4	1	0.513	42.5	42.0	5.5	46.5	95
2DH	4	2	0.506	57.2	56.5	7.5	62.6	100
2UH[b]	5	1	0.251	69.5	68.5	9.1	75.9	108
2WL	5	2	0.256	57.3	56.5	7.5	62.6	83
1UH	6	1	0.250	42.4	38.3	4.9	42.1	507
1WH	6	2	0.251	44.1	39.8	5.1	43.7	500
1UL	7	1	0.250	33.9	33.9	4.5	44.9	228
1WL	7	2	0.251	42.8	42.8	5.7	56.7	228
1DH	8	1	0.251	23.2	23.3	3.1	26.9	425
1DL	8	2	0.250	15.4	15.4	2.1	17.8	365
1UH[b]	9	1	0.511	31.6	31.6	4.1	34.5	355
1UHa[c]	9	2	0.501	60.1, 90.5	60.1, 90.5	7.7, 11.7	65.6, 98.8	308
2UH	10	1	0.251	41.5	42.4	5.5	45.3	314
2UH[c]	10	2	0.250	45.5, 53.8	46.5, 54.8	6.1, 7.2	49.7, 58.8	539

[a]About 11.8% (molar) Ar tracer included in CO cylinder
[b]Not included in kinetic data sets for parameter estimation, see Section 2.3.5
[c]Values for lower total flow and higher total flow rates, respectively

Run 10 includes separate samples of 2UH run in each reactor and analyzed on separate columns and detectors but on the same GC. The data from the two reactors are in very close agreement and are combined into a single kinetic data set for estimating activation energy and pre-exponential terms for 2UH including data collected between 207 and 313 h on stream and also between 529 and 539 h on stream.

The data for Run 10 collected between 314 h and 528 h are partial pressure kinetic data at 250 °C. For data in this time period, the CO conversion in reactor 1 is intentionally high in order to provide more total flow to reactor 2. Only the data from reactor 2 is used to find the dependence of

the rate on partial pressures of CO and H_2 in Section 4.7. The partial pressure data from reactor 2 are given in Table 4.11. The higher CO conversion data from reactor 1 are included in Appendix D.

4.2 Activity of CO Consumption

The activity of a catalyst at a given temperature is usually the first metric for choosing between catalysts for the same process. It is usually given the most attention, though selectivity and stability may be more important depending on the application.

4.2.1 Activity Calculations

For this study, rates of CO depletion are determined by measuring CO conversion in the FB reactor operated as a differential reactor and using the form of the reactor performance equation given in Equation 4.1.

$$-r_{\mathrm{CO}} = \frac{F^0_{\mathrm{CO}} X_{\mathrm{CO}}}{W_{cat}} \tag{4.1}$$

Experimental rate constant (k) values are determined for every data point from the rate data using Equation 4.2 by assuming the P_{CO} and $P_{\mathrm{H_2}}$ dependencies proposed by Eliason [56]. Values of P_{H_2} and P_{CO} are simple averages of the inlet and outlet partial pressures of each gas.

$$k = \frac{-r_{\mathrm{CO}}}{P^{-0.05}_{\mathrm{CO}} P^{0.6}_{\mathrm{H_2}}} \tag{4.2}$$

Activation energy and pre-exponential factor for each catalyst are regressed from k versus T data using the Arrhenius relationship from Equation 4.3.

$$k = Ae^{-E_A/RT} \tag{4.3}$$

4.2.2 Statistical Considerations

Before presenting and discussing results of activity experiments on the catalysts of this study, it is prudent to establish the ability to differentiate between results in a statistical manner. Much of the variance in catalyst activities of repeat preparations is attributed to variation between preparations. 1UH and 1UHa (a repeat preparation of 1UH) provide insight into the repeatability of

catalyst preparations and also into the ability to discern meaningful trends from the data. Figure 4.1 shows values of rate constant for several temperatures for 1UH and 1UHa and also shows an Arrhenius fit and the 95% single-point confidence band for all the data on these two catalysts. This band represents the range in which a single additional data point would be expected to fall. Data outside this band have less than 5% probability of coming from the same treatment or population. The band was calculated assuming each data point (1,023 points, see Table 4.2) was an independent replicated measurement; however, calculating the bands on the basis of averaged values (about 16 data points) would not significantly increase the width of the band.

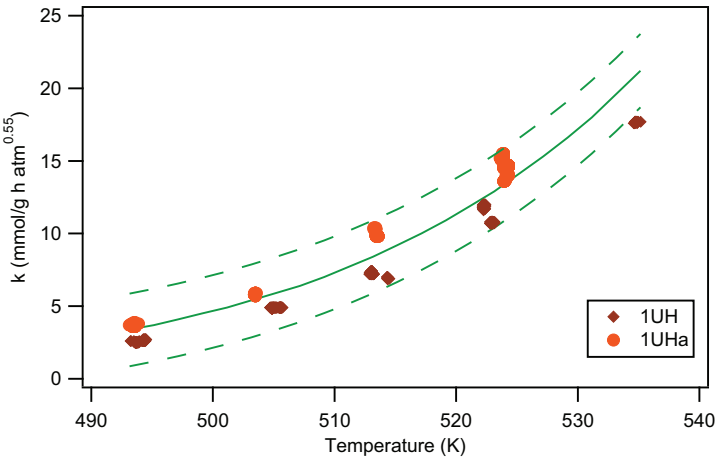

Figure 4.1: Rate constant as a function of temperature for 1UH and 1UHa catalyst kinetic data sets. The mean (solid line) of the values of k for these two catalysts and the 95% single-point confidence band (dashed lines) are shown in green.

In the analysis that follows, the variation between preparations for 1UH and 1UHa is assumed representative for all preparations. When data from one catalyst falls within the single point prediction band of another catalyst, the data are not statistically different; however, the fact that two data sets are not statistically different does not mean that they are the same. The four 1S catalysts were precipitated in a single batch and then calcined and reduced under the same conditions in order to minimize the variations between these samples. The four 2S catalysts were also carefully prepared to minimize variation. Trends presented in Sections 4.2.4 to 4.2.6 and 4.3 suggest that the care in preparing the catalysts provided meaningful correlations despite the potentially large variation between repeat reparations.

4.2.3 Activity Data

Figures 4.2 to 4.5 show experimental rate constant values as functions of temperature for all the catalysts of this study, and compare the kinetic data sets for this study. The solid lines are calculated from Equation 4.3 using the regressed values of A and E_A. The dashed lines in Figures 4.2 and 4.3 represent the single point prediction bands for 1UH and 1UHa and for 2UH, respectively. Kinetic data sets are gleaned from the FB experiments according to the criteria described in Section 2.3.5 and Table 2.5. The most active catalyst is 1UHa followed by 2UH, 1WL, 1ULa, 1UH, and 2UL. Excluding 1WL and 1WH which have low K loadings, all 1U and 2U catalysts are more active than W catalysts at 250 °C. D catalysts show the lowest activity at 250 °C. Except for 1UL and 2DL, H catalysts are more active than L catalysts. 1UH and 1UHa statistically differ from 1UL and 1WH at higher temperatures. 2UH statistically differs from 2WH and 2WL at temperatures greater than 510 K and different from 2UL at temperatures greater than 520 K. All data at low temperatures are difficult to distinguish as the rate of reaction approaches zero and the prediction bands for all data sets begin to overlap. It is the higher temperature data in which differences are most easily detected.

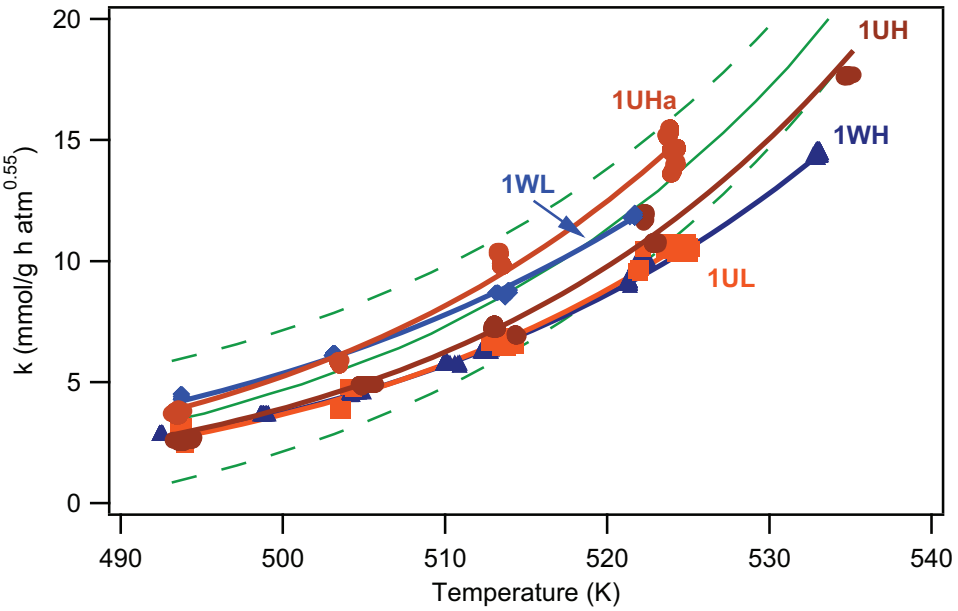

Figure 4.2: Rate constant as a function of temperature for 1S catalyst kinetic data sets.

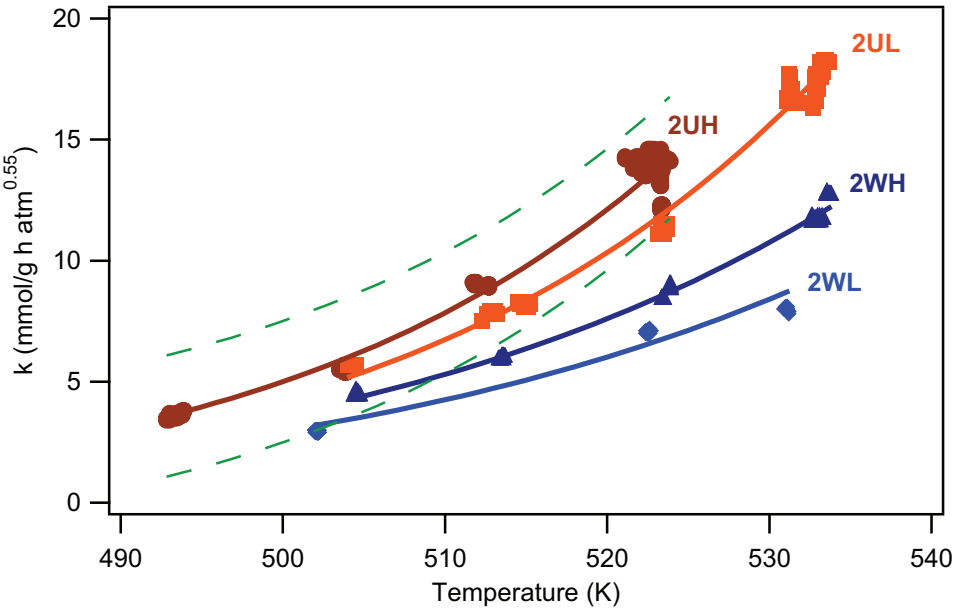

Figure 4.3: Rate constant as a function of temperature for 2S catalyst kinetic data sets.

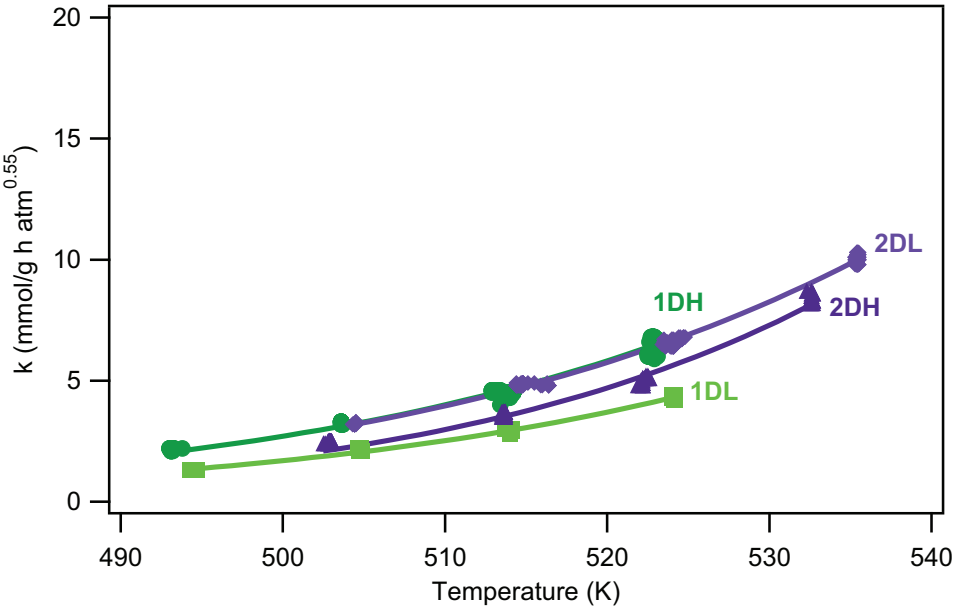

Figure 4.4: Rate constant as a function of temperature for D catalyst kinetic data sets.

Table 4.2 gives the estimated kinetic parameters, the number of data points used in the regression, and averaged experimental rates of reaction for each of the 12 principle catalysts and the 5 additional catalysts in this study. The differences in actual reactor temperatures and the five chosen tabulated temperatures for each catalyst are up to ± 5 °C; however, the average difference

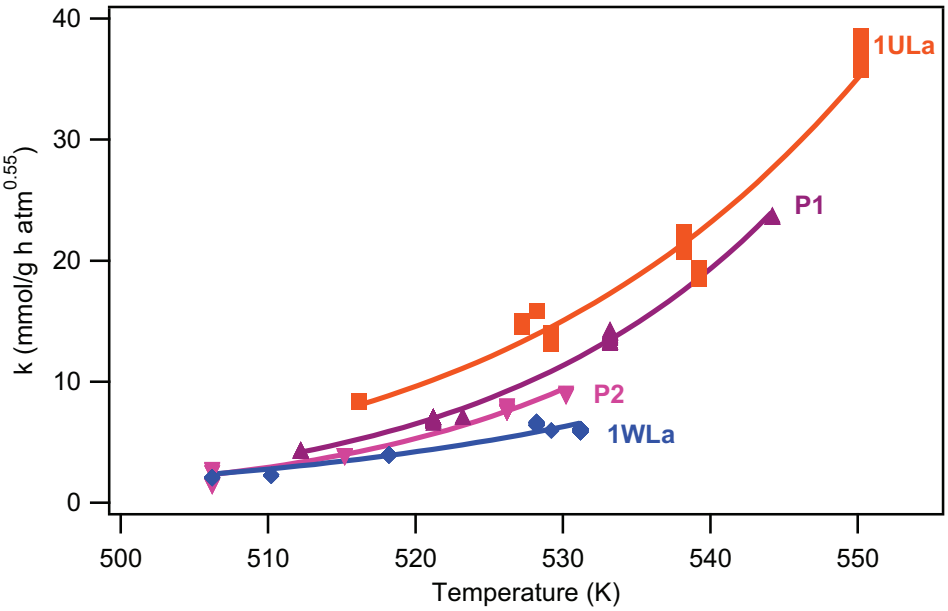

Figure 4.5: Rate constant as a function of temperature for other catalyst kinetic data sets.

in temperature over all conditions for each catalyst is less than 1.1 °C with the exception of 1ULa, 1WLa, and P2 for which the average differences are 4.3, 3.7, and 2.7, respectively. The absolute largest difference at any temperature for each catalyst is reported in the table. Rates are normalized to the indicated temperatures with the experimental activation energies and normalized to $P_{H_2} = P_{CO} = 6.21$ atm using the partial pressure dependencies in Equation 4.4.

$$-r_{CO} = Ae^{-E_A/RT} P_{CO}^{-0.05} P_{H_2}^{0.6} \tag{4.4}$$

The activation energy reported for Eliason's model is 92 kJ/mol. The activation energy for 1UHa is very similar at 93.8 kJ/mol, but all other activation energies for unwashed 1S and 2S catalysts are higher (94.3–98.9 kJ/mol) and activation energies for washed 1S and 2S catalysts are lower (76.6–90.6 kJ/mol).

Because E_A and A are correlated, simple confidence intervals for each parameter do not adequately express the confidence of the regressed values. Instead, a joint confidence region is plotted for the correlated parameters. Figure 4.6 gives the approximate joint 95% confidence region of the estimated values of E_A and A for 1UH. The joint confidence regions for all other catalysts are given in Appendix B. Like a confidence interval which indicates the possible range the true value

Table 4.2: Kinetic parameters, number of data points, and average normalized rates of reaction at 5 temperatures for all catalysts of this study. Rates are normalized to each T with the experimental E_A for each catalyst and to $P_{H_2} = P_{CO} = 6.21$ atm using Equation 4.4.

					$-r_{CO}$ $mmol_{CO}/g_{cat}/h$				
Catalyst	points	E_A[a]	A[a]	ΔT[b]	220 °C	230 °C	240 °C	250 °C	260 °C
1UH	454	98.9	8.43E10	2.6	6.8	12.1[c]	19.7	31.3	45.0
1UL	171	95.0	3.06E10	1.3	6.3	10.3	17.5	27.6	41[d]
1WH	376	90.6	1.10E10	4.5	7.9	11.8[c]	17.6	27.3	39.4
1WL	196	79.0	9.59E08	1.8	11.7	16.7	23.2	34.2[c]	47.7[d]
2UH	355	95.7	4.97E10	2.0	9.8	14.6	25.6	37.9	57.1[d]
2UL[e]	195	94.3	3.09E10	2.0	8.6[d]	14.7	21.0	30.5	48.7
2WH	139	79.4	7.19E08	1.6	7.6[d]	11.5	16.1	23.1	32.6
2WL	93	76.6	2.95E08	2.3	6.3[d]	8.4	13.0[d]	19.7	23.4
1DH	285	82.8	1.22E09	1.1	6.0	8.7	12.0	18.0	25.5[d]
1DL	262	84.3	1.09E09	1.7	3.3	5.5	7.7	11.3	16.3[d]
2DH	135	101	5.87E10	1.3	3.6[d]	6.5	9.6	13.3	22.6
2DL	139	82.7	1.18E09	1.7	5.5[d]	8.4	12.3	17.4	25.3
1UHa	569	93.8	3.32E10	1.2	10.0	15.6[c]	27.0	38.5	58.2[d]
1ULa[e]	298	103	1.97E11	5.0	7.2[d]	11.8[d]	19.8[c]	33.6[c]	45.4[c]
1WLa[e]	233	91.7	6.82E09	5.0	3.6[d]	5.0[c]	7.0[c]	13.2[c]	19.7[c]
P1	148	127	3.56E13	2.0	3.6[d]	6.7[d]	11.9	20.4[c]	37.1
P2	54	131	7.50E13	3.0	2.8[d]	4.9[c]	9.6[c]	18.0[c]	29.3[c]

[a]Units on E_A are kJ/mol and units on A are $mmol/g/h/atm^{0.55}$
[b]absolute largest difference between reactor and tabulated temperature in °C
[c]average correction to rate for temperature and pressure was $> 10\%$
[d]calculated rate
[e]dried at 120 °C instead of 100 °C

is likely to lie within, a joint 95% confidence region shows the possible combinations of values of regressed parameters which the true values could lie within. There is a 5% probability that the true values of E_A and A for 1UH are not within the region shown in Figure 4.6. The confidence region shows that if the value of A is fixed, then the 95% confidence interval of E_A is a very narrow range of values and visa versa.

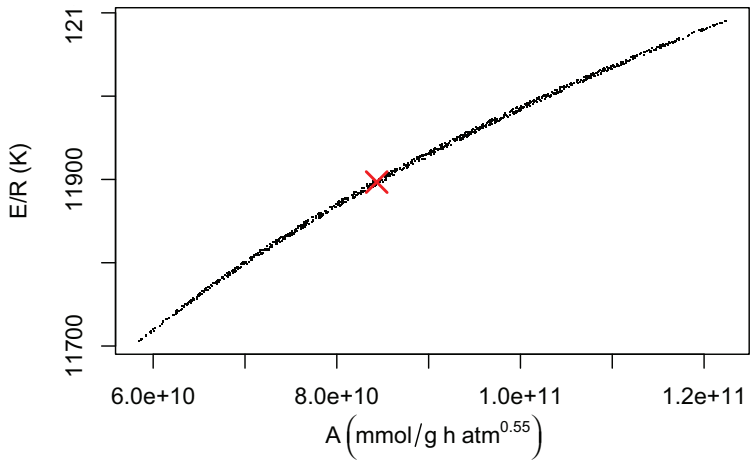

Figure 4.6: Approximate joint 95% confidence region of E_A and A for 1UH with values of the least-squares estimate marked by a red "X".

4.2.4 Results of Factorial Experiments

The results of the factorial experiments are illustrated well by the activities of the catalysts. Ignoring 1WL and 1WH, not washing increases catalyst activity significantly and drying initially at a high temperature increases activity mildly. Figure 4.7 illustrates the effects of the factorial variables (U/W and H/L) on rate of reaction at 250 °C. The 1W catalysts were excluded to avoid confusion over compounding effects from the lower potassium loadings of these two catalysts. The figure shows higher rates for unwashed catalysts than for washed catalysts. For example, the 2U catalysts show an average 60% increase (14.0 mmol/g/h) in rate compared to 2W catalysts. In addition, for each pair of 1U, 2U, and 2W catalysts, H catalysts show an average 19% increase (5.2 mmol/g/h for 2S catalysts).

The effects of washing and drying on estimated activation energies are quantifiable. Effects are defined as the average of the simple difference between results at each level. For example, the effect of not washing is the average of the difference in E_A between each U/W pair: 1UH and 1WH, 1UL and 1WL, 2UH and 2WH, and 2UL and 2WL. Quantified effects are given in Table 4.3. Not washing increases 1S catalyst activation energy by 12.1 kJ/mol and 2S catalyst activation energy by 17.0 kJ/mol for a combined effect of 14.6 kJ/mol. The effect of drying at a higher temperature initially is an increase of 7.8 kJ/mol for 1S catalysts and 2.1 kJ/mol for 2S catalysts for a combined effect of 4.9 kJ/mol.

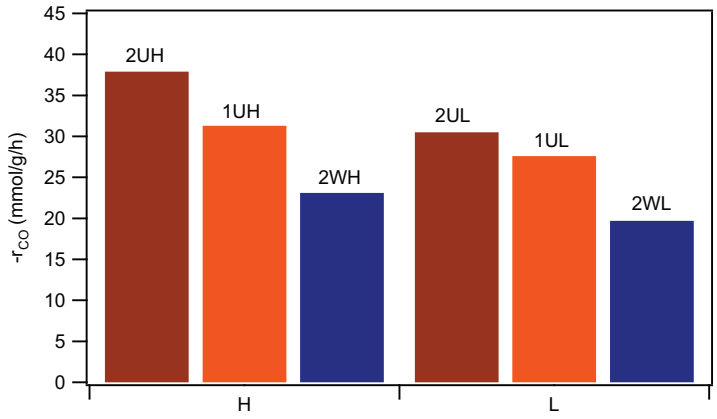

Figure 4.7: Effects of washing and drying on rate of reaction for 1S and 2S catalysts at 250 °C. 1WH and 1WL are not shown to avoid confusion over effects of low potassium loading.

Table 4.3: First order effects of factorial experiment variables (promoter addition, washing, and drying) on E_A and $-r_{CO}$ at 250 °C.

Parameter	1 Step	Unwashed	High Dry
E_A (kJ/mol)	4.4	14.6	4.9
$-r_{CO}$[a] (mmol/g/h)		14.0	5.2

[a]rate effects are for 2S catalysts only
effects are averaged differences of responses

It may be that 1WH and 1WL do not belong in this analysis because of their lower K loadings; however, excluding them would not eliminate these effects which are observed in both 1S and 2S catalysts. In addition, the values given above for 1S catalysts are similar enough to values for 2S catalysts (same order of magnitude and same sign) that there does not appear to be any reason to exclude the 1S catalysts other than the issue of nominal K loading. This shows that the robust nature of factorial experimental design provides relevant data on the design variables despite the loss of K in two catalysts. The effects indicate that the design variables influence catalytic properties regardless of promoter loading which suggests changes on a structural level that influence chemical behavior.

These activity results indicate that the washing step effects a fundamental change in the nature of the active sites. Site activity is related to binding energy. Sites with low binding energies

like planar sites can adsorb and desorb reactants quickly and may not allow for sufficient time and contact for the reaction to proceed efficiently. Sites with very high binding energies like corner sites or defect sites may bind reactants too strongly and prevent desorption of products. Sites with intermediate binding energies like edge sites found at the boundaries between crystallites may provide the majority of the turnover and activity. As speculated in Section 3.5.3, washing removes NH_4NO_3 from between particles and allows them to form larger, more ordered agglomerates as seen in the TEM images of 1WH (Figures 3.17 and 3.21). Images of 1WH show larger, smoother particles than do the images of 1UH. The surface reorganizations resulting from washing and subsequent grain growth during heat treatments appear to eliminate boundaries between crystallites, resulting in fewer edges and corners therefore eliminating active binding sites and resulting in lower catalyst activities.

The effect of adding the promoters in 1 step versus 2 steps is not immediately clear since only the U catalysts can be compared directly due to the issue of low potassium loading on 1W catalysts. 1S catalysts have an average 4.4 kJ/mol higher activation energy than 2S catalysts which is roughly the same as the effect of drying at high temperature and indicates a more active preparation. In contrast, the rates of reaction at 250 °C of 1U catalysts are lower than 2U catalysts, but the rates for 1W catalysts are higher than for 2W catalysts. Because of these trends, a conclusion about the effects of 1S versus 2S preparations is not given at this time.

The four D catalysts show lower activities than the eight 1S and 2S catalysts in this study, though they are very similar to the activity of 2WL which was the least active of the eight 1S and 2S catalysts. In addition, there is no discernible trend for the D catalysts from differences in initial drying temperature. Thus, drying the catalyst before washing neither preserves the precursor structure nor affords any benefit to catalyst activity which is contrary to the original hypothesis. Agglomeration theory provides an explanation for this observation. Since the catalysts were first dried before washing, they would have the mild agglomerate sizes of 1U and 2U catalysts which are 50–100% larger than catalysts dried at 120°C. The silica in the 1D catalysts helps preserve the pore and particle diameters of the dry precursors of these catalysts but does not prevent some agglomeration which results in moderate pore and particle diameters similar to 1WH and 2WH. With no silica in the 2D catalysts prior to washing, the washing process causes further agglomeration in these catalysts resulting in larger pore and particle diameters similar to 1WL and 2WL regardless

of the drying temperature. For both 1D and 2D catalysts, subsequent calcination and reduction procedures would cause large grain growth in the agglomerates which would eliminate active sites at grain boundaries.

4.2.5 Effect of Potassium Loading

For 2S catalysts, the order of decreasing activity is 2UH > 2UL > 2WH > 2WL. For 1S catalysts, the trend is different with 1WL > 1UH> 1UL > 1WH. It is surprising that 1WL exhibits such a high rate of reaction (34.2 mmol/g/h at 250 °C) since rates measured on 2WL and 2WH were so much lower (19.7 and 23.1 mmol/g/h, respectively, at 250 °C). The reason for the high activity may be due to lower K content of 1S washed catalysts. The relative mass loading of K for 1WL measured by ICP and reported in Section 3.3 is 0.3 parts K per 100 parts Fe by mass (pbm — equivalent to g per 100 g Fe) compared to the target of 4.0 pbm.

Studies show that activity increases as K loading increases on iron FT catalysts up to 0.25 pbm and then decreases upon further loading with potassium [18, 52, 56, 68]. For the unsupported catalysts prepared by Eliason, the catalyst promoted with a K/Fe molar ratio of 0.013 (0.9 pbm K) was more active for CO conversion than the catalyst promoted with a ratio of 0.061 (4.2 pbm K). This agrees with a DOE study of five unsupported Fe/K/Si catalysts with different K/Fe atomic ratios between 0 and 2.2 which found the lowest apparent activation energy and highest CO conversion rate for a catalyst with a K/Fe atomic ratio of 0.36 (0.25 pbm K) [52]. The K loading of 1WL is very similar to the catalyst with the highest activity in the DOE study and is likely the reason for its high rate.

The other 1W and 1D catalysts do not show as high activity as 1WL. The activity for 1WH is almost as high as 1UL and probably due to the low K content (0.3 parts) as with 1WL. In contrast, activities of the 1D catalysts are among the lowest in this study despite having measured K loadings of 0.4 pbm. The reasons for these differences are not known, but there are several possibilities. For instance, the drying rate for 1WL may lead to a more optimal promoter distribution for the washed catalyst compared with 1WH. Drying the catalyst completely before washing (1D catalysts) may result in more K-SiO_2 interactions that reduce the effective K loading. The science of the solvent deficient precipitation method will benefit from future studies on preparing low K catalysts for high temperature FTS that may included studies on these phenomena.

4.2.6 Correlation With Particle Diameter And Pore Diameter

Figures 4.8 and 4.9 show rate of reaction at 250 °C versus particle diameter and pore diameter, respectively, for 1U, 2S, 2D, 1UHa, and 1ULa catalysts (10 catalysts). All low K (1W, 1D, and 1WLa) catalysts are excluded from these charts. Rate of reaction increases with decreasing particle and pore diameters. U and WH catalysts have particle and pore diameters mainly between 10 and 20 nm which may be ideal for FTS while WL catalysts show larger diameters and lower rates.

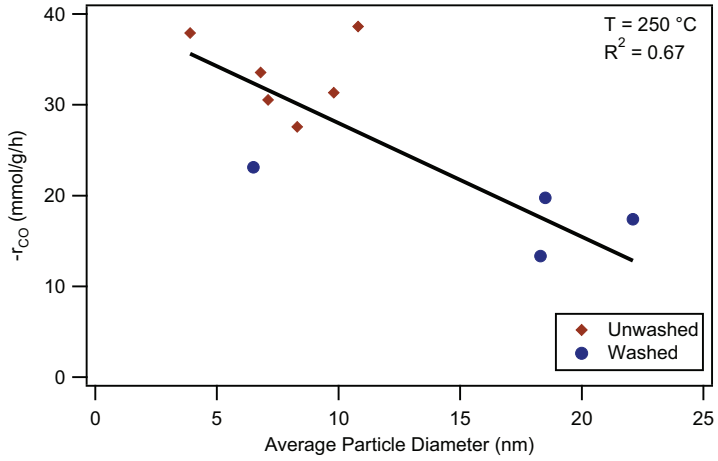

Figure 4.8: Rate of reaction after pretreatment and reaction at 250 °C versus average crystallite diameter after reduction.

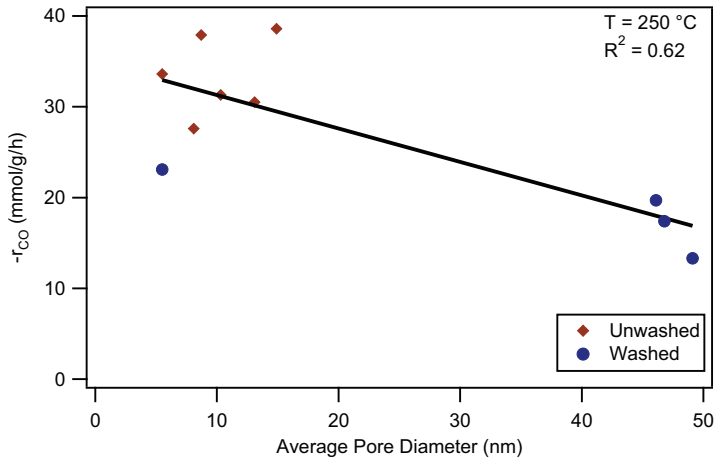

Figure 4.9: Rate of reaction at 250 °C versus average pore diameter after passivation.

4.2.7 Correlation With Surface Area

Figure 4.10 shows rate of reaction at 250 °C versus BET surface area for the same 10 catalysts. Again, all low K catalysts are excluded from the chart. Rate increases with increasing surface area, but the data points are not as well grouped as for the trends with particle and pore diameters. This suggests that the correlation between rate and surface area is weaker or less certain than between rate and particle and pore diameters. That surface area and rate do not correlate perfectly makes sense when one considers that the upper limit of surface area is the case of individual atoms (100% dispersion) and the lower limit is a single crystal ($< 1\%$ dispersion). As surface area increases, particle size decreases and surface energy increases resulting in larger binding energies which could decrease reaction rate. At the other end of the spectrum, decreasing surface area increases particle size and decreases surface energy which also results in lower reaction rates as binding energies are too small to allow reactants to dissociate efficiently. Somewhere in between these two extremes of surface area is the optimal condition where many sites exist which have the optimal level of uncoordination providing sufficient binding energy for the reaction to proceed at the highest rate.

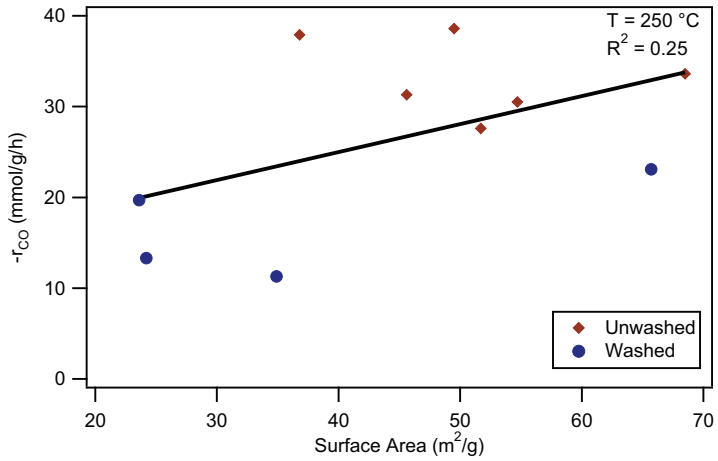

Figure 4.10: Rate of reaction at 250 °C versus surface area after passivation.

4.2.8 Correlation With Hydrogen Chemisorption

Figure 4.11 shows reaction rate at 250 °C versus hydrogen uptake for all 15 catalysts. Reaction rate generally increases with increasing hydrogen chemisorption measurements; however, there are a couple of exceptions, namely 1WLa and 1DL. In addition, the rates for unwashed catalysts are clustered above the rates for washed catalysts. Taken as a whole, the data do not indicate a strong correlation between reaction rate and hydrogen uptake since the spread of the clusters is so large. Considering washed and unwashed catalysts separately gives stronger positive trends. This suggests that chemisorption uptake is a good preliminary indicator of activity for catalysts of very similar preparations and compositions, but not a very good general metric between different catalysts.

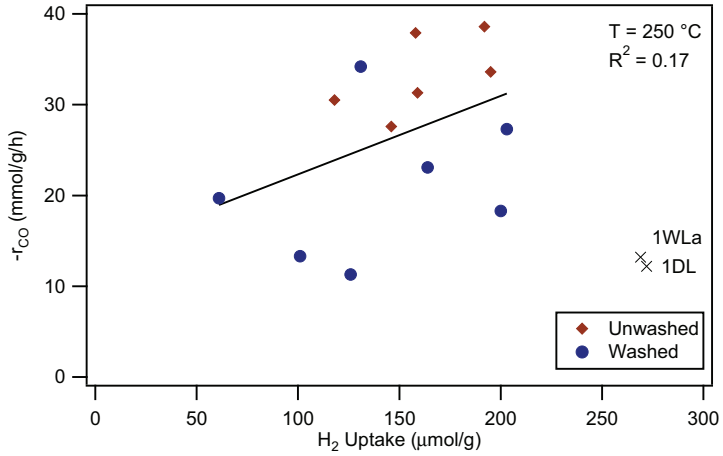

Figure 4.11: Rate of reaction at 250 °C versus hydrogen uptake. 1WLa and 1DL are labeled outliers and each is shown with an "X".

4.2.9 Correlation With XRD

It is probably not a coincidence that 1UL, 1WL, 2UH, and 2UL not only account for the four most active of the eight 1S and 2S catalysts, but also show the strongest XRD signal for Fe_2C and very weak or no signal for Fe_5C_2 and Fe_3O_4 (Section 3.7). This is not to say that Fe_2C is the active phase for FTS. There is a difference between bulk and surface phases and further studies using surface techniques like Mössbauer spectroscopy would be required to provide convincing

evidence. Indeed, other studies have attempted to use XRD in combination with surface techniques to identify the active phase [21] and both Fe_2C and Fe_5C_2 are candidates, but the debate in the scientific community continues.

4.2.10 Summary of Activity Results

In summary for catalysts of nominal promoter loading, activity appears to be related to particle size (amount of agglomeration) and degree of grain growth which are related to precursor structure and directly influenced by washing and drying steps. Catalysts with smaller particle sizes and smaller grains consistent with an unagglomerated ferrihydrite precursor show more activity than catalysts with larger particles and grains. Washing decreases activity by promoting the formation of larger particles and grains, especially in combination with drying at lower temperatures. The most active catalysts are unwashed and dried at high temperatures. These catalysts also have the highest activation energies. The higher activity of unwashed catalysts may be the result of preserving a dehydrated ferrihydrite structure through conversion to Fe_2O_3 and then to the reduced metal.

4.3 Selectivity

After activity, selectivity is a most important metric for catalyst performance and arguably the most important for FTS. The ideal catalyst would produce gasoline or diesel fuel exclusively; however, in practice a wide range of products are formed and even the best catalysts produce a range of products from methane to heavy molecular weight wax and species of every carbon number in between. Catalysts are chosen for their ability to produce a larger cut of the desired product and minimize the selectivity to products lighter than C_4H_8. Lighter products are more expensive to recover than their market value and are typically burned in the associated process utility furnace or else recycled and partially oxidized to enrich the H_2 content of the feed to the reactor.

4.3.1 To Water-Gas Shift

For H_2 deficient feed stocks like coal or biomass, the water gas shift (WGS) activity of Fe FT catalysts is important. Table 4.4 reports the mole percent of CO converted to CO_2 as an indicator of the WGS activity of each catalyst in this study at several temperatures. WGS selectivity increases with increasing temperature for all catalysts in this study. This suggests that the activation energy for the WGS reaction is larger than for the FT reactions.

Table 4.4: Selectivity of CO to CO_2 (mole%) for all catalysts in this study. 95% confidence intervals are less than $\pm 1.5\%$ ($\pm 0.25\%$ average) for all values.

	Selectivity to CO_2				
Cat.	220 °C	230 °C	240 °C	250 °C	260 °C
1UH[a]	35.2	41.7	43.1	45.2	46.7
1UL[a]	36.9	38.2	43.3	45.5	
1WH	7.4	10.7	14.4	18.9	24.4
1WL	7.8	9.8	14.2	18.0	
2UH	25.8	30.5	31.2	32.6	33.5
2UL		23.2	29.5	34.0	38.8
2WH		24.0	28.7	33.9	38.8
2WL		31.2	32.5	37.1	37.5
1DH	8.8	11.7	17.4	23.4	
1DL	7.5	10.3	14.8	20.4	
2DH		33.1	34.6	36.3	40.8
2DL		32.8	34.6	35.7	39.6
1UHa	25.8	29.0	31.5	32.6	34.4
1ULa[b]			33.7	36.2	38.6
1WLa[b]		16.7	21.0	26.3	33.0
P1[b]			18.9	24.5	31.6
P2[b]		24.1	27.9	32.3	37.4

[a] CO_2 peak split from C_3 peak by GC software
[b] values interpolated from data between the temperatures.

Figure 4.12 shows CO_2 selectivities versus temperature for the eight 1S and 2S catalysts. WGS activity increases with increasing temperature for all 1S and 2S catalysts. WGS activities of catalysts with higher K loadings are less sensitive to temperature than catalysts with very little K

as indicated by the slopes of the trend lines i.e. 0.0028 for 1U catalysts compared to 0.0040 for 1W catalysts. Promotion of the WGS reaction by K is well documented [14, 18, 56, 68].

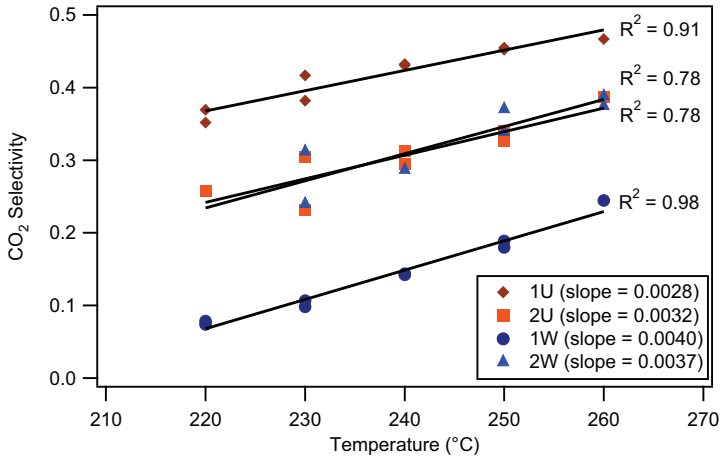

Figure 4.12: CO_2 selectivity versus temperature for the eight 1S and 2S catalysts.

The 1U catalysts exhibit the highest WGS activity with 35.2–46.7% selectivity to CO_2. 1W and 1D catalysts show the lowest WGS activity of the twelve 1S, 2S, and D catalysts with 7.4–24.4% selectivity. 2S and 2D catalysts fall between these levels. The differences in selectivities are due to the content and dispersion of K in the catalysts. The higher WGS activities of 1U catalysts may be due to more even distribution and greater dispersion of K while the low WGS activities of the 1W and 1D catalysts are due to almost complete loss of K during washing (K loadings < 0.4 pbm). The intermediate WGS activities of 2S and 2D catalysts reflect K distributions less uniform than 1S catalysts (see Section 3.3).

The difference between 1UHa and 1UH (32.6% and 45.2% respectively) is not easily explained except as variation between batches. In the 1S preparation, the $KHCO_3$ was added to the NH_4HCO_3 and thoroughly mixed before the precipitation of the metal salts which resulted in a very uniform distribution of potassium. In the 1UHa preparation, less care may have been taken to distribute the $KHCO_3$ in the NH_4HCO_3 before precipitation. Microprobe images of promoter distributions are not available for 1UHa, but it may be that the distribution of promoters in 1UHa is less uniform than in the 1S catalysts.

4.3.2 To Methane

Molar selectivity of CO to hydrocarbons is reported in three groups, namely the selectivity to CH_4, the selectivity to C_2H_6, and the selectivity to C_{2+} hydrocarbon species. Since CH_4 consumes the most H_2 per mole CO and provides the least value, CH_4 make should be minimized. Table 4.5 reports the selectivity to CH_4 at several temperatures for each catalyst.

Table 4.5: Selectivity of CO to CH_4 (mole%, CO_2-free basis) for all catalysts in this study. 95% confidence intervals are less than $\pm 0.7\%$ (average $\pm 0.09\%$) for all values.

	Selectivity to CH_4				
Cat.	220 °C	230 °C	240 °C	250 °C	260 °C
1UH	3.6	4.7	5.3	6.3	7.5
1UL[a]	3.9	4.0	4.6	5.0	
1WH	13.8	14.8	15.5	15.1	15.6
1WL	10.3	10.8	12.0	12.5	
2UH	5.1	6.9	7.2	8.4	9.5
2UL[b]		3.6	4.9	6.0	7.6
2WH[b]		3.1	3.8	4.9	6.1
2WL[a]		5.1	5.5	7.2	7.6
1DH	14.8	14.6	16.8	17.3	
1DL	13.5	14.1	15.0	15.5	
2DH		7.4	8.4	9.1	10.1
2DL		7.8	8.6	9.3	10.8
1UHa	3.6	4.2	4.7	5.3	4.9
1ULa[c]			6.2	7.2	8.1
1WLa[c]		9.1	11.2	13.7	16.8
P1[c]			4.9	6.1	7.7
P2[c]		8.6	9.2	9.8	10.5

[a] CH_4 peak split from C_2H_4 peak by GC software
[b] CH_4/C_2H_4 peak split estimated from other by GC data
[c] values interpolated from data between the temperatures.

CH_4 selectivity increases with increasing temperature as shown in Figure 4.13. Selectivities for the eight 1S and 2S catalysts appear to increase at about the same rate with temperature suggesting that K loading has little or no effect on the activation energy of the methane reaction.

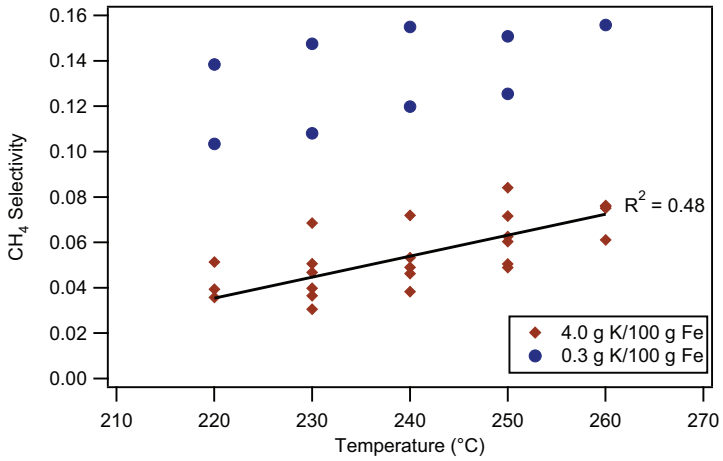

Figure 4.13: CH_4 selectivity versus temperature for the eight 1S and 2S catalysts.

Figure 4.14 shows selectivity to CH_4 at 250 °C versus potassium loading. 1W and 1D catalysts (0.3–0.4 pbm K) have selectivities 50–200% higher than catalysts with nominal potassium loading (3.6–5.2 pbm K). 1WLa has an intermediate potassium loading (1.1 pbm K) and follows the decreasing CH_4 selectivity with increasing loading trend. Decreasing CH_4 selectivity with increasing K loading is well documented [14, 18, 52, 68]. The higher selectivity to CH_4 of 2UH is likely due to poor promoter distribution as discussed in Section 3.3.

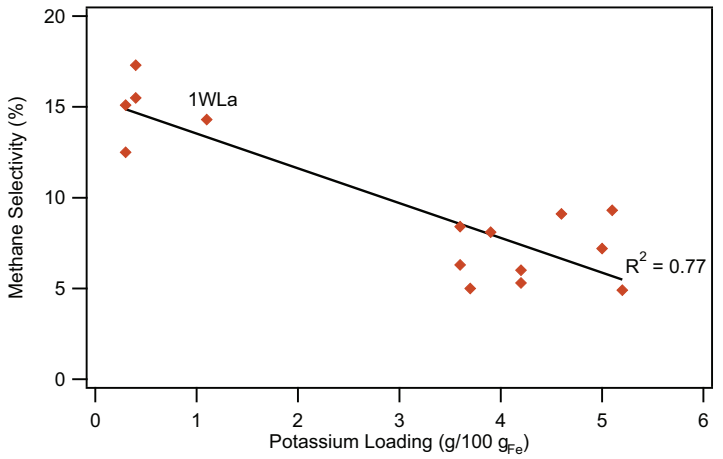

Figure 4.14: CH_4 selectivity versus potassium loading for the 15 SDP catalysts.

4.3.3 To Ethane

Selectivity to C_2H_6 (along with selectivity to CH_4) provides an indicator of the FT product slate with high C_2H_6 selectivity corresponding to light products and low selectivity corresponding to heavier products. Table 4.6 lists the selectivity to C_2H_6 at several temperatures for each catalyst. The low K catalysts show very high C_2H_6 selectivities (7.2–14.1%) while high K catalysts excluding 2UH have low C_2H_6 selectivities (0.6–4.1). 2UH shows unusually high C_2H_6 selectivity possibly as a result of poor promoter distribution and more potassium-silica interactions.

Table 4.6: Selectivity of CO to C_2H_6 (mole%, CO_2-free basis) for all 17 catalysts. 95% confidence intervals are less than ±0.8% (average ±0.08%) for all C_2H_6 selectivity values. Also shown are olefin to paraffin ratios at 250 °C.

	Selectivity to C_2H_6					
Cat.	220 °C	230 °C	240 °C	250 °C	260 °C	O/P[a]
1UH	0.9	1.3	1.2	1.5	1.8	2.0
1UL	1.4	1.1	1.4	1.8		2.4
1WH	7.7	8.2	8.7	8.7	9.0	0.1
1WL[b]	7.2	7.9	10.0	12.8		—
2UH	5.5	7.1	7.9	10.1	10.5	0.8
2UL		0.7	0.9	1.0	2.0	2.6
2WH		0.6	0.7	0.8	1.2	3.4
2WL		1.6	2.3	3.4	3.7	0.9
1DH	7.1		8.6	9.2		0.1
1DL	12.0		13.1	14.1		—
2DH		1.8	2.2	2.3	2.2	2.3
2DL		1.7	2.0	2.1	2.2	1.9
1UHa	2.5	3.2	4.1	3.9	4.1	—
1ULa[c]			3.1	3.6	4.0	0.9
1WLa[c]		3.1	4.5	6.6	9.6	0.3
P1[c]			1.5	2.2	3.4	1.0
P2[c]		2.3	2.5	2.6	2.8	1.0

[a]Olefin to paraffin ratio at 250 °C
[b]Includes both C_2H_6 and C_2H_4
[c]values interpolated from data between the temperatures.

The selectivity-temperature data for 1S and 2S catalysts are plotted in Figure 4.15. Selectivity to C_2H_6 generally increases with increasing temperature, though 1W (low K) catalysts and 2UH increase more than 1U and 2S (high K) catalysts.

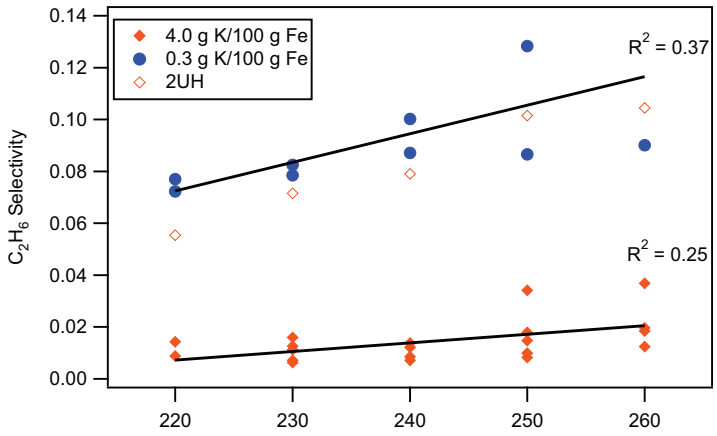

Figure 4.15: C_2H_6 selectivity versus temperature for 1S and 2S catalysts.

Table 4.6 also reports olefin to paraffin ratios (O/P) at 250 °C. Olefin to paraffin ratios are estimated with less certainty than the selectivity values. As described in Appendix A.5, C_2H_4 peaks in many cases eluted with other peaks or were partially cut off or not recorded at the end of a GC run. For FB runs showing merged peaks, estimates of the constituent peak areas were obtained by the GC software or else by analysis of fortuitous GC data from the same FB run. C_2H_4 peak areas were not calibrated with a gas standard but were estimated from published relative response ratios for TCDs.

Despite the uncertainties in the olefin quantification, it is instructive to examine the O/P and the total C_2 selectivity. Figure 4.16 gives O/P for 1U, 2U, 1WH, and 2WH catalysts versus temperature (data is not available for 1WL and is missing at several points for 2WL). The lowest O/P is for 1WH, consistent with a low K loading catalyst. 2UH also shows low O/P which decreases with increasing temperature despite its higher K loading. In contrast, 1UL shows the highest O/P with a maximum of 4.5 at 230 °C. The remaining catalysts (1UH, 2UL and 2WH) show maximum O/P at 250 °C with 2WH giving the highest ratio at 3.4. At 250 °C, the total C_2 selectivity ($C_2H_4 + C_2H_6$) for 1UH, 1UL, 2UL, and 2WH are two thirds or less of the totals for 1WH and 2UH. 1WH has

a very low O/P but very high selectivity to C_2H_6; therefore, the amount of C_2H_4 it makes is only slightly lower than the other catalysts. This suggests heavier product selectivities as expected for high K catalysts (except 2UH) and lighter product selectivities for low K loading catalysts. The issue with product selectivity on 2UH may be a result of poor promoter distribution possibly in combination with a large amount of K-SiO_2 interactions.

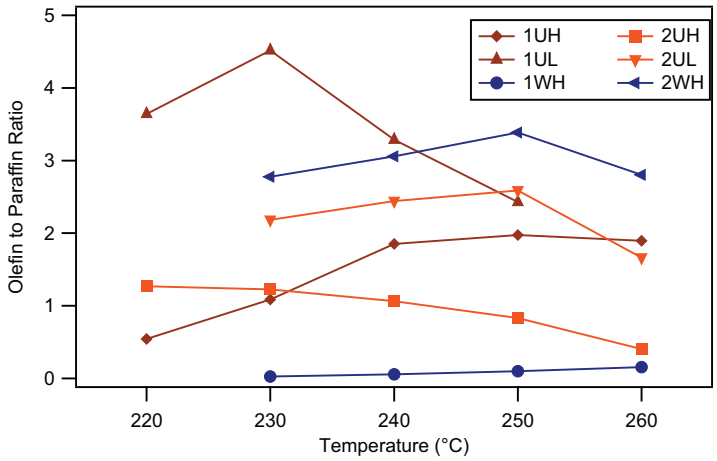

Figure 4.16: Olefin to paraffin ratios versus temperature for 1S and 2S catalysts excluding WL catalysts.

Low K and high K catalysts are ideal for different systems. For high temperature FTS intended for gasoline production, the lighter product slate of low K catalysts like 1WL is preferred. For low temperature FTS intended for making wax which is cracked to make diesel fuel, the heavier product slate of high K catalysts like 1UL is preferred.

4.3.4 To Higher Hydrocarbons

The selectivity to C_{2+} hydrocarbon products on a CO_2-free basis at several temperatures is given for each catalyst in Table 4.7. For all catalysts, these selectivities are for C_2 and higher hydrocarbon products including paraffins, olefins, alcohols, waxes, and other oxygenated, unsaturated, and branched species. Selectivity to higher hydrocarbons for all catalysts generally decreases (albeit slightly) with increasing temperature which is the opposite trend observed for methane selectivity versus temperature since C_{2+} selectivity is calculated by subtracting methane selectivity

from 1. As indicated in previous sections, high potassium catalysts give the highest selectivities to heavier products (88.6–96.9 compared to 81.3–92.6).

Table 4.7: Selectivity of CO to C_{2+} hydrocarbons (mole%, CO_2-free basis) for all catalysts in this study.

	Selectivity to C_{2+} hydrocarbons				
Cat.	220 °C	230 °C	240 °C	250 °C	260 °C
1UH	96.4	95.3	94.7	93.7	92.5
1UL	96.1	96.0	95.4	95.0	
1WH	86.2	85.2	84.5	84.9	84.4
1WL	89.7	89.2	88.0	87.5	
2UH	94.9	93.1	92.8	91.6	90.5
2UL		96.4	95.1	94.0	92.4
2WH		96.9	96.2	95.1	93.9
2WL		94.9	94.5	92.8	92.4
1DH	85.2	85.4	83.2	82.7	
1DL	86.5	85.9	85.0	84.5	
2DH		92.6	91.6	90.9	89.9
2DL		92.2	91.4	90.7	89.2
1UHa	96.4	95.8	95.3	94.7	95.1
1ULa			93.8	92.8	91.9
1WLa		90.9	88.8	86.3	83.2
P1			95.1	93.9	92.3
P2		91.4	90.8	90.2	89.5

4.3.5 Preliminary Catalyst Discrimination

Section 4.2 shows that the highest activity catalysts are 1UH, 1WL, 2UH, 2UL, 1UHa and 1ULa. With the selectivity data presented above, some preliminary observations can made about which preparation methods produce the best catalysts. Table 4.8 summarizes the activities and selectivities at 260 °C of the six most active catalysts of this study.

For high K catalysts, the 1UH, 2UL and 1UHa have good selectivities to C_{2+} with 1UH and 1UHa making the least amount of CH_4 + C_2H_6. Selectivities for 2UH and 1ULa are less favorable even though they are the second and third most active high potassium catalysts. Thus,

Table 4.8: Activity and selectivity at 260 °C of the six most active catalyst of this study listed in order of decreasing rate of reaction. Hydrocarbon selectivities are CO_2-free.

		Selectivity (mol% CO)			
Cat.	$-r_{CO}$[a]	CO_2	CH_4	C_2H_6	Other[b]
high potassium					
1UHa	38.5	34.4	4.9	4.1	91.0
2UH	37.9	33.5	9.5	10.5	80.0
1ULa	33.6	38.6	8.1	4.0	87.8
1UH	31.3	46.7	7.5	1.8	90.7
2UL	30.5	38.8	7.6	2.0	90.4
low potassium					
1WL[c]	34.2	18.0	12.5	12.8	74.7

[a]mmol/g/h
[b]other hydrocarbons, CO_2-free
[c]all 1WL data at 250 °C

the 1UH preparation in general gives the best combination of high activity and high selectivity to heavy hydrocarbons of all the catalysts in this study and suggests that adding promoters in 1 step is superior to adding promoters in 2 steps.

For low K (1W and 1D) catalysts, the activity of 1WL is by far the highest and the selectivity to CH_4 is the lowest. Since making low K catalysts was not the intention of the factorial design of experiments in this study, there are no unwashed low K catalysts to compare against 1WL.

4.4 Stability

In addition to activity and selectivity, catalyst stability is a key metric for discerning between catalysts. Both catalyst activity and selectivity can change with time. Figure 4.17 shows the reaction rate constant for 1UH (R1 of FB Run 6) as a function of time-on-stream for all steady state periods of data including data taken during the startup period not included in kinetic data sets. Data collected at other temperatures were adjusted to 250 °C with the E_A reported in Table 4.2 and data collected at $X_{CO} > 0.25$ were corrected for pore diffusion resistance using a calculated effectiveness factor (η) of 0.91. The data span more than 500 hours and show little or no downward

trend with time suggesting that this catalyst has excellent activity stability. The variation (scatter) in apparent rate constant measurements may be due in part to inaccurate orders of reaction used to calculate k.

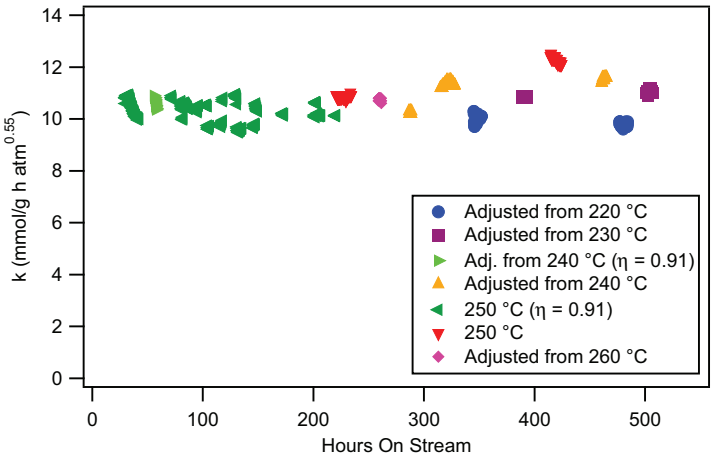

Figure 4.17: Experimental rate constant values at 250 °C as a function of time-on-stream for catalyst 1UH. All data were adjusted to 250 °C using the E_A given in Table 4.2. Data collected at $X_{CO} > 0.25$ were corrected for pore diffusion effects using $\eta = 0.91$.

Figure 4.18 shows the rate constant as a function of time for all steady state data for 1WL from FB Run 7 including data taken during the startup period which are excluded from the kinetic data sets. All rate constant values are adjusted to 250 °C using the E_A in Table 4.2. Unlike 1UH, 1WL shows a longer activation period requiring nearly 150 h to reach steady activity, but the data after 150 h to the end of the run after 220 h shows good stability. The reason for the longer activation period needed to reach steady state may be related to the larger average particle size of 1WL (29.5 nm versus 9.8 nm). Larger particles require more time for complete carbidization. Longer activation time also may be related to the fact that washed catalysts retain the precursor ferrihydrite structure through calcination which may resist conversion to carbide or else the conversion to carbide occurs through a different structural pathway. Since washed catalysts show the highest extents of reduction (up to 50%), it seems unlikely that the ferrihydrite structure interferes with reduction to the metal. It is possible that conversion of Fe_3O_4 to carbide is faster than the conversion of metal to carbide. This would explain why 1WL with one of the highest extents of reduction requires more time during activation than does 1UL.

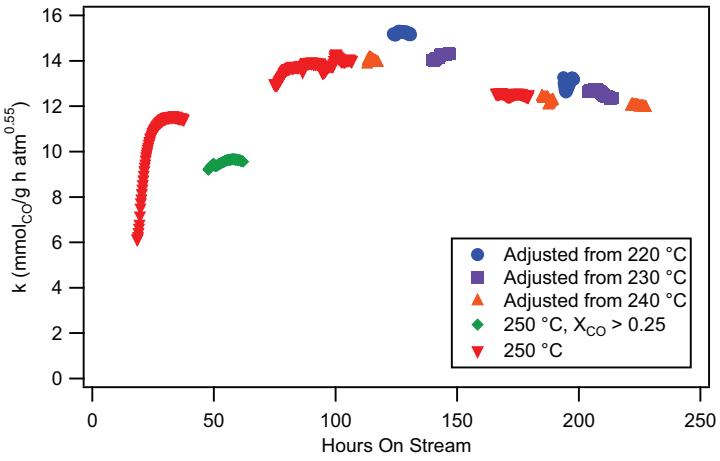

Figure 4.18: Experimental rate constant values at 250 °C as a function of time-on-stream for catalyst 1WL. Data collected at temperatures other than 250 °C were adjusted to 250 °C using the E_A given in Table 4.2. Data collected at CO conversion > 0.25 were normalized with $\eta = 0.98$ (negligible pore diffusion effects).

Figure 4.19 shows values of the rate constant calculated using Eliason's $m = -0.05$ and $n = 0.60$ for 2UH from FB Run 10 (R2 data set) including high conversion data which were not included in kinetic data sets. Rate constants were adjusted to 250 °C using the E_A given in Table 4.2. In contrast with the apparent stability of 1UH and 1WL, 2UH shows an apparent constant rate of decrease in activity (deactivation). For illustration purposes, a linear slope and intercept are regressed to the data recorded at 250 °C, excluding the temperature and partial pressure experiments, and are represented by the dark line in Figure 4.19. The rate of deactivation has the opposite sign of the slope and is the ratio of the slope to the intercept ($0.0056/16 = 0.00035$ h^{-1}). Activity at any time is $a_k = k(t)/k(0) = 1 - 0.00035t$ (Equation 2.18). The value of activity at the end of the 559 h FB run is 0.80 representing an activity loss of 20%. The decrease in activity is not simply a prolonged activation phase as is the case in 1WL because the decline is linear and constant over the full 559 h of the run. The cause of the deactivation is probably carbon deposition on the catalyst surface where the concentration of K appears to be higher. The scatter in the P_{CO}/P_{H_2} experiments indicates a problem with the assumed orders of reaction for CO and H_2. The partial pressure and deactivation issues are not independent and are more fully discussed in Section 4.7.

In summary, despite the high activity of 2UH, the better stability and CH_4 selectivity of 1UH indicate that the 1UH preparation produces the better catalyst for heavy FT wax production.

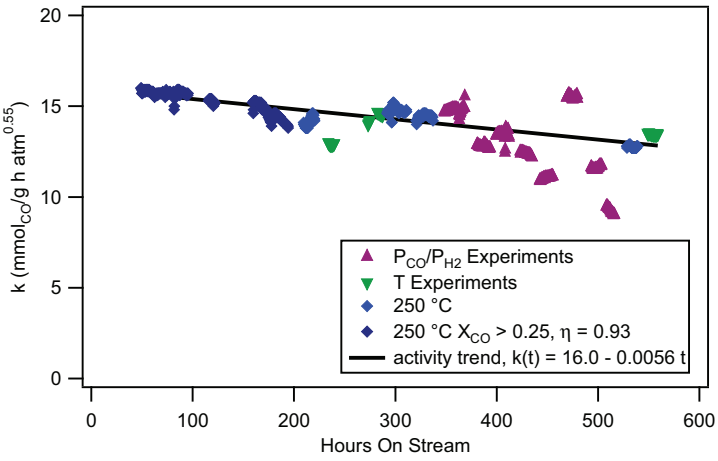

Figure 4.19: Experimental rate constant values at 250 °C as a function of time-on-stream for catalyst 2UH. Data collected at temperatures other than 250 °C were adjusted to 250 °C using the E_A given in Table 4.2. All data were adjusted for pore diffusion effects with values of η calculated at each point.

4.5 Comparison to Published Catalysts

The data and analysis given above allow for a comparison of the most active catalysts in this study (1UHa and 2UH) with some of the most active catalysts reported in the literature.

4.5.1 Data for Comparison

A convenient and informative comparison of active iron FT catalysts is given by Bukur et al. [16] and includes catalysts developed by researchers at Texas A & M University (TAMU), by Ruhrchemie, and by Mobil Research and Development Corporation. Data for the TAMU and Ruhrchemie catalysts come from tests at TAMU in a stirred tank slurry reactor while data for the Mobil catalyst come from a report describing data taken in a slurry bubble column reactor [69]. The data for these six catalysts (four reported catalysts and two from this study) are given in Table 4.9.

4.5.2 Activity Comparison

The catalysts from this study compare well with the published catalysts. Units of the rate constant are given as mmol/g/h/MPa to represent $\text{mmol}_{\text{H}_2+\text{CO}}/\text{g}_{\text{Fe}}/\text{h}/\text{MPa}_{\text{H}_2}$ in the following discussion. Values of the apparent first-order rate constants are 238 mmol/g/h/MPa for 2UH,

Table 4.9: Comparison of 1UHa and 2UH with four published, highly active iron catalysts [20].

	catalyst[a]								
	TAMU		TAMU		Ruhrchemie		Mobil	BYU	
Run ID	SA-1665		SA-2186		SB-2886		CT-256-13	1UHa	2UH
Pretreatment[b]	240$H_2$2h		TAMU		250$H_2$4h		280S12h	300$H_2$16h	
Test conditions									
T (°C)	260	260	260	260	260	260	257	261	260
P (MPa)	1.5	2.2	1.5	2.2	1.5	1.5	1.5	2.1	2.1
H_2CO feed	0.67–0.69		0.67–0.69		0.67–0.69		0.73	0.63–1.0	1.0
SV (nL/g_{Fe}/h)	2.3	3.4	3.9	5.8	4.1	2.3	2.3	15.1–17.0	32.8
TOS (h)	220	361	145	314	86	215	475	348	547
X_{CO}	84	80	81	84	66	82	90	31	18
X_{H_2CO}	79	76	77	79	63	79	82	32–44	12
%CO to CO_2	48.5	48.4						33.9	28.4
Apparent rate constant[c]									
mmol/g/h/MPa	250		400–450				155–265	251–414	238
Distribution of HC, mass%, CO_2- and oxygenate-free									
CH_4	3.2	3.0	3.9	3.0	5.3	6.4	2.7	5.1	8.1
C_2	3.4	3.8	4.4	4.0	3.0	4.4	2.9	7.7[d]	18.0
C_2–C_4	8.8	9.9	11.5	10.1	11.7	13.8	8.2	(20.1)[d]	(28.7)[d]
C_5–C_{11}	12.8	12.7	19.7	16.2	19.9	27.2	18.1	18.0	17.4
C_{12+}	71.9	70.5	60.6	66.6	60.1	48.2	68.1	49.2	27.8
Productivity									
g_{HC}/g_{Fe}/h	0.38	0.53	0.58	0.86	0.51	0.36	0.39	0.64	0.77

[a]TAMU: 100 Fe/3 Cu/4 K/16 SiO2, Ruhr.: 100 Fe/5 Cu/4.2 K/25 SiO2, Mobil: Fe/Cu/K
[b]240$H_2$2h is 240 °C in H_2 for 2h; TAMU is proprietary, S is syngas with $H_2/CO = 0.7$
[c]apparent first order rate constant ($mmol_{H_2CO}/g_{Fe}/h/MPa_{H_2}$)
[d]C_3–C_4 estimated using $C_2/(C_3 + C_4) = 2.6$; C_2H_4 estimated using $O/P = 1.0$

251–414 mmol/g/h/MPa for 1UHa, 250–450 mmol/g/h/MPa for the TAMU catalysts, and 155–265 mmol/g/h/MPa for the Mobil catalyst. The value for 2UH increases to 340 mmol/g/h/MPa if corrected for deactivation ($a_k = 0.7$). The range of values for the Mobil catalyst were calculated by Bukur and Lang using a simple computational reactor model and reflects uncertainties in the specifics of the gas-liquid mass transfer. The ranges for values of the 1UHa data reflect uncertainty in the H_2 feed flow rate and are discussed in detail in Section 4.5.5.

4.5.3 Selectivity Comparison

It is not the intent of this dissertation to provide a detailed selectivity analysis of any catalysts, but rough product distribution estimates for 1UHa and 2UH are presented here for comparison with published catalysts. The selectivity to CO_2 is not available for all of the reported catalysts; however, the TAMU value of 48.5% is typical for low H_2 to CO feed ratios to iron FT catalysts with high potassium loadings. The lower CO_2 selectivity values for the BYU catalysts are due in part to the higher H_2/CO feed ratio (1.0) and also due to promoter distribution as described in Sections 3.3 and 4.3. The selectivity for 1UH at 260 °C of 46.7% (Table 4.4) is very close to the TAMU values.

The hydrocarbon distributions of the BYU catalysts are not complete. Analysis of the liquid and wax products is described in Section 2.4.3. The C_3–C_5 species are almost entirely missing from the data due to inadequacies in product collection and online GC analysis. Better analysis would be achieved by analyzing the reactor gas effluent with an FID in series with the TCD and by avoiding loss of product with a more sophisticated collection vessel. In addition, products collected for the reported catalysts were produced at the conditions specified while the products of the BYU catalysts were collected only after the run was complete including 332 h (1UHa) or 539 h (2UH) at 220–250 °C. Nevertheless, the comparison of the hydrocarbon distribution data is informative. The methane selectivity (percent of total hydrocarbon mass) for 1UHa is 5.1% while 2UH is 8.1% compared to 2.7–6.4% for reported catalysts. The high methane make of 2UH was discussed in Section 4.3.2.

The selectivity to C_2 hydrocarbons is very revealing. The value for 1UHa is an estimated 7.7% (assumed $C_2H_4/C_2H_6 = 1.0$) while the value for 2UH is 18.0%. In contrast, reported catalyst C_2 selectivities are 2.9–4.4%. Higher C_2 product make suggests a lighter overall product slate. 1UHa and 2UH values for the C_3–C_4 range are estimated from an assumed $C_2/(C_3 + C_4) = 2.6$, similar to the TAMU catalysts.

Selectivities to C_5–C_{11} (gasoline range) for 1UHa and 2UH (18.0% and 17.4%, respectively), are between the 12.7 and 27.2% for reported catalysts. Selectivity to C_{12+} for 1UHa (49.2%) is near the value for the Ruhrchemie catalyst (48.2), but well below the other reported catalysts (60.1–71.9%). The value for 2UH is well below (27.8%) the others.

4.5.4 Comparison of Productivity

Catalyst productivities for the BYU catalysts (0.64 g_{HC}/g_{Fe}/h for 1UHa and 0.77 g_{HC}/g_{Fe}/h for 2UH) are quite good and are higher than all the others except for SA-2186 (TAMU proprietary pretreatment). Productivity is a function of reactor type and of process variables and increases with increasing *SV* (which decreases X_{CO}) and with increasing total pressure [20]. CO conversions on the BYU catalysts (31% for 1UHa and 18% for 2UH) are much lower (by design with much higher *SV*) than for the reported catalysts (66–90%), but the total pressure for the BYU tests is 2.1 MPa compared to 2.2 MPa for two of the conditions on the TAMU catalysts. In consideration of these factors and of the different types of reactors, the productivities of the BYU catalysts are probably competitive with the productivities of the published catalysts.

4.5.5 Flow Rate Considerations for 1UHa

The range of values for activity, space velocity (*SV*), and syngas conversion (X_{H_2CO}) for 1UHa in Table 4.9 reflect some peculiarities of the data starting at 309 h on stream. Data after 309 h are given in Table 4.9, but are not included in kinetic data sets for parameter estimation because they appear to be different from earlier data of the same run even though they are steady state data. After 309 h, steady state data at 230 °C and at 260 °C appear to show much higher H_2 usage and conversion than earlier data. The H_2 to CO usage ratios for earlier data are between 0.73 (250 °C) and 0.98 (220 °C) whereas the ratio after 309 h at 230 °C is 4.0 and the ratio at 260 °C is 1.88. The H_2 conversions appear unusually high at 46% and 59% for 230 °C and 260 °C, respectively, compared with only 12% conversion at an earlier test of 230 °C. Despite the much higher H_2 conversion at the later time, the CO conversion for 230 °C before and after 309 h is the same at 11.4% in both instances. Because the CO rate and conversion appeared normal, these differences in the later data were unnoticed during the reactor run. Post analysis of the data and discussions with the operator identify a false reading on the H_2 mass flow controller as the likely reason for the discrepancies, though the cause is unknown. The total flow rate during the time in question was not verified by the available soap film flow meter. Data from other runs were examined for these phenomena, but no other instances from this study were found. Assuming a H_2 to CO usage ratio of 0.7, the estimated H_2 feed flow rate is 37% less than was expected for the

flow controller setpoint. This assumption gives the lower value estimates of the activity, SV, and X_{H_2CO} in Table 4.9 while the higher values are for the data as recorded. That the lower estimate of the rate constant (251 mmol/g/h/MPa) is still within the upper range of the Mobil and TAMU SA-1665 catalysts (155–265 mmol/g/h/MPa) shows how active 1UHa is. The estimated H_2 flow rate gives a H_2 to CO feed ratio of 0.63 compared to 1.0 before 309 h.

4.5.6 Summary

Using 1UHa and 2UH as proxy, catalysts made by the solvent deficient precipitation method show great potential for having activity, selectivity, and productivity comparable to those of some of the most active and selective catalysts in the literature. The TAMU SA-2186 and SA-1665 tests were on the same catalyst, but SA-2186 was subject to an optimized pretreatment process that significantly enhanced the catalyst activity and productivity. The Mobil catalyst was also subject to an optimized pretreatment. The BYU catalyst pretreatment has not been optimized yet and improvements in catalyst preparation techniques and pretreatment are expected to improve catalytic properties significantly.

4.6 Repeatability of Catalyst Preparations

Repeatability of the preparation method is demonstrated by 1UHa and 1ULa. Table 4.10 compares properties of 1UH to 1UHa and 1UL to 1ULa. Synthesis of 1UH and 1UHa were very similar. Both 1UHa and the 1S precursors were prepared in 30 g_{Fe} batches. 1UHa was dried, calcined, and reduced using the same conditions as for 1UH. The resulting SA, V_{pore}, H_2 uptake, and d_c of 1UHa are all $\leq 20\%$ larger than 1UH. The d_{pore} of 1UHa is 45% larger than 1UH. The E_A of 1UHa is 5% less than the E_A of 1UH. The rate of reaction for 1UHa at 250 °C is 23% higher than the rate of 1UH. Selectivity to CO_2 of 1UHa is 28% less than that of 1UH. The CH_4 selectivity of 1UHa is 16% less than that of 1UH. One possibility for the differences in the preparations is that the $KHCO_3$ for the 1UHa preparation may not have been thoroughly mixed with the NH_4HCO_3 before the precipitation of the metal salts resulting in a non-uniform distribution of K.

Synthesis of 1UL and 1ULa were less similar. The batch size for 1ULa was 11 g Fe while 1UL was prepared as part of the 30 g Fe 1S batch of precursor. 1ULa was one of the first catalysts

Table 4.10: Comparison of 1UH and 1UHa physical and chemical properties. Rate, rate constant and selectivities are for 250 °C.

Cat.	SA m^2/g	V_{pore} mL/g	d_{pore} nm	H_2 uptake μmol/g	d_c nm	$-r_{CO}$ mmol/g/h	E_A kJ/mol	S_{CO_2} %	S_{CH_4} %
1UH	45.6	0.14	10.3	159	9.8	31.3	98.9	45.2	6.3
1UHa	49.5	0.16	14.9	192	10.8	38.5	93.8	32.6	5.3
1UL	51.7	0.13	8.1	146	8.3	27.6	95.0	45.5	5.0
1ULa	68.5	0.13	5.5	195	6.8	33.6	103	36.2	7.1

prepared for this study and one of the first four catalyst tested in the FBR while 1UL was prepared between FB Runs 5 and 6. In addition, the final drying temperature for 1ULa was 120 °C instead of the 100 °C for 1UL. Despite these differences, the SA, d_{pore}, H_2 uptake, and d_c of 1ULa are within 34% of values for 1UL. Pore volumes of the two catalysts are the same to two significant figures. The rate of 1ULa at 250 °C is 22% larger than the rate of 1UL. CO_2 selectivity for 1ULa is 20% lower than for 1UL. CH_4 selectivity of 1ULa is 42% higher than 1UL.

Based on the above two comparisons, the variability of reproducing any catalyst property in a second preparation is about 30%; however, the repeatability should increase significantly if consistent methods, practices, and equipment are used in repeat preparations. 1ULa was the first fully developed and tested catalyst prepared for this study. 1UHa was the last catalyst prepared. Methods and techniques for preparing catalysts and for testing catalysts improved significantly and the use of some equipment (drying ovens and furnaces) changed within the time between those two preparations. A specific recommendation is to ensure good integration and mixing of the $KHCO_3$ in NH_4HCO_3 and of the SiO_2 in the metal salts prior to precipitation.

Besides 1UHa and 1ULa, 1WLa is also a repeat preparation; however, FB Run 2 (Table 2.5) for 1WLa and P2 may be unreliable due to operator error. The H_2 tank was accidentally shut off at about 28 h into the run and the catalyst remained at 233 °C in a CO/Ar/He environment for a period of about 16 h until H_2 flow was restored. The effect of exposing the catalyst to a pure CO environment in this manner is unknown, but another study compared the effects of pretreating the catalyst with H_2, CO, or $H_2 + CO$. The study shows that using pure CO during pretreatment (8 h at 280 °C) results in lower initial activity and higher initial CH_4 selectivity which may be caused by carbon deposition on the catalyst surface [21]. The startup transient for the catalyst reduced

in CO lasted up to four times longer than for the catalyst reduced in H_2. The selectivity to CH_4 decreased continuously from 4% to 3% during the 140 h of the reaction. The steady state activity of the catalyst was equal to the activity of the catalyst reduced in H_2. In contrast, activity of 1WLa is among the lowest of the catalysts in this study while the activity of 1WL is among the highest. It may be that depositing the carbon after 28 h of FTS resulted in irreversible deactivation due to a phase change in the carbide species and blocking of active sites.

4.7 Partial Pressure Dependence

As mentioned in Section 4.4, the P_{CO} and P_{H_2} dependencies (m and n of Equation 2.11, respectively) of the power law rate equation proposed by Eliason ($m = -0.05$ and $n = 0.6$ in Equation 4.4) may not be appropriate for the catalysts in this study. Data from FB Run 10 (Table 4.1) in which P_{CO} and P_{H_2} were varied are used to determine the inherent dependencies for 2UH. The same steady state criteria for selecting temperature kinetic data sets applies to selecting partial pressure kinetic data sets for this study. The R2 data of Run 10 are for $X_{CO} < 0.25$) while the R1 data are for $X_{CO} > 0.25$. Only data from R2 are discussed in this section; however, the high conversion data from R1 are provided in Appendix D.

4.7.1 Kinetic Data

Averages of data taken at various P_{CO} and P_{H_2} from R2 of FB Run 10 on 0.250 g of 2UH after 200 h on stream are given in Table 4.11. The table is divided into temperature kinetic data and partial pressure kinetic data; however, the data will be referred to hereafter as the kinetic data set without distinguishing between temperature or partial pressure data. The values of η in the table are calculated using Equations 2.12–2.14 from the new regressed value of m after accounting for deactivation as discussed in Section 2.7.3 and are different from the values that would be calculated using the partial pressure dependence of the Eliason rate model.

Rate constant values as a function of time for the full 559 h data set for 2UH (R2 of FB Run 10) are shown in Figure 4.20. The rate constant is calculated assuming $m = -0.05$ and $n = 0.6$ from the Eliason rate model. All values of rate are adjusted for temperature with the E_A given in Table 4.2 for 2UH and adjusted for pore diffusion effects with η calculated at each point using

Table 4.11: Temperature and partial pressure kinetic data on 0.250 g of 2UH from R2 of FB Run 10. The time on stream of the first data point for each condition is given in the first column. Values of η are calculated using $m = 0.29$.

TOS h	T °C	F^0_{H2} mmol/h	F^0_{CO} mmol/h	F^0_{Ar+He} mmol/h	X_{CO} %	X_{H_2} %	$-r_{CO}$ mmol/g/h	P_{CO}[a] atm	P_{H_2}[a] atm	η
208	250	46.0	46.9	56.3	19.6	14.8	36.7	6.0	6.1	0.92
232	231	46.0	46.9	56.3	8.0	7.2	15.0	6.4	6.3	0.97
271	220	46.0	46.9	56.3	5.4	4.6	10.1	6.5	6.4	0.98
280	240	46.0	46.9	56.3	13.1	10.0	24.6	6.3	6.3	0.95
292	250	45.5	46.5	55.8	20.4	14.7	37.9	6.0	6.1	0.92
528	250	53.8	54.8	66.0	15.2	11.8	33.4	6.2	6.2	0.86
547	260	68.4	69.7	83.8	18.1	13.3	50.6	6.0	6.1	0.78
348	250	27.1	37.3	26.6	24.1	22.0	36.0	7.6	5.6	0.94
380	250	24.1	33.3	43.8	20.9	19.0	27.8	6.3	4.6	0.95
399	251	143.7	71.7	32.5	18.2	8.1	52.3	5.6	11.9	0.89
423	250	29.9	41.5	53.3	16.3	16.0	27.1	6.5	4.7	0.94
442	250	90.7	45.5	152.3	15.8	7.5	28.8	3.1	6.5	0.89
469	250	42.5	58.4	41.6	16.5	16.4	38.4	8.0	5.8	0.94
493	251	135.4	67.6	30.5	16.7	7.3	45.1	5.6	11.9	0.90
508	250	84.8	42.6	142.8	14.4	5.9	24.5	3.1	6.5	0.90

[a]Averaged partial pressure in reactor

$m = -0.05$. Values of η for $m = -0.05$ are 0.96–0.99 for $T < 250$ °C and 0.92–0.96 for all other conditions. The data show a general decline of the catalyst activity with time as was mentioned in Section 4.4. The straight line in the figure was regressed only from the data collected at 250 °C excluding the partial pressure data, but including the high conversion data before 200 h. Rate constant values free of pore diffusion effects and deactivation are referred to as intrinsic values.

Despite all of the adjustments to the data for partial pressure and temperature, the data show a large amount of scatter (12.7–15.2 mmol/g/h for T experiments and 9.0–15.7 mmol/g/h for P experiments) as a result of poor estimates m and n. Better estimates of m and n will give a much narrower range of scatter for the experimental rate constant; however, obtaining better estimates requires that the data be adjusted to account for pore diffusion and deactivation effects.

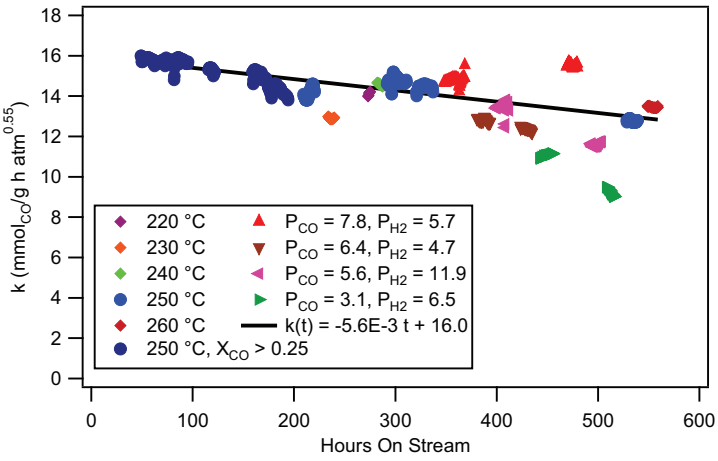

Figure 4.20: Experimental rate constant versus time for 2UH in R2 of FB Run 10 using Equation 4.4. All data are adjusted to 250 °C with E_A and to account for diffusion resistance with calculated η at each condition.

4.7.2 Rate Model for 2UH

Best estimates of the kinetic parameters, deactivation parameters, and pore diffusion effects are obtained using the analysis and algorithms described in Sections 2.7.2 to 2.7.4. The value for the rate of deactivation is 0.000533 h^{-1}. Values of the other regressed parameters and the resulting rate model are given in Equation 4.5 and Table 4.12. Units on rate are $mmol_{CO}/g_{cat}/h$ for t in h, T in K, and P in atm.

$$-r_{CO} = \eta\,(1 - 0.000533t)\,3.09 \cdot 10^{11} e^{-12{,}700/T} P_{CO}^{0.29} P_{H2}^{0.63} \tag{4.5}$$

Table 4.12: Values of regressed kinetic parameters from the partial pressure study on 2UH including confidence intervals and correlation coefficient matrix.

			correlation coefficients			
Parameter	Value	±95% CI	E/R	A	m	n
E/R (kJ/mol)	12.7	0.44	1.0	-1.0	0.0	-0.2
A (mmol/g/h/atm$^{0.92}$)	3.1E11	0.26E11	-1.0	1.0	-0.1	-0.3
m	0.29	0.022	0.0	-0.1	1.0	0.3
n	0.63	0.015	-0.2	-0.3	0.3	1.0

The 95% confidence intervals associated with the regressed parameters somewhat overstate the uncertainty in the parameter values, especially for highly correlated parameters (e.g. correlation coefficient of -1.0 on E/R and A). Joint confidence regions more accurately portray uncertainty; however, multidimensional confidence regions are difficult to produce and to interpret. Joint confidence regions and a discussion the regions and of parameter correlation are given in Appendix D.

Almost any fit of a data set can be improved by increasing the number of fitted parameters; however, to be justified, the added parameters must be able to explain variation in the data significantly better than the original model. A statistical F-test between nested mathematical models (where one restricted model like Equation 4.4 is contained within an unrestricted model with more parameters like Equation 4.5) for a given set of data indicates whether the larger number of parameters is justified. The F statistic between Equation 4.5 (two parameters) and Equation 4.4 (seven parameters) for just the temperature experiments is $F_{5,157} = 54$. Since the F statistic is larger than the critical F statistic at 95% confidence ($F_{5,157} = 2.3$), the additional five parameters of the new model are justified and explain variation in the data better than the two parameters of the old with much more than 95% confidence. It is impressive that Equation 4.5 outperforms Equation 4.4 on the smallest data subset (temperature experiments) without any partial pressure data for which it was created; however, because this was temperature data (very little partial pressure variation) the increased ability to explain the data probably comes from r_d and η rather than improved estimates of m and n.

Figures 4.21 and 4.22 are scatter plots comparing calculated rates of reaction with experimental rates of reaction for Equation 4.4 and Equation 4.5, respectively. The predicted rates in Figure 4.21 show significant positive deviations for rates larger than 25 mmol/g/h while rates in Figure 4.22 are tightly grouped around the identity line. This shows that accounting for deactivation and pore diffusion effects significantly reduces the amount of unexplained variation in the data and allows for much better estimates of E_A, A, m, and n.

The new E_A (105.6 kJ/mol) is significantly higher than the original E_A (95.7 kJ/mol) for 2UH. The new value of m (0.29) is positive and significantly different from the value proposed by Eliason (-0.05). The value of n (0.63) is essentially the same as the value proposed by Eliason (0.6).

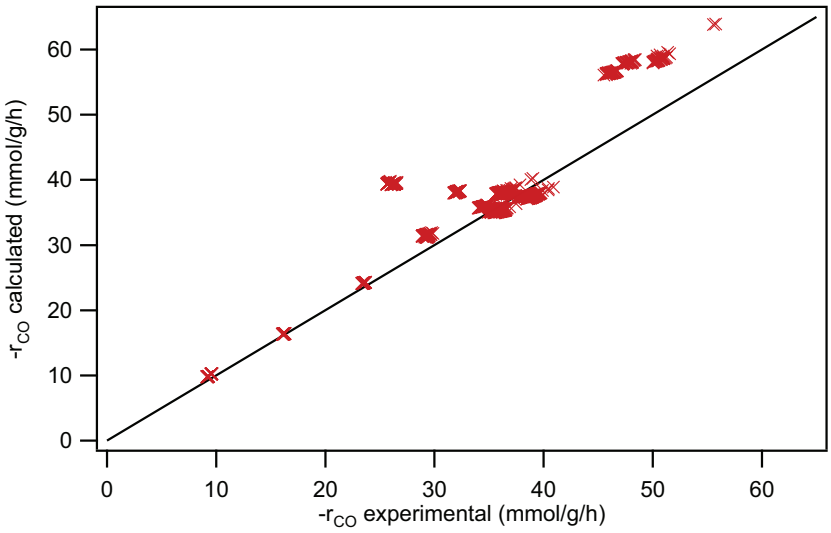

Figure 4.21: Scatter plot of rate of reaction calculated with Equation 4.4 versus experimental rate.

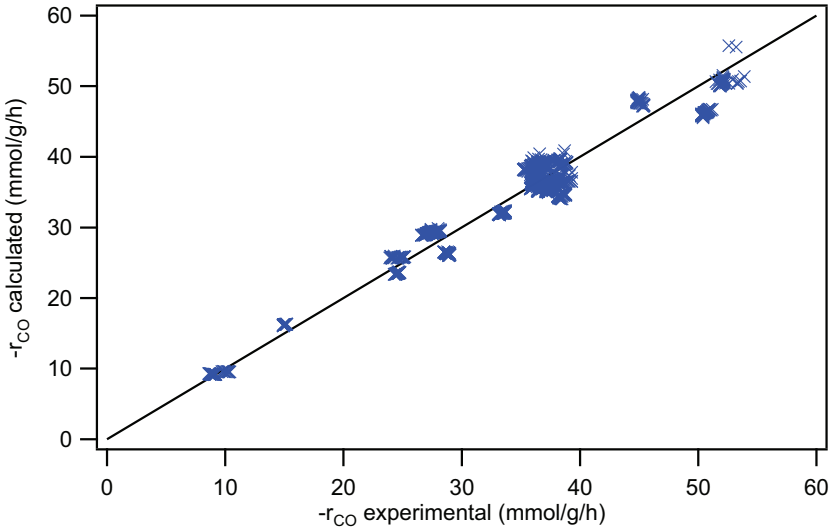

Figure 4.22: Scatter plot of rate of reaction calculated with Equation 4.5 versus experimental rate.

Intrinsic rate constant values (k_{int}) are calculated from experimental rate values using Equation 4.6.

$$k_{int} = \frac{-r_{CO}}{\eta\,(1-0.000533t)\,P_{CO}^{0.29}P_{H2}^{0.63}} \tag{4.6}$$

Figure 4.23 shows a plot of intrinsic rate constant values versus time for 2UH. The range of k_{int} is 8.0–10.0 $mmol_{CO}/g/h/atm^{0.92}$ with no trends up or down after fitting new parameters as described above. Figure 4.23 shows a much narrower spread of both partial pressure and temperature experiment rate values with the new parameters compared with Figure 4.20.

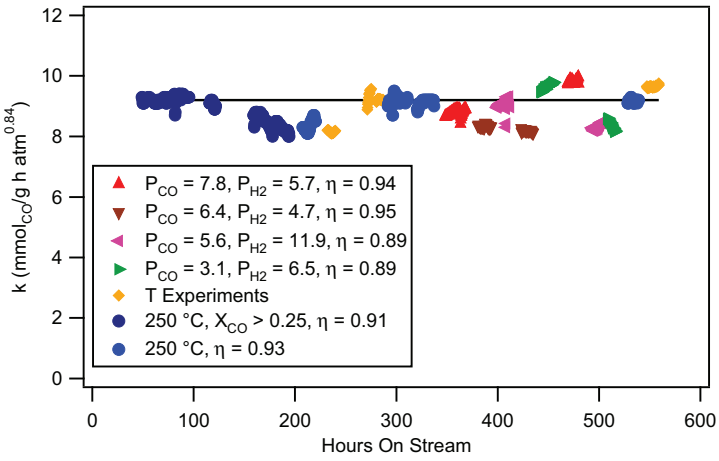

Figure 4.23: Normalized intrinsic rate constant versus time for 2UH. All data are adjusted to 250 °C and corrected for pore diffusion resistance and deactivation.

Since the units on k are different for the two models, the magnitude of the variance in k from the two models will be inherently different. For a fair comparison, a relative standard deviation is calculated by dividing sample standard deviation by the value of the average rate constant ($RSD = s_N/\bar{k}$). *RSD* is a normalized measure of variation for comparing variation in data sets with different means such as values of k calculated from Equations 4.4 and 4.5. The *RSD* of the new values of k calculated from the temperature experiments is 12% lower than for the old values of k (4.8% compared to 5.4%). The *RSD* of the new values of k for the partial pressure experiments is 53% less than for the old values of k (6.6% compared to 14.1%). The *RSD* for the new values of k for the entire data set is 49% lower than for the old values of k (5.7% compared to 11.1%).

Eliason compared several published power law rate models developed on catalysts with various K/Fe ratios. For catalysts with no K, values of m were between -0.51 and 0.54 and values of n were between 1.0 and 1.4. For catalysts with K loadings between 0.9 pbm and 1.1 pbm, values of m were between -0.18 and 0.0 and values of n were between 0.6 and 0.91. No catalysts with higher K loadings were given. A different study summarized the values of m and n for power law rate models of iron FTS (no details of K loading given) to be -0.25–0.5 and 0.5–1.6, respectively, which agrees with the previous summary [70]. Values of m (0.29) and n (0.63) for this study are within these ranges.

4.7.3 Implications for Other Catalysts

The analysis above shows a significant reduction in the variation of experimental rate constants for partial pressure data when the new partial pressure dependencies are used. This suggests that the partial pressure dependence for catalysts with nominal potassium loadings (4 pbm) may not follow the Eliason model which was developed on a catalyst with a lower K loading (0.9 pbm).

The E_A and A for all 17 catalysts were regressed a second time using the temperature kinetic data sets and the new values of m and n; however, the sums of the square errors were larger (up to 20% in some cases) than for the original fits. This is not unexpected since the temperature kinetic data had very little partial pressure variation. The increase in explained variation for the temperature experiments of 2UH described in Section 4.7.2 was likely due to the additions of the deactivation and pore diffusion parameters rather than a change in the values of m and n. Better estimates of m and n for the other catalysts require full partial pressure kinetic experiments.

4.8 External Catalyst Testing of 1ULC

1ULC is a catalyst prepared by Cosmas, Inc. (Springville, UT) using the 1ULa method. Results of an isothermal (230 °C) fixed-bed test of 1ULC performed by Emerging Fuels Technologies (Tulsa, OK) are presented here.

4.8.1 1ULC Rate of Reaction

Figure 4.24 shows the rate of reaction as a function of time for 350–870 h on stream. Data before 350 h are not available. Step changes in the data at 400, 700, and 800 h correspond with changes in operating pressure from 28.5 to 23.2 atm, from 23.2 to 18.3 atm, and from 18.3 to 12.4 atm. The rate data are very flat over 500 h of reaction (allowing for the pressure changes) showing no deactivation even as the run approaches 36 days on stream. This is an excellent example of the kind of catalyst stability required for industrial production.

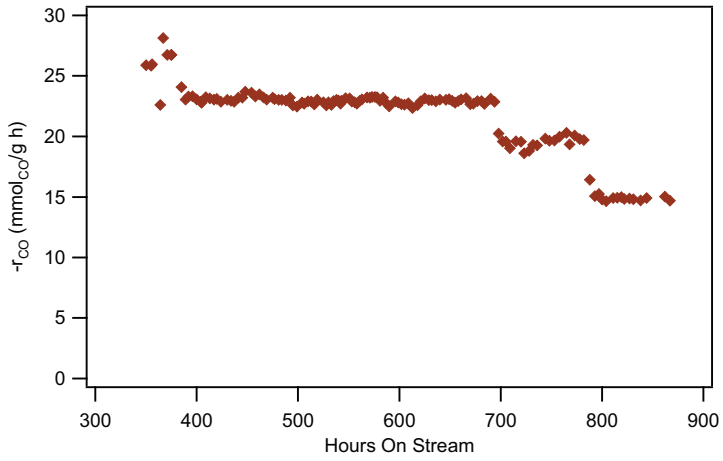

Figure 4.24: Rate of reaction versus time for 1ULC at 230 °C.

4.8.2 1ULC Product Distribution

Product selectivities on a carbon atom basis are very stable over this same period of time as shown in Figure 4.25 with CO_2 and C_{5+} selectivities on the left axis and C_1–C_4 species on the right axis. CO_2 selectivity is constant near 44% with C_{5+} selectivity just a little higher at 45%. CH_4 selectivity is 2.8%. The catalyst produces 3–4 times more C_3 (3.2%) and C_4 (2.2%) olefin species than paraffins (0.8% each). C_2H_4 is not quantified, but selectivity to C_2H_6 is nearly equal to selectivities of C_3–C_4 paraffins at 0.8%.

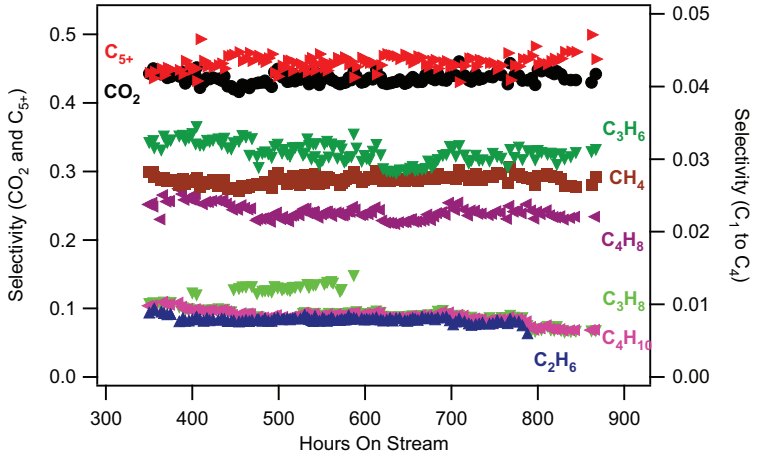

Figure 4.25: Selectivities to product species versus time for 1ULC on a C atom basis.

Wax and liquid products (hot and cold traps, respectively) collected before each change in pressure show changes in selectivity with changes in pressure. Post reaction analysis of these products by a GC equipped with a flame ionization detector (FID) provides product distributions at each pressure as given in Table 4.13. The unassigned fraction accounts for peaks that were measured but not identified. The hydrocarbon and CO_2 selectivities are not surprising; however, the oxygenate selectivity is quite high and will be discussed further.

Table 4.13: Total product distribution for 1ULC (%C atom).

	%C Distribution		
Product	23 atm	18 atm	12 atm
Hydrocarbons	47.4	45.8	49.9
Oxygenates	6.1	6.7	4.0
CO_2	43.4	44.0	43.9
Unassigned	3.2	3.5	2.2

4.8.3 1ULC Hydrocarbon Selectivity

The distribution of hydrocarbon products can be represented by the Anderson-Schultz-Flory propagation probability. For 1ULC, the probability was calculated on C_{10+} products to be 0.92 at all three pressures. This is within the 0.90–0.95 range for industrial iron catalysts [5, 71] and shows good production of heavy hydrocarbon products.

Table 4.14 gives the distribution of hydrocarbons only (excluding oxygenates, CO_2, and unassigned species) and includes a breakdown to paraffins and olefins on a carbon atom basis (equivalent to mass percent of carbon consumed). The methane make is higher (5.4%–6.0%) than some reported catalysts (2.9%–5.1%) [16], but is still quite low. The C_2–C_4 fraction (13.1%–16.9%) agrees well with reported values (15.7%–22.5%). and C_5–C_{11} fractions are surprisingly low (7.3%–10.8% compared with 15.8%–20.8%. There is likely a trade off between making hydrocarbons in these ranges and making the analogous oxygenated species. It may be that some peaks were misidentified as oxygenates when in fact they should have been counted among the hy-

drocarbons. Even if half of the oxygenated species were reassigned as hydrocarbons, the fractions of these mid-range hydrocarbons would still be low. The distribution shows that a majority of the carbon becomes hydrocarbons larger than C_{18} which is ideal for wax production. No explanation is given for the exceptionally high C_{19+} selectivity of the 12 atm. That the value is so much higher than at the other conditions (59.4% compared to 45.0%) is questionable. Even if the value is accurate, then the issue for scaling up would be to balance the design and productivity benefits of operating at lower pressure (higher selectivity) with the drawback of lower reaction rate.

Table 4.14: Hydrocarbon product distributions of 1ULC (%C atom) on a CO_2- and oxygenate-free basis for three total pressures.

	%C to Paraffins			%C to Olefins			%C to Total HC		
HC	23 atm	18 atm	12 atm	23 atm	18 atm	12 atm	23 atm	18 atm	12 atm
C_1	5.7	6.0	5.4				5.7	6.0	5.4
C_2–C_4	5.6	5.2	2.8	11.3	11.7	10.4	16.9	16.8	13.1
C_5–C_{11}	4.0	4.9	3.6	6.8	6.8	3.7	10.8	11.7	7.3
C_{12}–C_{18}	16.1	13.9	9.9	4.6	6.5	4.8	20.6	20.4	14.7
C_{19+}	45.8	44.7	59.0	0.2	0.4	0.4	46.0	45.0	59.4

4.8.4 1ULC Alcohol Selectivity

The distribution of converted carbon atoms in oxygenates is shown in Figure 4.26 and summarized in in Table 4.15. It is assumed that the oxygenates are all alcohols, though in reality they also include organic acids and other oxygenated species. The largest fraction of oxygenates is the C_5–C_{11} cut. Alcohols in this range are valuable for their use in making surfactants and are sold for a premium. As mentioned above, the alcohol selectivity is quite high and it is possible that some of the peaks identified as alcohol were misidentified. Even if the total amount of alcohols is not accurate, the product distribution with a peak in the C_5–C_{11} range is very good.

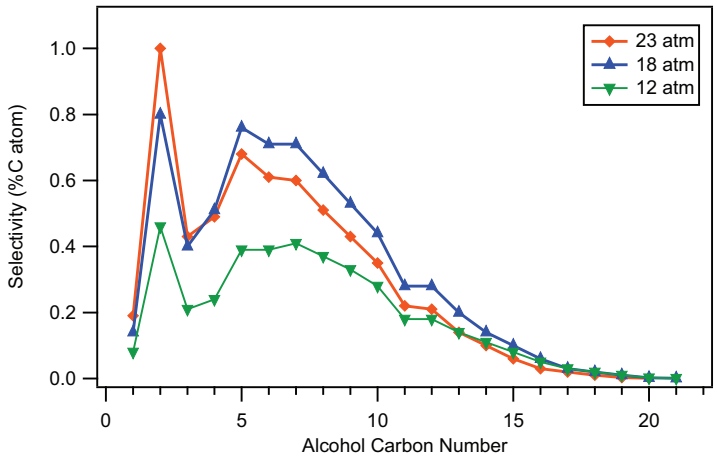

Figure 4.26: Selectivities to oxygenated species for 1ULC on a C atom basis.

Table 4.15: Oxygenate distribution (%C atom) of 1ULC products on a CO_2- and hydrocarbon-free basis.

	%C of all Oxygenates		
HC	23 atm	18 atm	12 atm
C_1	3.1	2.1	2.1
C_2–C_4	31.6	25.4	22.9
C_5–C_{11}	55.9	60.0	59.5
C_{12}–C_{18}	9.3	12.4	15.3
C_{19+}	0.1	0.1	0.3

4.8.5 Comparison of 1ULC to 1U Catalysts

Comparing the performance of 1ULC with the catalysts of this study is not direct because the 1ULC FB run was at a higher H_2/CO feed ratio (1.5 compared to 1.0), higher conversions, and different operating pressures. Because data for 1ULC were taken at four different total pressures, it is possible to estimate the values of the rate constant at 230 °C and the partial pressure dependencies on CO and H_2. The estimates of k, m, and n are 6.6 $mmol_{CO}$/g/h (CO consumption, not syngas), 0.16, and 0.55, respectively. In comparison, the values of m and n from the partial pressure study on 2UH in Section 4.7.2 are $m = 0.29$ and $n = 0.63$. With these parameters, the data may be adjusted for a fair comparison.

Table 4.16 compares reaction rates and operating conditions of 1ULC to 1UH, 1UL, and 1UHa. 1ULC shows very high activity which is likely the result of the activation at high conversion and 260 °C for 10 h (compare Sections 2.3.5 and 2.8). Different activation procedures have been shown to increase catalyst activity 60–80% or more [20, 21]. Adjusting the rate of 1ULC to $P_{CO} = P_{H_2} = 6.21$ atm using the regressed kinetic parameters gives $-r_{CO} = 24.5$ mmol/g/h which is 100% larger than 1UH and 140% larger than 1UL. The CH_4 selectivities of the four catalysts are very similar, but the 1ULC CO_2 selectivity is 5–15% larger than 1UL and 1UH and 50% larger than 1UHa. Overall, rate on 1ULC is high, but the CO_2 and CH_4 selectivities are very similar to 1UL and 1UH.

Table 4.16: Comparison of 1ULC performance to 1UH, 1UHa, and 1UL. All data are for 230 °C.

Cat.	Mass g	F^0_{CO} mmol/h	X_{CO} %	$-r_{CO}$ mmol/g/h	k[a]	Total P atm	P_{H_2} atm	P_{CO} atm	S_{CO_2} %	S_{CH_4}[b] %
1ULC	10.86	480	59.1	26.0	8.19	28.5	7.7	4.1	44.2	2.7
		526	47.5	23.0	8.04	23.2	6.4	3.6	43.4	2.7
		525	40.5	19.6	7.74	18.3	5.1	3.0	44.0	2.8
		523	31.1	15.0	7.35	12.4	3.5	2.1	43.9	2.7
calculated				24.5	6.6		6.2	6.2		
1UL	0.250	33.9	8.4	10.3	4.23	21.2	5.9	6.0	38.2	2.5
1UH	0.250	38.3	9.4	12.1	4.54	21.2	6.8	6.1	41.7	2.7
1UHa	0.501	69.8	11.3	15.6	6.03	20.9	6.2	6.2	29.0	3.0

[a]Assuming $m = -0.05$ and $n = 0.6$, units are mmol/g/h/atm$^{0.55}$
[b]Total mole fraction of consumed CO

4.8.6 Comparison With Published Catalysts

The complete product distribution analysis provided above allows a unique opportunity to compare 1ULC with some of the most active catalysts in literature. Table 4.17 compares rate and selectivity data for 1ULC with similar data for two active and selective catalysts published in the literature [16]. One of the published catalysts is promoted with 8 pbm SiO_2 and the other is promoted with 24 pbm SiO_2. Differences in reaction conditions for the three catalysts include

temperature (235 °C versus 230 °C), pressure (1.5–3.0 MPa versus 1.3–2.3 MPa), H_2:CO in the feed (1.0 versus 1.5), and time on stream (72–169 h versus 385–788 h).

Table 4.17: Comparison of activity and selectivity data for 1ULC with two catalysts reported by Bukur et al. [16]. *SV* for the published catalysts are based on unreduced catalyst and are given at 273 K and 1 atm. Active metal and promoter amounts are 100Fe/5Cu/4.2K by mass.

Parameter	8 SiO_2			24 SiO_2		1ULC		
TOS (h)	72	145	169	73	145	385	698	788
T (°C)	235	235	235	235	235	230	230	230
P (MPa)	1.5	3.0	1.5	1.5	3.0	2.3	1.8	1.3
SV ($L_{STP}/g_{cat}/h$)	4.0	4.0	2.0	4.0	4.0	5.5	5.5	5.5
X_{CO}	64.5	46.4	52.9	39.4	50.1	47.5	40.5	31.1
X_{H_2+CO}	52.8	42.7	44.8	38.5	48.7	32.4	27.0	20.2
H_2/CO_{In}	1	1	1	1	1	1.5	1.5	1.5
H_2/CO_{Out}	1.79	1.25	1.46	1.03	1.06	2.23	2.08	1.90
k[a]	246	105[b]	100	197	131	88	92	100
Extent WGS[c]	0.73	0.73	0.76	0.56	0.67	0.77	0.79	0.78
HC Selectivities (wt%)								
CH_4	3.0	2.9	3.3	5.1	3.9	5.7	6.0	5.4
C_2–C_4	15.7	17.7	17.6	22.5	21.7	16.9	16.8	13.1
C_5–C_{11}	20.8	16.8	20.3	18.1	15.8	10.8	11.7	7.3
C_{12+}	60.5	62.6	58.8	54.3	58.6	66.6	65.4	74.1
Product Distribution (mass%)								
HC	52.3	58.3	52.9	61.7	62.6	47.4	45.8	49.9
Oxygenates	2.9	2.2	2.4	2.9	2.4	6.1	6.7	4.0
CO_2	42.1	42.2	42.3	33.6	37.1	43.4	44.0	43.9
Unaccounted	2.7	-2.7	2.4	1.8	-2.1	3.2	3.5	2.2
Olefin Selectivity (wt%)								
C_2–C_4	76.9	75.4	75.1	72.7	72.3	73.2	75.8	78.8
C_5–C_{11}	77.0	75.9	77.6	78.5	77.3	62.5	58.1	50.5

[a] Apparent first-order rate constant in $mmol_{CO+H_2}/g_{Fe}/h/MPa_{H_2}$
[b] Calculated from available data
[c] $P_{CO_2}/(P_{CO_2}+P_{H_2O})$

1ULC shows slightly lower values of the first-order rate constant (88–100 mmol/g/h/MPa) which is explained by its lower reaction temperature (230 °C compared to 235 °C). The activ-

ity of 1ULC may be corrected up to 235 °C using an estimate of activation energy for 1ULa (102.6 kJ/mol) which was regressed from the first order (in H_2) syngas ($H_2 + CO$) rate constant and temperature data of 1ULa. The resulting increase in activity is 127% bringing the activities up to 112 (2.3 MPa), 117 (1.8 MPa), and 127 mmol/g/h/MPa (1.3 MPa). The adjusted activities are between the activities of the 8 SiO_2 catalyst (105 mmol/g/h/MPa) and the 24 SiO_2 catalyst (131 mmol/g/h/MPa) after 145 h. Both published catalysts show significant loss of activity (up to 59%) within the first 145 h. In contrast, 1ULC shows excellent stability over more than 400 h of reaction time from 385 to more than 788 h on stream. As shown in Figure 4.24, reaction rate is remarkably stable with time.

The apparent increase in the rate constant in Table 4.17 for 1ULC is related to lower total operating pressure coupled with the poor assumption of first-order activity in hydrogen and zero-order in CO. As discussed in Section 4.8.5, estimates of *k*, *m*, and *n* can be calculated using the full 1ULC data set including 4 different total pressures and they are 10.7 $mmol_{CO+H_2}/g_{cat}/h/atm^{0.82}$ (note units for syngas consumption), 0.38, and 0.44, respectively (not 0 and 1). This illustrates the need for caution in comparing rate constants as a measure of activity across different conditions with assumed kinetic parameters.

The 1ULC methane make is higher (5.4%–6.0%) than the reported catalysts (2.9%–5.1%) [16], but is still quite low. The C_2–C_4 fraction (13.1%–16.9%) is similar to reported values (15.7%–22.5%). C_5–C_{11} fractions are surprisingly low (7.3%–10.8% compared with 15.8%–20.8%), but the C_{12+} fraction is higher than the others. The most glaring difference is the oxygenate make which is 2–3 times higher.

4.8.7 Summary of 1ULC

In summary, 1ULC demonstrates the repeatability of the 1U preparation method in general. Since it was prepared and tested by industrial collaborators, it provides an added measure of confidence to the performance of these catalysts. It appears that 1ULC is about 50% more active than 1UL probably due to more optimal pretreatment conditions e.g. carbiding at 260 °C and $X_{CO} = 0.7$ for 10 hours (Section 2.8). 1ULC compares well with some of the most active catalysts published in the literature.

CHAPTER 5. REACTOR MODEL DEVELOPMENT, VALIDATION, AND COMPARISON

This chapter describes the development of a 1-D trickle fixed-bed recycle reactor model for the Fischer-Tropsch synthesis on iron and cobalt catalysts. Except for Section 5.8, this material was published in a peer reviewed journal available at `www.degruyter.com/view/j/ijcre` [44]. The actual code is given in Appendix F.

5.1 Reactor Model Description

Reactor design, construction, and operation can be among the most significant costs in building and running a chemical facility. In more than 80 years since its first development, the Fischer-Tropsch (FT) synthesis (FTS) has been carried out in a variety of reactors. Fixed-bed (FB) reactors allow for high through-puts and relatively easy maintenance while avoiding the difficult wax-catalyst separation problem in slurry-bubble column (SBC) applications. FB reactors have the advantage of well-established design and operating procedures. Along with relatively simple and direct scalability, these factors make FB reactors the preferred choice for smaller-scale applications such as biomass to liquids (BTL) and in some cases coal to liquids (CTL) [4, 5]. To improve temperature control, prolong catalyst life, and optimize conversion, effluent gas is typically recycled in these reactors. FB reactors for FTS are often operated in a trickle-flow regime, defined as the condition in which the mass flux of the liquid is approximately equal to that of the gas. The bed entrance does not operate within trickle flow conditions unless some of the liquid product is recycled. Liquid recycle presents the additional challenge of evenly distributing the liquid to each tube.

Presented here is a 1-D trickle-fixed-bed reactor model applicable to both cobalt and iron catalysts which accounts for gas and liquid recycle. Included with the model are a selection of kinetic models for both iron and cobalt catalysts and the ability to easily input a wide variety of

Langmuir-Hinshelwood (LH), Eley-Rideal (ER), and power law kinetic models. While the model is 1-D, a correlation is used to account for radial thermal conductivity and heat transfer [37]. Traditional pressure drop calculations for a packed column were modified with a correlation [38] to account for trickle-flow conditions. The model was validated by matching published full-scale plant data from the SASOL Arge reactors. This chapter presents results of varying fundamental theoretically-based parameters (i.e. effective diffusivity, Prandtl number, friction factor, etc.). Chapter 6 presents the results of varying physical, directly-controllable parameters (i.e. recycle ratio, inlet pressure, pellet shape and size, tube diameter, etc.).

5.1.1 Fischer-Tropsch Chemistry

Stoichiometric equations of the FTS used in this study are given in Equations 5.1–5.5.

$$CO + 3H_2 \longrightarrow CH_4 + H_2O \tag{5.1}$$

$$CO + \frac{7}{3}H_2 \longrightarrow \frac{1}{3}C_3H_8 + H_2O \tag{5.2}$$

$$CO + \frac{2n_p+1}{n_p}H_2 \longrightarrow \frac{1}{n_p}C_{n_p}H_{2n_p+2} + H_2O \tag{5.3}$$

$$CO + 2H_2 \longrightarrow \frac{1}{n_o}C_{n_o}H_{2n_o+1}OH + \frac{n_o-1}{n_o}H_2O \tag{5.4}$$

$$CO + H_2O \rightleftharpoons CO_2 + H_2 \tag{5.5}$$

Equations 5.3 and 5.4 represent the range of paraffinic hydrocarbons and paraffinic alcohols in the FT products. The stoichiometric coefficients n_p and n_o are the carbon number of the FT product species for paraffins and oxygenates, respectively. Equations 5.1 and 5.2 are specific cases ($n_p = 1$ and $n_p = 3$) of Equation 5.3 and represent methane and propane formation, respectively. Equation 5.5 is the water-gas-shift reaction, which is important in FTS on Fe catalysts, but not on Co catalysts. It is assumed that olefin and other product species not represented above have properties similar to their paraffin counterparts.

The reactor model was developed with a simplified, fixed selectivity in which the user specifies the fractions of reacted moles of carbon monoxide converted to (1) methane (Equation 5.1), (2) gaseous light hydrocarbons ($C_{2–4}$, Equation 5.2), (3) liquid heavy hydrocarbons (C_{5+}, Equa-

tion 5.3), (4) gaseous oxygenates (Equation 5.4), and (5) carbon dioxide (Equation 5.5). The physical properties of the hydrocarbon product ranges are determined from the properties of propane for the C_{2-4} fraction and by the properties of either $C_{20}H_{42}$ (iron catalysts) or $C_{25}H_{52}$ (cobalt catalysts) for the C_{5+} fraction. Physical properties of the oxygenated fraction are determined from the properties of methanol.

In reality, the product slate is a complex function of temperature, total pressure, reactant partial pressures, choice of metal catalyst, choice of promoters, preparation procedures, and reduction procedures. Development of a general selectivity model that accounts for even the first four variables in the above list continues to elude the FT community. FT products generally follow the Anderson-Schulz-Flory distribution, but deviate significantly especially in the lighter hydrocarbon products. Attempts have been made to account for these deviations [72]; however, further work and more industrially relevant data are needed. Some have opted for individual rate equations for each product species [7, 73], but to generalize such a model would be difficult. A fixed selectivity model is the most simple and direct for modeling an existing reactor system, but potentially the poorest for predicting product selectivity for reactor design or optimization. Fixed models are insensitive to all variables that determine product slate, but have the flexibility to allow user input of observed data without the constraints of a model that may predict significant deviations from reality. The main drawback to a fixed selectivity model is the burden on the user of determining an accurate product slate for the conditions represented in the model.

5.1.2 Trickle Fixed-Bed Reactor

The trickle-flow reactor described by the model of this study is a shell and tube heat exchanger with catalyst pellets packed in the tubes (Figure 5.1). In FT trickle flow reactors, gas and liquid flow down the reactor over catalyst pellets. It is assumed that the heavy hydrocarbon products are the only liquids formed during reaction and that water is present as a vapor in the gas effluent along with the fixed gases and light hydrocarbon products. Flash calculations at reactor conditions for Fe and Co support this assumption and show less than 1% of the water in the liquid phase at 40 atm and 490 K. Conceptually, the liquid product is separated from the gas effluent in the hot trap. Water and lighter condensable hydrocarbons are separated from the non-condensables in the cold trap. Portions of the liquid product and non-condensable gases may be recycled to the

reactor. It is assumed that dimensions, reactions, and conditions in a single tube are identical to those of all the tubes in the bundle. In keeping with a 1-D model, radial and intra particle gradients are ignored; however, an effective radial thermal conductivity term accounts for radial heat transfer and an effectiveness factor accounts for pore diffusion resistance. It is also assumed that the bed is uniform in porosity with no channeling, that the catalyst has constant activity, and that physical properties for large groups of species can be represented by the properties of a single species.

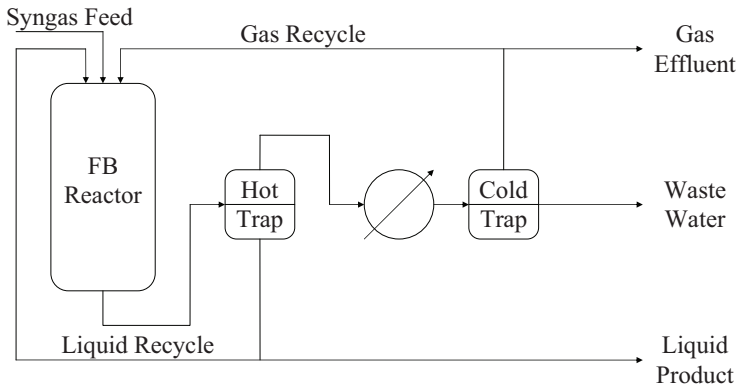

Figure 5.1: PFD of fixed-bed reactor with recycle for FTS

5.1.3 Conservation Equations and Numerical Method

The reactor design equations for mass, energy, and momentum given by Davis and Davis [74] (Equations 5.6 and 5.7) and Froment and Bischoff [38] (Equation 5.8) are solved numerically using a fourth-order Runge-Kutta Method [75] with a step size of 3.0 mm.

$$-\frac{dF_A}{dz} = A_{cs}\eta\rho_b(-r_{CO}) \tag{5.6}$$

$$u\rho c_p\frac{dT}{dz} = -\Delta H_{rxn|T^0}\eta\rho_b(-r_{CO}) - \frac{4U}{d_t}(T - T_{wall}) \tag{5.7}$$

$$\frac{dP}{dz} = \frac{\delta_{GW}}{\left(1-\frac{\varepsilon_l}{\varepsilon_b}\right)^3} - \rho_g g \tag{5.8}$$

All variables are defined in Section 0.1. The user specifies separate gas and liquid recycle ratios (water is not recycled) and the CO conversion at the reactor exit. Conversion (X_A) is defined as the fraction of species A that has reacted (Equation 5.9) where F_A^0 and F_A are inlet and instantaneous molar flow rates of A, respectively.

$$X_A = \frac{F_A^0 - F_A}{F_A^0} \tag{5.9}$$

From the reactor inlet, the model steps through the reactor in the axial direction, solving the differential equations at each node, until the predicted conversion of CO equals the specified conversion. Alternatively, the user may model a reactor of specified length and calculate conversion, but these calculations are iterative due to the issue of recycle.

5.1.4 Catalyst Physical Properties

Pellet geometry and size affect void fraction and thereby strongly influence pressure drop within a reactor. Void fraction (ε_b) is estimated from the generalized correlation developed by Benyahia and O'Neill [76] which is given in Equation 5.10.

$$\varepsilon_b = 0.1504 + \frac{0.2024}{\phi_p} + \frac{1.0814}{\left(\frac{d_t}{d_p} + 0.1226\right)^2} \tag{5.10}$$

The correlation depends on tube diameter (d_t), pellet diameter (d_p), and on sphericity (ϕ_p) which is defined as the ratio of the surface area of a sphere of equivalent volume to the surface area of the pellet. The correlation is valid for sphericity factors of 0.42–1.0 and for tube to pellet diameter ratios of 1.5–50, though the smallest diameter pellets used in collecting data were 2.0 mm. Benyahia and O'Neill reported an average error of 5.2% between this correlation and experimental data.

Pellet density (ρ_p) and pellet porosity (ε_p) are calculated from bed void fraction (ε_b), bed density (ρ_b), and pore volume (V_p) (Equations 5.11 and 5.12).

$$\rho_p = \frac{\rho_b}{1 - \varepsilon_b} \tag{5.11}$$

$$\varepsilon_p = \rho_p V_p \tag{5.12}$$

Geometry also dictates effective diffusion length which is critical in accounting for pore diffusion influences on reaction rate. Four catalyst pellet geometries were considered in developing the model: spheres, cylinders, hollow cylinders, and trilobes. Table 5.1 shows particle geometries, sphericity factors, predicted void fractions, and diffusion lengths for 2.0 mm pellets with an aspect ratio of 3 (except for spheres) in a 25.4 mm diameter tube.

Table 5.1: Properties for 2 mm diameter pellets of four pellet geometries ($d_t = 25.4$ mm, aspect ratio = 3). Bed void fraction was calculated from a correlation [76].

Shape	Surface Area (mm^2)	Sphericity	Bed Void Fraction	Diffusion Length (mm)
Sphere	12.6	1.000	0.359	$d_p/6$
Cylinder	44.0	0.779	0.428	$d_p/4$
H. Cyl.[a]	55.9	0.567	0.524	$(d_p - d_i)/4$
Trilobe	42.1	0.645	0.478	$d_p/8$

[a]Hollow cylinder inner diameter $d_i = 0.667$ mm

5.1.5 Kinetics

The intrinsic rate of consumption of CO ($-r_{CO}$) is described qualitatively by a kinetic rate expression and quantitatively by a kinetic model. The reactor model accepts a variety of Langmuir-Hinshelwood (LH), Eley-Rideal (ER), and power law (PL) kinetic models as given by Equation 5.13.

$$-r_{CO} = \frac{k_0 P_{CO}^m P_{H_2}^n}{\left(B + k_1 P_{CO}^{z1} + k_2 P_{CO}^{z2} P_{H_2}^{z3} + k_3 P_{H_2O}^{z4} + k_4 P_{CO_2}^{z5}\right)^{z6}} \tag{5.13}$$

The constant z_6 is 2 for LH rate expressions and 1 for ER expressions. Each of the kinetic constants (k_i) in Equation 5.13 has temperature dependence expressed by the Arrhenius equation (Equation 5.14).

$$k_i = A e^{-E_A/RT} \tag{5.14}$$

Four kinetic models each are given for iron and cobalt catalysts. The iron kinetic models are given by Equations 5.15–5.18 and are referred to as Fe1–Fe4, respectively.

$$-r_{CO} = \frac{6.70 \cdot 10^5 e^{-10{,}200/T} P_{CO}^{0.50} P_{H_2}^{0.75}}{\left(1 + 5.81 \cdot 10^{-7} e^{6{,}220/T} P_{CO}^{0.50} P_{H_2}^{0.25}\right)^2} \tag{5.15}$$

$$-r_{CO} = \frac{4.80 \cdot 10^5 e^{-9{,}710/T} P_{CO} P_{H_2}}{P_{CO} + 7.03 P_{H_2O} + 0.480 P_{CO_2}} \tag{5.16}$$

$$-r_{CO} = \frac{4.80 \cdot 10^5 e^{-9{,}970/T} P_{CO} P_{H_2}}{P_{CO} + 4.64 P_{H_2O} + 0.346 P_{CO_2}} \tag{5.17}$$

$$-r_{CO} = \frac{127\, e^{-8{,}000/T} P_{CO} P_{H_2}}{P_{CO} + 1.90 \cdot 10^{-5} e^{7{,}870/T} P_{H_2O}} \tag{5.18}$$

Units on Equations 5.15–5.18 are mol/(kg·s) when partial pressures are in atm and temperature is in K. Equation 5.15 was developed from a micro kinetic model using data taken on a 20 Fe/1 K/1 Pt alumina-supported catalyst (20% Fe loading by mass) at the BYU Catalysis Laboratory [61]. Equations 5.16 and 5.17 were reported by Zimmerman and Bukur [77] for unsupported catalysts containing 100Fe/0.3Cu/0.2K and 100Fe/5Cu/4.2K/25SiO_2, respectively. Equation 5.18 was developed by Liu and Li [78] for a Fe/Cu/K catalyst (composition was not given). Equation 5.15 is a LH form while Equations 5.16–5.18 are ER forms. Notably, Equation 5.15 depends only on P_{CO} and P_{H_2} while Fe2–Fe4 also include P_{H_2O} and P_{CO_2}.

The cobalt kinetic models are given in Equations 5.19–5.22, referred to as Co1–Co4, respectively.

$$-r_{CO} = \frac{1.27 \cdot 10^8 e^{-11{,}400/T} P_{CO}^{0.5} P_{H_2}^{0.75}}{\left(1 + 0.0750\, e^{812/T} P_{CO}^{0.5} P_{H_2}^{0.25}\right)^2} \tag{5.19}$$

$$-r_{CO} = \frac{1.96 \cdot 10^7 e^{-10{,}200/T} P_{CO}^{0.5} P_{H_2}}{\left(1 + 0.0494\, e^{850/T} P_{CO}^{0.5} P_{H_2}^{0.5}\right)^2} \tag{5.20}$$

$$-r_{CO} = \frac{142\, e^{-4{,}070/T} P_{CO} P_{H_2}^{0.5}}{\left(1 + 1 \cdot 10^{-9} e^{9{,}440/T} P_{CO} + 0.0024\, e^{2{,}150/T} P_{H_2}^{0.5}\right)^2} \tag{5.21}$$

$$-r_{CO} = \frac{163\, e^{-4{,}520/T} P_{CO} P_{H_2}^{0.5}}{\left(1 + 3.52 \cdot 10^{-9} e^{8{,}740/T} P_{CO}\right)^2} \tag{5.22}$$

Units on Equations 5.19–5.22 are $mol_{CO}/(mol_{site} \cdot s)$ when partial pressures are in atm and temperature is in K. All 4 equations are LH models developed from a large pool of rate data (more than 100 data points) for supported cobalt catalysts gleaned from literature [79]. Equation 5.19 assumes that the co-rate determining steps are CO hydrogenation and H_2O formation. Equation 5.20 assumes that carbonylation is the rate determining step. Equations 5.21 and 5.22 reflect the assumption that CO dissociation is assisted by adsorbed hydrogen and differ only in the number of fitted parameters (6 and 4, respectively).

When modeling a reactor system which utilizes a catalyst with well characterized kinetics, the kinetic expression and constants representing that specific catalyst can be entered into the model. When the kinetics are not known, Equations 5.15–5.22 give intrinsic reaction rates representative of a range of industrial catalyst behavior and suitable for upper and lower bound estimates for reactor design. Figures 5.2 and 5.3 compare the rates predicted by these models as functions of temperature for specific partial pressures of CO and H_2 for iron ($P_{CO} = 6.2$ atm, $P_{H_2} = 11.4$ atm) and cobalt ($P_{CO} = 10.3$ atm, $P_{H_2} = 21.3$ atm), respectively.

5.1.6 Limitations

Limitations of this FB reactor model are (1) the use of a fixed selectivity model instead of a predictive selectivity model; (2) the assumptions used in determining the effectiveness factor, which include a) use of the n^{th}-order Thiele modulus approach and b) use of the Wheeler single pore model to determine effective diffusivity; and (3) the use of a one-dimensional model with an effective radial thermal conductivity term instead of a rigorous two-dimensional approach.

Although assuming a fixed selectivity model and lumped product treatment as described in Section 5.1.1 introduces some error in the mass flow rate of liquids, the effect on reactor model predictions is small. For example, the overall effect of 5% more liquid on heat transfer and pressure drop calculations is less than 1% each. The effects of liquid products on heat transfer and pressure drop are discussed in Sections 5.5 and 5.6, respectively. The authors are currently working on developing improved selectivity models.

Using an n^{th}-order Thiele modulus and a Wheeler single pore model to calculate effective diffusivity can have significant effects on the model predictions. Since the FTS exhibits shifting-order kinetic behavior, selecting a single order of reaction will give some error in calculations

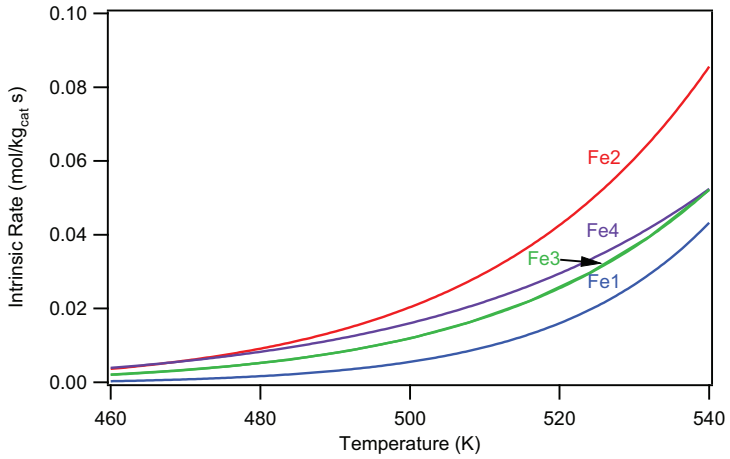

Figure 5.2: Comparison of intrinsic reaction rates for 4 integrated kinetic models for iron catalysts (see Equations 5.15–5.18). $P_{CO} = 6.2$ atm, $P_{H_2} = 11.4$ atm.

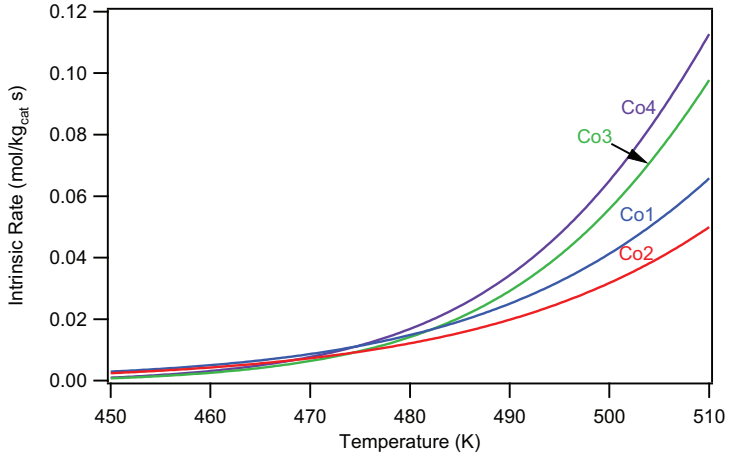

Figure 5.3: Comparison of intrinsic reaction rates for 4 integrated kinetic models for cobalt catalysts (see Equations 5.19–5.22). $P_{CO} = 10.3$ atm, $P_{H_2} = 21.3$ atm.

wherever conditions vary greatly from the chosen value (i.e. at the entrance and/or exit of the bed); however, increasing recycle produces more uniform conditions throughout the bed and can help minimize this error. Errors from the Wheeler single pore model are not so easily minimized. For example, assuming a tortuosity of 3.5 if the actual tortuosity was 4.5 would result in overestimating effective diffusivity by 30% and overestimating the effectiveness factor by 8%, resulting in a 12% shorter predicted bed length. The sensitivity of the model to assumptions about diffusivity and order of reaction is discussed in Section 5.4.

An effective radial thermal conductivity correlation attempts to account for heat transfer in a 1-D model that by definition ignores radial temperature gradients. Analysis shows that radial

temperature gradients in the bed are at least 2–3 K and are probably larger. The effective radial thermal conductivity term is discussed in Section 5.5.1 and the implications of radial temperature gradients are explored in Section 5.5.4 and shown in Figure 5.15.

5.2 Base Case

A discussion of the sensitivity of the model to input values or on the significance of an assumption in the model requires a standard set of conditions and results against which all other conditions and results are compared. The standard conditions for both iron and cobalt in this work are representative of the first stage of a biofuels-to-liquids plant, i.e. a plant that operates at a CO conversion of 60%, with productivity of 500 bbl/day. The standard conditions for iron and cobalt catalysts are given in Table 5.2, and the results of simulations for these conditions are given in Figures 5.4 and 5.5 and Table 5.3.

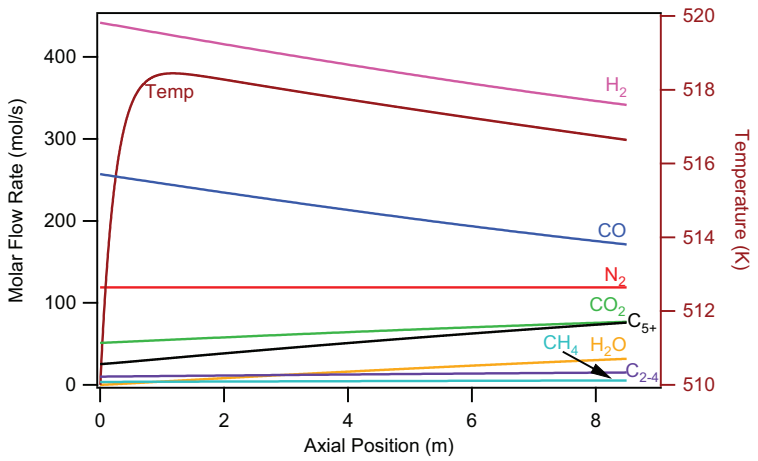

Figure 5.4: Temperature and species profiles for the Fe base case ($RR = 2$). C_{5+} ($C_{20}H_{42}$) and $C_{2–4}$ (C_3H_8) molar rates are multiplied by 20 and 3, respectively.

Parametric studies of the effects of kinetic models and important parameters in the mass, energy, and momentum balances are illustrated and discussed in the following sections.

Table 5.2: Base case or standard conditions used in this study for iron and cobalt catalysts. Conditions represent plants operating at 60% CO conversion with productivity of 500 bbl/day.

Inputs	Iron	Cobalt
Flow Rate (SCFH)$\times 10^{-5}$	11.3	10.05
Mole Fraction of CO	0.360	0.285
Mole Fraction of H_2	0.540	0.595
Mole Fraction of N_2	0.100	0.120
Inlet Temperature (K)	510	484
Wall Temperature (K)	510	478
Inlet Pressure (atm)	25	40
Gas Recycle Ratio[a]	2	2
Liquid Recycle Ratio[a]	0.5	0.5
Final CO Conversion (%)	60	60
Selectivity to CH_4	0.021	0.050
Selectivity to C_{2-4}	0.059	0.080
Selectivity to C_{5+}	0.592	0.860
Selectivity to oxygenates	0.028	0.010
Selectivity to CO_2	0.300	0.000
Kinetic Model	Fe1	Co3
Reaction Order[b]	0.2	-0.1
Catalyst Activity	1	1
Number of Tubes	2,750	1,300
Tube Diameter (mm)	25.4	25.4
Pellet Diameter (mm)	2	1.3
Pellet Geometry	trilobe	trilobe
Pellet Aspect Ratio	3	3.5
Pellet Pore Volume (cm^3/g)	0.30	0.42
Bed Density (kg/m^3)	800	600
Pellet Density (kg/m^3)	1,534	1,159

[a]recycle/outlet ratio

[b]for Thiele modulus calculation

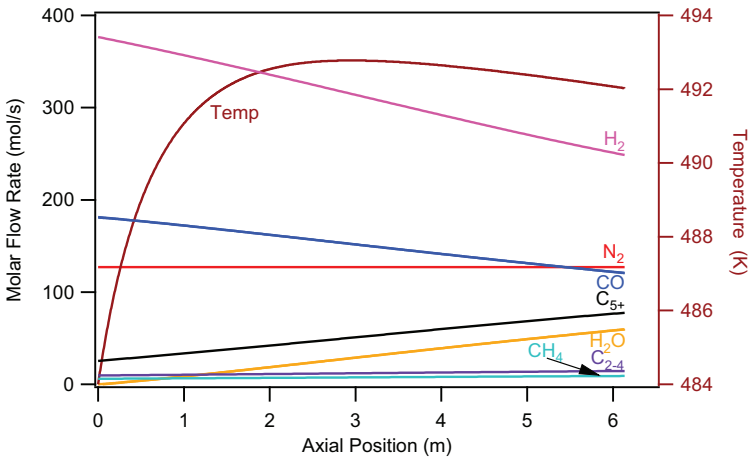

Figure 5.5: Temperature and species profiles for the Co base case ($RR = 2$). C_{5+} ($C_{25}H_{52}$) and C_{2-4} (C_3H_8) molar rates are multiplied by 25 and 3, respectively.

Table 5.3: Results predicted under standard conditions for iron and cobalt catalysts.

Predicted Values	Iron	Cobalt
Outlet Temperature (K)	517	492
Max Temperature (K)	518	493
HT Coefficient (W/m^2K)	761	1114
Reactor Length (m)	8.5	6.1
Mass of Catalyst (kg)	9,471	2,425
Pressure Drop (atm)	2.46	3.86
Productivity ($g_{HC}/g_{cat}h$)	0.27	1.08
Avg. Effectiveness Factor	0.63	0.77

5.3 Kinetic Models

Figures 5.6 and 5.7 compare the axial temperature profiles predicted by the four reactor models for Fe and Co, respectively, using the base case conditions. The inherent differences in activity of the representative kinetic models produce some variation in predicted reactor length. Some of the variation in reactor length is due to higher bed temperatures predicted for more active rate models. When the feed and cooling wall temperatures are adjusted to give the same maximum temperature (T_{max}) for each case, the variation in reactor length is reduced to 35% for the four iron models (Figure 5.8) and for the four cobalt models (Figure 5.9).

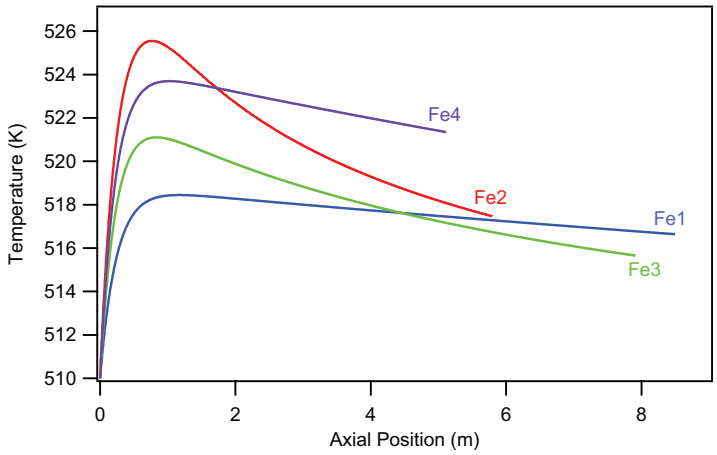

Figure 5.6: Temperature profiles for the four representative iron kinetic models. All other parameters are for the iron base conditions.

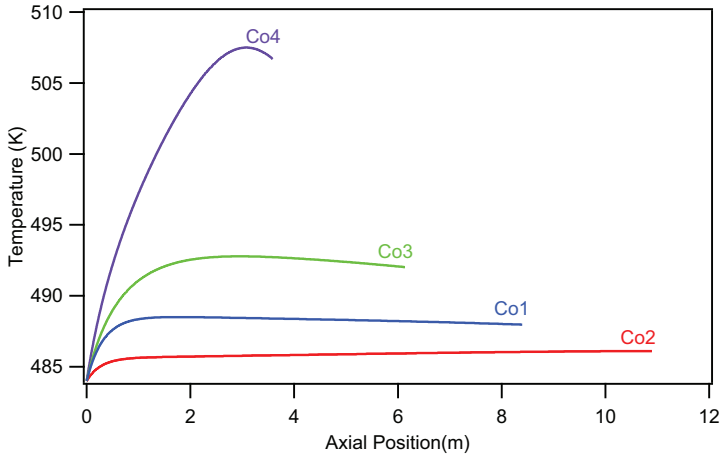

Figure 5.7: Temperature profiles for the four representative cobalt kinetic models. All other parameters are for the cobalt base conditions.

5.4 Effectiveness Factor, Thiele Modulus, and Diffusivity

The overall effectiveness factor (η) reconciles observed reaction rate with intrinsic reaction rate by accounting for transport limitations due to internal and external heat and mass transfer. Only internal mass transfer (pore diffusion) resistance is considered in this paper since criteria calculations show that external heat and mass transfer and internal heat transfer resistances are negligible. The effectiveness factor is calculated from the Thiele modulus (ϕ) as given by Equation 5.23.

$$\eta = \frac{tanh(\phi)}{\phi} \tag{5.23}$$

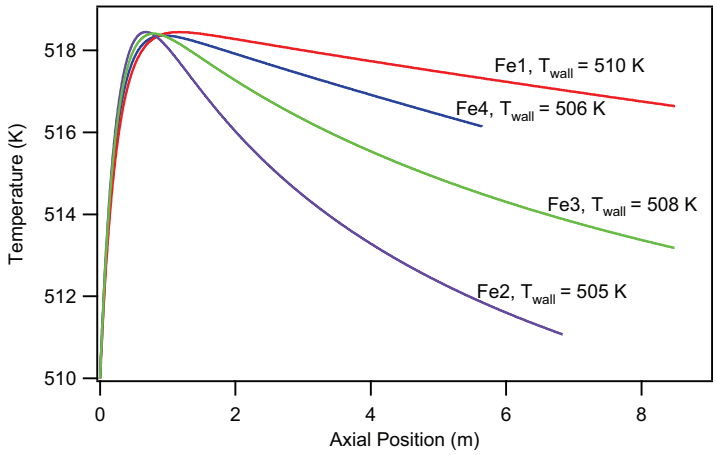

Figure 5.8: Temperature profiles for the four iron kinetic models. Feed and wall temperatures were adjusted to give $T_{max} = 518$ K for each profile. All other parameters are for the iron base conditions.

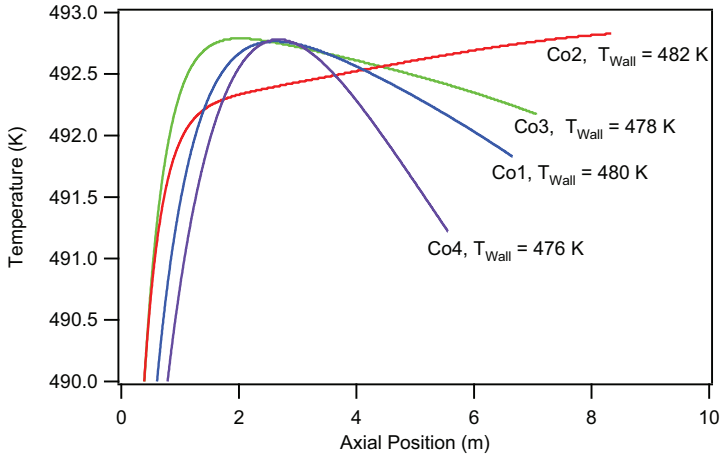

Figure 5.9: Temperature profiles for the four cobalt kinetic models. Feed and wall temperatures were adjusted to give $T_{max} = 492.8$ K for each profile. All other parameters are for the cobalt base conditions.

An nth-order Thiele modulus is used in the reactor model where k_e is the effective nth-order intrinsic rate constant and n_{ro} is the assumed reaction order (Equations Equation 5.24 and Equation 5.25).

$$\phi = L_{p_e}\sqrt{\frac{k_e C_A^{n_{ro}}\left(n_{ro}+1\right)}{2D_e C_A}} \tag{5.24}$$

$$k_e = \frac{-r_{CO}}{C_A^{n_{ro}}} \tag{5.25}$$

Since the kinetic models in the base cases have LH forms, the effective order of reaction shifts with conversion; hence the need for an assumed effective reaction order. Average effective orders for the base cases were chosen for iron and cobalt by careful analysis of the rate equations over the range of conditions modeled and are given in Table 5.2. Analysis shows that varying those values by ± 0.5 from the base case values results in ± 2 m variation in reactor length for both iron and cobalt.

The effective diffusivity (D_e) in Equation 5.24 is calculated from the Wheeler pore diffusion model given by

$$D_e = \frac{D\varepsilon_p}{\tau} \tag{5.26}$$

where τ is tortuosity (assumed to be 3.5). D is the resistance sum of Knudsen (D_k) and bulk (D_{ab}) diffusivities given by Equation 5.27.

$$\frac{1}{D} = \frac{1}{D_k} + \frac{1}{D_{ab}} \tag{5.27}$$

Values for D_k were calculated to be 2 orders of magnitude larger ($3 \cdot 10^{-6}$ m^2/s) than values for D_{ab} ($2 \cdot 10^{-8}$ m^2/s) and were included in calculations even though D_k could be neglected since it is assumed that the catalyst pores are liquid filled and that reactant gases must diffuse through wax products to react on the surface which gives the higher diffusional resistance.

An extensive study of the bulk diffusivities of H_2, CO, and various n-alkanes in $C_{20}H_{42}$, $C_{28}H_{58}$, and FT wax from a Co catalyst at elevated temperatures (298–573 K) and pressures (14.7–500 psi) produced a comprehensive model (Equation 5.28) for predicting bulk diffusivities in alkanes [80–82].

$$D_{ab} = \frac{94.5 \cdot 10^{-9}\sqrt{T}}{M_a^{0.239} M_b^{0.781} (\sigma_a \sigma_b)^{1.134}} (\bar{V} - \bar{V}_0) \tag{5.28}$$

The measured bulk diffusivities in the FT wax were consistent with calculated diffusivities in $C_{25}H_{52}$.

Diffusion of CO in wax was chosen as the characteristic diffusivity because CO diffusion is slower than H_2 diffusion and CO is most often the limiting reactant in FT applications. Table 5.4 shows calculated bulk and effective diffusivities. The usage ratios of H_2 to CO for Co and Fe are estimated to be 2.1 and 1.2, respectively, depending on the product slate and (for Fe) water-

gas-shift activity. Sasol reports a usage ratio of 1.7 [10]. Accordingly, under most FT reactor conditions, CO diffusion (not H_2 diffusion) limits reaction rate. Thus, the CO diffusivity should be used as the characteristic diffusivity in calculating the effectiveness factor in most cases. It could be appropriate to use the H_2 diffusivity for severely H_2-deficient applications.

Table 5.4: Bulk and effective diffusivities for CO and H_2 in heavy alkanes ($C_{20}H_{42}$ for Fe and $C_{25}H_{52}$ for Co) at 503 K. D_{ab} calculated from Equation 5.28.

Solute (a)	Solvent (b)	$D_{ab}\times10^9$ m^2/s	$D_e\times10^9$ m^2/s
CO	$C_{20}H_{42}$	19.6	2.6
H_2	$C_{20}H_{42}$	49.3	6.5
CO	$C_{25}H_{52}$	15.9	2.2
H_2	$C_{25}H_{52}$	40.1	5.6

Figure 5.10 compares values of the effectiveness factor as a function of effective diffusivity for 3 different assumed orders of reaction each for iron and cobalt. Wall temperatures were varied to give average bed temperatures of 518 K and 492 K for iron and cobalt, respectively. The effectiveness factor for normal FTS conditions in a FBR can be significantly less than unity and it increases with increasing diffusivity and decreasing order of reaction. This illustrates the need for careful determination of D_e and evaluation of the kinetics to choose an appropriate CO reaction order. The D_e value greatly affects the effectiveness factor, e.g. for iron with an assumed CO order of 0.2, the average effectiveness factor is 0.63 when the D_{ab} value for CO is used, while it is 0.80 when the D_{ab} value for H_2 is used.

Figure 5.11 shows the effects of diffusivity on reactor length and temperature profile with all other inputs consistent with the iron base case. Increasing effective diffusivity increases the effectiveness factor and thereby increases the observed rate of reaction and bed temperature. The result is that increasing effective diffusivity by a factor of 2.5 (from $2.8\cdot10^{-9}$ m^2/s to $7.1\cdot10^{-9}$ m^2/s, the values assuming CO and H_2 diffusion, respectively) predicts a higher temperature (523 K vs. 518 K) and much shorter bed length (5.7 m vs. 8.5 m) to achieve a conversion of 60% in the

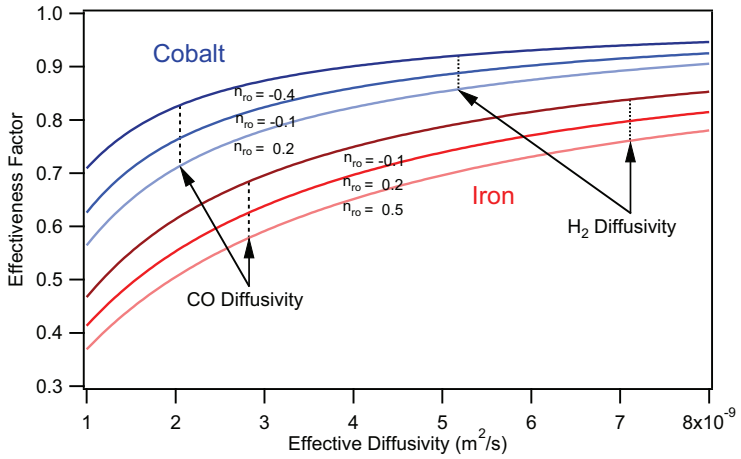

Figure 5.10: Average predicted effectiveness factor for the Fe and Co base cases as a function of effective diffusivity for several reaction orders. Wall temperatures were varied for each run to give average bed temperatures of 518 K and 492 K for iron and cobalt, respectively. Values corresponding to CO and H_2 diffusion at reactor conditions are indicated.

base case for iron. Clearly, the choice of effective diffusivity (whether H_2 or CO) impacts model predictions dramatically.

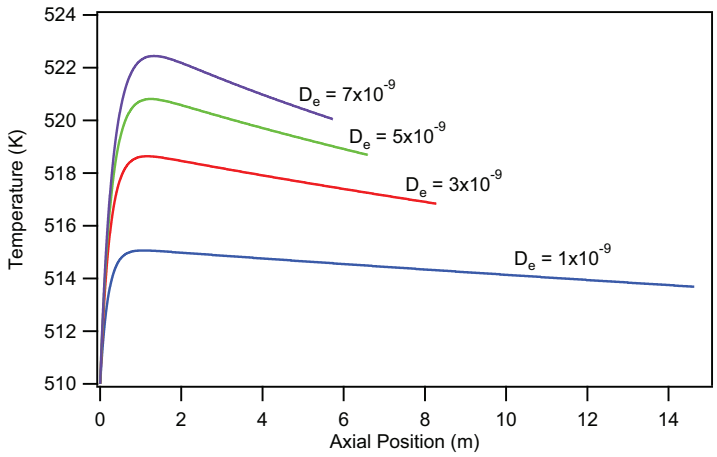

Figure 5.11: Effects of diffusivity on reactor length and temperature profile for the iron base case. Diffusivities are given and have units of m^2/s.

5.5 Heat Transfer Parameters

The overall heat transfer coefficient (U) accounts for heat transfer in the radial direction by convection, conduction, and radiation through the catalyst particles, the liquid, and the gas. Studies on heat transfer in packed beds show that heat transfer in the central core of the bed is different from heat transfer near the wall, presumably due to particle-wall interactions and channeling [37, 38, 83, 84]. Consequently, heat transfer in a reactor tube can be modeled by an effective radial thermal conductivity in the core of the bed (λ_{er}) in series with an effective radial heat transfer coefficient at the wall (h_{wall}). These heat transfer terms are combined in Equation 5.29 and discussed individually in subsequent sections.

$$\frac{1}{U} = \frac{1}{h_{wall}} + \frac{d_t}{8\lambda_{er}} \tag{5.29}$$

5.5.1 Effective Radial Thermal Conductivity

Matsuura et al. [37] modified a correlation by Yagi and Kunii [83] for effective radial thermal conductivity (λ_{er}) which accounts for static (λ^s_{er}) and dynamic contributions for gas (λ^g_{er}) and liquid (λ^l_{er}) flow in a packed bed (Equation 5.30).

$$\lambda_{er} = \lambda^s_{er} + \lambda^g_{er} + \lambda^l_{er} \tag{5.30}$$

λ^s_{er} accounts for conduction and radiation through the bed. At FT temperatures, radiation contributions are negligible and for gas-liquid flow Matsuura et al. [37] simplified λ^s_{er} to Equation 5.31.

$$\lambda^s_{er} = 1.5\lambda_l \tag{5.31}$$

λ^s_{er} values for the base cases calculated using Equation 5.31 were less than 2% of λ_{er} in each case.

λ^g_{er} and λ^l_{er} account for radial mixing of gas and liquid within the void space and are given by Equation 5.32.

$$\lambda^g_{er} + \lambda^l_{er} = (\alpha\beta)_g \lambda_g Re_g Pr_g + (\alpha\beta)_l \lambda_l Re_l Pr_l \tag{5.32}$$

Values for the constant $(\alpha\beta)_g$ are given in Table 5.5. The Reynolds and Prandtl numbers for the gas are based on superficial mass flux (G_g), viscosity (μ_g), specific heat capacity ($c_{p,g}$), thermal conductivity (λ_g) and pellet diameter (d_p) as given in Equations Equation 5.33 and Equation 5.34. The Reynolds and Prandtl numbers for the liquid are calculated using the liquid counterparts of each of these terms.

$$Re_g = \frac{G_g d_p}{\mu_g} \tag{5.33}$$

$$Pr_g = \frac{c_{p,g}\mu_g}{\lambda_g} \tag{5.34}$$

$(\alpha\beta)_l$ has no clear dependence on liquid flow rate, but increases slightly with gas flow rate, indicating that radial mixing of the fluid is enhanced by gas flow. A simple expression for $(\alpha\beta)_l$ based on the gas Reynolds number is given by Equation 5.35. Values of the fitted constants a and b are given in Table 5.5.

$$(\alpha\beta)_l = a\,(1 + bRe_g) \tag{5.35}$$

Table 5.5: Fitted constants for Equation 5.35 as given by Matsuura et al. [37].

d_p	$(\alpha\beta)_g$	$(\alpha\beta)_l$	
(cm)	–	a	b
0.12	0.412	0.201	$2.83\cdot10^{-2}$
0.26	0.334	0.167	$1.34\cdot10^{-2}$
0.43	0.290	0.152	$6.32\cdot10^{-3}$

The full equation for λ_{er} is given in Equation 5.36 [37].

$$\lambda_{er} = 1.5\lambda_l + (\alpha\beta)_g G_g c_{p,g} d_{p_e} + (\alpha\beta)_l G_l c_{p,l} d_{p_e} \tag{5.36}$$

Individual contributions of the static, gas, and liquid terms to λ_{er} for the iron base case are shown in Figure 5.12. Trends for the cobalt base case are qualitatively similar, but the value of λ_{er} is larger (35 W/mK compared to 27 W/mK). λ_{er} increases almost linearly through the reactor. The increase in λ_{er}^l as a result of increased liquid flow rate accounts for all of the increase in λ_{er}. λ_{er}^s remains

relatively insignificant throughout the length of the reactor while λ_{er}^{g} decreases slightly. These trends suggest that the presence of liquid facilitates heat transfer within the core of a fixed-bed.

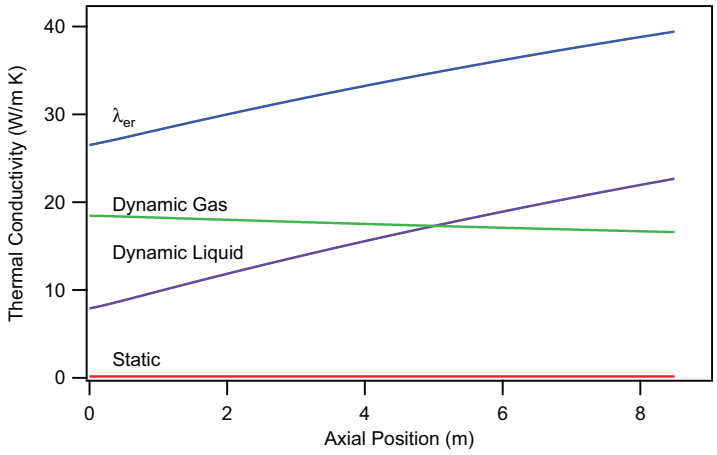

Figure 5.12: λ_{er} vs. axial position for the iron base case. Also shown are the static, gas, and liquid contributions to λ_{er}.

In a reactor with no liquid recycle, the entrance of the bed will be relatively dry as liquid products begin to accumulate. It is also near the bed entrance that the majority of the temperature rise occurs and risk of runaway is greatest. Recycling a portion of the gas and liquid product to the reactor entrance can improve temperature control in this critical region of the reactor and throughout the bed. Gas recycle improves heat transfer by increasing flow rate, decreasing partial pressures of reactants in the feed, and increasing thermal performance. Increasing flow rate increases the rate of heat transfer by convection thereby decreasing the main heat transfer resistance in fixed beds. Decreasing partial pressures of reactants decreases the rate of reaction and therefore of heat generation. Nonreactive gas from the recycle stream acts as a thermal buffer and decreases temperature rise from the exothermic reaction. Recycling a portion of the liquid improves heat transfer at the top of the bed where a large temperature rise could lead to runaway. Recycle for temperature control becomes increasingly more important in order to prevent runaway as the FT process is intensified. The reactor model under discussion allows for gas and liquid recycle.

5.5.2 Radial Heat Transfer Coefficient at the Wall

In theory, the effective wall heat transfer coefficient (h_{wall}) accounts for interactions of the gas, the liquid and the solid with the tube wall. The volumetric flow rate of liquid products out of a single tube for the iron base case was calculated to be 0.030 L/min (compared with 31 L/min of gas). At this low liquid flow rate, the liquid would have little interaction with the gas, would bathe the catalyst particles, and would have little contact with the tube wall except in the static void spaces where the catalyst contacts the wall. Prior work shows that although the presence of liquid could increase h_{wall} by as much as an order of magnitude, in low interaction gas-liquid flow regimes h_{wall} approaches one-phase (gas-solid) correlation values because most of the wall has no liquid contact [85, 86]. Accordingly, a gas-solid wall heat transfer correlation [38, 87] was used to model this situation (Equation 5.37).

$$h_{wall} = \frac{10.21\lambda_{er}^{s}}{d_t^{\frac{4}{3}}} + 0.033\frac{\lambda_g}{d_p}Pr_g Re_g \tag{5.37}$$

As with λ_{er}, h_{wall} is divided into static and dynamic terms. The static term depends on tube diameter and on λ_{er}^{s} , which was modified to account for the presence of liquids (see Section Section 5.5.1). The dynamic contribution to h_{wall} which accounts for convection to the wall is determined from the pellet diameter, the thermal conductivity of the gas, and from the Prandtl and Reynolds numbers of the gas.

Figure 5.13 compares the individual contributions of the static and dynamic terms to h_{wall} for the Fe base case. h_{wall} decreases slightly with reactor length primarily as a result of decreasing gas flow rate due to volumetric contraction resulting from a decrease in the total number of moles through the reactor. The cobalt base case also follows this trend, although the magnitude of h_{wall} is larger (about 1200 W/m^{2}K compared to 800 W/m^{2}K). Increasing gas recycle ratio increases total gas flow in the reactor which increases the Reynolds number and thereby increases heat transfer to the wall. The static term accounts for a significant portion of h_{wall} (25% for Fe, 20% for Co).

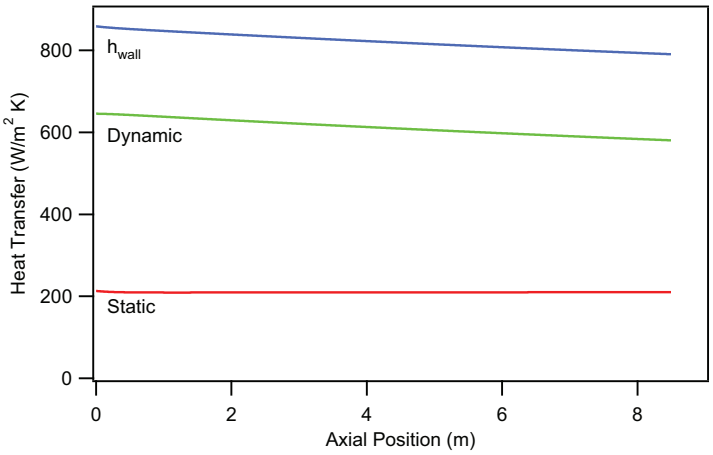

Figure 5.13: h_{wall} vs. reactor length for the iron base case. Also shown are static and dynamic contributions to h_{wall}.

5.5.3 Overall Heat Transfer Coefficient

Having defined and analyzed heat transfer in the bed and at the wall, Figure 5.14 shows overall heat transfer resistance $(1/U)$ and resistance contributions within the bed $(d_t/8\lambda_{er})$ and at the wall $(1/h_{wall})$ for Fe. $1/U$ and $1/h_{wall}$ increase through the bed while $d_t/8\lambda_{er}$ decreases. Thus, h_{wall} influences U much more than λ_{er}, but λ_{er} is not insignificant. These trends are also true for the cobalt base case and are consistent with the work of others [37, 38, 84, 85, 87].

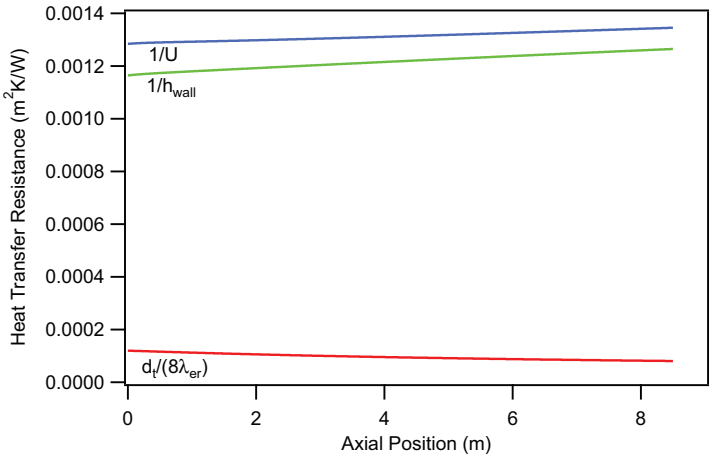

Figure 5.14: Overall heat transfer resistance $(1/U)$ vs. reactor length for the iron base case. Also shown are resistance contributions of λ_{er} and h_{wall} to $1/U$.

5.5.4 Radial Temperature Gradients

Heat transfer in the design of FTS reactors is especially important in order to prevent runaway and hot spots that may result in faster deactivation of the catalyst and an undesirable product slate. Since the model discussed in this work is 1-D, it is not capable of producing a predictive radial temperature profile within the reactor tubes; however, radial gradients can be estimated using numerical methods. Temperature profiles for radial positions are generated for the cobalt base case in order to illustrate this point.

To generate the radial temperature profiles, the energy equation is solved for the radial dimension in cylindrical coordinates (Equation 5.38). Axial temperature gradients and velocity gradients are ignored in this exercise.

$$\frac{d}{dr} r q_r = r \eta \rho_b \left(-r_{CO}\right) \Delta H_{rxn|T^0} \tag{5.38}$$

Applying the chain rule followed by Fourier's law of heat transfer and collecting thermal conductivities gives Equation 5.39.

$$-\lambda \left(\frac{d^2T}{dr^2} + \frac{1}{r}\frac{dT}{dr} \right) = \eta \rho_b \left(-r_{CO}\right) \Delta H_{rxn|T^0} \tag{5.39}$$

The derivative terms of Equation 5.39 are discretized using finite centered difference formulas. Boundary conditions account for symmetry at the core of the bed and for effective radial heat transfer at the wall (Equations Equation 5.40 and Equation 5.41). Derivatives of the boundary conditions are discretized using a first order forward finite difference of a second order linear approximation (Equation 5.42).

$$\frac{dT}{dr} = 0, r = 0 \tag{5.40}$$

$$h_{wall}\left(T_{wall} - T_R\right) = \lambda \frac{dT}{dr}, r = \frac{d_t}{2} \tag{5.41}$$

$$\frac{dT_i}{dr} = -\frac{T_{i+2} - 4T_{i+1} + 3T_i}{2\Delta r} \tag{5.42}$$

This treatment assumes a constant rate of reaction at each node (radial direction) and no radial concentration gradients. This assumption is reasonable as long as the partial pressures of reactants and the temperature do not vary greatly between the core and the wall. Equation 5.39 was

solved numerically by successive substitution with 10 equidistant points in r. Figure 5.15 shows the 1-D model predicted axial temperature profile (dashed line) along with center ($r = 0$ mm), intermediate ($r = 4.2$ mm and $r = 8.5$ mm), and near-wall ($r = 12.7$ mm) temperature profiles for a single tube for the cobalt base case. As can be seen, the radial temperature gradient within the bed is on the order of 2–3 K for 2.54 cm diameter reactor tubes. This calculated temperature gradient would increase significantly if changes in concentration and the rate of reaction in the radial direction were accounted for (fully 2-D model). Increasing tube diameter would also increase the temperature gradient and make temperature control more difficult.

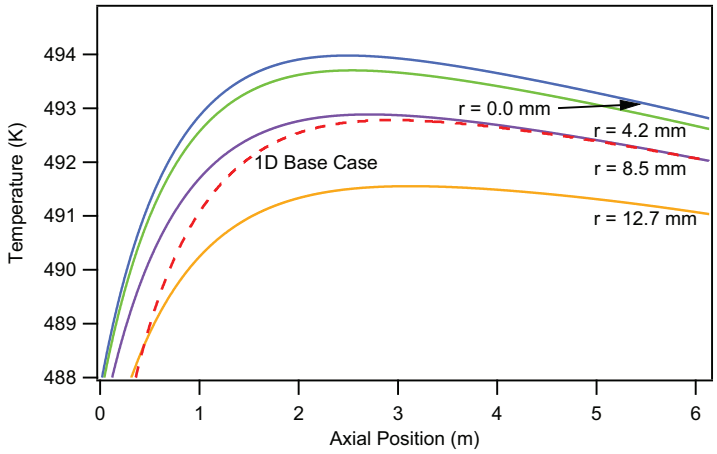

Figure 5.15: Representative 1-D (dashed line), core ($r = 0$ mm), intermediate, and near-wall ($r = 12.7$ mm) axial temperature profiles for a single tube in the cobalt base case.

5.5.5 Prandtl Number

Both the heat transfer coefficient in the bed and at the wall depend on Prandtl number. It is common practice to assume a constant value for the gas Prandtl number of 0.7. While calculations of the Prandtl number for pure gases support this assumption, calculations of the Prandtl number using molar averages for the gas mixture ranges of the iron and cobalt base cases predict average Prandtl numbers of 0.24 and 0.26, respectively, over the lengths of the reactors. Calculations of Prandtl number using mixing rules published by Reid et al. [88] and Walas [89] give less than 2% deviation from calculations using molar averages, indicating that molar averages of properties are

suitably accurate for FT FBR simulations. Figure 5.16 shows the reactor temperature profile for the cobalt base case calculated using a constant Prandtl number of 0.7 compared with the profile using predicted Prandtl numbers. It indicates that assuming a constant Prandtl number of 0.7 predicts reactor lengths up to 5 m longer and temperatures up to 10 K lower than calculations using Prandtl numbers based on molar-averaged properties. Using larger Prandtl numbers increases predicted values of thermal conductivity and heat transfer coefficients in the bed and at the wall leading to erroneously small heat transfer resistances and unrealistically low temperatures through the bed. Analysis of the iron base case gave similar results. Since heat transfer is important in FT reactor design, Prandtl numbers based on molar averages provide more realistic predictions of temperature profiles and catalyst requirements.

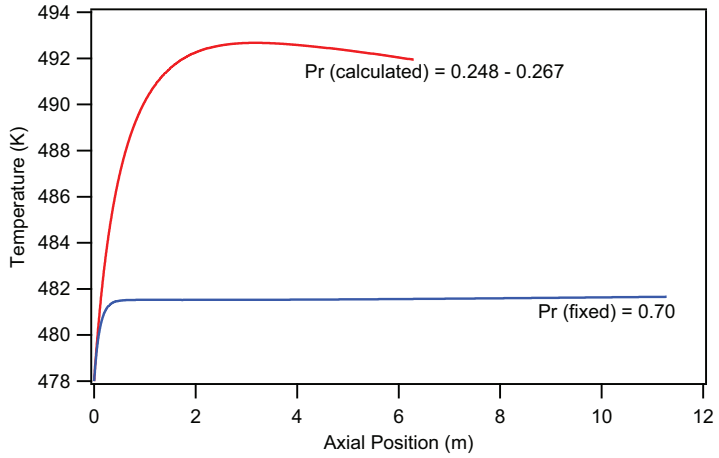

Figure 5.16: Temperature profiles for the cobalt base case using $Pr = 0.7$ and Pr calculated from molar-averaged gas properties.

5.6 Pressure Drop

The momentum balance (Equation 5.8) given by Froment and Bischoff [38] predicts pressure drop in a packed bed (δ_{GW}) including the effect of dynamic liquid holdup (ε_l) which reduces void space (ε_b). This treatment is valid for a packed bed reactor with gas and liquid down flow in a trickle flow regime. Equation 5.43 gives the dynamic liquid holdup as determined by Satterfield

and reported by Froment and Bischoff [38]

$$\varepsilon_l = c\left(\frac{\rho_l d_p L}{\mu_l A_{cs}}\right)^{\alpha}\left(\frac{d_p^3 g \rho_l^2}{\mu_l^2}\right)^{\beta} = \left(\frac{\mu_l u_l}{d_p^2 g \rho_l}\right)^{1/3} \tag{5.43}$$

where α, β, and c are fitted constants. The final equality in Equation 5.43 is true for $\alpha = -\beta = 1/3$ and $c = 1$. Pressure drop for gas flowing through a packed bed is given by Equation 5.44.

$$\delta_{GW} = \frac{1-\varepsilon_w}{\varepsilon_w^3}\frac{\rho_g u_g^2}{d_p} f_k \tag{5.44}$$

ε_w is the void fraction adjusted for the static liquid holdup ($\varepsilon_w = \varepsilon_b - \varepsilon_l$) and f_k is the friction factor for fluid flow in a packed bed commonly given by the Ergun equation (Equation 5.45).

$$f_k = 1.75 + 150\frac{1-\varepsilon_b}{Re_g} \tag{5.45}$$

Hicks [90] showed that the Ergun equation is only valid for $Re_g/(1-\varepsilon_b) < 500$ due to the assumption that the turbulent contribution to friction is constant. Typical values of $Re_g/(1-\varepsilon_b)$ for FTS are above 500 (e.g. for the base cases $Re/(1-\varepsilon_b) = 2,850$ for iron and $3,005$ for cobalt). Tallmadge [40] added a Reynolds number dependence to the turbulent term of the Ergun equation (see Equation 5.46) and thereby increased the valid range of the correlation to $0.1 < Re_g/(1-\varepsilon_b) < 100,000$.

$$f_k = 4.2\left(\frac{1-\varepsilon_b}{Re_g}\right)^{1/6} + 150\frac{1-\varepsilon_b}{Re_g} \tag{5.46}$$

Both the Ergun and Tallmadge equations ignore friction losses at the tube wall which become important when $d_t/d_p < 50$. The Mehta and Hawley [41] modification to the Ergun equation accounts for frictional losses at the tube wall as well as within the bed, but like Ergun, assumes that the turbulent contribution to friction is independent of Reynolds number (Equation 5.47).

$$f_k = \left(1 + \frac{2d_p}{3(1-\varepsilon_b)d_t}\right)^2\left(\frac{1.75}{1+\frac{2d_p}{3(1-\varepsilon_b)d_t}} + 150\frac{1-\varepsilon_b}{Re_g}\right) \tag{5.47}$$

Figure 5.17 compares pressure drop versus reactor length for the cobalt standard conditions predicted using the Ergun, Tallmadge, and Mehta-Hawley equations. The Mehta-Hawley equation predicts the largest pressure drop (7.14 atm) followed by the Ergun equation (6.37 atm) and then the Tallmadge equation (3.86 atm). Since typical Reynolds numbers for FB FTS are greater than the accurate range of the Ergun equation and since the Mehta-Hawley equation perpetuates the same assumption for turbulence, the authors choose to use the Tallmadge equation in this model.

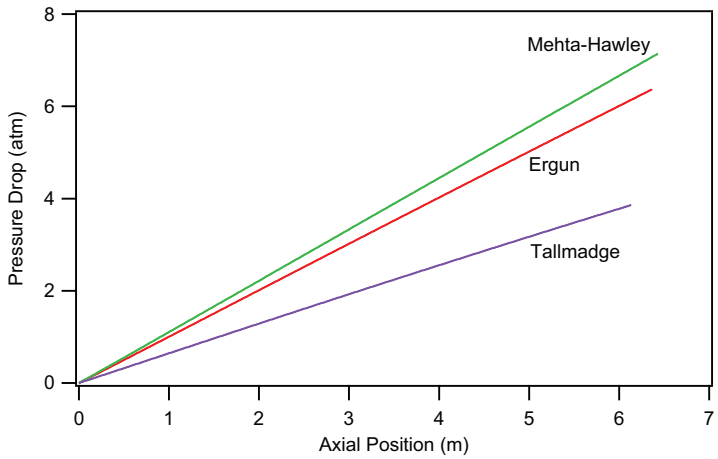

Figure 5.17: Comparison of pressure drop as a function of axial position for the Ergun, Tallmadge, and Mehta-Hawley equations for the cobalt base conditions (Average $Re_g/(1-\varepsilon_b) = 3,005$).

5.7 Validation

Complete sets of pilot and/or full-scale plant data for FT FB reactors are very scarce or non-existent in the literature. Studies on the SASOL Arge Trickle-FB reactors (TFBR) provide enough partial data for a validation of the model for iron catalysts [1, 10, 14, 71, 91–93]. A limited amount of data are available on the Shell Bintulu MTFB reactor [4, 10, 91, 94, 95], but not enough to validate the model for cobalt. Reported data on the SASOL and Shell reactors are given in Table 5.6.

To validate the model for iron catalyst systems, input parameters from the cited studies were entered into the model and the predicted results were compared with the corresponding reported values. Wall temperature and catalyst activity were varied in order to match the specified bed

Table 5.6: Reported parameters for the Sasol Arge TFBR (iron) and Shell MTFB (cobalt) reactors. The Arge reactor values were used to validate the model. [1, 4, 5, 10, 14, 71, 91–93, 95–98]

Parameter	Sasol Arge TFBR (Fe)	Shell MTFB (Co)
Productivity (bbl/d)	500	3,675
Productivity (tonne/y)	21,000	144,000
Pressure (bar)	27	30
Bed Volume (m^3)	40	
Number of Tubes	2050	26,150
Tube Length (m)	12	12.865
Tube Diameter(cm)	5.0	2.6
Pellet Diameter (mm)	2.5	1-3
Catalyst Pore Volume (cm^3/g)[a]	0.37	
CH_4 in Feed (%)	11.0	0.5
H_2:CO Feed	1.8	1.8–2.1
H_2:CO Usage	1.7	2.1
H_2+CO Conversion (%)	60–66	
Recycle/Feed Ratio	2.2–2.5	
Liquid Recycle Ratio	0	
CH_4 Selectivity[b]	0.02	
C_{2-4} Selectivity[b]	0.04	
C_{5+} Selectivity[b]	0.925	0.92
Oxygenate Selectivity[b]	0.015	
CO_2 Selectivity		0.01
Propagation Probability	0.95	0.86–0.90

[a]after 212 hours of FT reaction
[b]CO_2-free basis

length and average bed temperature. As the studies did not report all of the necessary inputs for the reactor model, 6 parameters were input as given and 11 parameters were calculated from the given data. Feed temperature was set equal to the wall temperature. The catalyst kinetics were represented by model Fe3 (Equation 5.17). Since none of the sources reported the geometry or aspect ratio of the extruded catalyst, it was assumed that the catalyst was extruded as cylinders with an aspect ratio of 3. Calculated input values are given in Table 5.7, and the results of the validation (comparison of varied and predicted values) are given in Table 5.8.

Table 5.7: Calculated parameters for the iron model validation and for the cobalt simulation. Brackets ([]) indicate assumed values for the cobalt simulation.

Parameter	Sasol Arge TFB (Fe)	Shell MTFB (Co)
Flow Rate (SCFH·10^5)	9.0	46.3
Space Velocity (h^{-1})	637	733
CO in Feed (%)	31.8	31.4[a]
H_2 in Feed (%)	57.2	65.8[a]
CO Final Conversion (%)	62.2	[81.3][b]
Recycle/Tailgas Ratio[c]	5.0	0
Catalyst Charge (tonne)	26.1	[176]
Cat. Prod. ($kg_{C_{5+}}/kg_{cat}$·h)	0.099	[0.110]
Bed Porosity[d]	0.42	[0.42]
Bed Density (kg/m^3)	652[e]	[988]
Pellet Density (kg/m^3)	1,119	[1,696]
CH_4 Selectivity	0.018	0.03
C_{2-4} Selectivity	0.035	0.04
C_{5+} Selectivity	0.811	0.92
CO_2 Selectivity	0.123	0.01
Oxygenate Selectivity	0.013	[0]
Density of C_{5+} (kg/m^3)[f]	777	794

[a]based on CH_4 and CO_2 content of syngas
[b]from CO+H_2 conversion [94]
[c]no water, oil, or wax in recycle [10]
[d]based on assumed shape (cylinder) and aspect ratio (3)
[e]based on charge and volume of test reactor [14]
[f]based on volumetric and mass productivities

Even though a validation for cobalt is not possible at present, a simulation using the available data for the Shell Bintulu MTFB reactor is given for the convenience of the reader in comparing the performance of this model to other models. The syngas feed is produced from partial oxidation of natural gas at 95% conversion of carbon to CO, giving a H_2:CO ratio of 1.7. As this is much lower than the usage ratio (just over 2.0), the feed is enriched with a steam-reformed portion of recycled tailgas [99]. Since this model cannot account for the reforming process, the feed rate and composition were adjusted to account for the addition of the reformed tailgas, and recycle streams were not modeled. Values of assumed parameters necessary to model a reactor are

Table 5.8: Results of iron model validation and cobalt simulation. Values of wall temperature and catalyst activity were varied to match bed length and average bed temperature.

	Sasol Arge TFBR (Fe)		Shell MTFB (Co)	
Parameter	Arge TFB	Model	Bintulu SMDS	Predicted
Wall and Feed T (K)[a]	493–498	495		480
Catalyst Activity[a]		0.48		0.10
Bed Length (m)	9.94[b]	9.94	12.865	12.864
Average Bed T (K)	503	503	473–503	490
Pressure Drop (bar)	3–7[c]	0.55		0.22
Average η		0.509		0.861

[a]varied to match bed length and average bed temperature
[b]calculated from bed volume, number of tubes, and tube diameter (see Table 5.6)
[c]Espinoza et al. [92]

given in Table 5.7 and results of the simulation are given in Table 5.8. The catalyst kinetics were represented by model Co3 (Equation 5.21). The results of the simulation for the Shell reactor are not discussed.

For the iron validation, four different validation simulations were run representing the extremes of the reported ranges of recycle to feed ratio (2.2–2.6) and H_2+CO conversion (0.6–0.66). In each case, bed length and average bed temperature were matched within 1% of reported values by varying wall temperatures (493–495 K) and catalyst activities (0.48–0.57). The predicted pressure drop (0.39–0.55 bar) was far lower than reported (3–7 bar). The discrepancy in pressure drop might be explained by considering that the original wax productivity (500 bbl/day) and feed rate (500 h^{-1}) were greatly increased over time [14]. It is unclear whether the reported pressure drop range was typical of the original feed rate or of the increased rate. The predicted 0.55 bar seems reasonable for pressure drop considering the low space velocity (637 h^{-1}), large tube diameter (5.0 cm), large pellet size (2.5 mm), and reactor length (9.94 m). The reported 3–7 bar pressure drop represents 11–27% of the operating pressure (27 bar). The calculated density of the average hydrocarbon product (C_{5+}) corresponds to the liquid density of $C_{20}H_{42}$ at 383 K. The catalyst activity of 0.48–0.57 suggests that the kinetic model used (Fe3 Equation 5.17) overestimates the activity of the catalyst at these low temperatures which is consistent with a kinetic model developed on a fresh catalyst ($<$ 500 hours on stream) compared with the activity of a commercial catalyst

after several months on stream. In summary, by varying two variables (wall temperature and activity), two performance parameters (bed temperature and bed length) were matched within 1% of reported values, suggesting that the model is capable of predicting industrial reactor performance well and may be considered validated.

5.8 Comparison to Published Models

5.8.1 Data and Input for Simulations

Simulation results from this reactor model are compared with model predictions reported by Wang et al. [7] for iron (1-D model) and by Jess and Kern [12] for cobalt (2-D model). Table 5.9 gives the input variables for both cases. Neither published model allows for liquid recycle, but it is included with other base case parameters when we attempt to match their predictions. Jess and Kern did not give a pellet porosity or pore volume, so the cobalt base case value is assumed. In each case, only catalyst activity is varied in our model to give a predicted bed length that is within 0.3% of the published value (12 m for Co and 7.0 m for Fe).

5.8.2 Cobalt Simulation Results

Figure 5.18 compares the predicted axial temperature profile for this model with the published prediction from the Jess and Kern model for a cobalt catalyst. Our model matched the temperature rise and maximum average bed temperature of the 2-D Jess and Kern model very well. The predicted outlet temperature was less than 3 K lower than reported. To achieve this close match, a catalyst activity of 1.833 was assumed, suggesting that the kinetics used in the Jess and Kern model are inherently more active than Equation 5.19. The fact that our 1-D model matched the average 2-D model profile so well is a result of using an effective radial thermal conductivity term in addition to the typical 1-D heat transfer coefficient at the wall. While Jess and Kern included separate rate equations for methanation and for hydrocarbon production, our model employed a single kinetic expression (with a fixed selectivity model) to calculate the consumption of CO. Our model uses the diffusivity of CO in liquid FT wax to calculate effective diffusivity while the Jess and Kern model uses the diffusivity of H_2. Our previous work shows that the diffusivity of

Table 5.9: Input parameters for model simulations of other published models. Assumed (base case) values are indicated by brackets ([]).

Parameter	Jess and Kern [12]	Wang et al.[7, 33]
Catalyst	Cobalt	Iron
Flow Rate (SCFH)	2,932,800[a]	99[b]
Feed Mole % of CO	33.4	30.59
Feed Mole % of H_2	66.6	57.75
Feed Mole % of CO_2	0.0	7.00
Feed Mole % of CH_4	0.0	0.58
Feed Mole % of N_2	0.0	4.08
Inlet Temperature (K)	478	523
Wall Temperature (K)	478	523
Inlet Pressure (atm)	23.7	24.7
Gas Recycle:Effluent Ratio	5.3	4.956
Liquid Recycle Ratio	[0.5]	[0.5]
Final CO Conversion	0.63	0.735
Selectivity to CH_4	0.066	0.149
Selectivity to C_{2-4}	0.055	0.084
Selectivity to C_{5+}	0.879	0.498
Selectivity to CO_2	0.0	0.269
Reaction Order[d]	[-0.1]	[0.2]
Catalyst Activity[e]	[1.833]	[0.050]
Number of Tubes	2,000	1
Tube Diameter (mm)	46	40
Pellet Diameter (mm)	2.7	2.5
Pellet Geometry	cylinder	cylinder[e]
Pellet Aspect Ratio	1.9	3[e]
Pellet Pore Volume (cm^3/g)	[0.42]	0.262[f]
Bed Density (kg/m^3)	700	1128

[a]calculated from $u_s = 0.55$ m/s and $\rho_{mol} = 563$ mol/m^3
[b]$GHSV = 500\ h^{-1}$
[c]for Thiele modulus calculation
[d]catalyst activity varied to achieve 12 m tube length
[e]assumed based on pellet size given (2.5×5–10 mm)
[f]calculated from pellet density (1950 kg/m^3) and porosity (0.51)

CO may be a better choice based on relative diffusion rates, kinetic rate dependence at low concentrations (as expected inside catalyst pores), and relative abundance [44]. Choosing the diffusivity of H_2 instead of CO can result in over estimating the overall effectiveness factor (ratio of observed and intrinsic rate values $= 0.89$ compared with 0.77) which will affect heat generation and mass

conversion calculations. Thus, if Jess and Kern had used CO diffusivity instead of H_2 diffusivity, our model probably have achieved a match using an activity closer to one.

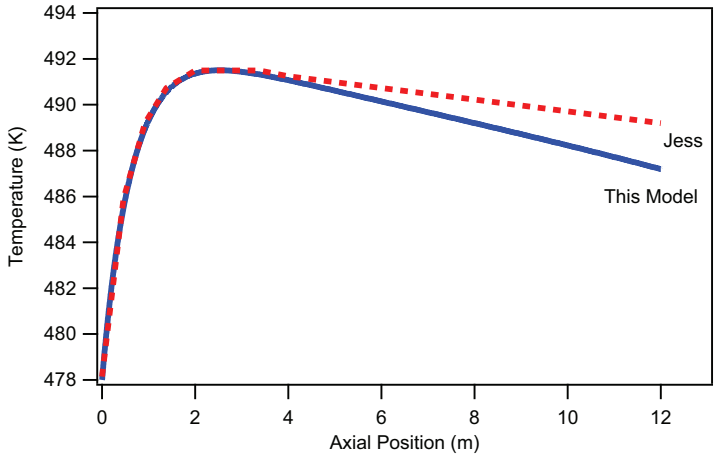

Figure 5.18: Temperature profiles predicted with this model and with the model published by Jess and Kern [12].

5.8.3 Iron Simulation Results

Predicted and reported temperature profiles for the Wang et al. reactor model for an iron catalyst are compared in Figure 5.19. The reported profile is 2–3 K hotter at T_{max} than our model, but both models predict an outlet temperature within 1 K of each other. Wang et al. developed a sophisticated collection of tools specifically for modeling the FTS in FBRs including a detailed kinetic model , a generalized gas-wax equilibrium correlation, and a diffusion-reaction model for wax-filled catalyst pellets. The authors did not report a predicted pressure drop for comparison, but their model uses a friction factor correlation developed by Hicks [90]. The Hicks correlation was only intended to show the limitations of the Ergun equation and not to be generally applicable to pressure drop in a FB. We recommend the equation proposed by Tallmadge [40] as it is generally applicable to Reynold's numbers over 5 orders of magnitude; however, it does not account for pellet-wall interactions which are significant for $d_t/d_p < 15$. It is unclear why our kinetic model is so much more active (nearly 20 times) than the Wang et al. model. Some possibilities for the low activity include that the catalyst may not be very active, the test reactors may have been filled

with a combination of catalyst and diluent (quartz), the reported bed length may have been a tube length and the tube was not completely full, or the catalyst may have been intentionally exposed to harsh conditions (deactivated) during the startup of the kinetic testing to eliminate transient catalyst behavior quickly and to more fully establish consistent kinetic activity on a fully carbided catalyst [100].

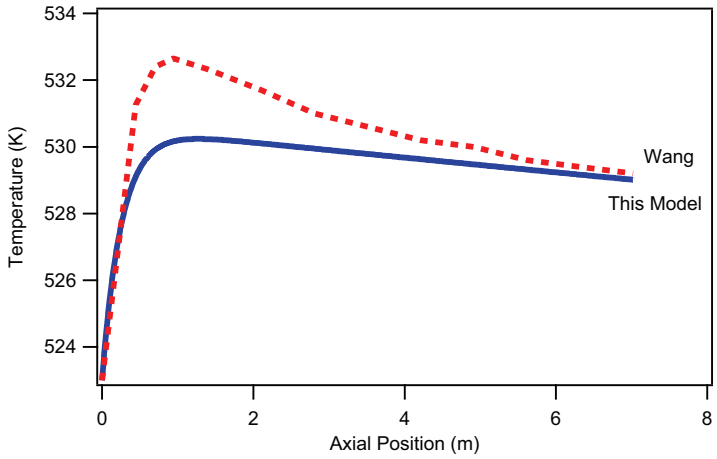

Figure 5.19: Temperature profiles predicted with this model and with the model published by Wang et al. [7].

5.8.4 Summary of Model Comparisons

Our simple model predicts results in good agreements with more sophisticated models in the literature.

CHAPTER 6. EFFECTS OF PROCESS VARIABLES ON REACTOR MODEL PREDICTIONS

6.1 Introduction

The model described in Chapter 5 is useful for predicting reactor response to changes in process variables. Reactor response is observed in a series of parametric runs for each variable in order to reveal useful trends around common operating conditions. The base cases for the parametric studies for Fe and Co catalysts are described in Section 5.2. Results of parametric studies on 1) gas recycle ratio, 2) pressure, 3) feed flow rate, 4) tube diameter, 5) cooling temperature, and 6) pellet size and shape for both Co and Fe catalysts are presented and discussed in the following sections.

6.1.1 Definition of Effective Pellet Diameter

Spheres cannot be directly compared to other shapes which are some form of cylinder because of the disparity (roughly equal to the aspect ratio) in pellet masses and surface areas of the same diameter. For a fair comparison of catalyst geometries, pellet diameter studies are based on effective pellet diameter (d_{p_e}). Effective pellet diameter is the diameter of a sphere having the same catalyst volume and mass as the actual pellet. Table 6.1 gives actual d_p values of particle shapes used in this study for given effective spherical particle diameters (d_{p_e}).

6.2 Gas Recycle Ratio

Gas recycle greatly affects FT FB thermal performance and design. Recycle ratio is defined as the ratio of moles in the recycle to outlet streams. Figures 6.1 to 6.4 show the effects of varying gas recycle ratio (RR) on the bed lengths (L_{bed}) and temperature profiles of the Co and Fe base cases. Final X_{CO} was kept constant at 60%. Figure 6.1 shows profiles for several RR for cobalt

Table 6.1: Actual d_p values of particle shapes used in this study for given effective spherical particle diameters (d_{p_e}).

d_{p_e} (mm)	d_p (mm)					
	aspect ratio = 3 (Fe)			aspect ratio = 3.5 (Co)		
sphere	cylinder	h. cyl.	trilobe	cylinder	h. cyl.[b]	trilobe
0.5	0.30	0.32	0.34	0.29	0.30	0.32
1	0.61	0.63	0.68	0.58	0.60	0.65
2	1.21	1.26	1.36	1.15	1.20	1.29
4	2.42	2.52	2.72	2.30	2.39	2.58
8	4.85	5.04	5.44	4.60	4.79	5.17
16	9.69	10.1	10.9	9.21	9.58	10.3

[a]h. cyl. inner diameter = $d_p/3$

catalysts. For $RR = 1$, the model predicts a concave upward temperature spike up to 640 K within the first 1 m indicating a runaway scenario. Large initial temperature rises were observed by Marvast et al. [36] when simulating a fixed-bed FT reactor packed with Fe-HZSM5 and indicate that the bed entrance is more susceptible to temperature runaway (i.e. within about the first two meters). When $RR \geq 2$, temperature rise is more reasonable ($\leq$ 10 K) and concave downward. The profiles reach a maximum within the first 1–2 m before decreasing slightly, exhibiting good thermal control and stability. The magnitude of the temperature rise decreases as the gas recycle ratio increases, indicating that the recycle ratio plays an important role in thermal control.

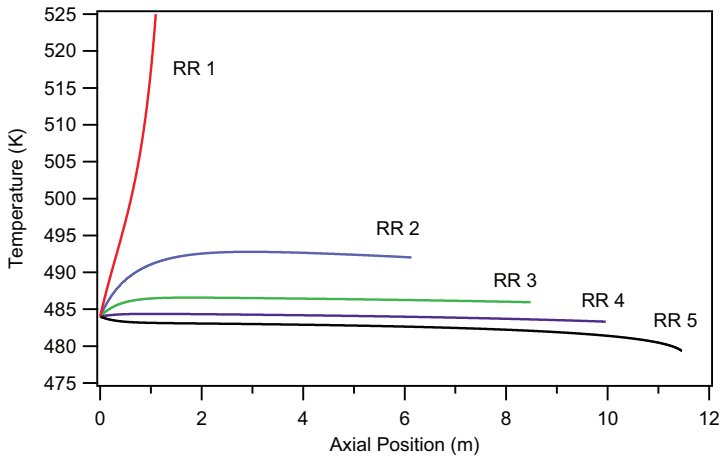

Figure 6.1: Effect of RR on axial temperature profile for the cobalt base case ($T_{wall} = 478$ K).

The predicted L_{bed} required to achieve $X_{CO} = 60\%$ shown in Figures 6.1 and 6.3 (for Co and Fe, respectively) increases significantly as *RR* increases. A large part of this variation results from lower reaction rates as average bed temperatures (T_{bed}) decrease with increasing *RR*. Constraining average bed temperature (T_{avg}) to 493 K by varying cooling temperature (T_{wall}) eliminates these thermal kinetic effects and allows for more direct comparison of bed lengths as shown in Figure 6.2. For $RR > 1$, temperature profiles increase to a maximum and then gradually decrease ($L_{bed} = 6.2 \pm 0.2$ m). For $RR = 0$–1, the T_{wall} is severe enough to reduce, but not eliminate, the runaway trend. Even after eliminating temperature effects, increasing *RR* increases bed length. Similar trends are seen for the Fe base case shown in Figures 6.3 and 6.4, except that the inherently lower kinetics for iron catalysts makes them more manageable and relatively more thermally stable (i.e. no runaway for $RR = 0$ or 1).

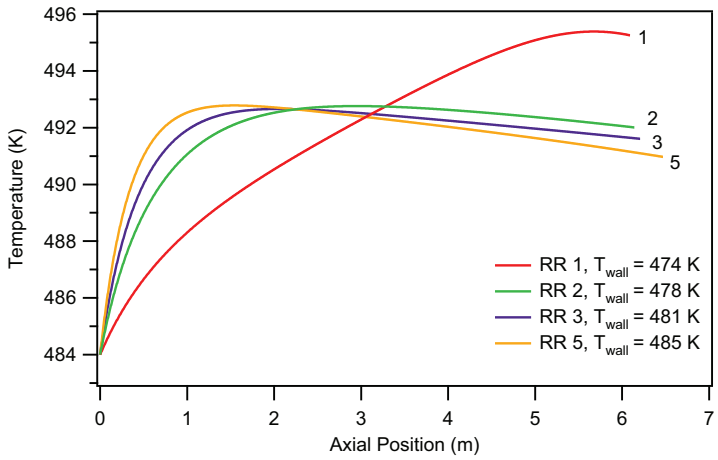

Figure 6.2: Effect of *RR* on axial temperature profile with $T_{avg} = 492$ K (varied T_{wall}) for the Co base case ($T_{wall} = 510$ K).

RR improves thermal transport by increasing flow rate, decreasing partial pressures of reactants (P_{CO} and P_{H_2}), and acting as a thermal sink. Increasing flow rate increases the rate of heat transfer by convection thereby decreasing the main heat transfer resistance in fixed beds. Decreasing P_{H_2} decreases the rate of reaction and therefore of heat generation. Nonreactive gases including product gases from the recycle stream act as a thermal sink and decrease temperature rise from the exothermic reaction. The combined effects of increased heat transfer, decreased partial pressure, and decreased bed temperature produce longer required bed lengths, but more stable operation.

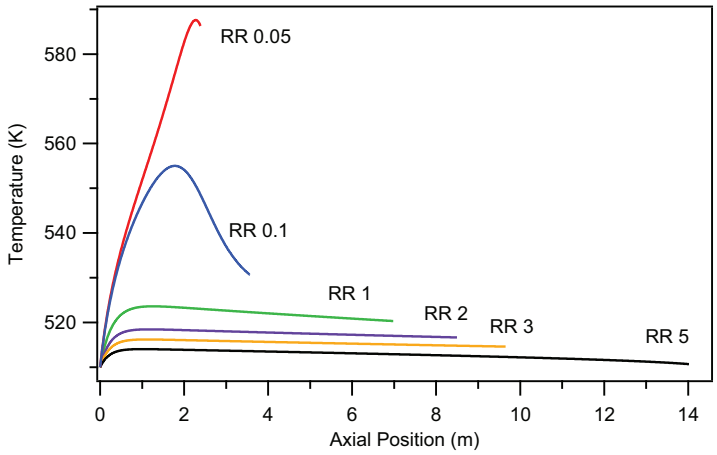

Figure 6.3: Effect of *RR* on axial temperature profile for the Fe base case.

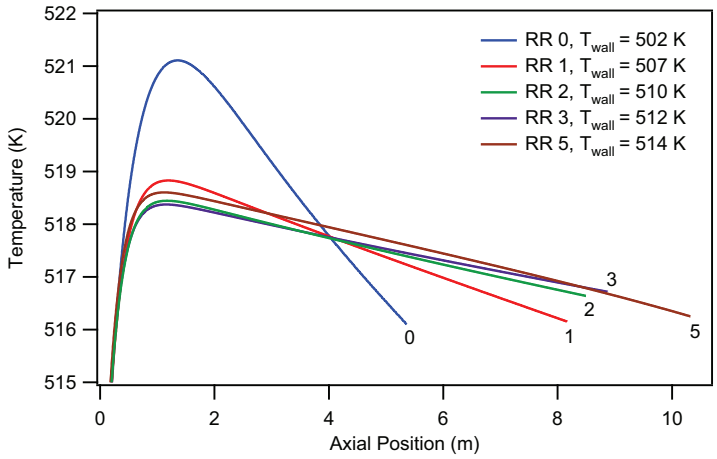

Figure 6.4: Effect of *RR* on axial temperature profile with $T_{avg} = 518$ K (varied T_{wall}) for the Fe base case.

6.3 Pressure

Inlet pressure (P_{in}) was varied from 25–50 atm for Co and 17–45 atm for Fe. The effects of varying P_{in} on temperature profiles for the Co and Fe base cases are shown in Figures 6.5 and 6.6, respectively. For cobalt, the temperature profiles except for 50 atm show good stability, increasing to a maximum (T_{max}) and then gently decreasing. At 50 atm, the profile shows runaway. For Fe, all of the profiles appear stable. For both Co and Fe, increasing P_{in} increases T_{max} and T_{avg} primarily as a result of increased P_{CO} and P_{H_2} which increase the kinetics and associated heat generation. For cobalt, increasing P_{in} from 25 to 45 atm reduces L_{bed} from 11.5 m to 5.1 m. For iron, increasing P

from 17 to 40 atm reduces L_{bed} from 16.8 m to 4.3 m. Similar trends for cobalt and iron catalysts were reported by others [7, 13].

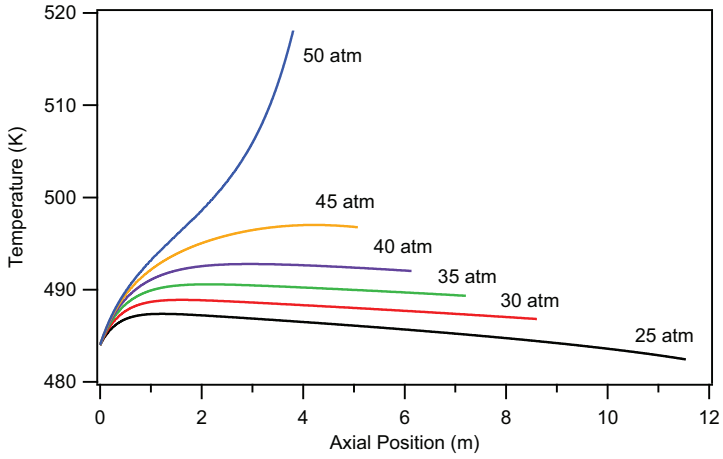

Figure 6.5: Effect of P_{in} on temperature profile for the Co base case.

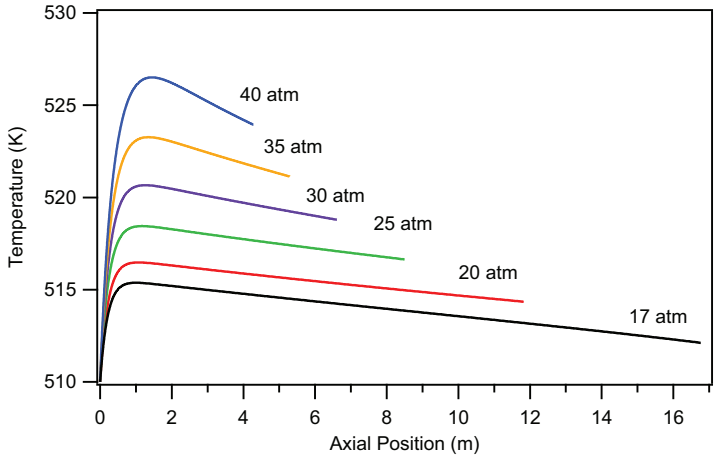

Figure 6.6: Effect of P_{in} on temperature profile for the Fe base case.

The reduction in L_{bed} and the elevated T_{bed} indicate more efficient use of catalyst as illustrated by the relationship between P_{in} and required catalyst mass (W_{cat}) in Figure 6.7. Both cobalt and iron show significantly higher W_{cat} for $P_{in} < 25$ atm, suggesting that significant savings in reactor size and cost can be realized by designing for operation at or above 25 atm.

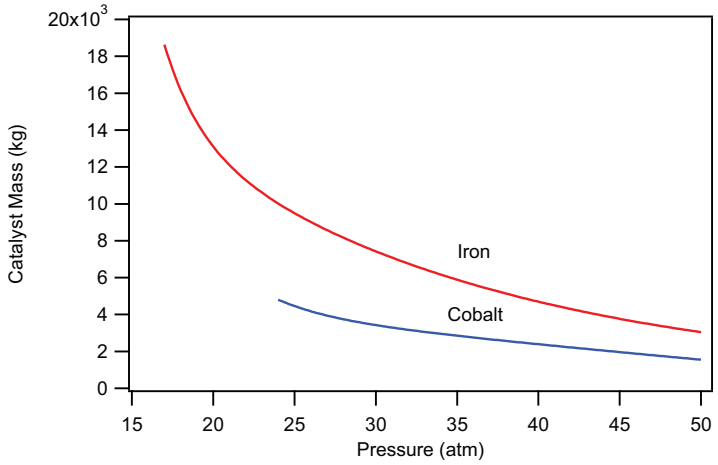

Figure 6.7: Effect of P_{in} on W_{cat} to achieve $X_{CO} = 0.60$ for the Co and Fe base cases.

In addition to the effect on W_{cat}, P_{in} also significantly affects pressure drop (ΔP) as shown in Figure 6.8. $\Delta P/L_{bed}$ decrease with increasing P_{in} as a direct result of decreasing linear velocity of the gas within the reactor with increasing P_{in} at a constant molar flow rate. $\Delta P/L_{bed}$ increases at a higher rate (curve inflection) for $P_{in} \leq 30$ atm for cobalt and ≤ 20 atm for iron, which suggest important design and operating minimums for efficient FT processes.

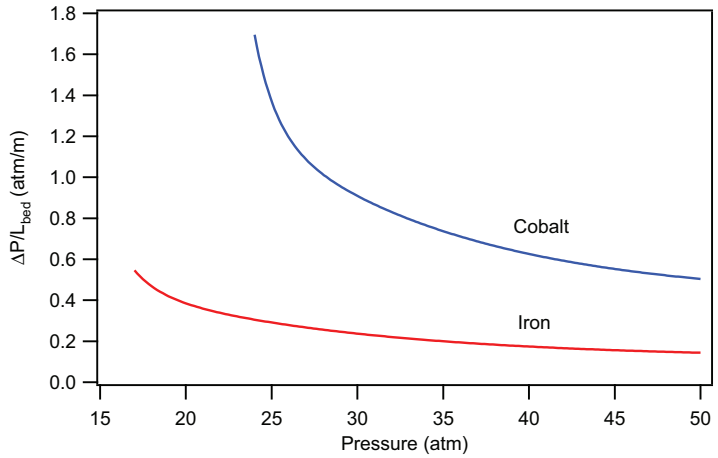

Figure 6.8: Effect of P_{in} on $\Delta P/L_{bed}$ for the Co and Fe base cases ($d_p = 1.3$ for Co and 2.0 for Fe).

In addition to the trends shown above, increasing P_{in} decreases methane selectivity and increases C_{5+} and olefin selectivities for cobalt catalysts [101]. Increased C_{5+} selectivity with increased P_{in} is also reported for iron catalysts [102]. While higher P_{in} favors selectivity to heavy

products, it also facilitates catalyst deactivation [103]. Benefits of increasing P_{in} on catalyst selectivity, kinetics, $\Delta P/L_{bed}$, and W_{cat} must be weighed against the drawbacks of decreased thermal stability and increased catalyst deactivation (e.g. shifting product slate, increased frequency of catalyst replacement, and down time).

6.4 Feed Flow Rate

Increasing reactant feed rate affects bed temperature and reactor length (for a given X_{CO}). Figures 6.9 and 6.10 show the effect of varying the flow rate of the feed on temperature profiles for the Co and Fe base cases. For both catalysts, decreasing reactant flow rate decreases L_{bed} and increases T_{bed} significantly. All profiles shown appear normal and stable with the exception of the lowest flow rate for Co ($0.9 \cdot 10^6$ SCFH). Increased T_{bed} is the result of directly decreasing heat transfer by reducing gas velocity and by reducing heat capacitance as a result of lower mass flow. Elevated temperatures accelerate the kinetics and contribute to the shorter L_{bed}; however, if T_{max} was held constant, L_{bed} would vary by the ratio of feed flow rates since X_{CO} is constant (instead of constant production rate).

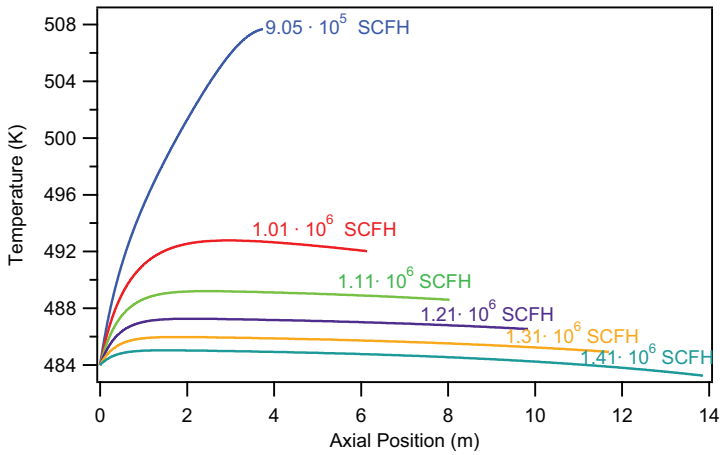

Figure 6.9: Effect of feed flow rate on temperature profile for the Co base case.

The effect of varying flow rate on $\Delta P/L_{bed}$ for Co and Fe catalysts is shown in Figure 6.11. Curves for both catalysts are concave up and $\Delta P/L_{bed}$ increases with increasing flow rate. Since n_{tubes} and d_t are constant, the linear velocity of the gas increases with increasing feed rate resulting

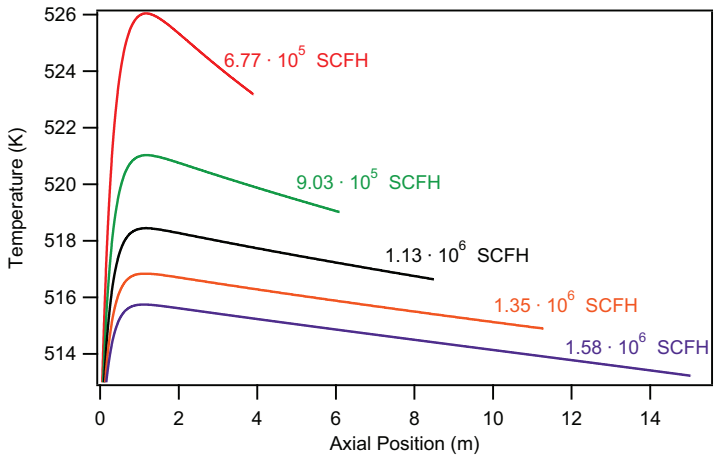

Figure 6.10: Effect of feed flow rate on temperature profile for the Fe base case.

in larger $\Delta P/L_{bed}$. Both base cases use trilobes for the pellet geometry, so the steeper ascent of the cobalt trend is attributed in part to the smaller pellet diameter (1.3 mm) of the Co base case compared to Fe (2.0 mm).

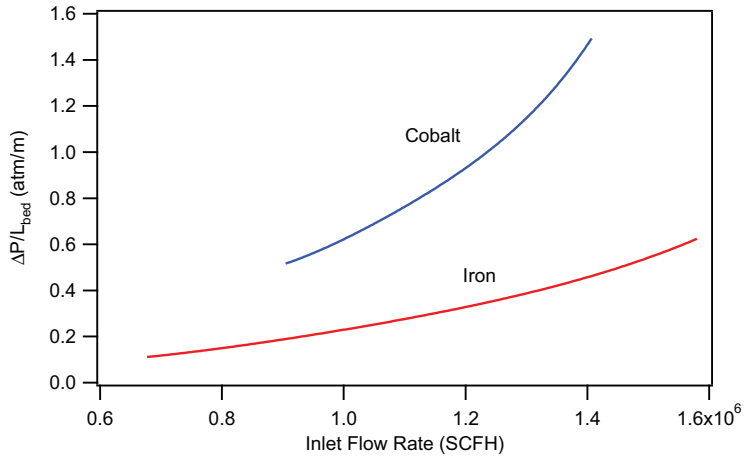

Figure 6.11: Effect of feed flow rate on $\Delta P/L_{bed}$ for the CO and Fe base cases.

The effect of changing flow rate on the overall heat transfer coefficient (U) is shown in Figure 6.12. U increases linearly with increasing gas flow rate for both Co and Fe catalysts which agrees with the reports of others that increasing flow rate increases the effective radial thermal conductivity and the wall heat transfer coefficient, and thus U [13, 104]. As demonstrated in Section 5.5 and by others [85–87], convection to the wall is the main heat transfer resistance and in

low gas-liquid interaction flow regimes, values of the heat transfer coefficient at the wall approach single phase (gas only) correlation values. Consequently, feed flow rate (along with *RR*) has a large effect on the performance of FT FB reactors.

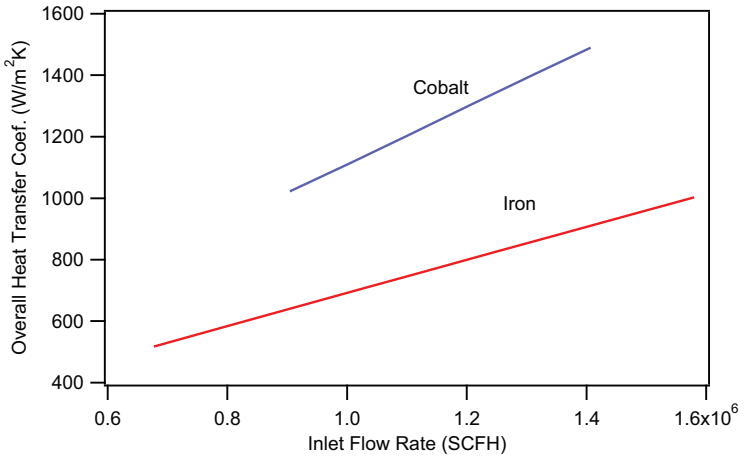

Figure 6.12: Effect of feed flow rate on U for the CO and Fe base cases.

6.5 Tube Diameter

Tube diameter (d_t) affects heat transfer and catalyst packing which can have significant effects on L_{bed}, W_{cat}, and thermal stability. In this study, the number of tubes (n_{tubes}) is varied along with the tube diameter in order to maintain a constant flow area (0.66 m^2 for Co, 1.39 m^2 for Fe) and therefore constant gas velocity. The n_{tubes} used and the d_t/d_p ratio as a function of d_t are shown in Table 6.2.

The effect of varying d_t on required W_{cat} for constant T_{wall} and for constant T_{avg} (varying T_{wall}) are shown in Figures 6.13 and 6.14, respectively. The range of reported tube diameters is limited to stable solutions from the model. The largest d_t which produce stable temperature profiles are $d_t = 25.4$ mm for Co and $d_t = 44.5$ mm for Fe. Both cobalt and iron show decreasing required W_{cat} with increasing d_t (Figure 6.13). This trend is unexpected unless one considers that a larger d_t decreases heat transfer which increases T_{max} and thereby accelerates kinetic activity, leading to lower required W_{cat}. When kinetic effects are removed by varying T_{wall} to keep T_{avg} constant, d_t has little effect on W_{cat} until $d_t/d_p < 5$ as in Figure 6.14.

Table 6.2: Tube diameters and number of tubes to maintain constant flow area (0.66 m^2 for Co, d_p = 1.3 mm and 1.39 m^2 for Fe, d_p = 1.3 mm).

	Cobalt		Iron	
d_t (mm)	d_t/d_p	n_{tubes}	d_t/d_p	n_{tubes}
6.4	4.9	20,800	3.2	44,000
12.7	9.8	5,200	6.4	11,000
19.1	14.7	2,311	9.6	4,888
25.4[a]	**19.5**	**1,300**	**12.7**	**2,750**
31.8	24.5	832	15.9	1,760
38.1	29.3	577	19.1	1,222
44.5	34.2	424	22.3	897

[a]base case

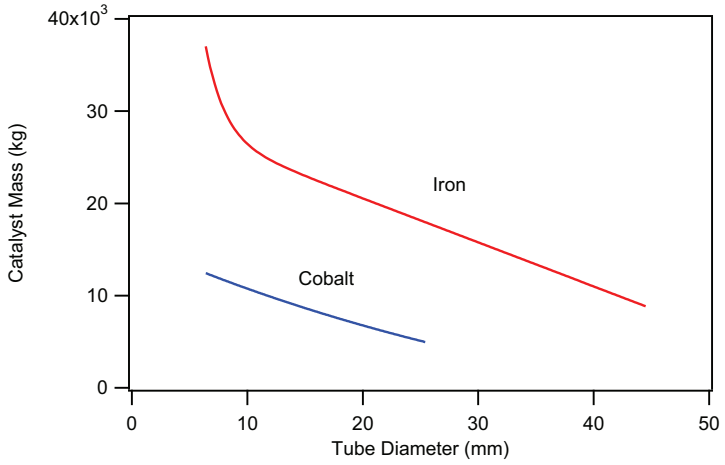

Figure 6.13: Effect of d_t on required W_{cat} to achieve $X_{CO} = 0.60$ for Co and Fe base cases. T_{avg} was allowed to vary. Total flow area was kept constant by changing n_{tubes} (Table 6.2).

The value of d_t/d_p in the trend above is important because tube walls affect local catalyst packing, particularly for pellet geometries other than spheres; however, these effects are small if tube diameter is much larger than pellet diameter. A general correlation for bed void fraction (Equation 5.10) as a function of tube and effective pellet diameters accounts for these effects with a valid range of $1.5 < dt/d_{p_e} < 50$ [76].

The effect of the d_t on U for constant T_{avg} (varying T_{wall}) is shown in Figure 6.15. Reducing the tube diameter reduces heat transfer resistance and increases U, making temperature control of

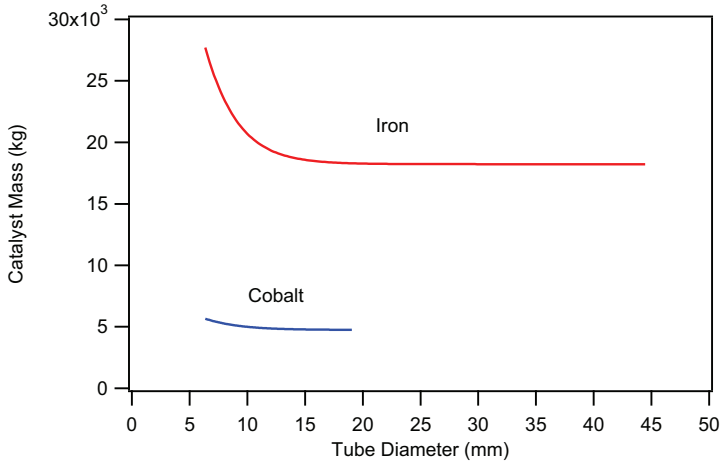

Figure 6.14: Effect of d_t on required W_{cat} to achieve $X_{CO} = 0.60$ for Co and Fe base cases. T_{avg} was kept constant by varying T_{wall}. Total flow area was kept constant by changing n_{tubes} (Table 6.2).

the reactor easier. A similar trend was reported by others [7, 36]. For $d_t < 15$ mm, U increases much faster as d_t decreases which gives support to the concept of microchannel reactors. With very small tubes, heat transfer in the reactor is very high allowing the reactor to be operated isothermally at the highest optimal temperature with little risk of runaway.

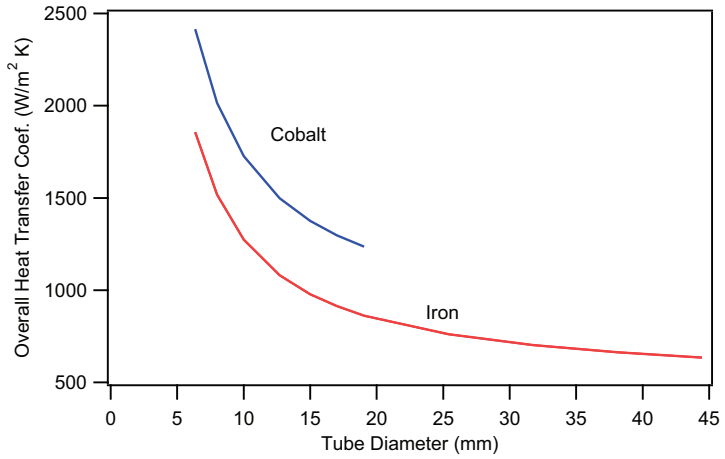

Figure 6.15: Effect of d_t on U for Co and Fe base cases. Total flow area was kept constant by changing n_{tubes} as in Table 6.2 and T_{avg} was kept constant (492 K Co, 518 K Fe) by varying T_{wall}.

FTS FBRs ideally operate at the highest possible temperature (for fastest kinetics) that is thermally stable and provides the correct product slate without deactivating the catalyst. The 2-D model by Marvast et al. [36] predicts a temperature difference at the position of T_{max} of about 20 K

between the wall and the center of the tube for a 19.1 mm tube with an iron catalyst and feed temperature of 565 K. This large temperature gradient which is highly dependent on d_t limits the operating temperature of the reactor and by extension the efficient use of the catalyst as most of the catalyst will see temperatures below the optimum while catalyst in the hot center will see hotter temperatures and as a result give a lighter product slate [104]. Even though a smaller number of tubes with a larger diameter may seem attractive from a manufacturing and investment point of view, using smaller tubes reduces the radial temperature gradient, gives better thermal control, and allows the reactor to be operated at higher, more efficient temperatures without sacrificing selectivity.

6.6 Cooling Temperature

Cooling temperature (T_{wall}) has a large and direct effect on model predictions through heat removal which, along with heat generation, determines bed temperature (T_{bed}). Temperature affects several parameters of the reactor model including reaction kinetics, the gas velocity, fluid viscosity, fluid density, and diffusivity of reactant gases. The calculated effect of T_{wall} on the axial temperature profile for the cobalt base case is shown in Figure 6.16. As T_{wall} increases, T_{bed} increases and reaction kinetics increase, generating more heat which affects ΔT, making heat transfer more difficult. For $T_{wall} > 480$ K, the temperature profiles are unstable and the value of T_{max} is too large. For the remaining profiles, after the first 2–3 m the T_{bed} decreases slightly. Trends for the iron catalyst are similar to the stable cobalt profiles as shown in Figure 6.17 except that T_{max} occurs within the first 1.5 m of the reactor after which the profiles gradually decrease 1–2 K. A 2 K increase in T_{wall} results in 30% shorter L_{bed} for Co and 15% shorter L_{bed} for Fe to achieve $X_{CO} = 60\%$. Shorter L_{bed} correspond with lower W_{cat} and lower ΔP; however, as mentioned previously, higher T_{bed} can result in an undesired shift to a lighter product slate and unstable reactor conditions [7, 36].

The comparison of Co and Fe is very interesting and shows Fe is less sensitive to T_{wall} than Co. This is true at least for the temperature range and the kinetic model chosen for this study.

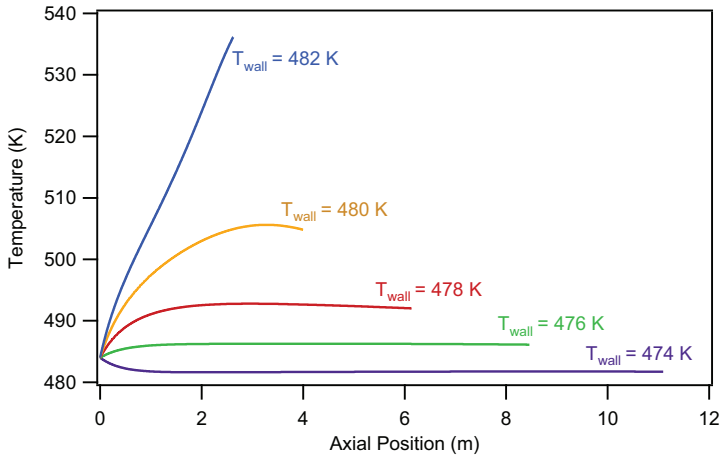

Figure 6.16: Effect of T_{wall} on temperature profile for the Co base case.

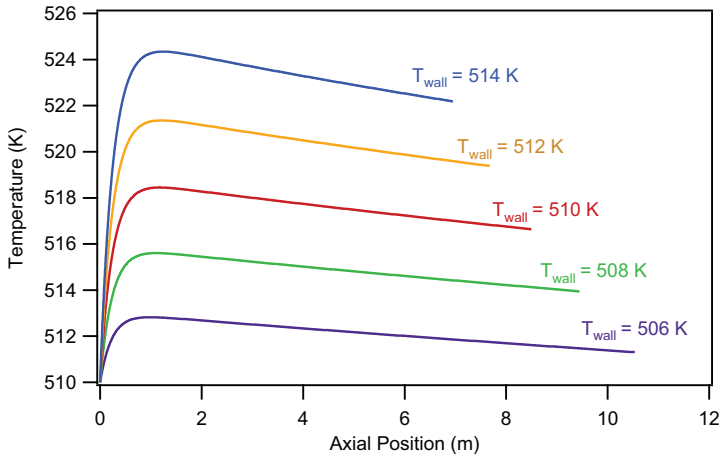

Figure 6.17: Effect of T_{wall} on axial temperature profile for the Fe base case.

6.7 Pellet Size and Shape

The ideal packed bed maximizes heat and mass diffusion and minimizes ΔP without compromising catalyst mechanical strength. Catalysts with low strength may be crushed and create fines in tall packed beds. Catalyst particle size and shape are important controllable variables in attempting to manage and optimize these factors. Unfortunately, these ideals are often in conflict as decreasing d_p for maximum transport decreases pellet strength and increases ΔP by decreasing ε_b which increases friction to fluid flow. The objective then is to find pellet geometries and sizes that optimize diffusion resistance and ε_b to give the lowest ΔP and highest reaction rate (for shortest L_{bed} and lowest W_{cat}).

Physical Properties of Advanced Catalyst Geometries

This section considers and compares four pellet shapes including spheres (S), cylinders (C), hollow cylinders (hC), and trilobes (Tr). Advanced pellet geometries (i.e. trilobes) offer a compromise between effective diffusion length (L_{p_e}) and d_p. For example, a 2 mm trilobe has half the L_{p_e} of a cylinder of the same diameter (0.25 mm compared to 0.5 mm) and larger ε_b (0.48 compared with 0.43). Non-spherical geometries assume aspect ratios of 3 for Fe catalysts and 3.5 for Co catalysts. Table 5.1 gives the properties for 2 mm pellets of the fours shapes with aspect ratios of 3.

Pellet shape and effective diameter (d_{p_e}) were varied in the following studies to explore their effects on model predictions. In some cases, T_{wall} was varied to maintain a constant T_{avg} of 490 K for Co and 510 K for Fe as noted. The results of the simulations are reported in Figures 6.18 to 6.28.

Overall Effect on Catalyst Mass

Figures 6.18 and 6.19 show the overall effect of increasing d_{p_e} on W_{cat} for Co and Fe catalysts, respectively. As d_{p_e} increases, the W_{cat} required to maintain the same X_{CO} and production rate of C_{5+} products increases. For a given d_{p_e}, the order of decreasing required W_{cat} with catalyst shape is spheres>cylinders>hollow cylinders>trilobes.

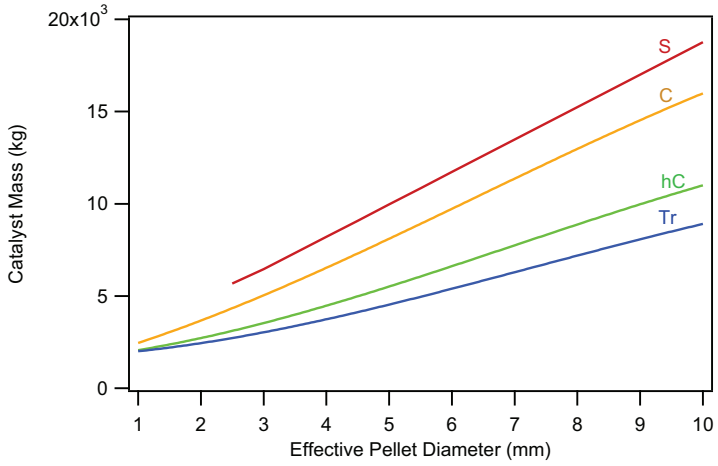

Figure 6.18: Effect of d_{p_e} and pellet shape on W_{cat} to achieve $X_{CO} = 0.60$ for the Co base case. T_{wall} varied to keep $T_{avg} = 492$ K.

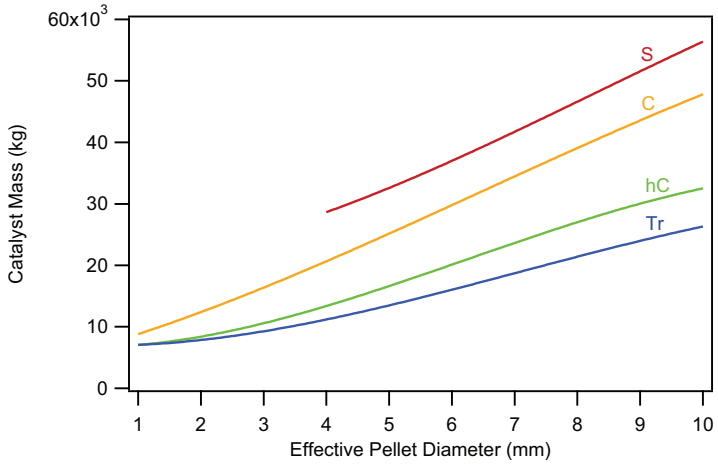

Figure 6.19: Effect of d_{p_e} and pellet shape on W_{cat} to achieve $X_{CO} = 0.60$ for the Fe base case. T_{wall} varied to keep $T_{avg} = 518$ K.

These overall effects are the results of combining the effects of several other variables that are affected by d_{p_e}. The following discussion considers the individual contributions of ε_b, $\Delta P/L_{bed}$, η, and U to the overall effect of pellet shape and size on required W_{cat}.

Bed Void Fraction Effects

Bed void fraction affects L_{bed} and $\Delta P/L_{bed}$. Before discussing the effect of d_{p_e} and shape on other variables, it is prudent to study the effect on ε_b. Figure 6.20 shows the effect of varying d_{p_e} and shape on ε_b for the iron base case. As d_{p_e} increases, ε_b increases. The order of increasing ε_b is spheres $<$ cylinders $<$ trilobes $<$ hollow cylinders. The increase in ε_b is due in part to pellet-wall interactions which become significant for $d_t/d_{p_e} < 15$ mm.

For a given W_{cat}, the bed length varies with ρ_b which is related to ε_b and pellet density ρ_p by Equation 5.11. Since pellet density is constant for this study, L_{bed} is directly affected by ε_b. Figures 6.21 and 6.22 show bed length (L_{bed}) as a function of d_{p_e} for Co and Fe, respectively. Bed length to achieve $X_{CO} = 0.60$ increases with increasing d_{p_e}. These figures are similar to Figures 6.18 and 6.19 except that Figures 6.21 and 6.22 show more curvature due to the influence of ε_b on ρ_b. They show a greater difference between trilobes and hollow cylinders and a lesser difference between spheres and cylinders due to the void fraction effect.

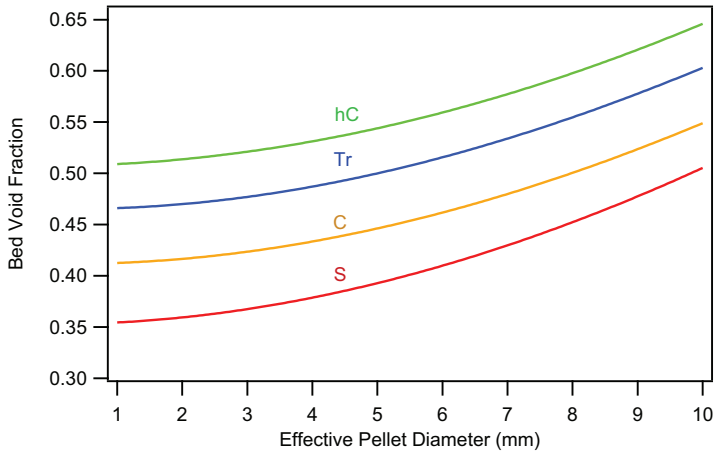

Figure 6.20: Effect of d_{p_e} and shape on ε_b for the Fe base case.

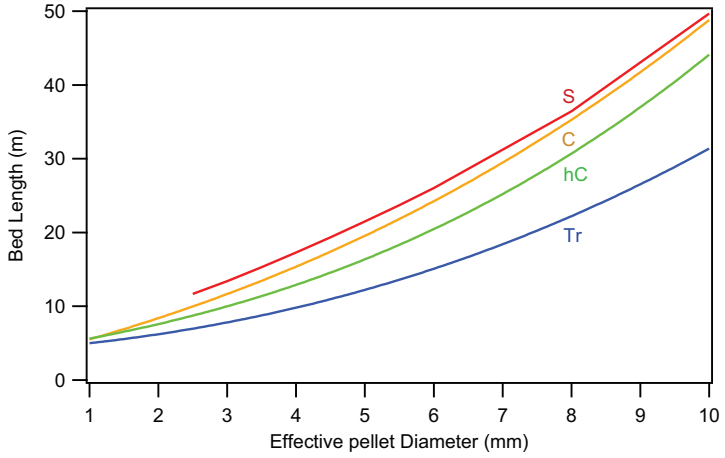

Figure 6.21: Effect of d_{p_e} and shape on L_{bed} to achieve $X_{CO} = 0.60$ for the Co base case. T_{wall} varied to keep $T_{avg} = 492$ K.

Pellet diameter and bed void fraction have significant effects on pressure drop as shown in Figures 6.23 and 6.24. $\Delta P/L_{bed}$ is strongly influenced by ε_b and hence d_{p_e} and shape. For $d_{p_e} < 2$ mm, $\Delta P/L_{bed}$ increases significantly as d_{p_e} decreases. For a given d_{p_e}, the order of shapes in decreasing $\Delta P/L_{bed}$ is spheres $>$ cylinders $>$ trilobes $>$ hollow cylinders.It is interesting to note that hollow cylinders give the smallest ΔP even though trilobes give lower W_{cat} and L_{p_e}. As the d_{p_e} increases, $\Delta P/L_{bed}$ for all pellet shapes approaches a minimum due to wall-pellet interactions and large void spaces.

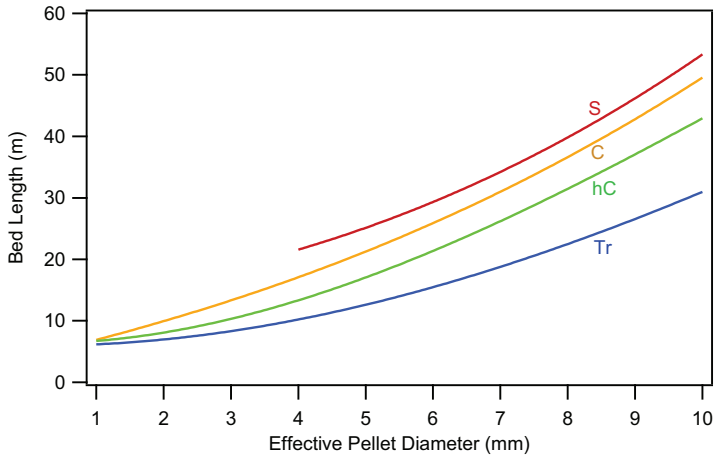

Figure 6.22: Effect of d_{p_e} and shape on L_{bed} to achieve $X_{CO} = 0.60$ for the Fe base case. T_{wall} varied to keep $T_{avg} = 518$ K.

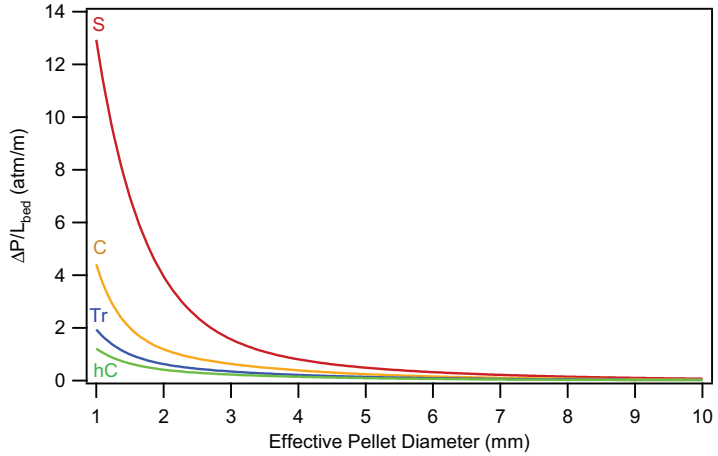

Figure 6.23: Effect of d_{p_e} and shape on $\Delta P/L_{bed}$ for the Co base case. T_{wall} varied to keep $T_{avg} = 492$ K.

Observed Reaction Rate Effects

Pellet size and shape affect the observed reaction rate through the effective diffusion length via ϕ and η according to the relationships in Equations 5.23 and 5.24. η accounts for diffusion resistance within the pellet and is defined as the ratio of the observed to the intrinsic rates of reaction. Figures 6.25 and 6.26 show the effects of d_{p_e} and shape on η. Effectiveness factor increases as d_{p_e} decreases. The increase is more significant for $d_{p_e} < 4$ mm which is the range of practical interest. The order of increasing η with shape is spheres $<$ cylinders $<$ hollow cylinders

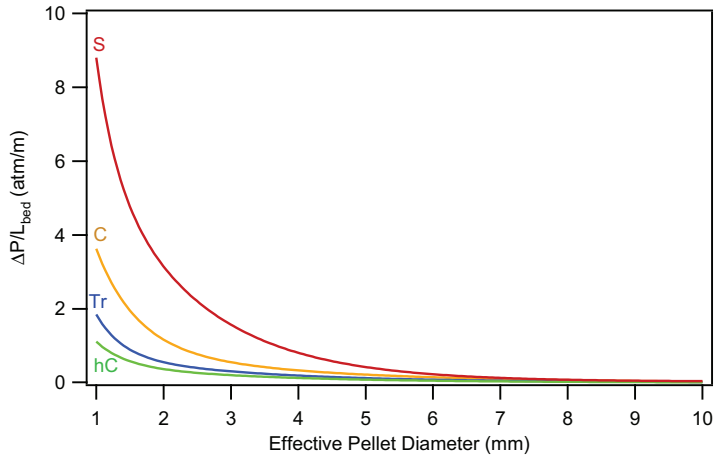

Figure 6.24: Effect of d_{p_e} and shape on $\Delta P/L_{bed}$ for the Fe base case. T_{wall} varied to keep $T_{avg} =$ 518 K.

$<$ trilobes. The order of performance of the shapes follows the order of decreasing L_{p_e} for pellets of the same volume. L_{p_e} is the ratio of pellet volume to surface area and is an indication of the relative resistance to diffusion. As L_{p_e} increases, diffusion resistance increases, η decreases, and the observed reaction rate decreases. A lower observed rate of reaction for larger d_{p_e} leads to larger required W_{cat} and longer bed length (L_{bed}).

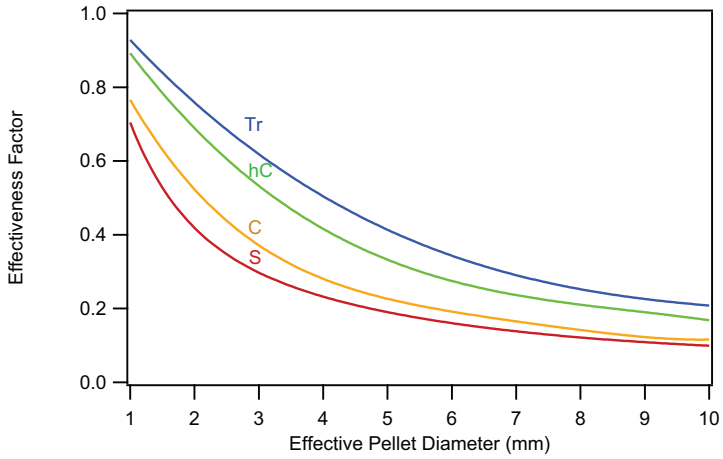

Figure 6.25: Effect of d_{p_e} and shape on η for the cobalt base case. $T_{avg} = 492$ K (vary T_{wall}).

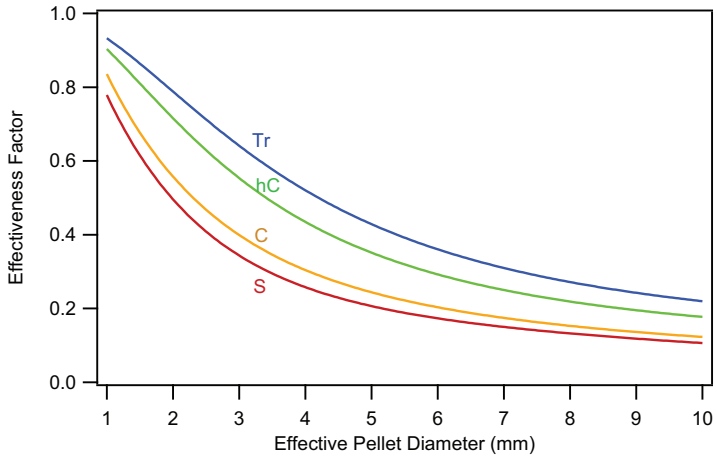

Figure 6.26: Effect of d_{p_e} and shape on η for the iron base case. $T_{avg} = 518$ K (vary T_{wall}).

Overall Heat Transfer Effects

Effective pellet diameter affects the overall heat transfer according to Equations 5.29, 5.33, 5.36 and 5.37. Figures 6.27 and 6.28 show the effect of varying d_{p_e} on U for Co and Fe catalysts, respectively. U increases with increasing d_{p_e}. As shown in Section 5.5 and by others [85, 86], the main heat transfer resistance in a packed bed is at the wall. In fact, heat transfer coefficients in trickle flow FBRs (two fluid phases) approach values of single phase correlations, indicating that gas-wall interactions and gas-bed mixing in the reactor are the most important heat transfer considerations. Increasing d_{P_e} increases ε_b as shown above which promotes more mixing of the gases with the bed and with the wall because of larger voids and thereby increases U.

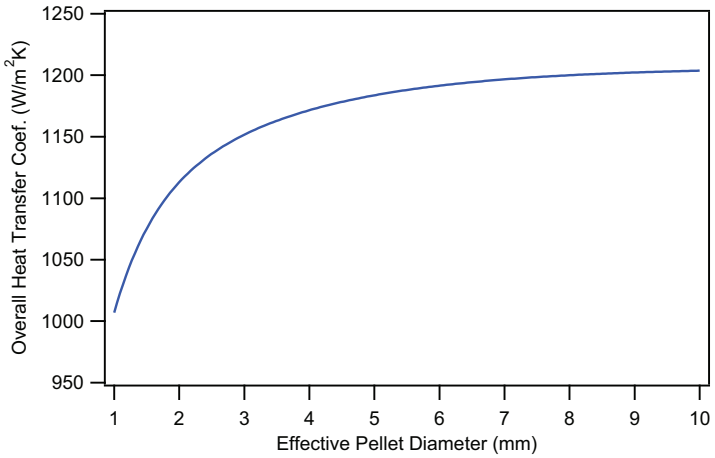

Figure 6.27: Effect of pellet diameter and shape on U with $T_{avg} = 492$ K (vary T_{wall}) for the cobalt base case.

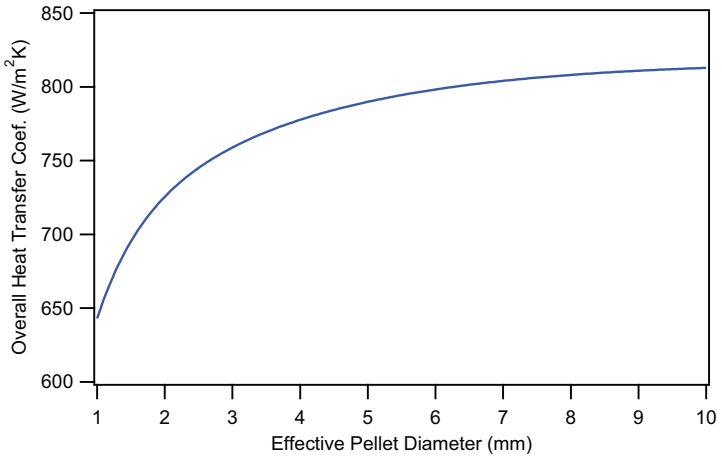

Figure 6.28: Effect of pellet diameter and shape on U with $T_{avg} = 518$ K (vary T_{wall}) for the iron base case.

CHAPTER 7. COMBINED PACKED-BED FRICTION FACTOR CORRELATION

Luke D. Harrison performed this research under the direction of the author and his advisor.

7.1 Published Correlations

Pressure drop in a packed bed is typically estimated by using Equation 7.1 with an appropriate correlation for the friction factor (f_k).

$$\frac{\Delta P}{L_{bed}} = \frac{\rho_l u^2 (1-\varepsilon_b)}{d_{p_e} \varepsilon_b^3} f_k \tag{7.1}$$

Many friction factor correlations have been proposed for packed bed pressure drop estimation. The most universally used is the Ergun equation, Equation 7.2 [39].

$$f_k = \frac{150(1-\varepsilon_b)}{Re} + 1.75 \tag{7.2}$$

Over the years, modifications to this correlation have attempted to correct for deviations between predicted values and experimental data observed under some specific conditions. These include high Re and low tube diameter to particle diameter ratios (d_t/d_p). Tallmadge (Tal) in 1970 showed that the applicable range of $Re/(1-\varepsilon_b)$ for the Ergun equation was from 0.1–500. He extended this range to 0.1–100,000 by modifying the turbulent term of the Ergun equation (1.75) to be a function of Re, resulting in his correlation, Equation 7.3 [40].

$$f_k = \frac{150(1-\varepsilon_b)}{Re} + \frac{4.2}{\left(\frac{Re}{1-\varepsilon_b}\right)^{1/6}} \tag{7.3}$$

Other improvements have been made to address packed-beds with $d_t/d_p < 10$, where wall-particle interactions have significant effect on pressure drop. In this paper we have considered three of these correlations, including one from Mehta and Hawley [41] (MH) and two from Liu

et al. [42]. The two from Liu et al. include the same wall effect terms. One correlation used the same constants and form as the Ergun equation and will be termed the Liu modified Ergun (LME) correlation, Equation 7.4.

$$f_k = \frac{150(1-\varepsilon_b)}{Re}\left(1+\frac{\pi d_{p_e}}{6d_t(1-\varepsilon_b)}\right)^2 + 1.75\left(1-\frac{\pi^2 d_{p_e}}{24d_t}\left(1-0.5\frac{d_{p_e}}{d_t}\right)\right) \tag{7.4}$$

The second correlation uses an original form and will be termed the Liu correlation. It is noteworthy that these three correlations only attempted to fit data in the laminar flow regime.

7.2 Combined Correlation

These different modifications give the possibility of two different combinations of the high *Re* modification with a wall-effect modification: Tal with the MH wall-effect terms (TMH) and Tal with the LME wall-effect terms (TL). The preferred combined correlation is TL which includes the high *Re* modification from Tal, Equation 7.3, with the low d_t/d_p modification of LME, Equation 7.4, into a single correlation, Equation 7.5, valid over a wide range of *Re* and d_t/d_p ratios.

$$f_k = \frac{K_{Lam}(1-\varepsilon_b)}{Re}\left(1+\frac{\pi d_{p_e}}{6d_t(1-\varepsilon_b)}\right)^2 + \frac{K_{Turb}}{\left(\frac{Re}{1-\varepsilon_b}\right)^{1/6}}\left(1-\frac{\pi^2 d_{p_e}}{24d_t}\left(1-0.5\frac{d_{p_e}}{d_t}\right)\right) \tag{7.5}$$

The TMH correlation is not given and will not be discussed further in this paper but data for this correlation are included in Table 2 for comparison. In Equation 7.5, the term in red shows the modification from the Tal correlation and the terms in blue are those added from the LME correlation.

The values of the two constants, K_{Turb} and K_{Lam}, in the TL correlation, Equation 7.5, were obtained by fitting them to published $\Delta P/L_{bed}$ data and minimizing the overall average relative absolute error (ARAE), Equation 7.6.

$$ARAE = \frac{1}{n}\sum_{i=1}^{n}\frac{|\,x_i'-x_i\,|}{x_i} \tag{7.6}$$

The values of the fitted constants ($K_{Lam} = 119.8$ and $K_{Turb} = 4.63$) differed slightly from those given by Ergun ($K_{Lam} = 150$ and $K_{Turb} = 1.75$) with the K_{Turb} value matching closely the value

used in the Tallmadge correlation ($K_{Turb} = 4.2$). This paper compares the performance of this equation to the performances of the other published equations in predicting a large set of pressure drop data from several published sources.

7.3 Published Data Sets

Pressure drop data, totaling 476 individual data points, were gathered from four different pressure drop studies: Burke and Plummer [105], Ergun and Orning [106], Oman and Watson [107], and Wentz and Thodos [108]. As the data were analyzed, it was found that the Oman and Watson data were consistently higher than predicted by any model. Variations about the other data sets, on the other hand, showed no trends (random variation). This suggested systematic variations with the Oman and Watson data rather than random data variations. Therefore, in this study the Oman and Watson data have been omitted leaving 324 data points.

The three data sets we considered included a wide range of Re, bed porosities (ε_b), and d_t/d_p ratios as shown in Table 7.1. Flow regimes covered by the data include: laminar to turbulent flow including the transition region, large wall effects ($d_t/d_p < 10$), and high porosity. The variety of flow regimes represented by the data allowed us to compare the combined correlation against the published correlations in their applicable ranges.

Table 7.1: Ranges of ε_b, d_t/d_p, and Re for experimental pressure drop data sets.

Parameter	Ergun and Orning	Burke and Plummer	Wentz and Thodos
points	52	175	97
ε_b	0.33–0.35	0.36–0.42	0.35–0.88
d_t/d_p	45–50	8.3–35	11
Re	0.32–29	1.4–970	1,500–7,700

7.4 Discussion

The data analysis for this study is presented in Figures 7.1 to 7.6 and Table 7.2. Figure 7.1 (TL, Ergun, Tal), Figure 7.2 (TL, MH, and Liu), and Figure 7.3 (TL, LME, and TMH) show plots

of f_k versus Re and compare the experimental data in the ranges shown in Table 7.1 to the predicted values from all of the correlations in this study. Figure 7.4 (TL, Ergun, Tal), Figure 7.5 (TL, MH, and Liu), and Figure 7.6 (TL, LME, and TMH) show plots of $\Delta P/L_{bed}$ versus Re and compare the experimental data to the predicted values from all of the correlations in this study. Plots were split up to avoid, as best possible, obscuring similar data points. The TL correlation fits the data well over the whole range of Re. The next best fit is the Tal correlation which is confirmed by the ARAE in Table 7.2. The only deviation of the Tal correlation is for low Re where it predicts slightly higher pressure drops than the experimental data. The biggest deviations on the graphs are with both the MH and LME correlations in the high Re region. This agrees well with the data in Table 7.2 where both correlations increased in ARAE as Re increased.

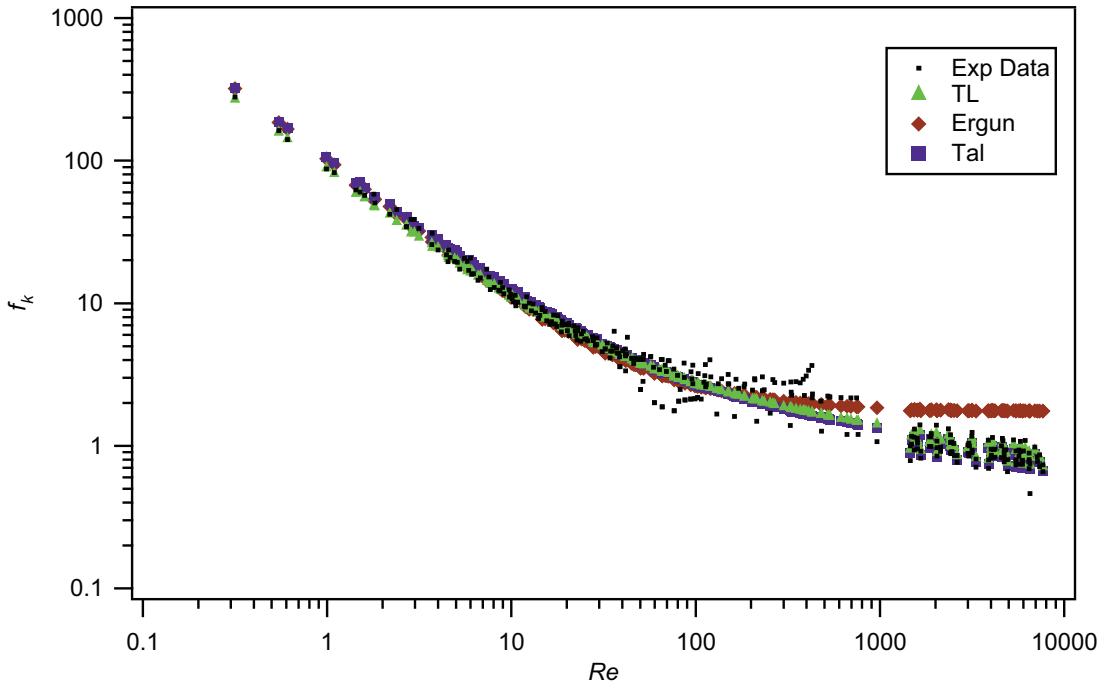

Figure 7.1: Friction factor as a function of Re for two published correlations (Ergun and Tal) and the preferred combined correlation (TL) compared to the 324 experimental data points from the literature. Tal is closely associated with TL.

Table 7.2 reports the ARAE of the five published correlations and the two combined correlations for three ranges of Re and three ranges of d_t/d_p. It also includes an overall ARAE over the full data set (324 points) for each correlation. The TL correlation yielded the lowest ARAE

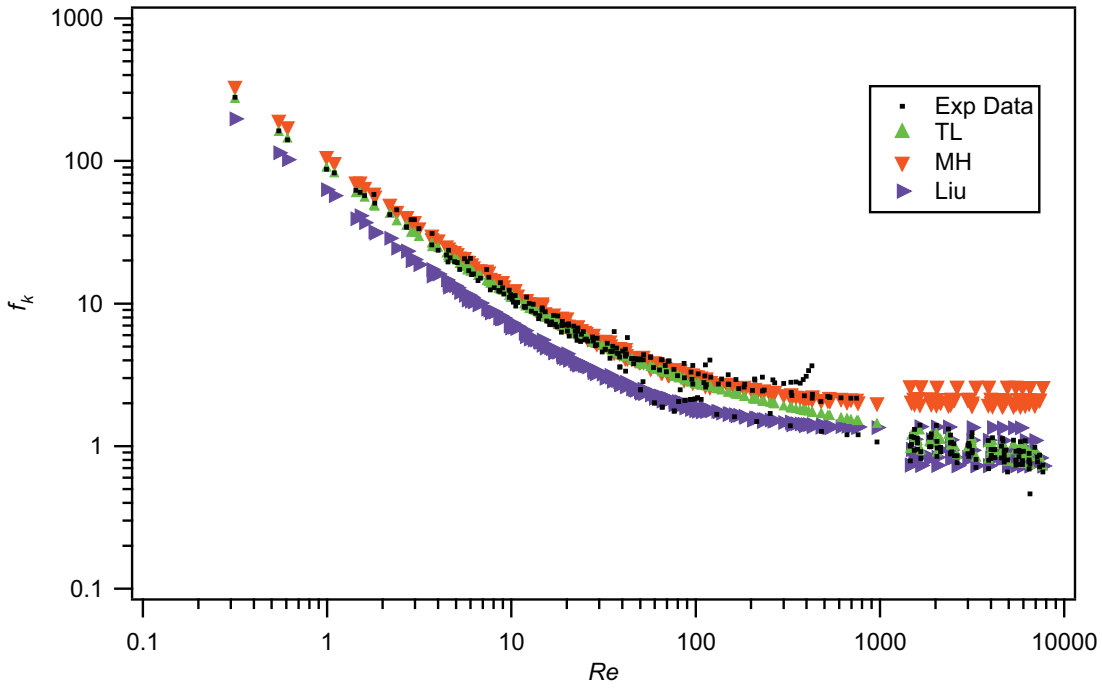

Figure 7.2: Friction factor as a function of *Re* for two published correlations (MH and Liu), and the preferred combined correlation (TL) compared to the 324 experimental data points from the literature.

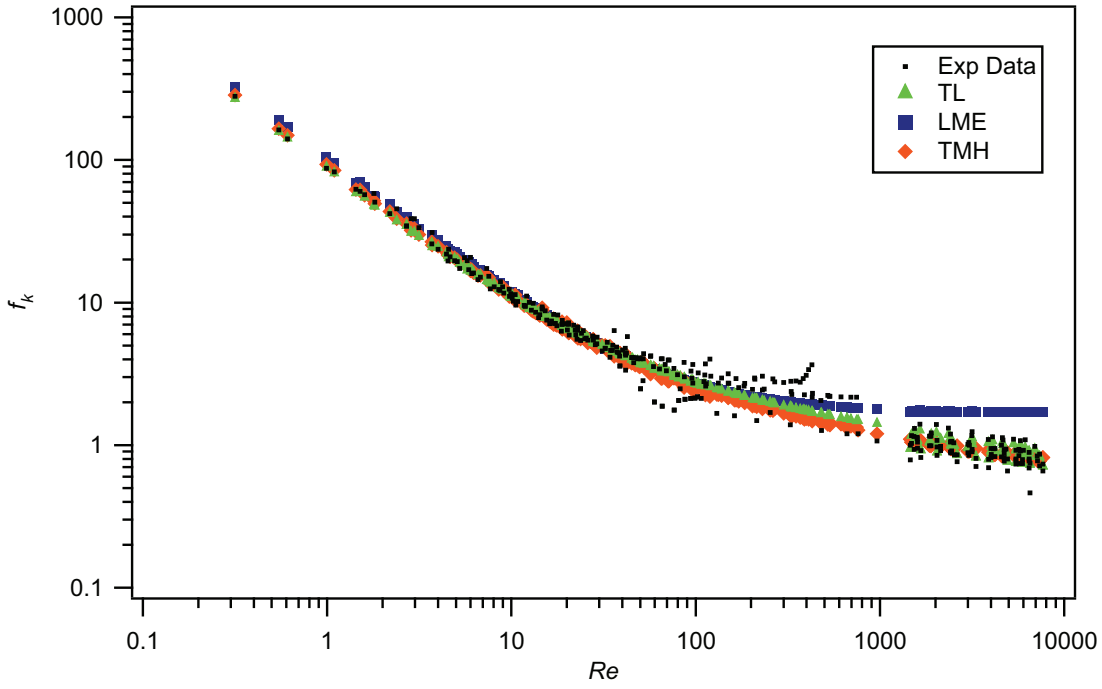

Figure 7.3: Friction factor as a function of *Re* for one published correlation LME, the alternate combined correlation (TMH), and the preferred combined correlation (TL) compared to the 324 experimental data points from the literature.

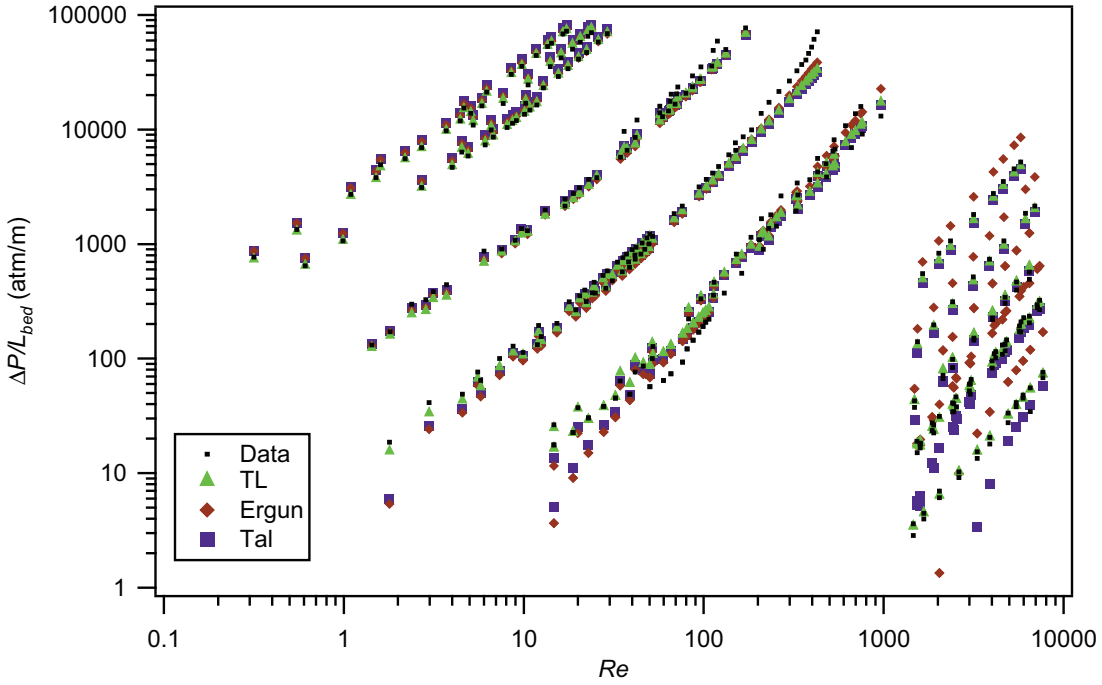

Figure 7.4: $\Delta P/L_{bed}$ as a function of Re for two published correlations (Ergun and Tal) and the preferred combined correlation (TL) compared to the 324 experimental data points from the literature.

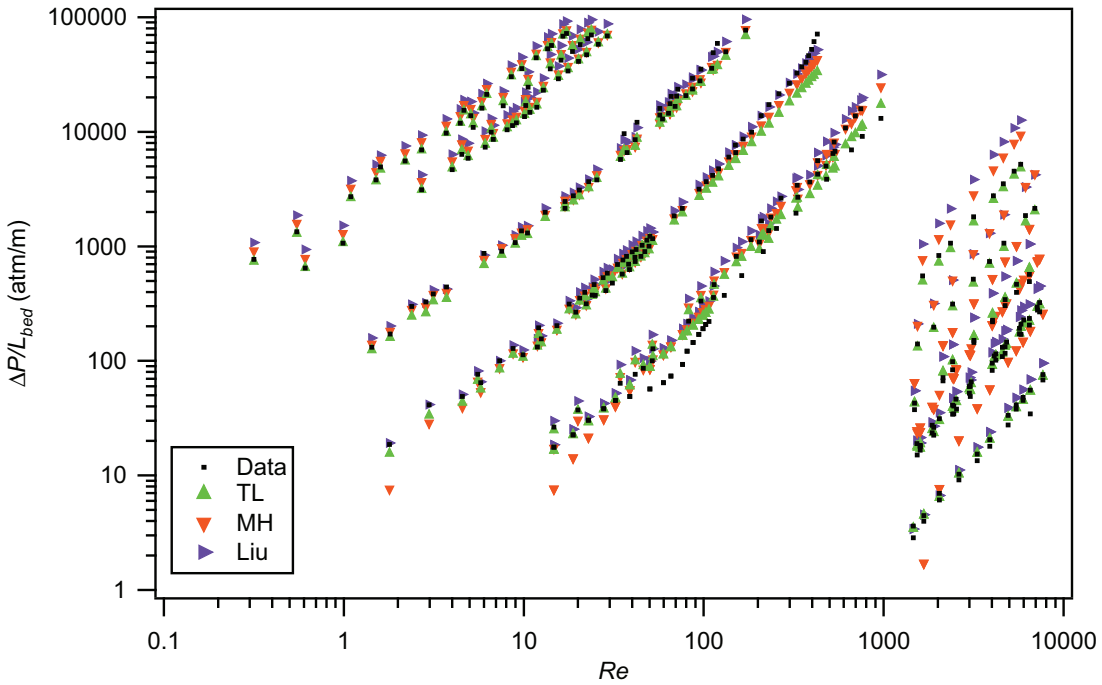

Figure 7.5: $\Delta P/L_{bed}$ as a function of Re for two published correlations (MH and Liu) and the preferred combined correlation (TL) compared to the 324 experimental data points from the literature.

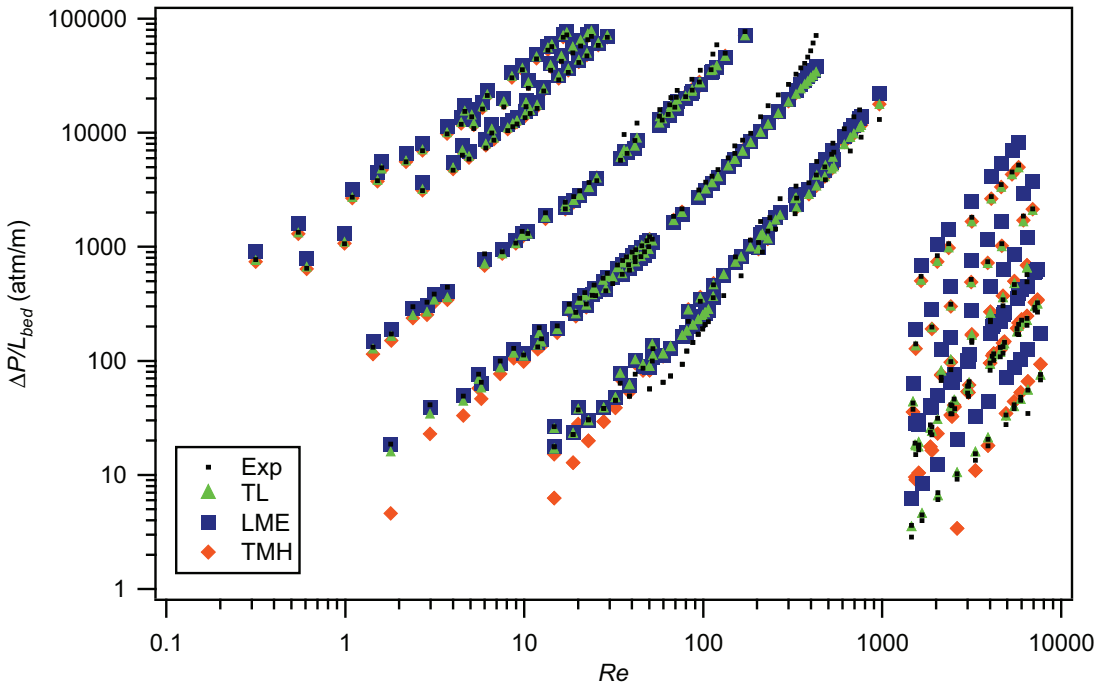

Figure 7.6: $\Delta P/L_{bed}$ as a function of *Re* for one published correlation (LME), the alternate combined correlation (TMH), and the preferred combined correlation (TL) compared to the 324 experimental data points from the literature.

in all regions except for $d_t/d_p < 10$. The best predictor for this region was the LME correlation with an ARAE of 25.8%. At 27.8%, the ARAE of the TL correlation was very close to the LME correlation. It should be noted that the range of ARAE for this region for all the correlations were between 25.8% and42.1% with none of them standing out as great predictors for this region. As the d_t/d_p ratio increased, the TL correlation was by far the better predictor of the pressure drop than the other correlations. For example, the region on the fringe of significant wall-particle interactions, $10 < d_t/d_p < 12.3$, showed great disparity between the TL correlation which had an ARAE of 12.6% and the MH and LME correlations which had ARAE of 78.3% and 60.3%, respectively. It should be noted that this subset of 162 data points included all of the Wentz and Thodos data (97 data points) which were all at high *Re* that laminar-regime correlations (MH and LME) would not have been expected to predict well.

The TL correlation had the lowest ARAE of all the correlations considered for each of the three *Re* regions. As expected, the errors for the correlations developed specifically for low *Re*, i.e. Ergun, MH, Liu, and LME correlations, increased as the *Re* increased. The opposite trend was

Table 7.2: Percent average relative absolute error (ARAE) between $\Delta P/L_{bed}$ data and the five previously reported correlations and the two combined correlations.

							Combined	
Flow Regime	points	Ergun	Tal[a]	MH[b]	Liu[c]	LME[d]	TMH[e]	TL[f]
$Re < 2300$	252	22.7	26.7	22.5	27.4	21.4	22.8	14.7
$2300 < Re > 4000$	26	57.1	35.3	108	40.8	82.6	14.0	8.5
$Re > 4000$	46	101	15.7	157	56.3	103.6	14.3	9.1
$d_t/d_p < 10$	50	28.3	30.8	32.8	42.1	25.8	34.3	27.8
$10 < d_t/d_p < 12.3$	162	55.0	32.6	78.3	38.2	60.3	24.4	12.6
$d_t/d_p > 12.3$	112	13.5	13.8	12.2	20.3	11.1	9.8	8.1
Overall	324	36.5	25.8	48.4	32.6	38.0	20.9	13.4

[a]Tallmadge, [b]Mehta and Hawley, [c]Liu et al. (1-D), [d]Liu et al. modified Ergun
[e]Combined Tallmadge and Mehta and Hawley, [f]Combined Tallmadge and Liu et al.

seen with the TL correlation. For the data in the turbulent region ($Re > 4000$), the ARAE of the TL correlation was an excellent 9.1% compared to Tal at 15.7%, Liu at 56.3% and the remaining three published laminar correlations which were all over 100%.

7.5 Summary

In summary, the combined Tallmadge and Liu correlation of this study predicts pressure drops more accurately than any other correlation analyzed. Its overall ARAE for the full data set (ranges in Table 7.1) was 13.4%. For comparison, the TMH correlation was 20.9%. The Tallmadge correlation had the best accuracy of the literature correlations with an overall average relative absolute error of 25.8%. The overall average relative absolute errors of the other correlations ranged from 32.6% for the Liu correlation to 48.4% for the MH correlation. Combining the portions of each correlation meant to improve the applicability of the original Ergun correlation in different flow regimes has created a single correlation that is accurate over all the different flow regimes. The combined correlation can be used with confidence over $0.32 < Re < 7,700$, $0.33 < \varepsilon_b < 0.88$, and $8.3 < d_t/d_p < 50$ to predict pressure drop in packed beds.

CHAPTER 8. SUMMARY, CONCLUSIONS, AND RECOMMENDATIONS

8.1 Summary

Demand for liquid fuel sources combined with potential political unrest in some of the regions most abundant in oil and natural gas and the recent natural gas boom from hydraulic fracturing have pushed global and domestic energy policies to focus on domestic production and sustainability. The Fischer-Tropsch synthesis is one attractive method for converting locally available and inexpensive hydrocarbon sources (natural gas, biomass, coal, organic waste, etc.) into liquid transportation fuels. Activity in FT research, development, and commercialization is growing with current world wide capacity at $410,000$ bbl/d in operation and an additional $260,000$ bbl/d announced and under construction with two major facilities announced by Shell and Sasol to be built in the United States.

This dissertation focused on two major aspects of FT research: catalyst development and reactor modeling. A novel iron catalyst preparation method was developed and described and makes use of a novel solvent deficient precipitation (SDP). Fifteen SDP catalysts were prepare, characterized, and tested at BYU for this study and a sixteenth catalyst was prepared and tested by industrial collaborators. The purpose of the catalyst experiments was to identify the effects of key preparation variables in the new precipitation on catalyst characteristics and performance. Kinetic experiments in temperature and pressure were performed and regressed kinetic parameters were reported for the catalysts in this study. Catalyst performance in activity and selectivity compared well against some of the most active catalysts reported in the literature.

In addition to catalyst preparation and testing, a trickle fixed-bed recycle reactor model applicable to iron and cobalt FT catalysts was developed and used to investigate the effects of theoretical (effective diffusivity, Prandtl number, friction factor, etc.) and physical (recycle ratio, pressure, feed flow rate, tube diameter, cooling temperature, and catalyst size and shape) process parameters on reactor model predictions. These effects suggest operating ranges and key param-

eters for optimizing reactor design and performance. The model was validated with full scale reactor data from Sasol's Arge fixed-bed reactors. The model was also compared with other published fixed-bed reactor models.

While developing the reactor model, it was found that available pressure drop correlations account for turbulent flow in large packed tubes (little or no pellet-wall interactions), or for laminar flow in smaller diameter packed tubes (high pellet-wall interactions), but none accounted for specific issues of turbulent flow in small diameter packed tubes which is the common regime for FT reactor design. Modifications of Ergun's friction factor equation for high Reynolds number and for high pellet-wall interactions were combined into a single equation and the correlation constants were fit to 324 data points gleaned from three classic pressure drop studies in the literature. The new correlation is reported and compared along with predictions of five published correlations to the experimental data.

Significant findings and observations from these three research activities are presented in the following sections. Following these conclusions, recommendations for future research activities are given.

8.2 Iron Catalyst Conclusions and Observations

The novel solvent deficient precipitation (SDP) method of making iron FT catalysts presents unique opportunities and challenges in catalyst preparation and in scale up for industrial production. The following observations were made in the course of the work described for this dissertation.

8.2.1 Synthesis

- SDP for iron catalyst preparation involves mixing hydrated iron nitrate with ammonium bicarbonate. The solids are both white (or slightly purple hued for the iron) to begin with, but as the solids contact each other, spots of bright red begin to appear. With mixing and as the precipitation proceeds, the waters of hydration are released and the solid is dissolved.

- SDP precursors began to re-disperse during the washing step as the amount of time in contact with water increased. Well dispersed precipitated iron is difficult to filter. Conventionally

precipitated catalyst particles also dispersed themselves in water at room temperature,but filtered easily at ice water temperatures.

- Decomposition of NH_4NO_3 byproduct occurs suddenly at 210 °C. TGA data show that the decomposition is initially endothermic but the completion of the decomposition is exothermic. White crystals of NH_4NO_3 believed to be recombined decomposition products were observed in the equipment after calcination and had plugged vent lines on at least one occasion.

8.2.2 Characterization

- Comparing surface areas of catalysts with and without SiO_2 (GWL to GWLa and 1WLa; GUL to GULa, GULb, and 1ULa) shows that adding SiO_2 increases surface area by more than 300% (4–6 fold increase).
- Washing catalyst precursors increases SA and pore volume.
- For the 1S preparation, unwashed catalysts have smaller pores and more narrow distributions of pores.
- Average pore diameters and average iron crystallite diameters are approximately equal.
- There is a structural difference between washed and unwashed catalysts resulting from some form of reorganization of the ferrihydrite matrix. This may be a transition from partially dehydrated ferrihydrite to fully hydrated ferrihydrite.
- Not washing results in at least partial conversion of ferrihydrite to Fe_2O_3 during calcination at 300 °C.
- The 1 step preparation method gives very even distributions of promoters.
- The 2 step preparation method gives a less uniform distribution of promoters which affects catalyst activity, selectivity, and possibly stability.

- Adding the potassium and silica promoters together as described for 2 step preparations may result in more potassium-silica interactions which lower the effective potassium loadings of the catalysts.

8.2.3 Activity, Selectivity, and Stability

- 1S catalysts appear to have superior properties to 2S catalysts for wax production from low H_2 feed stocks when considering rate, selectivity, and stability together.
- Unwashed catalysts are statistically more active than washed catalysts of the same potassium loading.
- Catalysts dried initially at 100 °C are more active than catalysts dried initially at 60 °C.
- Unwashed catalysts have an average 14.0 kJ/mol higher E_A than washed catalysts.
- Catalysts dried first at 100 °C (H) with nominal potassium loadings have an average 5.2 kJ/mol higher activation energy than catalysts dried first at lower temperatures.
- Drying catalysts completely before washing neither preserves the original precursor pore structure, nor provides any benefit in activity or selectivity.
- Catalysts with average particle diameters and average pore sizes both between 5 and 15 nm are up to 300% more active than catalysts with larger average particle (17–23 nm) and pore diameters (45–50 nm).
- Catalysts with higher surface areas tend to be more active, though the data has scatter.
- Catalyst activity generally increases with hydrogen chemisorption uptake; however, caution is advised when comparing uptakes of catalysts from different preparation methods.
- The most active catalysts show the weakest XRD signals for Fe_3O_4 and Fe_5C_2 and the strongest signal for Fe_2C. This does not mean that Fe_2C is the active phase for FTS.
- Water-gas shift activity of 1 step unwashed catalysts is greater than for 2 step catalysts.
- Selectivities to CO_2 and CH_4 increase with temperature for all catalysts.

- Catalysts containing the nominal 4 parts potassium per 100 parts iron have higher water-gas shift activity (22–45% compared to 8–22%) and lower methane selectivity (3–8% compared to 10–16%) than catalysts with lower potassium loadings.

- It appears that selectivity to CO_2 increases and selectivity to CH_4 decreases as the effective potassium loading increases. Effective potassium loading is higher for more uniformly distributed potassium and for catalysts with fewer potassium-silica interactions.

- 1UHa and 2UH show comparable activities to some of the most active catalysts in the literature. The selectivities of 1UHa were comparable in methane and C_{12+} hydrocarbon selectivities, but deviated in the other ranges due to the issues of averaging product make over several temperatures and conditions and of poor product collection methods. The selectivities of 2UH were higher in methane, propane, and ethane production presumably due to poor promoter distribution and potentially more potassium-silica interactions than for other catalysts.

- The variability of reproducing any catalyst property in a second preparation in this study was about 30%; however, the repeatability should increase significantly if consistent methods, practices, and equipment are used in repeat preparations.

- 1WLa may have had significant irreversible activity loss starting at 28 h on stream as a result of exposure to CO in the absence of H_2 for 16 h.

- 2UH showed significant (20%) loss of activity which appeared to be linear over 559 h of reactor testing. A deactivation model was developed to account for this loss. The deactivation was likely a result of the high potassium loading combined with poor distribution of both potassium and silica.

- 1UH and 1ULC show excellent stability over 559 h and 790 h of FTS, respectively.

- The CO partial pressure dependency of 2UH was a positive 0.29. This is very different from that measured by Eliason [56] (-0.05 order). The dependency on H_2 was 0.63 which is very similar to the 0.60 measured by Eliason.

- The partial pressure dependencies of 2UH (0.29 and 0.63) do not necessarily apply to the other SDP catalysts; however, dependencies of 1ULC were 0.16 for CO and 0.55 for H_2.

- A commercial collaborator prepared 1ULC using the 1ULa preparation method. Testing of this catalyst by a third party facility shows an extremely stable, highly active and selective catalyst comparable to some of the best catalysts in the literature.

8.3 Reactor Modeling Conclusions and Observations

A trickle fixed-bed recycle reactor model applicable for iron and cobalt Fischer-Tropsch catalysts has been developed and validated using data from SASOL's Arge reactors. The model allows the input of a wide range of kinetic models.

8.3.1 Model Development

- Choice of reaction order for the Thiele modulus calculation was found to have some effect on the value of the resulting effectiveness factor and should be chosen by careful analysis of the kinetic model over the range of partial pressures in the reactor being modeled.

- The bulk diffusivity of carbon monoxide is a better choice than the bulk diffusivity of hydrogen in calculating effective diffusivity. For the Fe base case using the bulk diffusivity of CO resulted in a 5 K lower bed temperature and a 50% greater required reactor length.

- Effective radial thermal conductivity (λ_{er}) is enhanced by the presence of liquids and increases almost linearly with bed length as liquid products accumulate. The dynamic contribution from the gas is significant and decreases slightly through the reactor as the reactants are consumed.

- The convective heat transfer at the wall (h_{wall}) decreases directly with the consumption of reactants. The static contribution to convective heat transfer is significant, but constant.

- The overall heat transfer coefficient (U) is most influenced by h_{wall}, but λ_{er} is also significant.

- Prandtl number should be calculated using molar averages of gas properties (0.24–0.27 for the base cases) rather than assuming a gas Prandtl number of 0.7. Averaged properties should also be used in calculating the gas Reynolds number.
- The Tallmadge friction factor equation is better suited for pressure drop calculations in FT FB reactors than the Ergun or Mehta-Hawley equations.
- Predictions of this reactor model matched predictions of two other published models very well.

8.3.2 Effects of Process Variables

The following conclusions apply to a fixed-bed Fischer-Tropsch reactor and are observations made using the reactor model developed in this study.

- FTS normal operation can be significantly influenced by pore diffusion ($\eta \approx 0.2$–0.8).
- As pellet diameter is decreased, the effect of decreased diffusion length (increasing the effectiveness factor) overcomes competing effects of decreased bed void fraction and increased pressure drop.
- Advanced pellet geometries (i.e. trilobes) help optimize the trade off between diffusion length and pressure drop and thereby decrease the required catalyst mass.
- Smaller tube diameters facilitate heat transfer and allow for higher operating temperatures without the risks of runaway, deactivation, or loss of selectivity.
- Small tube to pellet diameter ratios (< 15) result in longer required bed lengths as pellet-wall interactions become significant and bed void fraction decreases.
- Model predictions are extremely sensitive to the temperature of the tube wall.
- Operating pressure can greatly increase reaction rate and thereby decrease required bed length, but must be tempered against the trend to more quickly deactivate catalyst as shown in the literature.
- Recycle is necessary for thermal stability and control in a FT FBR.

8.4 Combined Friction Factor Correlation

The best predictor of pressure drop over the full range of experimental data is the proposed TL correlation which combines the Tallmadge high Reynolds number and the Liu et al. high pellet-wall interaction modifications of the Ergun equation.

- The average relative absolute error for this equation for all the data is a low 13.4% compared with the next best value of 25.8% for the Tallmadge correlation. The other published correlations ranged from 32.6–48.4%.

- None of the correlations predicted the experimental data for the $10 < d_t/d_p < 12.3$ flow regime very well which is the only flow regime in this study in which another correlation (barely) outperformed the TL equation. The TL equation average absolute relative error was 27.8% compared to 25.8% for the Liu et al.-modified Ergun equation.

- The TL equation is valid over five orders of magnitude in Reynolds number and for low and high pellet-wall interaction flow regimes. Its use is recommended for all general packed bed pressure drop calculations.

8.5 Major Findings

The following observations are emphasized for their importance and relevance to this work and to the scientific community.

- For iron catalysts prepared by the 2 Step SDP method, the activity of unwashed catalysts is statistically greater than for washed catalysts.

- Washing the catalyst precursor prepared by solvent-deficient precipitation results in a different catalyst structure (ferrihydrite) after calcination than for unwashed catalysts (Fe_2O_3). The presence of Fe_2O_3 after calcination for unwashed catalysts may be caused by more facile transformation of uncoordinated ferrihydrite particles to Fe_2O_3. Alternatively, the decomposition of NH_4NO_3 may catalyze the transformation.

- The activation energy for 1UHa is 93.8 kJ/mol. All activation energies for unwashed 1S and 2S catalysts are higher (94.3–98.9 kJ/mol) than activation energies for washed 1S and 2S catalysts (76.6–90.6 kJ/mol) and compare well to Eliason's model (92 kJ/mol).

- The CO partial pressure dependency of 2UH was a positive 0.29. This is very different from that measured by Eliason [56] (-0.05 order). The dependency on H_2 was 0.63 which is very similar to the 0.60 measured by Eliason.

- The bulk diffusivity of carbon monoxide is a better choice than the bulk diffusivity of hydrogen in calculating effective diffusivity in the Fixed-Bed reactor model. Other models have used hydrogen which underestimates diffusion resistance in a system that is typically reactant limited in CO.

- Smaller pellet diameters and advanced pellet geometries (i.e. trilobes) greatly decrease the required mass of catalyst by increasing the effectiveness factor.

- The proposed combined friction factor correlation predicts pressure drop over five orders of magnitude of Reynolds number better than previously published correlations.

8.6 Future Work and Recommendations

Based on the foregoing observations, the following future scientific investigations and activities are recommended.

- A wealth of knowledge on ferrihydrite has been published over several decades, but the context of these studies has largely been for soil studies or has been ignored by the FT catalyst community, presumably because the connection between iron FT catalyst precursors and ferrihydrite has not been well documented. A review of the available knowledge in ferrihydrite properties and synthesis in the context of FT catalyst preparation is recommended.

- Other variables that affect ferrihydrite synthesis and which may affect catalyst properties but which were not investigated in this work include, but are not limited to, calcination temperature, solvent viscosity, temperature of reactants during precipitation, and pH of solution

at the time of precipitation. Much will be learned by studies of these variables in FT catalyst development. Specifically relevant to the solvent deficient preparation method are the temperature of the reactants during precipitation and calcination temperature.

- Catalysts prepared for this study used promoter starting materials inherently free of hetero atoms in order to investigate specific preparation variables in a factorial experiment. These materials may not be the most effective materials to use. Specifically, a large range of Si containing compounds have been used in the literature. Washed (and perhaps unwashed) catalyst activity and selectivity may be increased by use of different materials (e.g. K_2SiO_3) and impregnation methods [22].

- The order of adding the potassium and silica promoters in two step catalysts should be investigated as adding them simultaneously may increase potassium-silica interactions which reduce the effectiveness of the potassium.

- A study on the final drying temperature of the precursor would be of interest. It is possible to skip the drying step altogether and calcine immediately after precipitation. Doing so would preserve the small crystallites which appear to influence activity greatly.

- The large quantity of NH_4NO_3 in unwashed precursors (nearly 50% by mass) affects catalyst properties, but the effects are as yet unknown. The presence of nitrogen compounds during calcination may be beneficial, or the extra crystalline structure in contact with the catalyst may have an effect on the organization and orientation of precursor agglomerates. Investigation of these phenomena coupled with a study on optimizing the calcination procedure is advised.

- Others have shown a nearly 100% increase in catalyst activity by using an optimized pretreatment for iron FT catalysts [20, 21]. The reduction of catalysts in this study was not optimized, but significant gains in activity are expected from experiments in optimizing pretreatment and reduction procedures.

- The science of the solvent deficient precipitation method for FT catalyst preparation will benefit from future studies on preparing low K catalysts for high temperature FTS.

- A repeat of the total pressure experiments of 1ULC will elucidate the interesting trend in this data to heavier hydrocarbon selectivity with decreasing operating pressure. If this trend is repeatable, it is counter to conventional wisdom.

- Experiments to determine the partial pressure dependencies of all catalysts in this study are advised in order to determine whether 0.2–0.3 for CO and 0.5–0.7 for H_2 are general for these catalysts. Prior work shows values of -0.5–0.5 for CO and 0.6–1.4 for H_2 for iron catalysts in general including supported catalysts and catalysts with various promoters [56].

- A full kinetic study on a catalyst prepared by the 1UH method with the goal of obtaining parameters for a Langmuir-Hinshelwood type rate expression is needed.

- A comprehensive and detailed deactivation study on these catalysts would answer questions about the life of the catalyst and deactivation pathways with insights into preparing a catalyst to minimize or block these pathways.

- Several excellent 2-D reactor models are already reported in literature, but the improvements given in this work for 1-D models may also be applicable to 2-D models.

- A predictive selectivity model is sorely lacking for FT reactor modeling, particularly for iron catalysts. No attempts thus far have fit industrially relevant data nor have they accounted for the different product slates of variously promoted catalysts. Specifically, development of a selectivity model which accounts for different promoter loadings of potassium would be a significant contribution.

- The Wheeler pore-diffusion model is a limitation of the reactor model described. Implementation of a more rigorous treatment would advance the reactor modeling work.

- The reactor model described makes use of lumped reaction kinetics, but more predictive and accurate models for the formation of CO_2 and CH_4 would be a significant step forward.

- The Thiele modulus calculation used in this work assumes a power-law form of the rate equation; however, the shifting order FT reaction is typically represented by Langmuir-Hinshelwood type kinetic expressions. Development of a more general Thiele modulus expression for shifting order kinetics is needed.

- None of the published friction factor correlations predicted experimental data in the $10 < d_t/d_p < 12.3$ flow regime very well despite attempts by others specifically targeted for this regime. Whether this is the result of poor experimental data or an as yet undescribed feature of high Reynolds number flow in this regime, an investigation of high flow rates in this flow regime is warranted.

REFERENCES

[1] C. H. Bartholomew, R. J. Farrauto, Fundamentals of Industrial Catalytic Processes, Wiley and Sons, Hoboken, 2nd edition. 1, 4, 5, 6, 14, 25, 156, 157

[2] R. Krishna, S. T. Sie, Design and scale-up of the Fischer-Tropsch bubble bolumn slurry reactor, Fuel Processing Technology 64 (2000) 73–105. 2

[3] B. Jager, Indirect conversion of coal to fuel and chemicals by the Sasol slurry phase distillate process, in: Proceedings — 14th Annual International Pittsburgh Coal Conference, pp. 12–22. 2

[4] M. E. Dry, Practical and theoretical aspects of the catalytic Fischer-Tropsch process, Applied Catalysis A: General 138 (1996) 319–344. 2, 130, 156, 157

[5] S. T. Sie, Process development and scale-up. iv. case history of the development of a Fischer-Tropsch synthesis process, Reviews in Chemical Engineering 14 (1998) 109–157. 2, 124, 130, 157

[6] H. E. Atwood, C. O. Bennett, Kinetics of the Fischer-Tropsch reaction over iron, Industrial and Engineering Chemistry Process Design and Development 18 (1979) 163–170. 4, 7

[7] Y. N. Wang, Y. Y. Xu, Y. W. Li, Y. L. Zhao, B. J. Zhang, Heterogeneous modeling for fixed-bed Fischer-Tropsch synthesis: Reactor model and its applications, Chemical Engineering Science 58 (2003) 867–875. xii, 7, 132, 160, 161, 162, 163, 168, 174, 175

[8] M. R. Rahimpour, H. Elekaei, Optimization of a novel combination of fixed and fluidized-bed hydrogen- permselective membrane reactors for Fischer-Tropsch synthesis in GTL technology, Chemical Engineering Journal 152 (2009) 543–555. 7

[9] R. Guettel, T. Turek, Comparison of different reactor types for low temperature Fischer-Tropsch synthesis: A simulation study, Chemical Engineering Science 64 (2009) 955–964. 7

[10] A. P. Steynberg, M. Dry, Introduction to Fischer-Tropsch technology, in: Fischer-Tropsch Technology, volume 152 of *Studies in Surface Science and Catalysis*, 2004, pp. 1–63, 533–601. 5, 6, 7, 145, 156, 157, 158

[11] G. Bub, M. Baerns, Prediction of the performance of catalytic fixed bed reactors for Fischer-Tropsch synthesis, Chemical Engineering Science 35 (1980) 348–355. 7

[12] A. Jess, C. Kern, Modeling of multi-tubular reactors for Fischer-Tropsch synthesis, Chemical Engineering Technology 32 (2009) 1164–1175. xii, 7, 8, 160, 161, 162

[13] A. Jess, R. Popp, K. Hedden, Fischer-Tropsch synthesis with nitrogen-rich syngas: Fundamentals and reactor sesign aspects, Applied Catalysis A: General 186 (1999) 321–342. 4, 7, 168, 171

[14] M. E. Dry, The Fischer-Tropsch synthesis, in: J. R. Anderson, M. Boudart (Eds.), Catalysis Science and Technology, volume 1, Springer-Verlag, New York, 1981, pp. 159–256. 5, 100, 102, 156, 157, 158, 159

[15] D. B. Bukur, X. Lang, J. A. Rossin, W. H. Zimmerman, M. P. Rosynek, E. B. Yeh, C. Li, Activation studies with a promoted precipitated iron Fischer-Tropsch catalyst, Ind. Eng. Chem. Res. 28 (1989) 1130–1140. 5

[16] D. B. Bukur, X. Lang, D. Mukesh, W. H. Zimmerman, M. P. Rosynek, C. Li, Binder/support effects on the activity and selectivity of iron catalysts in the Fischer-Tropsch synthesis, Ind. Eng. Chem. Res. 29 (1990) 1588–1599. 33, 52, 110, 124, 127, 128, 129

[17] D. B. Bukur, D. Mukesh, S. A. Patel, Promoter effects on precipitated iron catalysts for Fischer-Tropsch synthesis, Ind. Eng. Chem. Res. 29 (1990) 194–204.

[18] D. B. Bukur, D. Mukesh, S. A. Patel, M. P. Rosynek, W. H. Zimmerman, Development and Process Evaluation of Improved Fischer-Tropsch Slurry Catalysts, DOE Final Report DE95000382, Texas A&M University, 1990. 62, 65, 94, 100, 102

[19] D. B. Bukur, X. Lang, A pricipitated iron Fischer-Tropsch catalyst for synthesis gas conversion to liquid fuels, in: A. e. a. Parmaliana (Ed.), Studies in Surface Science and Catlysis, volume 119 of *Natural Gas Conversion V*, Elsevier Science, 1998, pp. 113–118.

[20] D. B. Bukur, X. Lang, Highly active and stable iron Fischer-Tropsch catalyst for synthesis gas conversion to liquid fuels, Ind. Eng. Chem. Res. 38 (1999) 3270–3275. 33, 111, 113, 127, 201

[21] D. B. Bukur, X. Lang, Y. Ding, Pretreatment effect studies with a precipitated iron firscher-tropsch catalyst in a slurry reactor, Applied Catalysis A: General 186 (1999) 255–275. 33, 60, 98, 115, 127, 201

[22] V. H. C. Vazquez, Spray Drying and Attrition Behavior of Iron Catalysts For Slurry Phase Fischer-Tropsch Synthesis, Master's thesis, Texas A&M University, 2003. 5, 21, 201

[23] S. Li, S. Krishnamoorthy, A. Li, G. D. Meitzner, E. Iglesia, Promoted iron-based catalysts for the Fischer-Tropsch synthesis: Design, synthesis, site densities, and catalytic properties, Journal of Catalysis 206 (2002) 202–217. 6

[24] B. Wu, L. Bai, H. Xiang, Y.-W. Li, Z. Zhang, B. Zhong, An active iron catalyst containing sulfur for Fischer-Tropsch synthesis, Fuel 83 (2003) 205–212. 6

[25] Y. Yang, H. Xiang, R. Zhange, B. Zhong, Y. Li, A highly active and stable Fe-Mn catalyst for slurry Fischer-Tropsch synthesis, Catalysis Today 106 (2005) 170–175. 6

[26] S. Liu, Q. Liu, J. Boerio-Goates, B. F. Woodfield, Preparation of a wide array of ultra-high purity metals, metal oxides, and mixed metal oxides with uniform particle sizes, Journal of Advanced Materials 39 (2007) 18–23. 6, 14

[27] S. J. Smith, Q. Liu, J. Boerio-Goates, B. F. Woodfield, The mechanism behind a novel two-step solid-state method for synthesizing metal oxide nanoparticles, in: Abstracts, Joint 63rd Northwest and 21st Rocky Mountain Regional Meeting of the American Chemical Society, Park City, Utah. 50

[28] S. J. Smith, R. E. Olsen, Q. Liu, S. Liu, B. F. Woodfield, J. Boerio-Goates, Mechanism behind a novel, green, two-step, general method for synthesizing metal and metal oxide nanoparticles, in: NASSC Conference.

[29] S. J. Smith, S. Liu, Q. Liu, R. E. Olsen, M. Rytting, D. Selck, C. Simmons, J. Boerio-Goates, B. F. Woodfield, Metal oxide nanoparticle synthesis via a robust solvent-deficient method, Chem. Mater. (2012). Manuscript submitted for publication, under revision. 50

[30] C. H. Bartholomew, B. F. Woodfield, H. Baiyu, R. E. Olsen, L. Astle, Method for making highly porous, stable metal oxides with a controlled pore structure, 2011. US 20110257008.

[31] B. F. Woodfield, S. Liu, J. Boerio-Goates, Q. Liu, Preparation of uniform nanoparticles of ultra-high purity metal oxides, mixed metal oxides, metals, and metal alloys, 2012. Application Number: WO2007US04279 20070216.

[32] C. L. Snow, K. I. Lilova, A. V. Radha, Q. Shi, S. Smith, A. Navrotsky, J. Boerio-Goates, B. F. Woodfield, Heat capacity and thermodynamics of a synthetic two-line ferrihydrite, $FeOOH{\cdot}0.027H_2O$ (2012). Manuscript submitted for publication, under revision. 6

[33] Y. N. Wang, Y. Y. Xu, H. W. Xiang, Y. W. Li, B. J. Zhang, Modeling of catalyst pellets for Fischer-Tropsch synthesis, Industrial & Engineering Chemistry Research 40 (2001) 4324–4335. 7, 161

[34] Y. N. Wang, Y. W. Li, Y. L. Zhao, B. J. Zhang, Study on solubility correlation of gases and liquid waxes systems in Fischer-Tropsch synthesis, Tianranqi Huagong 24 (1999) 48–53. 7

[35] Q.-S. Liu, Z.-X. Zhang, J.-L. Zhou, Steady-state and dynamic behavior of fixed-bed catalytic reactor for Fischer-Tropsch synthesis: I. mathematical model and numerical method, Journal of Natural Gas Chemistry 8 (1999) 137. 7

[36] M. A. Marvast, M. S. Sohrabi, S. Zarrinpashne, G. Baghmisheh, Fischer-Tropsch synthesis: Modeling and performance study for Fe-HZSM5 bifunctional catalyst, Chemical Engineering & Technology 28 (2005) 78–86. 7, 165, 174, 175

[37] A. Matsuura, Y. Hitaka, T. Akehata, T. Shirai, Effective radial thermal conductivity in packed beds with gas-liquid downflow, Heat Transfer — Japanese Research 8 (1979) 44–52. 8, 131, 147, 148, 151

[38] G. F. Froment, K. B. Bischoff, Chemical Reactor Analysis and Design, Wiley Series in Chemical Engineering, John Wiley & Sons, New York, 2nd edition, 1990. 8, 131, 133, 147, 150, 151, 154, 155

[39] S. Ergun, Fluid flow through packed columns, Chemical Engineering Progress 48 (1952) 89. 9, 184

[40] J. A. Tallmadge, Packed bed pressure drop — an extension to higher reynolds numbers, AIChE Journal 16 (1970) 1092–1093. 9, 155, 162, 184, 191, 199

[41] D. Mehta, M. C. Hawley, Wall effect in packed columns, Industrial & Engineering Chemistry Process Design and Development 8 (1969) 280–282. 9, 155, 184, 191

[42] S. Liu, A. Afacan, J. Masliyah, Steady incompressible laminar flow in porous media, Chemical Engineering Science 49 (1994) 3565–3586. 9, 185, 191, 199

[43] B. F. Woodfield, C. H. Bartholomew, K. Brunner, W. Hecker, X. Ma, F. Xu, L. Astle, Iron and cobalt based Fischer-Tropsch pre-catalysts and catalysts, 2012. Serial number 61/615,681. 11

[44] K. M. Brunner, J. C. Duncan, L. D. Harrison, K. E. Pratt, R. P. S. Peguin, C. H. Bartholomew, W. C. Hecker, A trickle fixed-bed recycle reactor model for the Fischer-Tropsch synthesis, International Journal of Chemical Reactor Engineering 10 (2012) 1–36. DOI: 10.1515/1542-6580.2840. 13, 130, 161

[45] S. J. Gregg, K. S. W. Sing, Adsorption, Surface Area and Porosity, Academic Press, second edition, 1982. 23

[46] C. Chu, M. Hamidy, K. Nobe, Prore-size distributions of coper oxide-alumina catalysts, Journal of Chemical and Engineering Data 16 (1971) 327–331. 23

[47] Accurate Determination of Pore Size Distributions of Catalysts and Supports, Presentation at Western States Catalysis Club, Provo, UT, 2010.

[48] E. P. Barrett, L. G. Joyner, P. P. Halenda, The determination of pore volume and area distributions in porous substances. i. computations from nitrogen isotherms, Industrial and Engineering Chemistry Process Design and Development 18 (1979) 163–170.

[49] J. M. Thomas, W. J. Thomas, Principles and Practice of Heterogeneous Catalysis, VCH, New York, 1997. 23

[50] R. D. Jones, C. H. Bartholomew, Improved flow technique for measurment of hydrogen chemisorption on metal catalysts, Applied Catalysis 39 (1988) 77. 24

[51] B. L. Critchfield, Statistical Methods For Kintetic Modeling Of Fischer-Tropsch Synthesis On A Supported Iron Catalyst, Thesis, Brigham Young University, 2006. 27

[52] B. H. Davis, E. Iglesia, Technology Development for Iron and Cobalt Fischer-Tropsch Catalysts, DOE Final Technical Report DE-FC26-98FT40308, University of Kentucky Research Foundation, 2002. 33, 94, 102

[53] Y.-N. Wang, W.-P. Ma, Y.-J. Lu, J. Yang, Y.-Y. Xu, H.-W. Xiang, Y.-W. Li, Y.-L. Zhao, B.-J. Zhang, Kinetics modelling of Fischer-Tropsch synthesis over an industrial Fe-Cu-K catalyst, Fuel 82 (2003) 195–213. 33

[54] A. E. Messner, D. M. Rosie, P. A. Argabright, Correlation of thermal conductivity cell response with molecular weight and structure, Analytical Chemistry 31 (1959) 230. 35

[55] R. A. Dictor, A. T. Bell, On-line analysis of Fischer-Tropsch synthesis products, Ind. Eng. Chem. Fundam. 23 (1984). 37

[56] S. A. Eliason, Deactivation by Carbon of Unpromoted and Potassium-Promoted Iron Fischer-Tropsch Catalysts, Ph.D. thesis, Brigham Young University, Provo, UT, 1994. 41, 46, 85, 94, 100, 116, 119, 121, 122, 196, 200, 202

[57] R Development Core Team, R: A Language and Environment for Statistical Computing, R Foundation for Statistical Computing, Vienna, Austria, 2011. ISBN 3-900051-07-0. 42, 48

[58] F. Baty, M.-L. Delignette-Muller, nlstools: tools for nonlinear regression diagnostics, 2011. R package version 0.0-11. 42, 48

[59] G. A. F. Seber, C. J. Wild, Nonlinear Regression, John Wiley & Sons, Inc., pp. 250–269. 44

[60] O. Levenspiel, Chemical Reaction Engineering, John Wiley & Sons, third edition, 1999. 45

[61] U. Paul, Microkinetic Model of Fischer-Tropsch Synthesis on Iron Catalysts, Ph.D. thesis, Brigham Young University, Provo, UT, 2008. 46, 136

[62] J. Zhao, F. E. Huggins, Z. Feng, G. P. Huffman, Ferrihydrite: Surface structure and its effects on phase transformation, Clays and Clay Minerals 42 (1994) 737–746. 50, 71

[63] R. A. Eggleton, R. W. Fitzpartrick, New data and a revised structural model for ferrihydrite, Clays and Clay Minerals 36 (1988) 111–124. 52, 71

[64] H. Tuysyz, E. L. Salabas, C. Weidenthaler, F. Schuth, Synthesis and magnetic investigation of ordered mesoporous two-line ferrihydrite, J. Am. Chem. Soc. 130 (2008) 280–287. 52

[65] M. Ristic, E. De Grave, S. Music, S. Popovic, Z. Orehovec, Transformation of low crystalline ferrihydrite to α-Fe_2O_3 in the solid state, Journal of Molecular Structure 834–836 (2007) 454–460. 67

[66] Z. Feng, J. Zhao, F. E. Huggins, G. P. Huffman, Agglomeration and phase transition of a nanophase iron oxide catalyst, Journal of Catalysis 143 (1993) 510–519. 67

[67] J. Xu, Rational Design of Silica-Supported Platinum Promoted Iron Fischer-Tropsch Synthesis Catalysts Based On Activity-Structure Relationships, Ph.D. thesis, Brigham Young University, Provo, UT, 2003. 80, 82

[68] H. Arakawa, A. T. Bell, Effects of potassium promotion on the activity and selectivity of iron Fischer-Tropsch catalysts, Industrial and Engineering Chemistry Process Design and Development 22 (1983) 97–103. 94, 100, 102

[69] J. C. W. Kuo, Two Stage Process for Conversion of Synthesis Gas to High Quality Transportation Fuels, DOE Final Report DE-AC22-83PC60019, Mobil Research and Development Corp., Paulsboro, N.J., 1985. 110

[70] E. S. Lox, G. F. Froment, Kinetics of the Fischer-Tropsch reaction on a precipitated promoted iron catalyst. 1. experimental procedure and results, Ind. Eng. Chem. Res. 32 (1993) 61–70. 121

[71] B. Jager, R. Espinoza, Advances in low temperature Fischer-Tropsch synthesis, Catalysis Today 23 (1995) 17–28. 124, 156, 157

[72] G. P. van der Laan, A. C. M. Beenackers, Hydrocarbon selectivity model for the gas-solid Fischer-Tropsch synthesis on precipitated iron catalysts, Ind. Eng. Chem. Res. 38 (1999) 1277–1290. 132

[73] A. Moutsoglou, P. P. Sunkara, Fischer-Tropsch synthesis in a fixed bed reactor, Energy Fuels 25 (2011) 2242–2257. 132

[74] M. E. Davis, R. J. Davis, Fundamentals of Chemical Reaction Engineering, McGraw Hill, Boston. 133

[75] S. C. Chapra, R. P. Canale, Numerical Methods for Engineers, McGraw Hill, Boston, 5th international edition. 133

[76] F. Benyahia, K. E. O'Neill, Enhanced voidage correlations for packed beds of various particle shapes and sizes, Particulate Science & Technology 23 (2005) 169–177. 134, 135, 173

[77] W. H. Zimmerman, D. B. Bukur, Rection kinetics over iron catalysts used for the Fischer-Tropsch synthesis, The Canadian Journal of Chemical Engineering 68 (1990) 292. 136

[78] Z.-T. Liu, Y.-W. Li, Intrinsic kinetics of Fischer-Tropsch synthesis over an Fe-Cu-K catalyst, Journal of the Chemical Society, Faraday Transactions 91 (1995) 3255. 136

[79] C. H. Bartholomew, U. P. Paul, G. W. Huber, Fischer-Tropsch synthesis on cobalt: A combined macro-microkinetic study, in: Abstracts of Papers, volume FUEL-042, 235th ACS National Meeting, New Orleans, LA. 137

[80] C. Erkey, J. B. Rodden, A. Akgerman, A correlation for predicting diffusion coefficients in alkanes, The Canadian Journal of Chemical Engineering 68 (1990) 661. 144

[81] C. Erkey, J. B. Rodden, A. Akgerman, Diffusivities of synthesis gas and n-alkanes in Fischer-Tropsch wax, Energy & Fuels 4 (1990) 275–276.

[82] A. Akgerman, Diffusivities of Synthesis Gas and Fischer-Tropsch Products in Slurry Media: Final Report, DOE Report DE88013683, Texas A and M University, 1987. 144

[83] S. Yagi, D. Kunii, Effective thermal conductivities in packed beds, AIChE Journal 3 (1957). 147

[84] A. S. Lamine, L. Gerth, H. Le Gall, G. Wild, Heat transfer in a packed bed reactor with cocurrent downflow of a gas and a liquid, Chemical Engineering Science 51 (1996) 3813–3827. 147, 151

[85] V. Specchia, G. Baldi, Heat transfer in trickle-bed reactors, Chem. Eng. Commun. 3 (1979) 483–499. 150, 151, 171, 182

[86] N. Habtu, J. Font, A. Fortuny, C. Bengoa, A. Fabregat, P. Haure, A. Ayude, F. Stuber, Heat transfer in trickle bed column with constant and modulated feed temperature: Experiments and modeling, Chemical Engineering Science 66 (2011) 3358–3368. 150, 182

[87] A. P. De Wasch, G. F. Froment, Heat transfer in packed beds, Chemical Engineering Science 27 (1972). 150, 151, 171

[88] R. C. Reid, J. M. Prausnitz, B. E. Poling, The Properties of Gases and Liquids, McGraw-Hill, Boston, 4th edition, p. 536. 153

[89] S. M. Walas, Phase Equilibria in Chemical Engineering, Butterworth Publishers, Boston, p. 505. 153

[90] R. E. Hicks, Pressure drop in packed beds of spheres, Industrial & Engineering Chemistry Fundamentals 9 (1970) 500–502. 155, 162

[91] M. E. Dry, The Fischer-Tropsch process: 1950–2000, Catalysis Today 71 (2002) 227–241. 156, 157

[92] R. L. Espinoza, A. P. Steynberg, B. Jager, A. C. Vosloo, Low temperature Fischer-Tropsch synthesis from a sasol perspective, Applied Catalysis A: General 186 (1999) 13–26. 159

[93] D. Gray, M. Lytton, M. Neuworth, G. Tomlinson, The Impact of Developing Technology on Indirect Liquefaction, DOE Report NTIS: DOEET10280T2, MITRE Corp., 1980. 156, 157

[94] M. E. Dry, A. P. Steynberg, Commercial FT process applications, in: A. Steynberg, M. Dry (Eds.), Fischer-Tropsch Technology, volume 152 of *Studies in Surface Science and Catalysis*, Elsevier, Boston, 2004, pp. 406–481. 156, 158

[95] A. Hoek, L. B. J. M. Kersten, The Shell middle distillate synthesis process: Technology, products and perspective, in: X. Bao, X. Yide (Eds.), Natural Gas Conversion VII, volume 147 of *Studies in Surface Science and Catalysis*, Elsevier, Boston, 2004, pp. 388–395. 156, 157

[96] A. Hoek, Towards a world scale project in Qatar: the pearl project, 2006. Presentation at DGMK-Conference Synthesis Gas Chemistry, Dresden.

[97] Mourik, Mourik international tubular devision, Mourik Magazine 33 (2005) 6–7.

[98] E. S. Lox, G. B. Marin, E. De Grave, P. Bussiere, Characterization of a promoted precipitated iron catalyst for Fischer-Tropsch synthesis, Applied Catalysis 40 (1988) 197–218. 157

[99] M. E. Dry, Fischer-Tropsch synthesis-industrial, Encyclopedia of Catalysis 3 (2003) 347–403. 158

[100] Z.-T. Li, Y.-W. Li, J.-L. Zhou, B.-J. Zhang, Intrinsic kinetics of Fischer-Tropsch synthesis over an fe-cu-k catalyst, J. Chem. Soc. Faraday Trans. 91 (1995) 3255–3261. 163

[101] S. Zheng, Y. Liu, J. Li, B. Shi, Deuterium tracer study of pressure effect on product distribution in the cobalt-catalyzed fischertropsch synthesis, Applied Catalysis A: General 330 (2007) 63–68. 169

[102] F. E. M. Farias, F. G. Sales, F. A. N. Fernandes, Effect of operating conditions and potassium content on Fischer-Tropsch liquid products produced by potassium-promoted iron catalysts, Journal of Natural Gas Chemistry 17 (2008) 175–178. 169

[103] B. H. Davis, Fischer-Tropsch synthesis: relationship between iron catalyst composition and process variables, Catalysis Today 84 (2003) 83–98. 170

[104] K. Pangarkar, T. J. Schildhauer, J. R. van Ommenc, J. Nijenhuis, J. A. Moulijn, F. Kapteijn, Experimental and numerical comparison of structured packings with a randomly packed bed reactor for fischertropsch synthesis, Catalysis Today 147S (2009) S2–S9. 171, 175

[105] S. P. Burke, W. B. Plummer, Gas flow through packed columns, Journal of Industrial and Engineering Chemistry 20 (1928) 1196. 186

[106] S. Ergun, A. A. Orning, Fluid flow through randomly packed columns and fluidized beds, Journal of Industrial and Engineering Chemistry 41 (1949) 1179. 186

[107] A. O. Oman, K. M. Watson, Pressure drops in granular beds, National Petroleum News 36 (1944) R795. 186

[108] C. A. J. Wentz, G. Thodos, Pressure drops in the flow of gases through packed and distended beds of spherical particles, AICHE Journal 9 (1963) 81–84. 186, 190

APPENDIX A. GAS CHROMATOGRAPHY

Example calculations, calibrations, and data for gas chromatography are presented here.

A.1 Example Calculations of Conversion, Rate, and Selectivity

A derivation of formulas for conversion, rate of reaction, and selectivity and example calculations for these quantities is given. Data for the example calculations of conversion, rate, selectivity, and productivity come from 1UH of FB run 6.

Constants

$\mu mol := 10^{-6} mol \qquad mmol := 10^{-3} mol \qquad R_g := 0.082058 \frac{L \cdot atm}{mol \cdot K}$

$mol_{Ar} := mol \quad parea := 1 \quad parea_{Ar} := 1 \quad H2 := 0 \quad Ar := 1 \quad CO := 2$ Indexes of vectors and matrices.

GC Data

$T_{rxn} := 261.6\,°C = 534.75\,K \qquad T_{ambient} := 21\,°C = 294.15\,K$ Ambient and reaction temperatures

$P_{ambient} := 12.5psi = 0.851 \cdot atm$ Ambient and back pressure regulator pressures

$P_{BPR} := 300psi + P_{ambient} = 21.264 \cdot atm$

$m_{cat} := 0.250gm \qquad x_{ArFeed} := 0.1167$ Mass of catalyst in reactor and mole/volume fraction of Ar in CO/ Ar feed

$$PA := \begin{pmatrix} 6957192 \\ 20743314 \\ 90040914 \\ 1328736 \\ 23790814 \\ 245171 \end{pmatrix} \quad \begin{pmatrix} H2 \\ Ar \\ CO \\ CH4 \\ CO2 \\ C2H6 \end{pmatrix}$$ Peak areas during reaction

$$PA_0 := \begin{pmatrix} 8185947 \\ 18384852 \\ 118261384 \\ 0 \\ 0 \\ 0 \end{pmatrix} \quad \begin{pmatrix} H2 \\ Ar \\ CO \\ CH4 \\ CO2 \\ C2H6 \end{pmatrix} \qquad BaseConst := \begin{pmatrix} 1 \\ 1 \\ 1 \\ 0 \\ 0 \\ 0 \end{pmatrix}$$

Peak areas of unreacted feed and vector indicating which species are present in baseline

$$RF := \begin{pmatrix} 0.04557 \\ 1 \\ 0.8901 \\ 0.6808 \\ 1.0451 \\ 1.0210 \end{pmatrix} \cdot \frac{parea}{mol} \cdot \frac{mol_{Ar}}{parea_{Ar}}$$

GC relative molar response factor from our calibration slope. Normalized to Ar.

$$\nu := \begin{pmatrix} 0 \\ 0 \\ 0 \\ 1 \\ 1 \\ 2 \end{pmatrix} \quad \begin{pmatrix} H2 \\ Ar \\ CO \\ CH4 \\ CO2 \\ C2H6 \end{pmatrix}$$

Stoichiometric coefficients of CO to each species

CO and H2 Conversion Derivation and Example Calculation

$$X_{CO} = \frac{F_{CO}^{0} - F_{CO}}{F_{CO}^{0}} = 1 - \frac{F_{CO}}{F_{CO}^{0}}$$

Definition of conversion in terms of molar flow rate of CO.

$$X_{CO} = 1 - \frac{y_{CO} \cdot F_{tot}}{y_{CO}^{0} \cdot F_{tot}^{0}}$$

Substitute $F_{CO} = y_{CO} * F_{tot}$ into conversion equation.

$$F_{Ar} = F_{Ar}^{0} = y_{Ar} \cdot F_{tot} = y_{Ar}^{0} \cdot F_{tot}^{0}$$

Relate total flow rates to the mole fraction of the inert tracer.

$$\frac{y_{Ar}^{0}}{y_{Ar}} = \frac{F_{tot}}{F_{tot}^{0}}$$

Rearrange to get an expression for the ratio of flow rates.

$$X_{CO} = 1 - \frac{y_{CO} \cdot F_{tot}}{y_{CO}^{0} \cdot F_{tot}^{0}} = 1 - \frac{y_{CO}}{y_{CO}^{0}} \cdot \frac{y_{Ar}^{0}}{y_{Ar}} = 1 - \frac{y_{CO}}{y_{Ar}} \cdot \frac{y_{Ar}^{0}}{y_{CO}^{0}}$$

Substitute inert mole fraction ratio for the total flow rate ratio.

$$y_A = \frac{PA_A}{RF_A} \cdot \frac{1}{\sum_i \frac{PA_i}{RF_i}}$$

Relate mole fraction to GC peak area and GC molar response factor (RF).

$$\frac{y_{CO}}{y_{Ar}} = \frac{PA_{CO}}{RF_{CO}} \cdot \frac{1}{\sum_i \frac{PA_i}{RF_i}} \cdot \frac{RF_{Ar}}{PA_{Ar}} \cdot \sum_i \frac{PA_i}{RF_i} = \frac{PA_{CO}}{RF_{CO}} \cdot \frac{RF_{Ar}}{PA_{Ar}}$$

Summations drop out of mole fraction ratios leaving only peak area and molar response ratios.

$$X_{CO} = 1 - \frac{PA_{CO}}{RF_{CO}} \cdot \frac{RF_{Ar}}{PA_{Ar}} \cdot \frac{RF_{CO}}{PA_{CO}^{0}} \cdot \frac{PA_{Ar}^{0}}{RF_{Ar}} = 1 - \frac{PA_{CO}}{PA_{Ar}} \cdot \frac{PA_{Ar}^{0}}{PA_{CO}^{0}}$$

Using an inert tracer makes conversion independent of GC calibration. This same derivation applies to hydrogen conversion.

$$X_{CO} := 1 - \frac{PA_{CO}}{PA_{Ar}} \cdot \frac{PA0_{Ar}}{PA0_{CO}} = 0.325$$

Conversion of CO based on peak ratios of CO to Ar

$$X_{H2} := 1 - \frac{PA_{H2}}{PA_{Ar}} \cdot \frac{PA0_{Ar}}{PA0_{H2}} = 0.247$$

Conversion of H2 based on peak ratios of H2 to Ar

Reactor Feed Rates and Composition

$$F := \begin{pmatrix} 42.376 \\ 4.911 \\ 38.289 \\ 42.063 \end{pmatrix} \cdot \frac{mmol}{hr} \begin{pmatrix} H2 \\ Ar \\ CO \\ He \end{pmatrix}$$

Molar flow rate of each species through Reactor 1 from mass flow controllers.

Rate of CO Consumption and of H2+CO

$$r_{CO} := -\frac{X_{CO} \cdot F_{CO}}{m_{cat}} \qquad -r_{CO} = 49.8 \cdot \frac{mmol}{gm \cdot hr}$$

Rate of consumption of CO is independent of GC calibration.

$$r_{H2CO} := -\frac{X_{H2} \cdot F_{H2} + X_{CO} \cdot F_{CO}}{m_{cat}} \qquad -r_{H2CO} = 91.6 \cdot \frac{mmol}{gm \cdot hr}$$

Rate of consumption of H2+CO.

Selectivity Derivation and Calculations

$$S_A = \frac{\nu}{X_{CO}} \cdot \frac{F_A}{F_{CO}^{0}} = \frac{\nu}{X_{CO}} \cdot \frac{y_A \cdot F_{tot}}{y_{CO}^{0} \cdot F_{tot}^{0}}$$

Definition of selectivity of moles of CO converted to species A

$$S_A = \frac{\nu}{X_{CO}} \cdot \frac{y_A}{y_{CO}^{0}} \cdot \frac{y_{Ar}^{0}}{y_{Ar}} = \frac{\nu}{X_{CO}} \cdot \frac{PA_A}{RF_A} \cdot \frac{RF_{CO}}{PA_{CO}^{0}} \cdot \frac{RF_{Ar}}{PA_{Ar}} \cdot \frac{PA_{Ar}^{0}}{RF_A}$$

Substitute mole fraction ratios for flow ratios and peak area ratios for mole fraction ratios as above.

$$S_A = \frac{\nu}{X_{CO}} \cdot \frac{PA_A}{PA_{CO}^{0}} \cdot \frac{PA_{Ar}^{0}}{PA_{Ar}} \cdot \frac{RF_{CO}}{RF_A}$$

Simplifying results in an expression for selectivity of species A that is dependent on PA and on GC RF.

$$S := \overrightarrow{\left(\frac{\nu}{X_{CO}} \cdot \frac{PA}{PA0_{CO}} \cdot \frac{PA0_{Ar}}{PA_{Ar}} \cdot \frac{RF_{CO}}{RF} \right)}$$

Selectivities of CO to each species.

$CH4 := 3 \quad CO2 := 4 \quad C2H6 := 5 \quad other := 6 \quad C2p := 7 \quad He := 3$

Define indexes for other species.

$$S_{other} := 1 - \sum_{i=3}^{5} S_i \qquad S_{C2p} := S_{other} + S_{C2H6}$$

Selectivities of other species and of C_{2+} hydrocarbons.

$$S = \begin{pmatrix} 0 \\ 0 \\ 0 \\ 0.04 \\ 0.467 \\ 0.01 \\ 0.483 \\ 0.493 \end{pmatrix} \begin{pmatrix} H2 \\ Ar \\ CO \\ CH4 \\ CO2 \\ C2H6 \\ Other \\ C2plus \end{pmatrix}$$

Selectivity of moles of CO to each species.

Gas Composition at Reactor Exit

Assume that only water will condense. Realistically, this means that we are ignoring all C_3-C_6 species.

$$n_{rxn} := \begin{bmatrix} F_{H2} \cdot (1 - X_{H2}) \\ F_{Ar} \\ F_{CO} \cdot (1 - X_{CO}) \\ F_{CO} \cdot X_{CO} \cdot S_{CH4} \\ F_{CO} \cdot X_{CO} \cdot S_{CO2} \\ F_{CO} \cdot X_{CO} \cdot S_{C2H6} \div \nu_{C2H6} \\ F_{He} \\ F_{CO} \cdot X_{CO} \cdot (1 - 2 \cdot S_{CO2}) \end{bmatrix} = \begin{pmatrix} 8.867 \\ 1.364 \\ 7.177 \\ 0.138 \\ 1.615 \\ 0.017 \\ 11.684 \\ 0.228 \end{pmatrix} \cdot \frac{\mu mol}{s} \begin{pmatrix} H2 \\ Ar \\ CO \\ CH4 \\ CO2 \\ C2H6 \\ He \\ H2O \end{pmatrix}$$

Molar flow rates of gasses exiting reactor. Does NOT include C_2H_4 for which we have no calibration of our own, but its RF is between CH_4 and C_2H_6.

Water is estimated from the fact that every mole of CO produces 1 mol water (excluding oxygenates and CO_2) and every mole of CO_2 consumes 1 mole of water.

$$y_{rxn} := \frac{n_{rxn}}{\sum_{i=0}^{7} n_{rxn_i}} = \begin{pmatrix} 28.52 \\ 4.39 \\ 23.08 \\ 0.45 \\ 5.19 \\ 0.05 \\ 37.58 \\ 0.73 \end{pmatrix} \cdot \% \quad \begin{pmatrix} H2 \\ Ar \\ CO \\ CH4 \\ CO2 \\ C2H6 \\ He \\ H2O \end{pmatrix}$$

The error in not including C_2H_4 will be less than the mole fraction of CH_4.

$$P_{rxn} := P_{BPR} \cdot y_{rxn} = \begin{pmatrix} 6.064 \\ 0.933 \\ 4.909 \\ 0.095 \\ 1.105 \\ 0.012 \\ 7.991 \\ 0.156 \end{pmatrix} \cdot atm \quad \begin{pmatrix} H2 \\ Ar \\ CO \\ CH4 \\ CO2 \\ C2H6 \\ He \\ H2O \end{pmatrix}$$

Partial pressures at the reactor exit.

Syngas Usage Ratio

$$H2COst := \frac{X_{H2} \cdot F_{H2}}{X_{CO} \cdot F_{CO}} = 0.84$$

Stoichiometric hydrogen to carbon monoxide ratio. This is quite low.

Hydrocarbon Productivity (C2+)

$$H2CO_{avg} := \frac{42}{20} = 2.1$$

Assume an overall average product and calculate the H2:CO ratio.

$$m_{C2plus} := X_{CO} \cdot F_2 \cdot S_7 \cdot \left(12.011 \frac{gm}{mol} + H2CO_{avg} \cdot 1.0079 \frac{gm}{mol} \right)$$

$$m_{C2plus} = 0.087 \cdot \frac{gm}{hr}$$

Mass of C2+ hydrocarbons produced based on assumed average product species (C20H42). Changing average HC species to C8H18 results in 1.1% increase in total HC mass. This shows that the calculated total HC mass is relatively unaffected by choice of average hydrocarbon species.

$$p_{C2plus} := \frac{m_{C2plus}}{m_{cat}} = 0.347 \cdot \frac{gm}{gm \cdot hr}$$

A.2 GC Valve Plumbing and Flow Path

Figure A.1 shows the valve positions and flow paths for injecting and sampling on GC B. Figures A.2 to A.4 show valve positions and flow paths for GC F during sample loop filling from the reactors, during injecting, and during sample loop filling from the gas standard line.

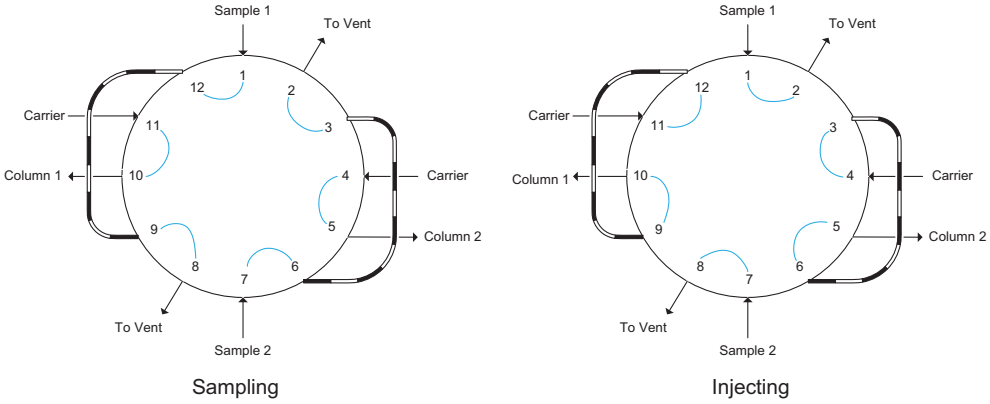

Figure A.1: GC B 12-port valve plumbing diagram.

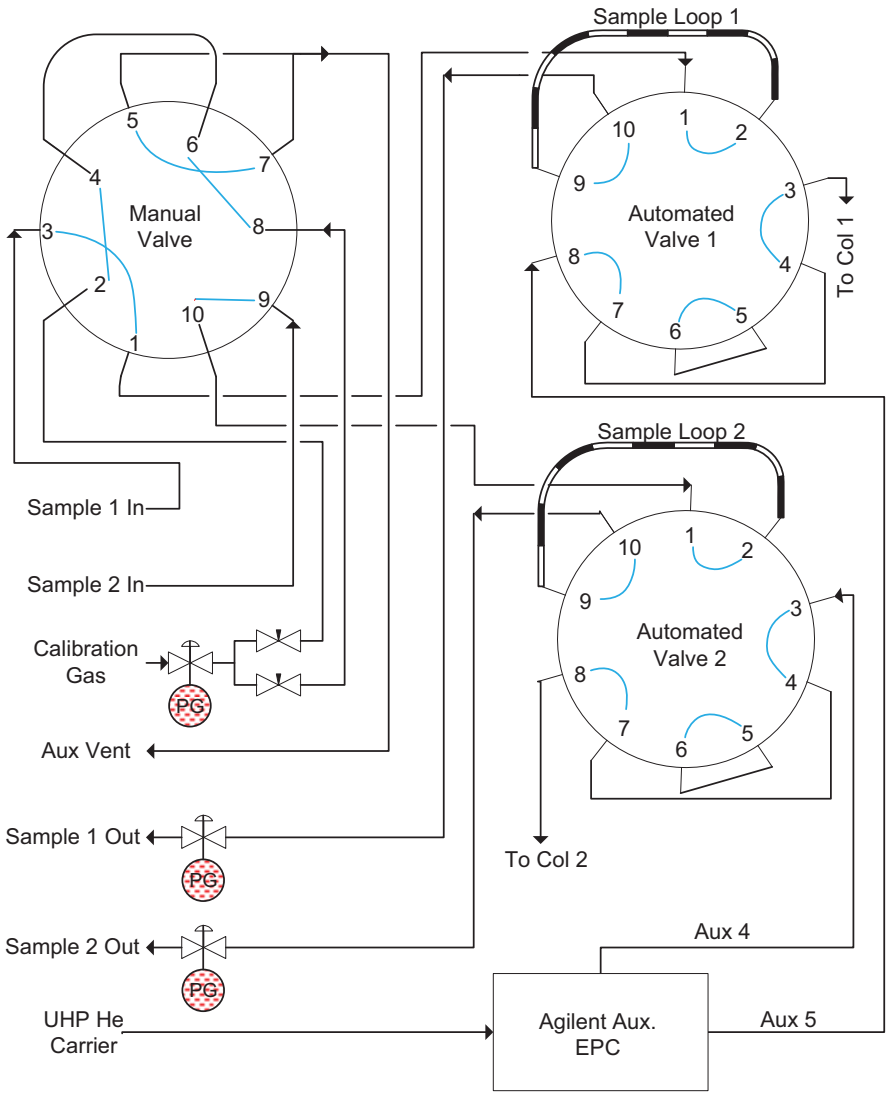

Figure A.2: GC F plumbing and valve position during sample loop filling.

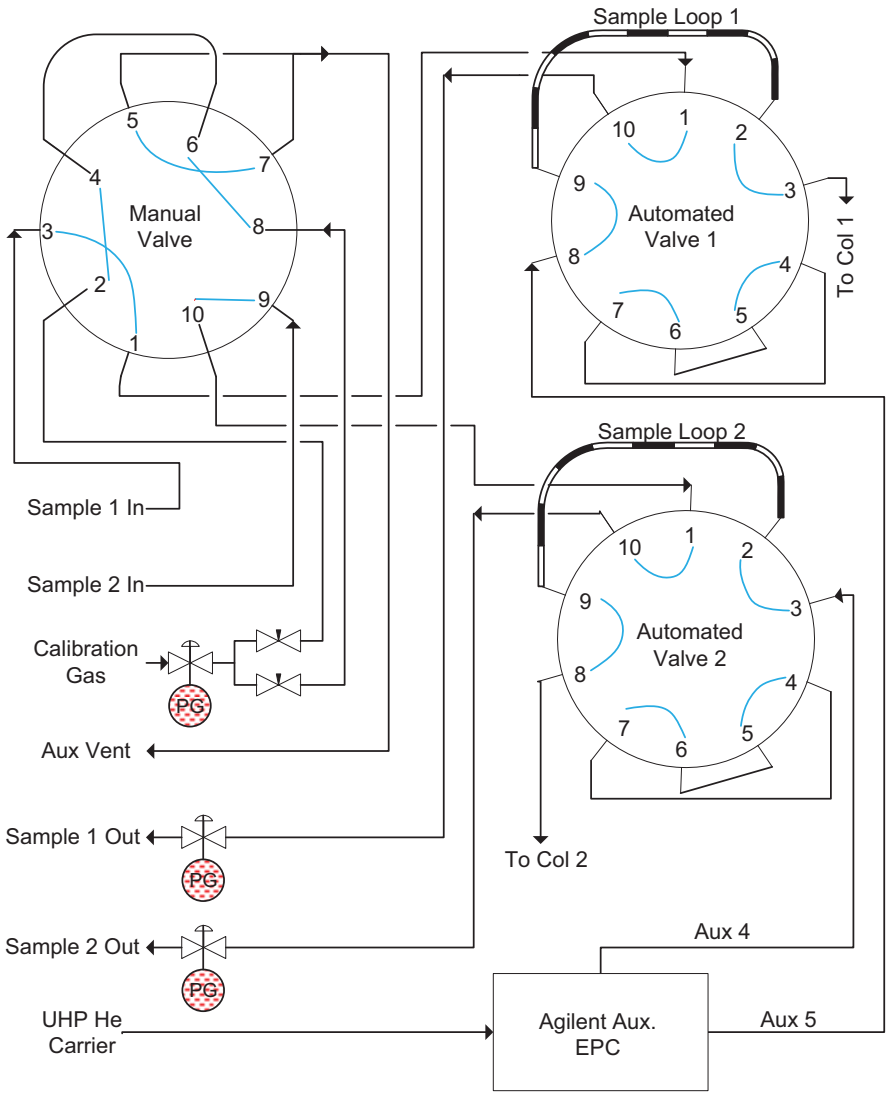

Figure A.3: GC F Plumbing and valve position during sample injection.

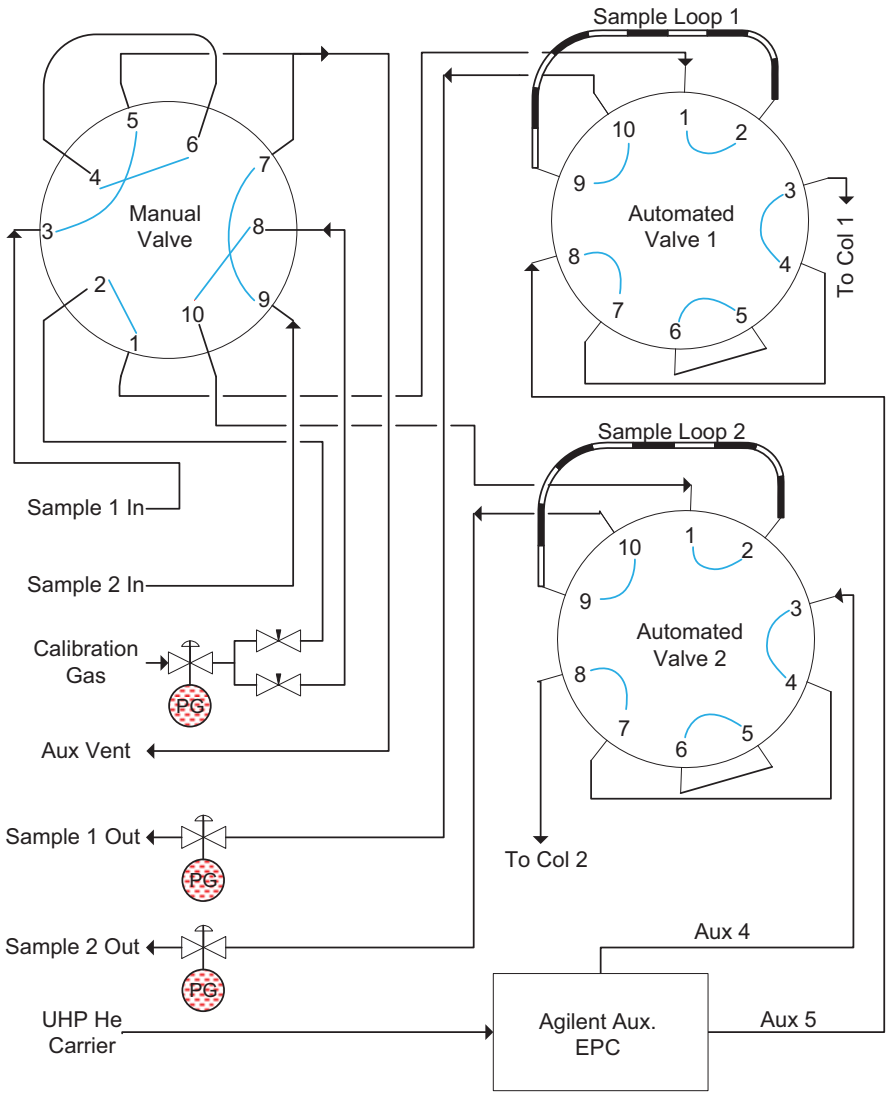

Figure A.4: GC F Plumbing and valve position during GC calibration.

A.3 Example TCD Calibration

The GC TCDs were calibrated with a standard calibration gas with a known composition (e.g. 36.0% H_2, 4.0% Ar, 29.1% CO, 1.0% CH_4, 2.0% CO_2, 0.5% C_2H_6, 27.4% He) by changing the total number of moles of sample in the sample loop via the sample loop back pressure regulator. Figures A.5 to A.10 show the resulting calibration slopes and the relative response factors (*RF*) normalized to Ar for TCD A of GC F. Calibration slopes for TCD B of GC F and for GC B are similar. Table A.1 gives the relative response factors for all three detectors.

Table A.1: Relative response factors for the reactor effluent gases for the three TCD detectors on the GC instruments (two on GC F and one on GC B).

TCD	H_2	Ar	CO	CH_4	CO_2	C_2H_6
F A	0.0695	1.00	0.878	0.714	1.21	1.19
F B	0.0629	1.00	0.892	0.722	1.20	1.20
B	0.0462	1.00	0.888	0.682	1.05	1.02

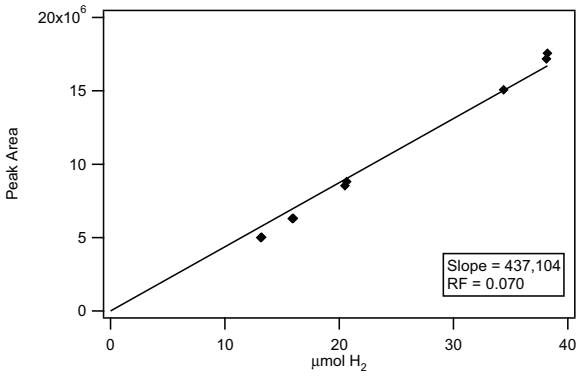

Figure A.5: Calibration curve for H_2 on TCD A of GC F and the relative response factor.

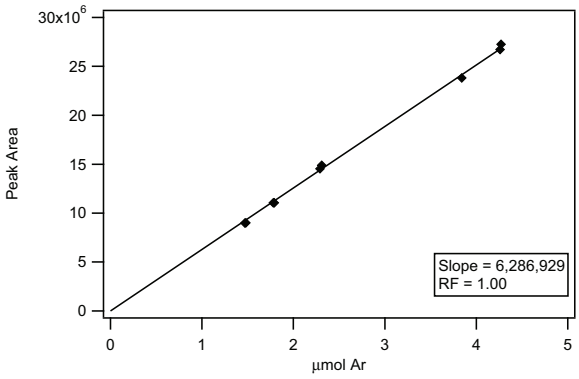

Figure A.6: Calibration curve for Ar on TCD A of GC F and the relative response factor.

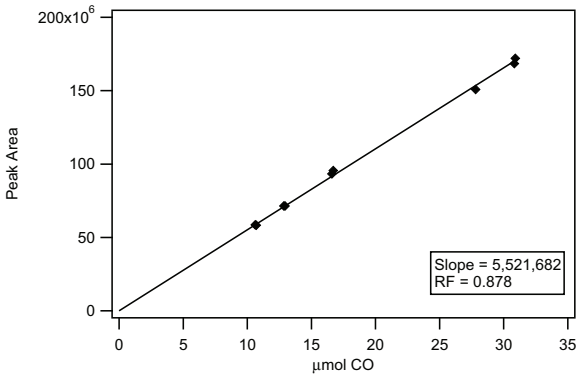

Figure A.7: Calibration curve for CO on TCD A of GC F and the relative response factor.

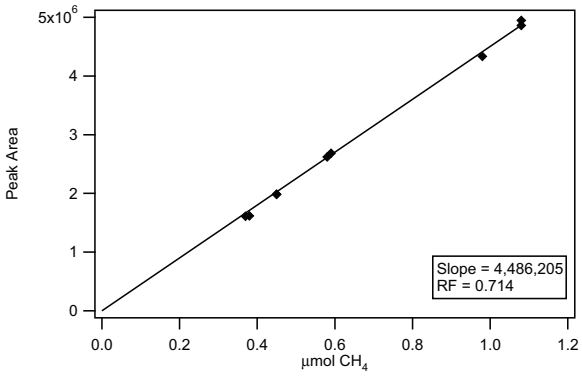

Figure A.8: Calibration curve for CH_4 on TCD A of GC F and the relative response factor.

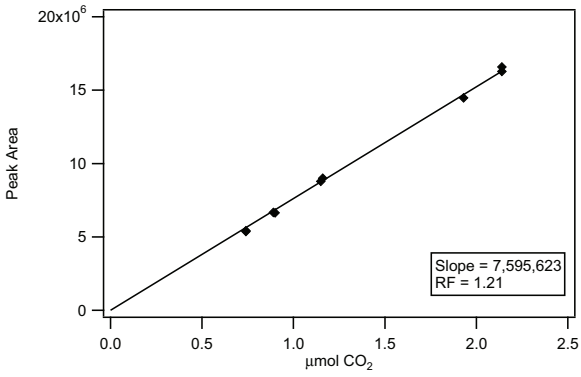

Figure A.9: Calibration curve for CO_2 on TCD A of GC F and the relative response factor.

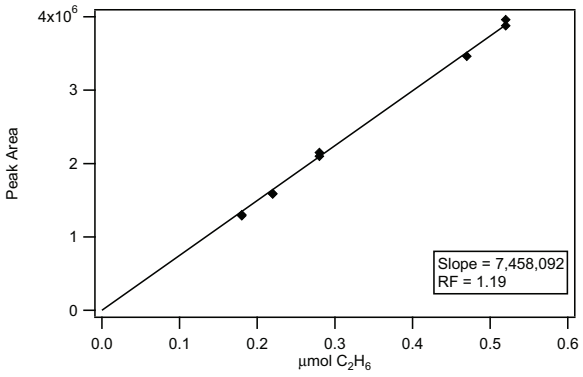

Figure A.10: Calibration curve for C_2H_6 on TCD A of GC F and the relative response factor.

A.4 Example Chromatograms

Three Agilent GC instruments were used in analyzing the FT feed gases and products. Two were Agilent 6890 GC instruments and were used for continuous online analysis of the reactor effluent gases by TCD for different runs (see Section 2.3.5 and Table 2.5). These two instruments, their operation, and their oven programs are described in Section 2.4.1. The third instrument was an Agilent 7890 GCMS and was used only for peak identification of liquid and wax products and is described in Section 2.4.3 along with its operation and oven program. One of the 6890 instruments (GC B) was equipped with an FID detected and capillary column and was used for quantification of liquid and wax products.

A.4.1 Gas Products and Feed Gases

Gas products and feed gases were analyzed using a TCD detector in an Agilent 6890. Figure A.11 shows an example chromatogram of the reactor effluent gas from 349.9 h on stream of R2 of FB run 10 (2UH). The C_{3+} species shown is not observed with every catalyst.

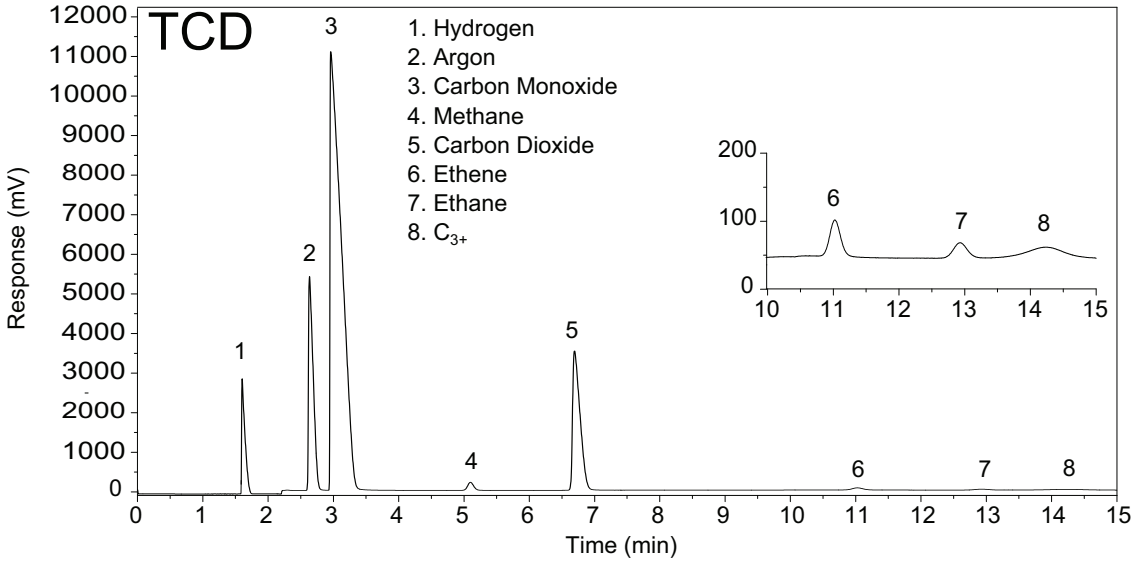

Figure A.11: Example chromatogram of effluent gas from R2 of FB run 10 (2UH) at 349.9 h ($T = 250$ °C, $X_{CO} = 0.24$, $H_2/CO = 0.73$) analyzed by TCD. The inset shows details of the small peaks of ethene, ethane, and C_{3+} (not always observed) products. The instrument and settings are described in Section 2.4.1.

A.4.2 Aqueous Products

Cold trap products in the aqueous phase were quantified by FID in GC B. A chromatogram from the GCMS (MS) with an overlay of a chromatogram from GC B (FID) is shown in Figure A.12. The FID chromatogram was stretched so that matching GCMS and FID peaks appear at about the same distance from the left hand side of the image.

A.4.3 Oil Products

Cold trap products in the organic phase were analyzed by FID in GC B. A chromatogram from the GCMS (MS) with an overlay of a chromatogram from GC B (FID) is shown in Fig-

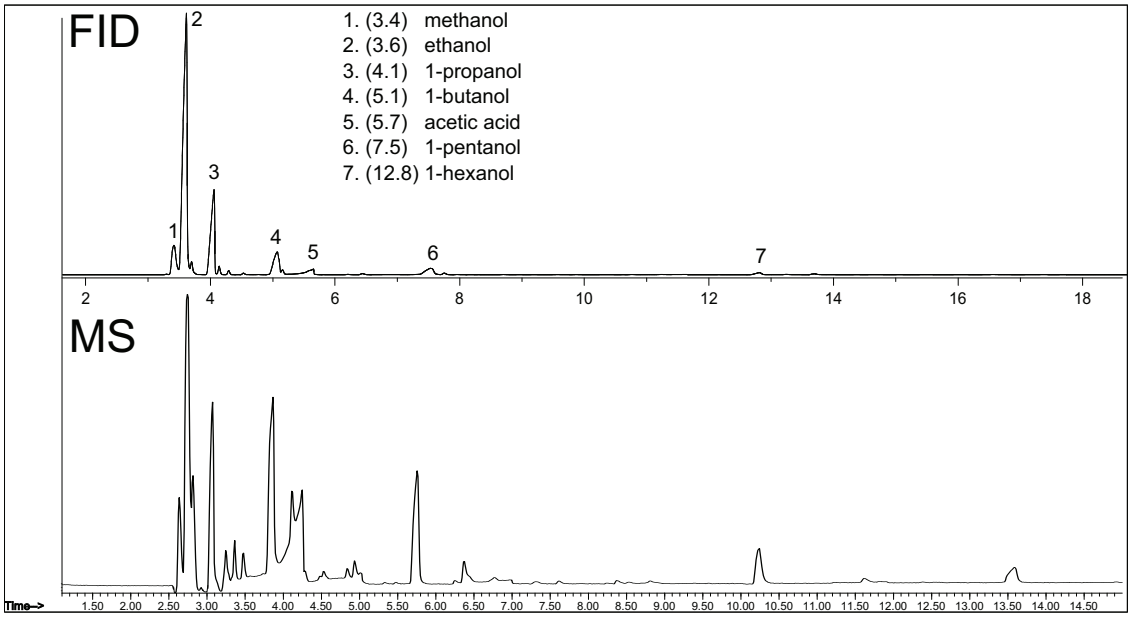

Figure A.12: GCMS chromatogram with FID overlay of aqueous products of 2UH from R1 of FB run 2. GC equipment, procedures, and oven programs are given in Sections 2.4.1 and 2.4.3.

ures A.17 to A.21. The chromatogram is split to show better detail. The FID chromatogram was stretched so that matching GCMS and FID peaks appear at about the same distance from the left hand sides of the images. Peaks on the FID chromatogram are labeled since these are the quantified peaks. Only major peaks are labeled and identified repeatedly. Relative peak heights are preserved among the figures.

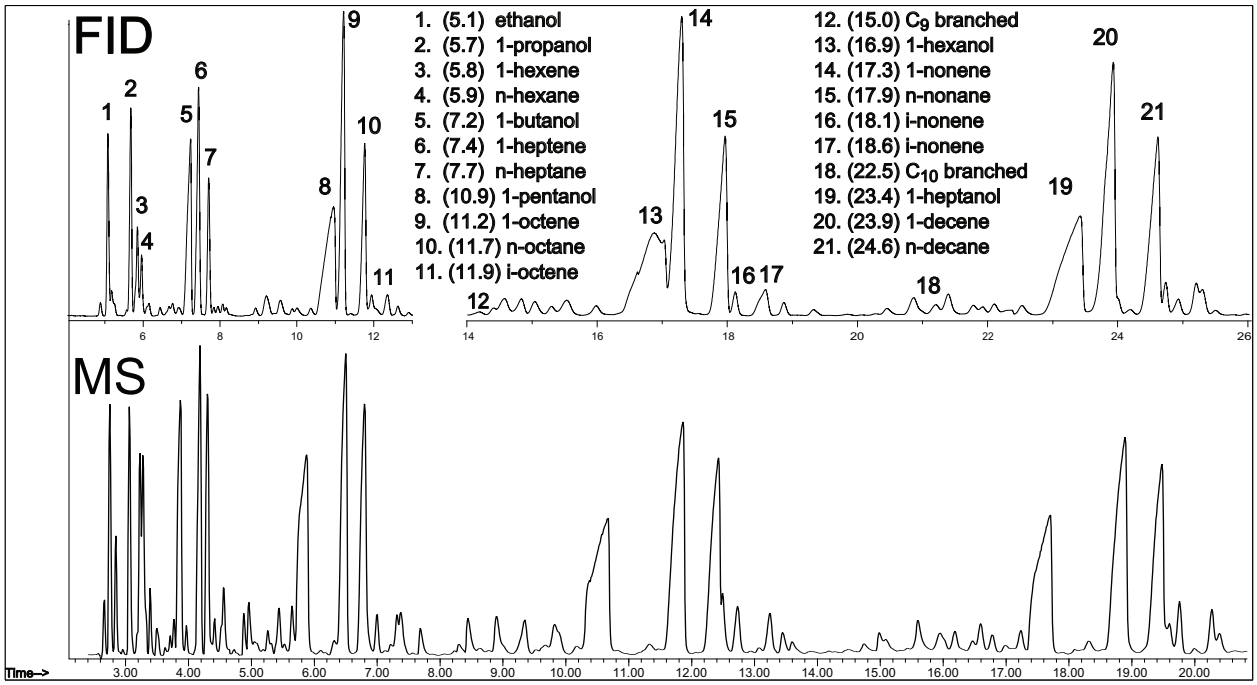

Figure A.13: GCMS chromatogram with FID overlay of oil products of 2UH (R1, FB run 10) (0–21 min). GC equipment, procedures, and oven programs are given in Sections 2.4.1 and 2.4.3.

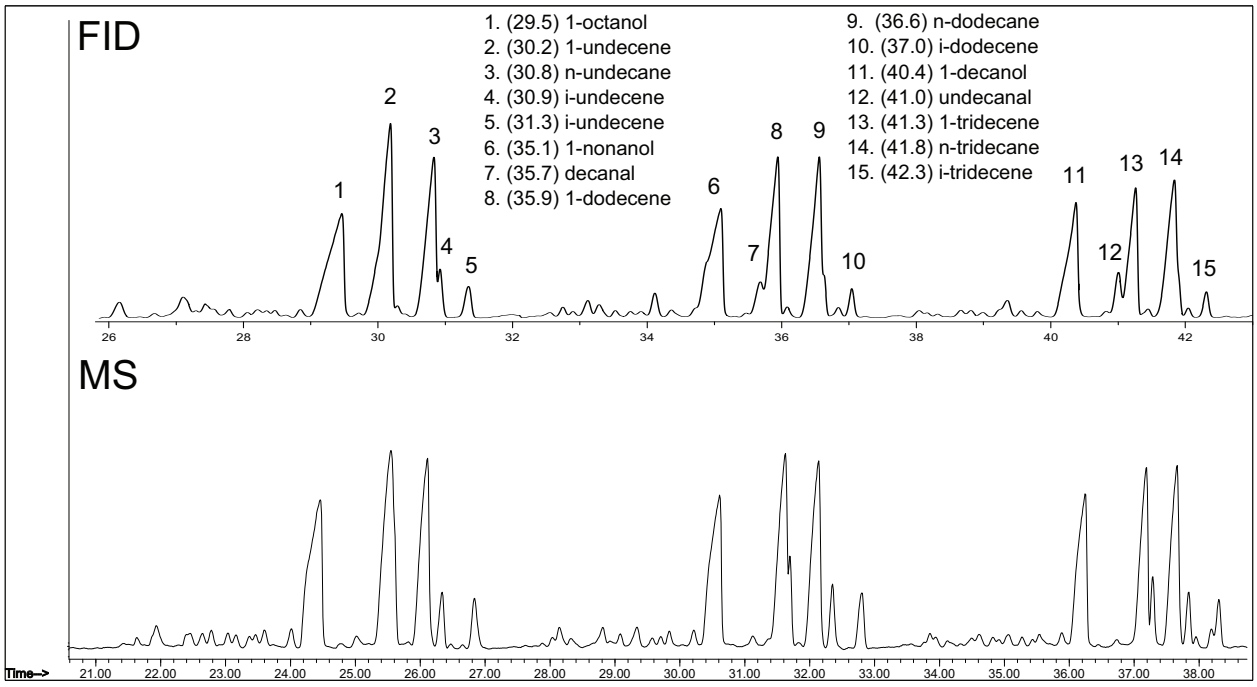

Figure A.14: GCMS chromatogram with FID overlay of oil products of 2UH (R1, FB run 10) (21–39 min). GC equipment, procedures, and oven programs are given in Sections 2.4.1 and 2.4.3.

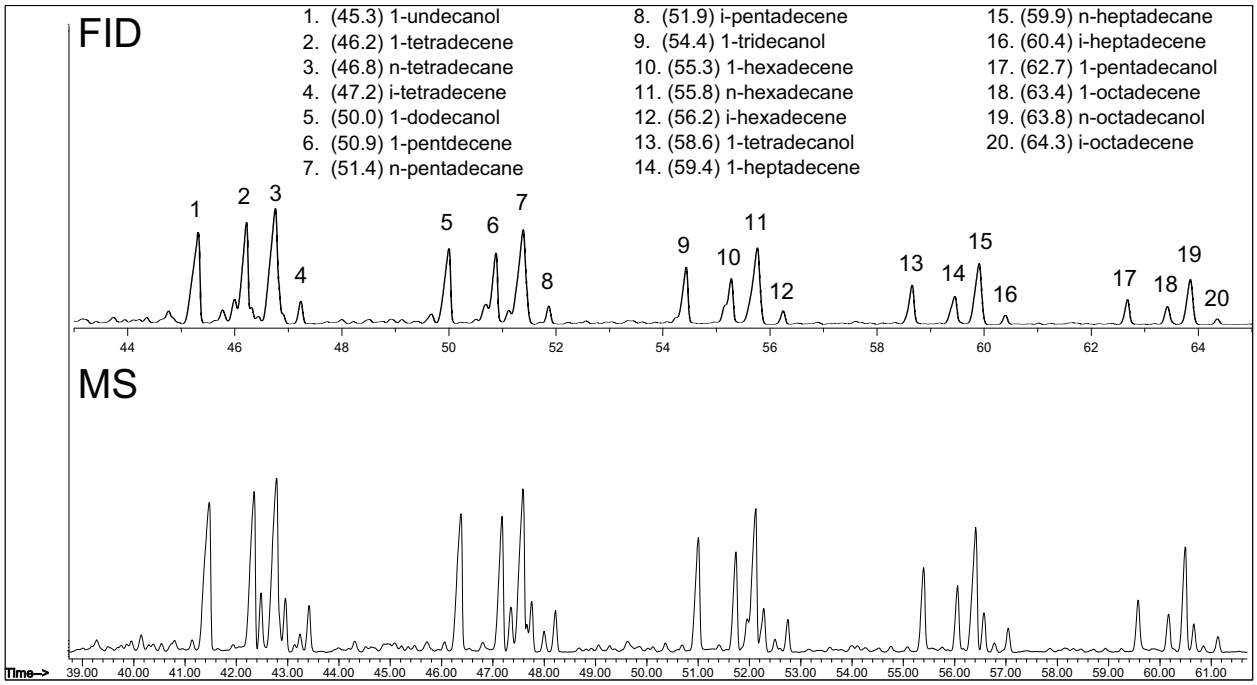

Figure A.15: GCMS chromatogram with FID overlay of oil products of 2UH (R1, FB run 10) (39–62 min). GC equipment, procedures, and oven programs are given in Sections 2.4.1 and 2.4.3.

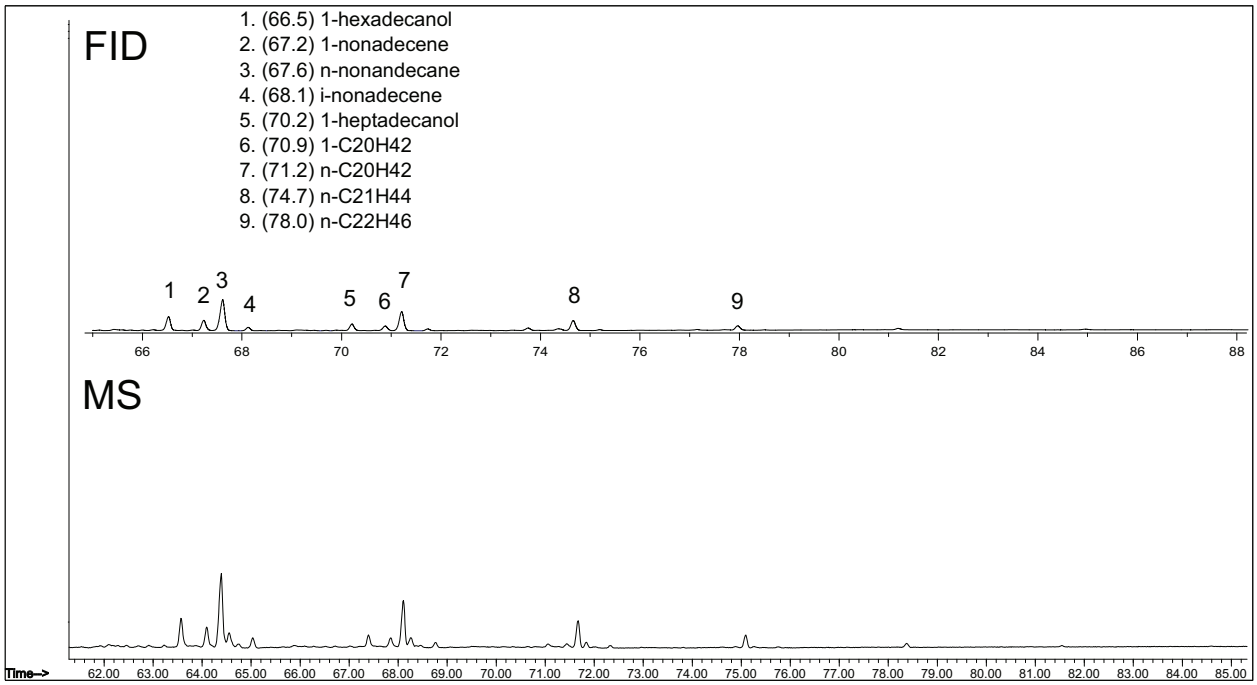

Figure A.16: GCMS chromatogram with FID overlay of oil products of 2UH (R1, FB run 10) (61–86 min). GC equipment, procedures, and oven programs are given in Sections 2.4.1 and 2.4.3.

A.4.4 Wax Products

Wax products were dissolved in a solvent (CH_2CL_2 or hexanes) and quantified by FID in GC B. A chromatogram from the GCMS (MS) with an overlay of a chromatogram from GC B (FID) is shown in Figures A.17 to A.21. The chromatogram is split to show better detail. The FID chromatogram was stretched so that matching GCMS and FID peaks appear at about the same distance from the left hand sides of the images.

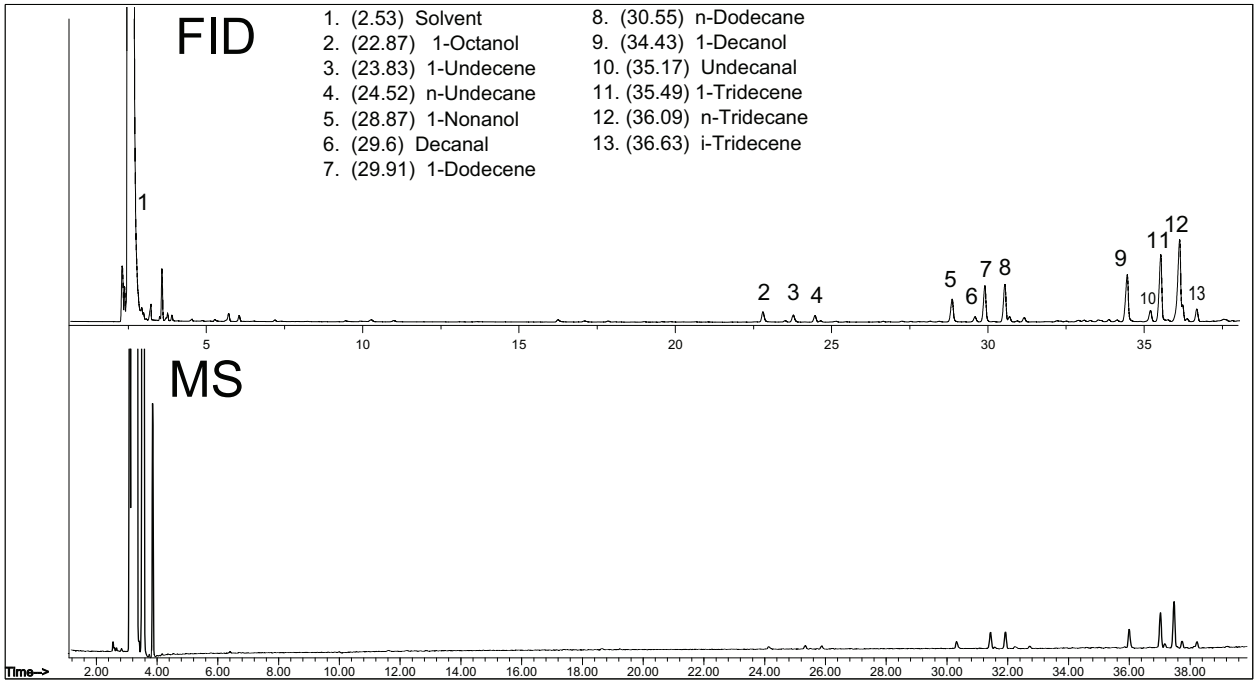

Figure A.17: GCMS chromatogram with FID overlay of wax products of 2UH (R1, FB run 10) (0–40 min). GC equipment, procedures, and oven programs are given in Sections 2.4.1 and 2.4.3.

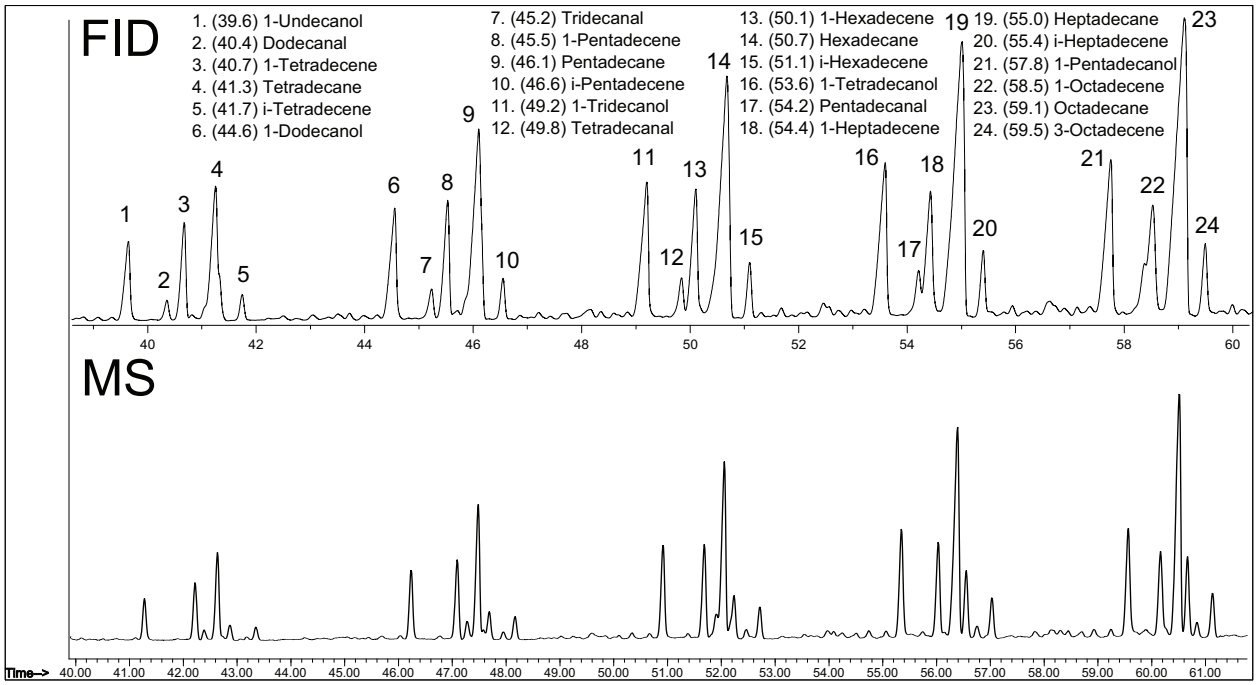

Figure A.18: GCMS chromatogram with FID overlay of wax products of 2UH (R1, FB run 10) (40–62 min). GC equipment, procedures, and oven programs are given in Sections 2.4.1 and 2.4.3.

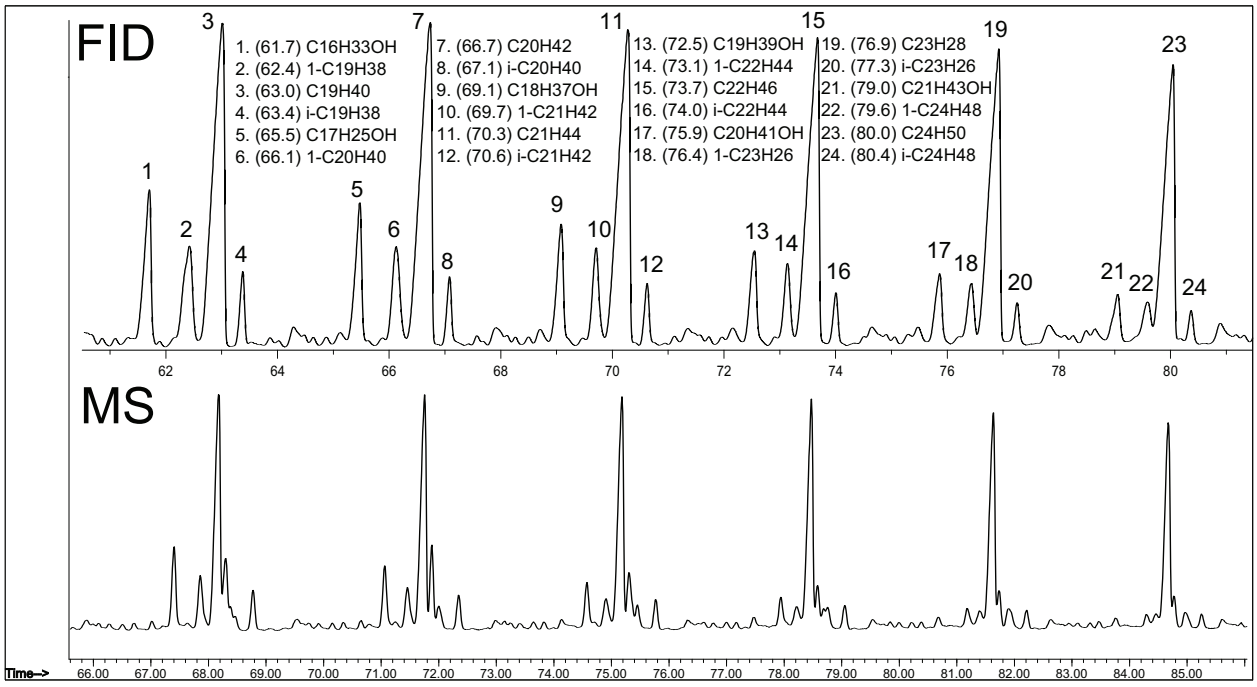

Figure A.19: GCMS chromatogram with FID overlay of wax products of 2UH (R1, FB run 10) (66–86 min). GC equipment, procedures, and oven programs are given in Sections 2.4.1 and 2.4.3.

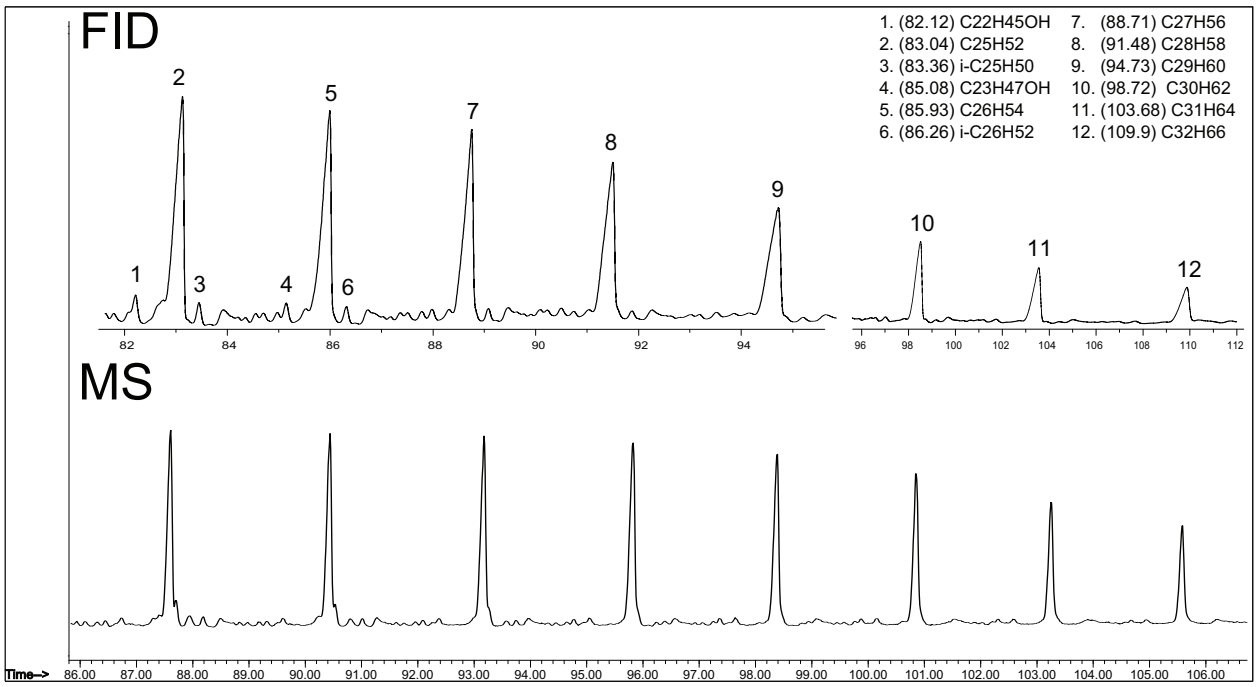

Figure A.20: GCMS chromatogram with FID overlay of wax products of 2UH (R1, FB run 10) (86–107 min). GC equipment, procedure, and oven program are given in Sections 2.4.1 and 2.4.3.

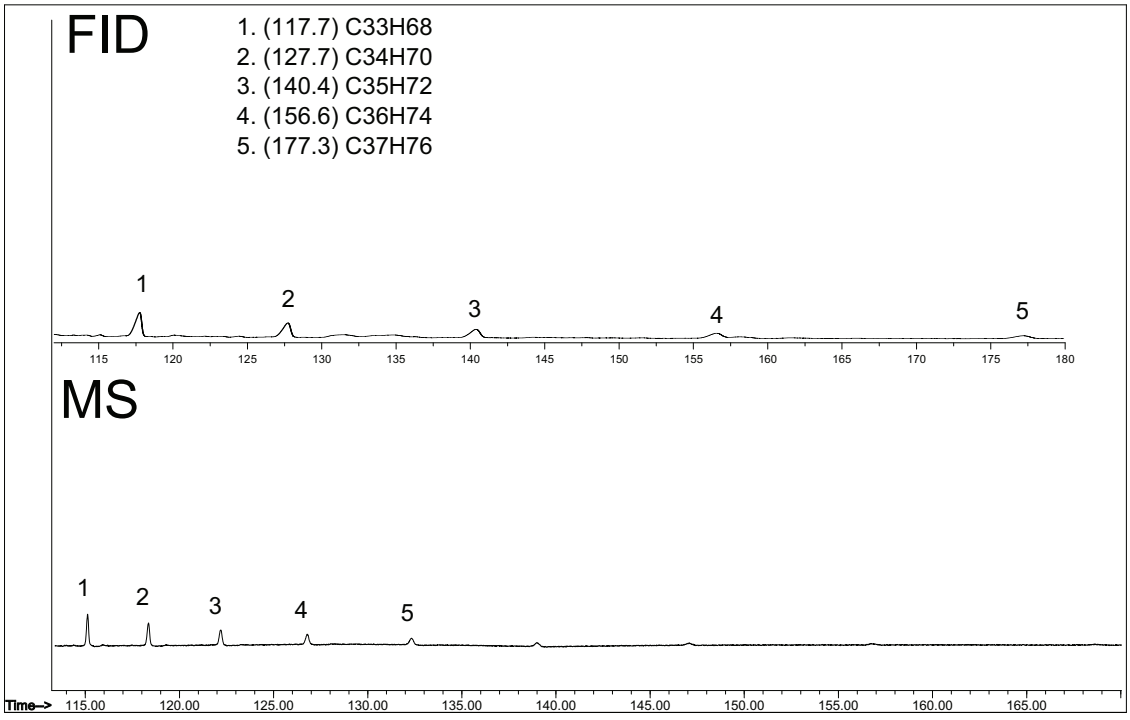

Figure A.21: GCMS chromatogram with FID overlay of wax products of 2UH (R1, FB run 10) (105–170 min). GC equipment, procedure, and oven program are given in Sections 2.4.1 and 2.4.3.

A.5 Overlapping GC Peaks

Due to operator error in devising GC oven programming, the C_2H_4 and C_2H_6 peaks were not always completely recorded on chromatograms or may have eluted near other peaks. For oven programs that were < 13 min on GC B or < 15.2 min on GC F, the C_2H_4 and C_2H_6 peaks from one injection eluted with peaks of a second injection after retention in the column during the cool down between injections. Where possible, overlapping peaks were split or else were estimated from chromatograms in the same FB run that did not suffer from peak overlap.

In the case of FB run 6 (1UH and 1WH), the C_2H_4 peak was closely associated with the CO peak; however, the peak area of C_2H_4 was less than 1% of the peak area of CO ($< 1,000,000$ counts compared to $> 100,000,000$ counts) which is about equal to the uncertainty in the calculations of CO conversion and rate of reaction.

For R2 of FB run 7 (1WL), the C_2H_4 and C_2H_6 peaks are merged and are quantified together using the GC response for C_2H_6 which underestimates the molar count of C_2H_4 by $< 5\%$. This means that the estimate of C_2H_6 for this catalyst is in error, but the total C_2 count is reasonably accurate.

For FB run 3 (2UL and 2WH), the C_2H_4 peak was merged with the CH_4 peak; however, some unexplained variation in the GC automation resulted in an occasional, random injection and start of GC analysis that occurred before the oven had completely cooled to the starting temperature which resulted in complete separation of the C_2H_4 and CH_4 peaks. The resulting ratios of C_2H_4 to CH_4 peak areas were consistent throughout the FB run at about 0.22 and 0.28 for 2UL and 2WH, respectively, and these ratios were used to estimate the relative peak areas of these two species from the combined peak area in the chromatograms. The values of the ratios may have been as low as 0.15 and 0.19 which correspond with up to a 10% increase in the estimates of the CH_4 selectivities and a 33% decrease in the estimates of the C_2H_4 selectivities.

For FB runs 1 (P1 and 1ULa), 2 (P2 and 1WLa), and 4 (2DH, and 2DL), the chromatograms appeared to capture only 50–90% of the peak area for C_2H_6 depending on the run, but no correction was made to the reported selectivity of C_2H_6.

For runs 8 (1DH and 1DL) and 9 (1UH and 1UHa), the C_2H_4 peak was likely eluted during oven cool down between GC injections and no values for C_2H_4 are reported.

APPENDIX B. AUXILIARY KINETIC DATA

This appendix reports joint confidence regions, an example calculation for integral reactor performance analysis, and the script used for fitting parameters and generating confidence regions. The joint confidence regions are of the pre-exponential factors and activation energies for all catalysts in this dissertation. The example calculation includes an error analysis for calculating rate constant using the differential performance equation instead of the integral equation.

B.1 Approximate Joint Confidence Regions for Estimated Parameters

Approximate joint 95% confidence regions for estimated pre-exponential factors and activation energies of the 17 catalysts in this study are reported here.

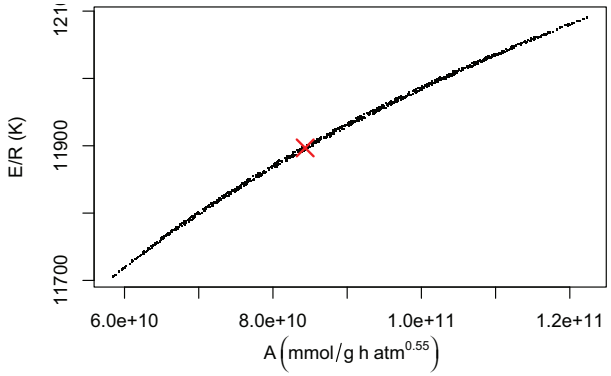

Figure B.1: Approximate 95% joint confidence region for estimated parameters for 1UH.

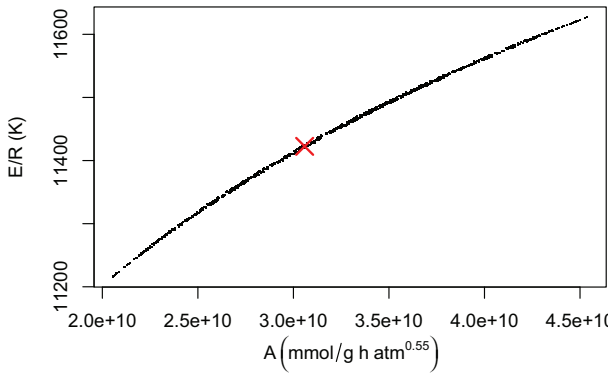

Figure B.2: Approximate 95% joint confidence region for estimated parameters for 1UL.

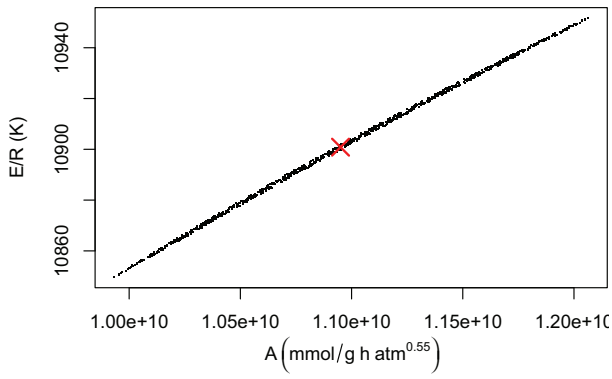

Figure B.3: Approximate 95% joint confidence region for estimated parameters for 1WH.

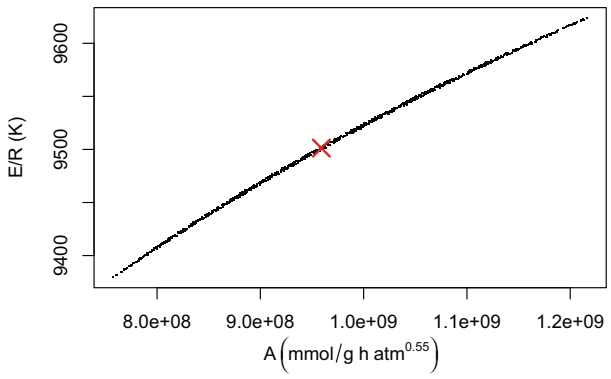

Figure B.4: Approximate 95% joint confidence region for estimated parameters for 1WL.

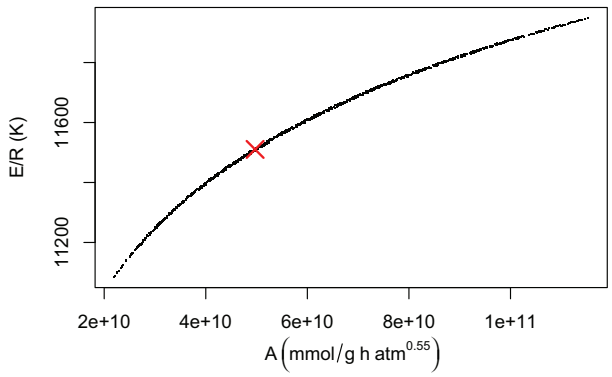

Figure B.5: Approximate 95% joint confidence region for estimated parameters for 2UH.

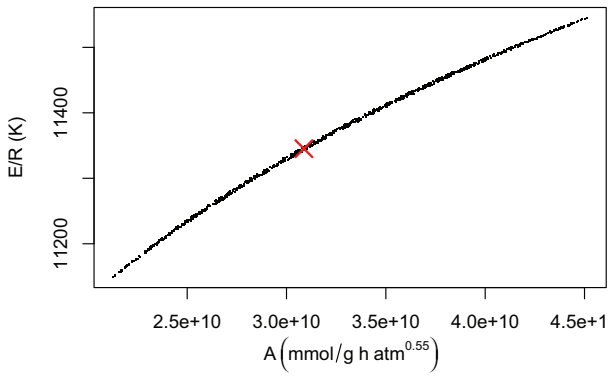

Figure B.6: Approximate 95% joint confidence region for estimated parameters for 2UL.

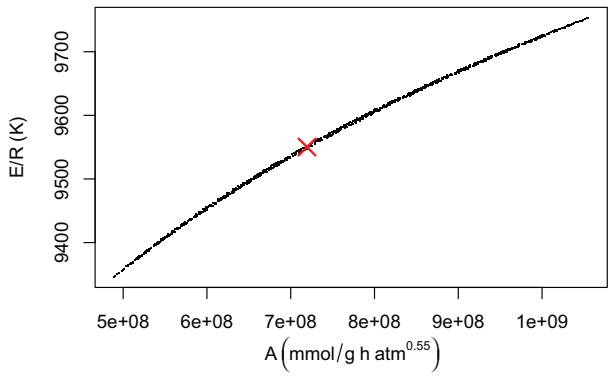

Figure B.7: Approximate 95% joint confidence region for estimated parameters for 2WH.

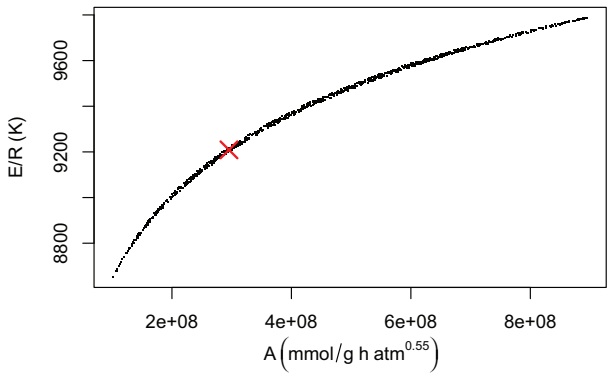

Figure B.8: Approximate 95% joint confidence region for estimated parameters for 2WL.

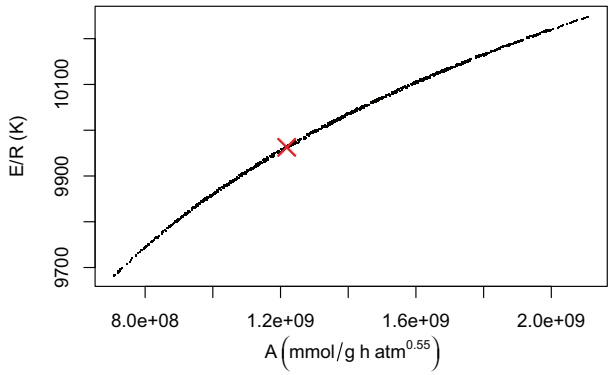

Figure B.9: Approximate 95% joint confidence region for estimated parameters for 1DH.

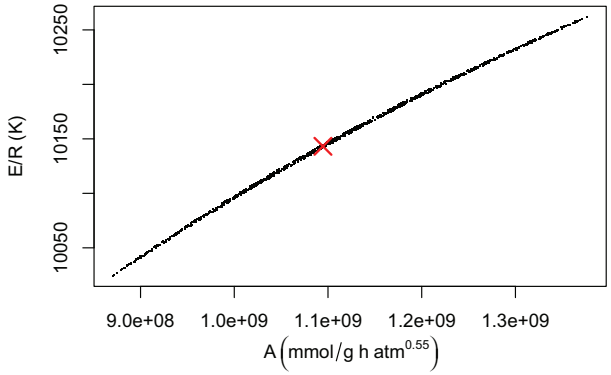

Figure B.10: Approximate 95% joint confidence region for estimated parameters for 1DL.

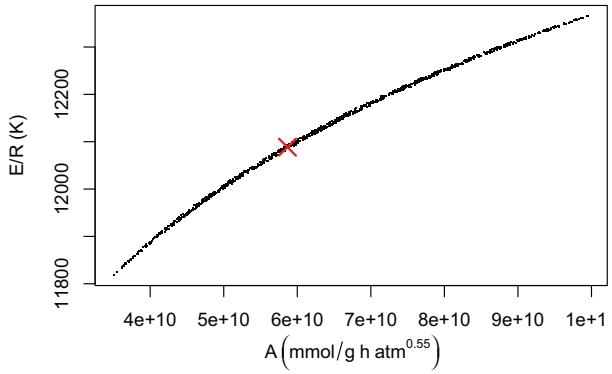

Figure B.11: Approximate 95% joint confidence region for estimated parameters for 2DH.

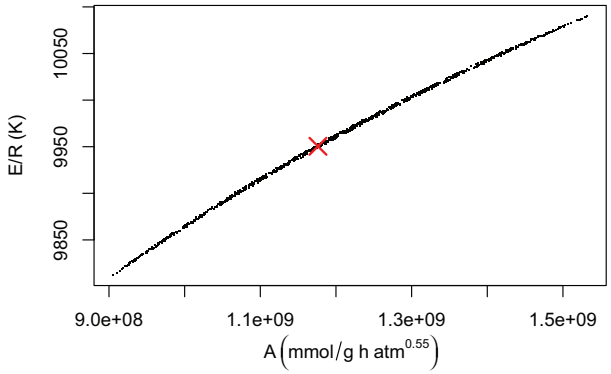

Figure B.12: Approximate 95% joint confidence region for estimated parameters for 2DL.

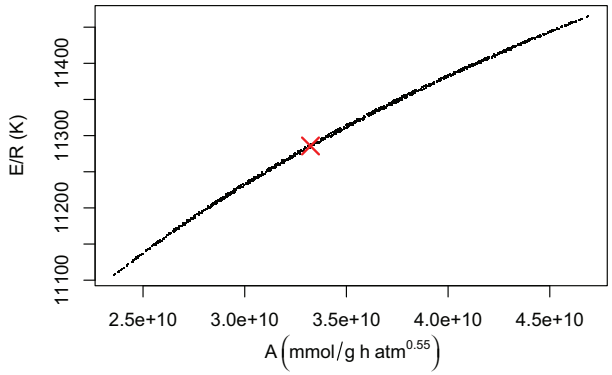

Figure B.13: Approximate 95% joint confidence region for estimated parameters for 1UHa.

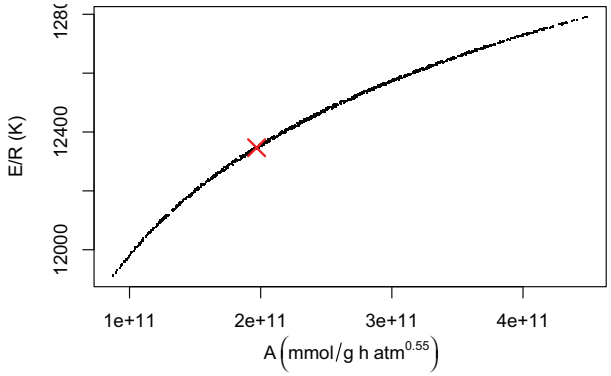

Figure B.14: Approximate 95% joint confidence region for estimated parameters for 1ULa.

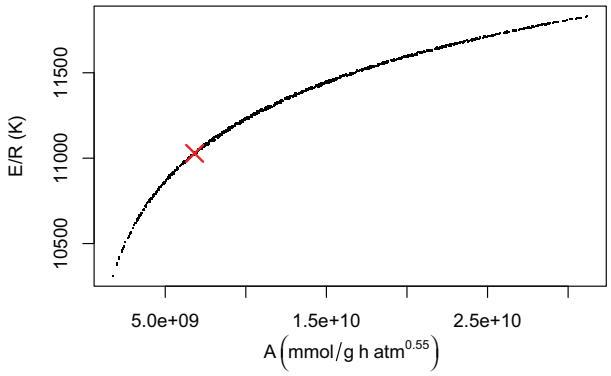

Figure B.15: Approximate 95% joint confidence region for estimated parameters for 1WLa.

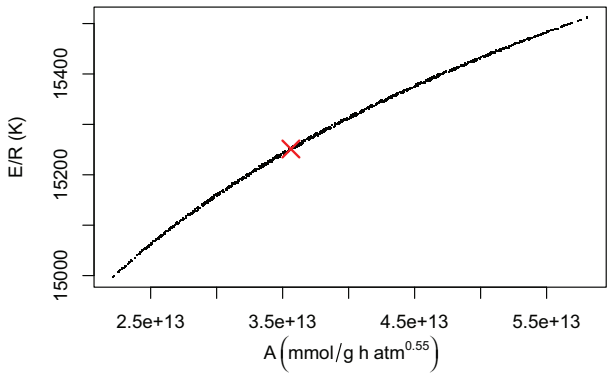

Figure B.16: Approximate 95% joint confidence region for estimated parameters for P1.

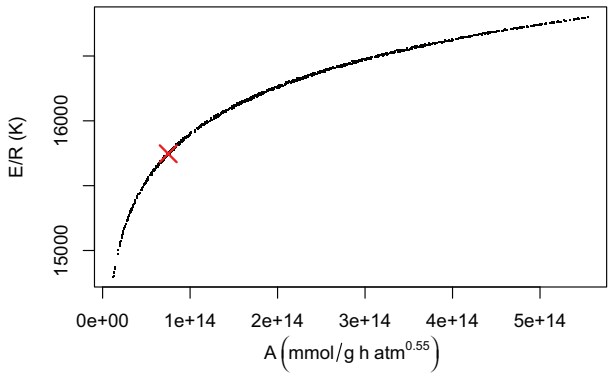

Figure B.17: Approximate 95% joint confidence region for estimated parameters for P2.

B.2 Example Calculation of the Integral Reactor Performance Equation

The following example calculation uses data from FB Run 2 on 1ULa. This is the data collected at 277 °C at a CO conversion of 60.7%.

Define constants and input the data

$mmol := 10^{-3}mol$ $H2COst := 0.7048$ Stoichiometric H_2 to CO ratio

$F_{CO0} := 76.532\frac{mmol}{hr}$ $F_{H20} := 74.639\frac{mmol}{hr}$ Feed flow rates of CO, H2, Ar, and He to the reactor.

$F_{Ar} := 10.744\frac{mmol}{hr}$ $F_{He} := 78.778\frac{mmol}{hr}$

$S_{CO2} := 0.4184$ $S_{CH4} := 0.06387$ $S_{C2H4} := 0.01635$ $S_{C2H6} := 0.03743$ Selectivities of products are assumed to be constant.

$P_{tot} := 21.246atm$ $W_{cat} := 0.499gm$ Mass of catalyst charged.

$k_{diff} := 35.866\frac{mmol}{gm\cdot hr\cdot atm^{0.55}}$ $X_{COF} := 0.6066$ Rate constant using the differential equation and final conversion

Reactor performance equation for an integral system

$$\frac{dW}{F_{CO0}} = \frac{dX_{CO}}{-r_{CO}(X_{CO})}$$ Reactor performance equation to be integrated.

$$\frac{1}{F_{CO0}}\cdot\int_0^{W_{cat}} 1\,dW = \int_0^{X_{COf}} \frac{1}{-r_{CO}(X_{CO})}\,dX_{CO}$$

Assume a rate equation

$-r_{CO} = k\cdot P_{CO}^{-0.05}\cdot P_{H2}^{0.6}$ Assume the Eliason partial pressure dependences.

Get partial pressures as functions of conversion

$F_{CO}(X_{CO}) := F_{CO0}\cdot(1 - X_{CO})$ Express molar flow rate of each species as a function of conversion.

$F_{H2}(X_{CO}) := F_{H20} - H2COst\cdot F_{CO0}\cdot X_{CO}$

$F_{Ar} := F_{Ar}$

$F_{He} := F_{He}$

$$F_{CO2}(X_{CO}) := X_{CO} \cdot F_{CO0} \cdot S_{CO2}$$

$$F_{CH4}(X_{CO}) := X_{CO} \cdot F_{CO0} \cdot S_{CH4}$$

$$F_{C2H4}(X_{CO}) := X_{CO} \cdot F_{CO0} \cdot \frac{S_{C2H4}}{2}$$

$$F_{C2H6}(X_{CO}) := X_{CO} \cdot F_{CO0} \cdot \frac{S_{C2H6}}{2}$$

$$F_{H2O}(X_{CO}) := X_{CO} \cdot F_{CO0} \cdot (1 - 2 \cdot S_{CO2})$$

1 mol H_2O not made + 1 mol H_2O consumed in WGS.

$$F_{tot}(X_{CO}) := F_{CO}(X_{CO}) + F_{H2}(X_{CO}) + F_{Ar} + F_{He} + F_{CO2}(X_{CO}) \ldots + F_{CH4}(X_{CO}) + F_{C2H4}(X_{CO}) + F_{C2H6}(X_{CO}) + F_{H2O}(X_{CO})$$

$$y_{CO}(X_{CO}) := \frac{F_{CO}(X_{CO})}{F_{tot}(X_{CO})}$$

Calculate the mole fractions of CO and H_2 as functions of CO conversion.

$$y_{H2}(X_{CO}) := \frac{F_{H2}(X_{CO})}{F_{tot}(X_{CO})}$$

$$P_{CO}(X_{CO}) := y_{CO}(X_{CO}) \cdot P_{tot}$$

Calculate partial pressures of CO and H_2 as functions of CO conversion.

$$P_{H2}(X_{CO}) := y_{H2}(X_{CO}) \cdot P_{tot}$$

Substitute back into the performance equation

$$\frac{1}{F_{CO0}} \cdot \int_0^{W_{cat}} 1 \, dW = \int_0^{X_{COf}} \frac{1}{k \cdot P_{CO}(X_{CO})^{-0.05} \cdot P_{H2}(X_{CO})^{0.6}} \, dX_{CO}$$

Full performance equation in terms of all the proper variables.

Solve for rate constant

$$k(X_{COf}) := \frac{F_{CO0}}{W_{cat}} \cdot \int_0^{X_{COf}} \frac{1}{P_{CO}(X_{CO})^{-0.05} \cdot P_{H2}(X_{CO})^{0.6}} \, dX_{CO}$$

Rearrange the performance equation to solve for rate constant.

$$k(X_{COF}) = 35.751 \cdot \frac{mmol}{gm \cdot hr \cdot atm^{0.55}}$$

This is the integrated value of the rate constant.

$$k_{error} := \frac{\left| k(X_{COF}) - k_{diff} \right|}{k(X_{COF})} = 0.323 \cdot \%$$

The error between the differential and integral rate constants.

B.3 R Script for Parameter Estimation and Confidence Region Calculation

The following script was written for R version 2.14.1 and was used to estimate kinetic parameters by non-linear least squares minimization for the catalysts in this dissertation in a single batch.

To use this script, the path name of the data files should be changed to the location of the data files. The script defines a function to perform the parameter estimation and a separate loop which calls the function. This setup allows for error handling through the try command which prevents one bad data set from stopping the entire batch. Data file names should be sequential to accommodate batch processing. The nls function performs the actual estimation and requires initial values of the parameters as inputs. The initial values of parameters should be within a couple of orders of magnitude of the best estimates or else nls returns an error. The nlsConfRegions function requires inputs for the number of data points to find within the CR (length variable) and the area over which to search for them (exp variable). If the search area is too small, only a portion of the CR will be found. The only downside to increasing the search area is an exponential increase in the computation time. The CR is saved as a PDF with a sequentially increasing name. The PDF dimensions are defined in inches. The points function adds a large red "X" at the value of the best estimates of the parameters.

```
##########################################################################
### This script uses the nls and nlsConfRegions functions of nlstools to ###
### estimate parameter values and approximate joint 95% confidence       ###
### regions.                                                             ###
### Inputs are 2-column tab-delimited text files containing experimental ###
### data for k (rate constant) and Temp (with those labels in the first  ###
### row of data) for each set of parameters to be fit.                   ###
### Outputs are 1) a *.csv file containing the parameter estimates and   ###
### some statistics of the estimate and 2) a pdf of the joint confidence ###
### region for each set of parameters.                                   ###
##########################################################################
```

```
### Load necessary packages
library(nlstools)

### Define the function for parameter estimation
E1 <- k ~ A * exp(-ER / Temp)

### Define a new function to perform the actual fitting.
nlsfitting <- function(i, dA){
  solA <- nls(E1, dA, start = list(A = 1E8, ER = 0.9E4),
    control = list(maxiter = 500))
  return(solA)
}

### Set up a loop to do all the fitting in one batch.
for(i in 1:17) {
  fo <- paste("C:\\Data_Folder_Name\\", i, sep = "")
  fo <- paste(fo, ".txt", sep = "")
  dA <- read.table(fo, header = TRUE)
  solA <- try(nlsfitting(i, dA))
  if(class(solA) == "try-error") next;
  if (i == 1) {solset <- coef(summary(solA))} else
    {solset <- rbind(solset, coef(summary(solA)))}
  pA <- nlsConfRegions(solA, length = 1000, exp = 4)
  svfile <- paste("C:\\Data_Folder_Name\\PDF_Name", i, sep = "")
  svfile <- paste(svfile, ".pdf", sep = "")
  pdf(svfile, width = 5.4, height = 3.3337)
  par(mar = c(4, 4, 0, 0) + 0.1)
  plot(pA$cr[,1], pA$cr[,2], pch = ".", xlab =
    expression("A"~bgroup("(",mmol/g~h~atm^{0.55},")")), ylab = "E/R (K)")
  points(coef(solA)[1], coef(solA)[2], col = "red", pch = 4, lwd = 2,
```

```
    cex = 2)
  dev.off()
}

### Save the table of parameter estimates to a *.csv file.
write.table(solset, file = "C:\\Data_Folder_Name\\solutions.csv", sep = ",",
  col.names = NA)

##############################################################################
### End script file                                                        ###
##############################################################################
```

APPENDIX C. STEADY STATE FIXED-BED REACTOR DATA

The steady state kinetic data for the 10 FB runs are presented here. Tables C.1 to C.3 report kinetic data, selectivity data, and effluent gas composition data, respectively. All values are averages of data collected at the reported conditions. Data not included in parameter estimation data sets are indicated by an asterisk.

Table C.1: Steady state kinetic data for the 10 FB runs. FB run numbers are given below each catalyst name e.g. rn6 indicates FB run 6. Data not included in parameter estimation data sets are indicated by an asterisk.

Cat.	TOS	T	$\overline{P_{H_2}}$	$\overline{P_{CO}}$	F_{H_2}	F_{CO}	F_{Ar}	F_{He}	$-r_{CO}$	$-r_{H_2}$	X_{CO}	X_{H_2}	Prod.
	h	°C	atm	atm	mmol/h				mmol/g/h		%	%	g/g/h
1UH	221	250	6.5	5.8	42.4	38.3	4.9	42.1	30.4	28.3	20.2	17.0	0.223
rn6	259	262	6.3	5.4	42.4	38.3	4.9	42.1	48.8	41.0	32.5	24.7	0.340
	286	241	6.7	6.0	42.4	38.3	4.9	42.1	19.9	18.7	13.3	11.3	0.152
	315	240	6.7	6.0	42.4	38.3	4.9	42.1	20.8	17.8	13.8	10.7	0.158
	345	221	6.9	6.3	42.4	38.3	4.9	42.1	7.7	9.7	5.1	5.9	0.069
	388	232	6.8	6.1	42.4	38.3	4.9	42.1	14.2	14.7	9.4	8.9	0.110
	414	249	6.5	5.7	42.4	38.3	4.9	42.1	33.3	30.2	22.2	18.2	0.239
	460	240	6.7	6.0	42.4	38.3	4.9	42.1	21.1	20.8	14.0	12.5	0.160
	477	221	6.9	6.3	42.4	38.3	4.9	42.1	7.3	9.3	4.9	5.6	0.064
	501	226	6.6	6.0	41.3	37.3	4.8	41.0	13.7	14.7	9.2	8.9	0.109
1UL	94	251	5.6	5.6	33.9	33.9	4.5	44.9	27.3	26.7	20.1	19.7	0.219
rn7	113	240	5.8	5.8	33.9	33.9	4.5	44.9	17.4	19.8	12.9	14.6	0.154
	124	221	5.9	6.0	33.9	33.9	4.5	44.9	8.5	12.1	6.3	9.0	0.091
	139	231	5.9	5.9	33.9	33.9	4.5	44.9	12.6	15.3	9.3	11.3	0.120
	166	249	5.7	5.6	33.9	33.9	4.5	44.9	25.1	22.2	18.5	16.4	0.183
	185	241	5.8	5.8	33.9	33.9	4.5	44.9	17.1	16.5	12.6	12.2	0.131
	195	221	6.0	6.0	33.9	33.9	4.5	44.9	6.4	8.7	4.7	6.4	0.055
	206	230	5.9	6.0	33.9	33.9	4.5	44.9	10.2	12.6	7.5	9.3	0.085
	223	241	5.8	5.8	33.9	33.9	4.5	44.9	17.9	18.0	13.2	13.3	0.136
1WH	217	249	6.2	6.1	44.1	39.8	5.1	43.7	26.9	53.2	16.9	30.2	0.260
rn6	243	260	6.0	5.9	44.1	39.8	5.1	43.7	38.4	67.1	24.1	38.1	0.346
	328	240	6.5	6.2	44.1	39.8	5.1	43.7	17.7	35.7	11.1	20.3	0.180

— Continued on next page —

Table C.1 — continued from previous page

Cat.	TOS	T	$\overline{P_{H_2}}$	$\overline{P_{CO}}$	F_{H_2}	F_{CO}	F_{Ar}	F_{He}	$-r_{CO}$	$-r_{H_2}$	X_{CO}	X_{H_2}	Prod.
	h	°C	atm	atm	mmol/h				mmol/g/h		%	%	g/g/h
	360	226	6.7	6.3	44.1	39.8	5.1	43.7	10.3	23.9	6.5	13.5	0.113
	393	231	6.6	6.3	44.1	39.8	5.1	43.7	12.8	28.8	8.1	16.4	0.137
	426	248	6.3	6.1	44.1	39.8	5.1	43.7	24.9	49.2	15.7	27.9	0.244
	440	237	6.5	6.2	44.1	39.8	5.1	43.7	16.0	36.3	10.1	20.6	0.166
	456	239	6.5	6.2	44.1	39.8	5.1	43.7	17.3	37.7	10.9	21.4	0.177
	486	219	6.8	6.3	44.1	39.8	5.1	43.7	8.1	19.8	5.1	11.2	0.091
	494	231	6.6	6.3	44.1	39.8	5.1	43.7	12.9	29.6	8.1	16.8	0.138
1WL	166	249	5.6	5.7	42.8	42.8	5.7	56.7	30.6	38.8	17.9	22.8	0.310
rn7	185	260	6.0	5.9	44.1	39.8	5.1	43.7	38.4	67.1	24.1	38.1	0.346
	194	240	6.5	6.2	44.1	39.8	5.1	43.7	17.7	35.7	11.1	20.3	0.180
	204	226	6.7	6.3	44.1	39.8	5.1	43.7	10.3	23.9	6.5	13.5	0.113
	221	231	6.6	6.3	44.1	39.8	5.1	43.7	12.8	28.8	8.1	16.4	0.137
2UH*	7	237	6.4	6.2	69.5	68.5	9.1	75.9	26.9	19.9	9.9	7.2	0.248
rn5*	53	251	6.3	5.9	69.5	68.5	9.1	75.9	51.7	33.0	19.0	11.9	0.399
*	63	230	6.5	6.3	69.5	68.5	9.1	75.9	18.2	15.5	6.7	5.6	0.163
*	83	258	6.2	5.8	69.5	68.5	9.1	75.9	67.3	39.6	24.7	14.3	0.491
*	89	268	6.0	5.5	69.5	68.5	9.1	75.9	91.3	50.7	33.5	18.3	0.631
*	96	275	6.0	5.3	69.5	68.5	9.1	75.9	100.1	53.6	36.7	19.4	0.689
*	104	242	6.4	6.3	69.5	68.5	9.1	75.9	25.1	18.4	9.2	6.6	0.204
2UH	206	249	6.0	6.0	41.5	42.4	5.5	45.3	37.0	30.3	21.9	18.3	0.324
rn10	232	230	6.2	6.4	41.5	42.4	5.5	45.3	15.0	17.8	8.9	10.8	0.137
R1	267	220	6.4	6.6	41.5	42.4	5.5	45.3	10.0	11.4	5.9	6.9	0.099
	280	239	6.3	6.3	41.5	42.4	5.5	45.3	24.9	21.9	14.7	13.2	0.225
	292	249	6.0	6.0	41.6	42.4	5.5	45.4	38.4	31.5	22.7	19.0	0.336
2UH	208	250	6.0	6.0	46.0	46.9	6.1	50.2	36.1	27.0	19.2	14.7	0.314
rn10	232	231	6.3	6.4	46.0	46.9	6.1	50.2	15.0	13.2	8.0	7.2	0.137
R2	271	220	6.4	6.5	46.0	46.9	6.1	50.2	10.1	8.4	5.4	4.6	0.102
	280	240	6.3	6.3	46.0	46.9	6.1	50.2	24.6	18.3	13.1	10.0	0.221
	292	250	6.1	6.0	45.5	46.5	6.1	49.7	38.2	26.8	20.5	14.7	0.330
	528	250	6.2	6.2	53.8	54.8	7.2	58.8	33.4	25.3	15.2	11.8	0.289
2UL	42	239	6.4	6.1	69.4	68.6	9.1	75.9	20.9	11.7	15.6	8.7	0.196
rn3	46	259	6.0	5.5	69.4	68.6	9.1	75.9	45.5	28.7	34.0	21.2	0.364
	67	250	6.2	5.8	69.4	68.6	9.1	75.9	31.1	18.5	23.3	13.7	0.273
	74	242	6.3	6.0	69.4	68.6	9.1	75.9	22.7	12.7	17.0	9.4	0.215
	85	240	6.4	6.0	69.4	68.6	9.1	75.9	21.7	12.0	16.2	8.9	0.208
	97	231	6.5	6.2	69.4	68.6	9.1	75.9	15.9	7.4	11.9	5.5	0.167
	105	260	6.0	5.4	69.4	68.6	9.1	75.9	48.3	27.6	36.2	20.4	0.385
2WH	51	260	6.1	5.6	57.2	56.5	7.5	62.6	31.7	18.7	28.9	16.8	0.256
rn3	64	250	6.2	5.9	57.2	56.5	7.5	62.6	23.0	14.1	21.0	12.7	0.206
	88	240	6.4	6.1	57.2	56.5	7.5	62.6	16.6	9.5	15.1	8.6	0.161

— Continued on next page —

Table C.1 — continued from previous page

Cat.	TOS	T	$\overline{P_{H_2}}$	$\overline{P_{CO}}$	F_{H_2}	F_{CO}	F_{Ar}	F_{He}	$-r_{CO}$	$-r_{H_2}$	X_{CO}	X_{H_2}	Prod.
	h	°C	atm	atm	mmol/h				mmol/g/h		%	%	g/g/h
	93	231	6.4	6.2	57.2	56.5	7.5	62.6	12.4	6.6	11.3	6.0	0.129
	110	261	6.1	5.5	57.2	56.5	7.5	62.6	34.5	20.0	31.4	18.0	0.281
	116	251	6.2	5.8	57.2	56.5	7.5	62.6	24.4	14.2	22.3	12.8	0.215
2WL	47	249	6.4	6.3	57.3	56.5	7.5	62.6	19.8	14.2	8.9	6.3	0.163
rn5	71	229	6.5	6.4	57.3	56.5	7.5	62.6	8.3	7.8	3.8	3.5	0.077
	80	258	6.4	6.2	57.3	56.5	7.5	62.6	22.3	15.6	10.1	7.0	0.182
1DH	168	250	5.5	6.1	23.2	23.3	3.1	26.9	17.4	33.5	18.7	36.3	0.155
rn8	211	241	5.7	6.3	23.2	23.3	3.1	26.9	11.8	26.1	12.7	28.2	0.115
	249	220	6.0	6.4	23.2	23.3	3.1	26.9	5.8	15.9	6.2	17.2	0.064
	374	231	6.0	6.3	23.2	23.3	3.1	26.9	8.7	17.8	9.3	19.2	0.092
	417	250	5.7	6.2	23.2	23.3	3.1	26.9	15.6	27.9	16.8	30.2	0.141
1DL	168	251	5.5	6.1	15.4	15.4	2.1	17.8	11.7	22.9	18.9	37.3	0.111
rn8	211	241	5.7	6.3	15.4	15.4	2.1	17.8	8.4	17.9	13.5	29.2	0.085
	249	221	6.0	6.4	15.4	15.4	2.1	17.8	4.2	10.3	6.8	16.8	0.047
	358	232	6.0	6.4	15.4	15.4	2.1	17.8	5.7	12.1	9.3	19.8	0.062
2DH	47	260	6.1	5.9	57.2	56.5	7.5	62.6	22.5	18.6	20.0	16.4	0.169
rn4	67	249	6.3	6.2	57.2	56.5	7.5	62.6	13.4	14.5	11.9	12.7	0.110
	73	241	6.3	6.3	57.2	56.5	7.5	62.6	9.7	12.9	8.6	11.3	0.082
	95	230	6.4	6.4	57.2	56.5	7.5	62.6	6.6	11.0	5.8	9.7	0.057
2DL	52	259	6.1	6.0	42.5	42.0	5.5	46.5	16.6	13.8	19.8	16.3	0.126
rn4	61	249	6.3	6.2	42.5	42.0	5.5	46.5	10.8	10.9	13.0	12.9	0.089
	83	240	6.3	6.3	42.5	42.0	5.5	46.5	7.8	10.2	9.4	12.0	0.066
	92	230	6.4	6.4	42.5	42.0	5.5	46.5	5.1	8.4	6.1	9.9	0.044
1UHa	85	251	5.9	5.7	61.5	61.5	7.9	67.2	36.4	27.4	29.6	22.3	0.329
rn9	95	251	6.0	5.8	75.3	75.3	9.7	82.2	37.8	28.9	25.1	19.2	0.340
	108	251	6.0	5.8	90.5	90.5	11.7	98.8	39.3	31.2	21.8	17.3	0.358
	127	251	5.8	5.5	62.9	62.9	8.1	68.7	38.2	30.2	30.5	24.1	0.341
	153	230	6.2	6.2	69.8	69.8	9.0	76.2	15.8	16.5	11.4	11.8	0.152
	174	220	6.3	6.3	60.1	60.1	7.7	65.6	10.4	10.2	8.6	8.5	0.105
	200	240	6.1	5.9	60.1	60.1	7.7	65.6	26.6	20.8	22.2	17.4	0.245
	231	251	6.0	5.7	69.8	69.8	9.0	76.2	40.6	28.9	29.1	20.8	0.363
	247	251	6.0	5.8	90.5	90.5	11.7	98.8	41.5	30.3	23.0	16.8	0.377
	267	220	6.3	6.3	60.1	60.1	7.7	65.6	10.2	9.2	8.5	7.7	0.103
	302	240	5.5	5.2	60.1	60.1	7.7	65.6	26.4	20.9	22.0	17.5	0.245
1ULa	12	266	5.7	5.6	63.2	64.8	9.1	66.7	49.7	40.7	38.3	32.1	0.577
rn2	68	265	5.6	5.5	63.2	64.8	9.1	66.7	56.7	43.7	43.6	34.5	0.649
	144	256	6.0	6.0	63.2	64.8	9.1	66.7	36.1	30.1	27.8	23.7	0.420
	212	254	5.9	5.9	63.2	64.8	9.1	66.7	39.1	32.3	30.1	25.5	0.454
	263	255	5.9	5.8	63.2	64.8	9.1	66.7	41.9	34.2	32.3	27.0	0.486

— Continued on next page —

Table C.1 — continued from previous page

Cat.	TOS	T	$\overline{P_{H_2}}$	$\overline{P_{CO}}$	F_{H_2}	F_{CO}	F_{Ar}	F_{He}	$-r_{CO}$	$-r_{H_2}$	X_{CO}	X_{H_2}	Prod.
	h	°C	atm	atm	mmol/h				mmol/g/h		%	%	g/g/h
	283	243	6.2	6.3	63.2	64.8	9.1	66.7	22.8	19.6	17.5	15.5	0.271
	297	277	5.4	4.9	74.6	76.5	10.7	78.8	93.0	65.6	60.7	43.8	1.048
1WLa	83	237	6.3	6.7	39.6	40.8	5.5	41.7	6.2	10.3	7.6	13.0	0.076
rn1	124	245	6.1	6.5	39.6	40.8	5.5	41.7	10.7	15.5	13.1	19.6	0.127
	171	255	5.8	6.3	39.6	40.8	5.5	41.7	17.1	23.0	21.0	29.0	0.197
	226	258	5.9	6.4	39.6	40.8	5.5	41.7	15.7	22.5	19.3	28.4	0.181
	287	256	5.9	6.3	39.6	40.8	5.5	41.7	15.9	21.1	19.5	26.7	0.182
	344	233	6.3	6.7	39.6	40.8	5.5	41.7	5.8	9.4	7.1	11.9	0.070
P1	33	260	5.7	6.1	62.6	64.2	9.0	66.1	35.7	41.8	27.9	33.4	0.446
rn2	105	260	5.8	6.1	62.6	64.2	9.0	66.1	34.3	38.4	26.8	30.8	0.421
	195	248	6.2	6.4	62.6	64.2	9.0	66.1	18.4	19.9	14.3	15.9	0.227
	269	250	6.2	6.4	62.6	64.2	9.0	66.1	19	18.8	14.8	15.0	0.230
	275	239	6.4	6.5	62.6	64.2	9.0	66.1	11.4	9.8	8.9	7.9	0.144
	309	271	5.7	5.6	73.3	75.2	10.6	77.4	60.9	50	40.6	34.2	0.704
P2	0	233	6.6	6.6	86.1	88.6	11.9	90.7	7.7	0	4.4	0	0.103
rn1	49	233	6.7	6.7	86.1	88.6	11.9	90.7	4.5	0	2.5	0	0.056
	141	242	6.6	6.6	86.1	88.6	11.9	90.7	11.2	0	6.3	0	0.136
	216	253	6.4	6.4	86.1	88.6	11.9	90.7	21.7	14.0	12.2	8.2	0.254
	265	257	6.3	6.4	86.1	88.6	11.9	90.7	25.0	18.3	14.1	10.7	0.289

Table C.2: Selectivity data for the 10 FB runs. FB runs are given below each catalyst name e.g. rn6 indicates FB run 6.

			Molar selectivity of consumed CO				
Cat.	TOS	T	CO_2	CH_4	C_2H_4	C_2H_6	C_{2+}
	h	°C	%	%	%	%	%
1UH	221	250	44.70	3.50	1.68	0.76	49.40
rn6	259	262	46.70	4.00	1.87	0.99	46.50
	286	241	42.90	3.10	1.36	0.68	52.00
	315	240	43.00	3.10	1.34	0.69	51.90
	345	221	34.40	2.40	0.40	0.55	62.30
	388	232	42.20	2.80	0.84	0.68	53.60
	414	249	45.80	3.40	1.49	0.88	48.40
	460	240	43.50	2.90	1.11	0.70	51.80
	477	221	35.90	2.30	0.23	0.59	61.00
	501	226	40.30	2.60	0.74	0.76	53.10

— Continued on next page —

Table C.2 — continued from previous page

Cat.	TOS h	T °C	Molar selectivity of consumed CO				
			CO_2 %	CH_4 %	C_2H_4 %	C_2H_6 %	C_{2+} %
1UL	94	251	40.60	2.60	2.30	0.89	53.70
rn7	113	240	35.20	2.20	2.34	0.76	59.40
	124	221	22.40	1.60	1.98	0.72	73.30
	139	231	30.40	1.90	2.12	0.60	65.00
	166	249	45.50	2.80	2.37	0.97	48.40
	185	241	42.90	2.60	2.34	0.67	51.50
	195	221	36.90	2.50	3.28	0.90	56.40
	206	230	38.20	2.50	3.12	0.69	55.50
	223	241	43.60	2.70	2.84	0.91	50.00
1WH	217	249	19.00	12.50	0.95	6.95	60.50
rn6	243	260	24.40	11.80	1.06	6.81	55.40
	328	240	14.80	13.30	0.47	7.52	64.00
	360	226	9.10	13.40	0.18	7.52	69.80
	393	231	11.10	13.10	0.21	7.38	68.20
	426	248	18.80	12.00	0.52	7.07	60.70
	440	237	13.70	13.30	0.39	7.41	65.30
	456	239	14.40	13.20	0.36	7.38	64.70
	486	219	7.40	12.80		7.13	72.70
	494	231	11.10	13.20	0.19	7.27	68.30
1WL	166	249	18.00	10.30		10.52	61.20
rn7	185	260	24.40	11.80	1.06	6.81	55.40
	194	240	14.80	13.30	0.47	7.52	64.00
	204	226	9.10	13.40	0.18	7.52	69.80
	221	231	11.10	13.10	0.21	7.38	68.20
2UH	7	237	30.10	4.50	2.66	2.63	60.10
rn5	53	251	40.10	5.40	2.74	3.31	48.50
	63	230	31.90	4.60	2.51	2.42	58.60
	83	258	42.20	6.10	2.54	3.68	45.50
	89	268	43.90	7.10	2.62	4.88	41.40
	96	275	43.50	7.70	2.58	5.28	40.90
	104	242	37.00	5.70	2.59	2.93	51.90
2UH	206	249	32.40	5.60	5.63	7.04	49.30
rn10	232	230	30.90	4.60	5.96	4.93	53.70
R1	267	220	26.20	3.70	5.17	4.25	60.60
	280	239	31.30	4.70	5.66	5.40	52.90
	292	249	32.70	5.40	5.57	6.82	49.60
2UH	208	250	32.20	6.30	5.90	7.35	48.30

— Continued on next page —

Table C.2 — continued from previous page

Cat.	TOS h	T °C	Molar selectivity of consumed CO				
			CO_2 %	CH_4 %	C_2H_4 %	C_2H_6 %	C_{2+} %
rn10	232	231	30.10	5.00	6.24	5.01	53.70
R2	271	220	24.80	4.00	5.30	3.84	62.10
	280	240	31.10	5.20	5.89	5.47	52.30
	292	250	32.80	6.00	5.74	7.06	48.40
	528	250	33.20	5.50	5.72	5.95	49.60
2UL	42	239	30.00	3.50	1.49	0.79	64.20
rn3	46	259	38.40	4.90	2.08	1.51	53.10
	67	250	34.00	4.00	1.69	0.66	59.70
	74	242	29.60	3.50	1.48	0.58	64.80
	85	240	28.80	3.40	1.43	0.54	65.90
	97	231	23.20	2.80	1.19	0.55	72.30
	105	260	39.10	4.50	1.91	0.87	53.60
2WH	51	260	38.90	3.70	2.14	0.78	54.40
rn3	64	250	33.50	3.20	1.81	0.53	61.00
	88	240	28.70	2.70	1.56	0.51	66.50
	93	231	24.00	2.30	1.33	0.48	71.90
	110	261	38.50	3.70	2.13	0.70	54.90
	116	251	34.40	3.30	1.89	0.57	59.80
2WL	47	249	37.10	4.50	2.00	2.15	54.30
rn5	71	229	31.20	3.50	1.04	1.10	63.20
	80	258	37.50	4.70	2.20	2.30	53.30
1DH	168	250	23.60	13.20		7.02	56.10
rn8	211	241	17.40	13.90		7.14	61.60
	249	220	8.40	13.60		6.50	71.50
	374	231	11.70	12.90	1.03		74.30
	417	250	22.80	13.40	1.02		62.80
1DL	168	251	20.40	12.30		11.24	56.00
rn8	211	241	14.80	12.80		11.16	60.50
	249	221	7.50	12.50		11.06	68.80
	358	232	10.30	12.60	1.70		75.40
2DH	47	260	40.80	6.00	3.46	1.30	48.50
rn4	67	249	36.30	5.80	3.36	1.48	53.10
	73	241	34.60	5.50	3.18	1.41	55.30
	95	230	33.10	4.90	2.85	1.20	57.90
2DL	52	259	39.60	6.50	2.75	1.32	49.80
rn4	61	249	35.70	6.00	2.56	1.35	54.40

— Continued on next page —

Table C.2 — continued from previous page

Cat.	TOS h	T °C	Molar selectivity of consumed CO				
			CO_2 %	CH_4 %	C_2H_4 %	C_2H_6 %	C_{2+} %
	83	240	34.60	5.70	2.40	1.28	56.10
	92	230	32.80	5.30	2.23	1.17	58.50
1UHa	85	251	32.50	3.50		2.42	61.60
rn9	95	251	32.70	3.60		2.41	61.30
	108	251	32.00	3.60		2.36	62.10
	127	251	33.20	3.60		2.89	60.30
	153	230	29.00	3.00		2.24	65.80
	174	220	25.60	2.70		1.89	69.80
	200	240	31.60	3.20		2.91	62.20
	231	251	33.10	3.60		3.02	60.30
	247	251	32.20	3.60		2.70	61.50
	267	220	26.00	2.60		1.77	69.70
	302	240	31.20	3.10		2.65	63.00
1ULa	12	266	38.23	3.91	1.93	1.91	51.32
rn2	68	265	40.61	5.03	1.88	2.67	49.80
	144	256	37.87	4.74	2.09	2.46	52.84
	212	254	38.27	4.69	1.99	2.37	52.68
	263	255	38.41	4.72	1.88	2.24	52.75
	283	243	33.16	4.32	2.11	2.09	58.32
	297	277	41.84	6.39	1.63	3.74	46.39
1WLa	83	237	18.77	8.75	2.06	3.31	67.11
rn1	124	245	24.52	9.47	1.53	4.28	60.20
	171	255	30.95	10.73	1.02	5.78	51.52
	226	258	30.00	11.33	1.04	5.99	51.63
	287	256	29.75	11.35	0.92	5.15	52.82
	344	233	19.09	10.93	4.00	5.25	60.73
P1	33	260	26.71	1.99	0.88	0.64	69.78
rn2	105	260	29.05	3.01	1.18	1.31	65.45
	195	248	25.48	4.20	1.61	1.38	67.33
	269	250	28.28	4.85	1.76	1.81	63.31
	275	239	21.15	4.38	1.80	1.51	71.16
	309	271	37.61	5.71	1.21	3.00	52.46
P2	0	233	6.57	5.11	0.81	0.42	87.10
rn1	49	233	16.59	7.72	7.36	1.05	67.28
	141	242	25.48	6.64	3.01	1.85	63.02
	216	253	33.22	6.68	1.83	1.71	56.57

— Continued on next page —

Table C.2 — continued from previous page

Cat.	TOS h	T °C	Molar selectivity of consumed CO				
			CO_2 %	CH_4 %	C_2H_4 %	C_2H_6 %	C_{2+} %
	265	257	35.30	6.85	1.68	1.89	54.27

Table C.3: Effluent gas composition data for the 10 FB runs. FB runs are given below each catalyst name e.g. rn6 indicates FB run 6.

Cat.	TOS h	T °C	Molar composition of reactor effluent								
			H_2 %	Ar %	CO %	CO_2 %	CH_4 %	C_2H_4 %	C_2H_6 %	He %	H_2O %
1UH	221	250	28.4	4.0	24.6	2.80	0.22	0.05	0.02	33.9	6.0
rn6	259	262	25.9	4.0	21.0	4.72	0.40	0.09	0.05	34.1	9.7
	286	241	30.1	3.9	26.5	1.74	0.13	0.03	0.01	33.6	3.9
	315	240	30.2	3.9	26.3	1.82	0.13	0.03	0.01	33.5	4.1
	345	221	31.7	3.9	28.9	0.54	0.04	0.00	0.00	33.4	1.5
	388	232	30.8	3.9	27.6	1.21	0.08	0.01	0.01	33.5	2.8
	414	249	28.0	4.0	24.0	3.14	0.23	0.05	0.03	33.9	6.6
	460	240	29.7	3.9	26.4	1.87	0.13	0.02	0.02	33.7	4.2
	477	221	31.8	3.9	28.9	0.53	0.03	0.00	0.00	33.4	1.5
	501	226	30.0	3.8	27.0	1.16	0.08	0.01	0.01	32.7	2.7
1UL	94	251	24.0	4.0	23.9	2.44	0.15	0.07	0.03	39.6	5.9
rn7	113	240	25.4	4.0	25.9	1.35	0.09	0.04	0.01	39.4	3.8
	124	221	26.9	4.0	27.7	0.42	0.03	0.02	0.01	39.2	1.8
	139	231	26.3	4.0	26.9	0.83	0.05	0.03	0.01	39.3	2.7
	166	249	24.7	4.0	24.1	2.49	0.15	0.06	0.03	39.2	5.3
	185	241	25.9	3.9	25.8	1.59	0.10	0.04	0.01	39.1	3.6
	195	221	27.4	3.9	27.9	0.51	0.03	0.02	0.01	38.8	1.4
	206	230	26.7	3.9	27.2	0.85	0.05	0.03	0.01	39.0	2.2
	223	241	25.6	3.9	25.6	1.70	0.10	0.06	0.02	39.1	3.8
1WH	217	249	25.4	4.2	27.4	1.06	0.70	0.03	0.19	36.2	4.9
rn6	243	260	23.0	4.3	25.5	1.98	0.95	0.06	0.28	36.9	7.1
	328	240	28.2	4.1	28.4	0.52	0.47	0.01	0.13	35.1	3.1
	360	226	30.0	4.0	29.3	0.18	0.27	0.00	0.08	34.4	1.8
	393	231	29.3	4.1	29.1	0.28	0.33	0.00	0.09	34.7	2.2
	426	248	26.1	4.2	27.6	0.96	0.62	0.04	0.18	35.9	4.5
	440	237	28.1	4.1	28.8	0.44	0.43	0.01	0.12	35.2	2.8

— Continued on next page —

Table C.3 — continued from previous page

Cat.	TOS h	T °C	Molar composition of reactor effluent								
			H_2 %	Ar %	CO %	CO_2 %	CH_4 %	C_2H_4 %	C_2H_6 %	He %	H_2O %
	456	239	27.9	4.1	28.6	0.50	0.46	0.01	0.13	35.3	3.0
	486	219	30.6	4.0	29.5	0.12	0.20	0.00	0.06	34.2	1.4
	494	231	29.2	4.1	29.1	0.28	0.34	0.00	0.09	34.8	2.2
1WL	166	249	23.6	4.1	25.1	0.99	0.56	0.00	0.29	40.5	4.9
rn7	185	260	23.0	4.3	25.5	1.98	0.95	0.06	0.28	36.9	7.1
	194	240	28.2	4.1	28.4	0.52	0.47	0.01	0.13	35.1	3.1
	204	226	30.0	4.0	29.3	0.18	0.27	0.00	0.08	34.4	1.8
	221	231	29.3	4.1	29.1	0.28	0.33	0.00	0.09	34.7	2.2
2UH	7	237	29.3	4.1	28.1	0.92	0.14	0.04	0.04	34.5	2.9
rn5	53	251	27.8	4.1	25.2	2.36	0.32	0.08	0.10	34.5	5.6
	63	230	29.7	4.1	29.0	0.66	0.10	0.03	0.03	34.4	2.0
	83	258	27.0	4.1	23.4	3.23	0.47	0.10	0.14	34.4	7.2
	89	268	25.7	4.1	20.6	4.56	0.74	0.14	0.25	34.3	9.6
	96	275	25.3	4.1	19.6	4.94	0.88	0.15	0.30	34.3	10.5
	104	242	29.4	4.1	28.2	1.06	0.16	0.04	0.04	34.4	2.7
2UH	206	249	25.9	4.2	25.3	2.30	0.40	0.20	0.25	34.7	6.7
rn10	232	230	28.1	4.2	29.3	0.88	0.13	0.09	0.07	34.4	2.7
R1	267	220	29.1	4.2	30.1	0.50	0.07	0.05	0.04	34.2	1.8
	280	239	27.4	4.2	27.5	1.49	0.22	0.13	0.13	34.4	4.5
	292	249	25.7	4.2	25.1	2.41	0.39	0.20	0.25	34.7	7.0
2UH	208	250	26.9	4.2	26.0	1.99	0.39	0.18	0.23	34.4	5.8
rn10	232	231	29.0	4.2	29.3	0.77	0.13	0.08	0.06	34.1	2.4
R2	271	220	29.7	4.1	30.0	0.42	0.07	0.05	0.03	33.9	1.6
	280	240	28.2	4.2	27.8	1.30	0.22	0.12	0.11	34.2	4.0
	292	250	26.8	4.2	25.5	2.16	0.39	0.19	0.23	34.3	6.2
	528	250	27.7	4.2	27.1	1.61	0.27	0.14	0.14	34.3	4.6
2UL	42	239	28.8	4.1	26.3	1.46	0.17	0.04	0.02	34.5	4.7
rn3	46	259	25.1	4.2	20.8	4.12	0.52	0.11	0.08	34.9	10.2
	67	250	27.3	4.1	24.0	2.48	0.29	0.06	0.02	34.7	7.0
	74	242	28.6	4.1	25.9	1.57	0.18	0.04	0.02	34.5	5.1
	85	240	28.7	4.1	26.1	1.46	0.17	0.04	0.01	34.5	4.9
	97	231	29.7	4.1	27.3	0.86	0.10	0.02	0.01	34.3	3.6
	105	260	25.2	4.1	20.0	4.43	0.51	0.11	0.05	34.7	10.8
2WH	51	260	26.3	4.1	22.2	3.51	0.34	0.10	0.04	34.6	8.7
rn3	64	250	27.6	4.1	24.7	2.20	0.21	0.06	0.02	34.7	6.4
	88	240	28.8	4.1	26.4	1.35	0.13	0.04	0.01	34.5	4.6

— Continued on next page —

Table C.3 — continued from previous page

Cat.	TOS h	T °C	Molar composition of reactor effluent								
			H_2 %	Ar %	CO %	CO_2 %	CH_4 %	C_2H_4 %	C_2H_6 %	He %	H_2O %
	93	231	29.6	4.1	27.6	0.84	0.08	0.02	0.01	34.4	3.4
	110	261	26.0	4.1	21.5	3.79	0.37	0.10	0.03	34.7	9.5
	116	251	27.6	4.1	24.3	2.39	0.23	0.07	0.02	34.6	6.7
2WL	47	249	29.5	4.1	28.2	1.03	0.12	0.03	0.03	34.3	2.7
rn5	71	229	30.3	4.1	29.8	0.36	0.04	0.01	0.01	34.3	1.1
	80	258	29.3	4.1	27.9	1.17	0.15	0.03	0.04	34.4	3.0
1DH	168	250	21.3	4.5	27.4	1.49	0.83	0.00	0.22	38.8	5.5
rn8	211	241	23.6	4.4	28.8	0.73	0.58	0.00	0.15	38.1	3.6
	249	220	26.4	4.3	30.1	0.17	0.27	0.00	0.07	37.0	1.7
	374	231	25.9	4.3	29.2	0.35	0.39	0.02	0.00	37.2	2.6
	417	250	23.0	4.4	27.6	1.27	0.74	0.03	0.00	38.2	4.8
1DL	168	251	21.1	4.5	27.4	1.30	0.79	0.00	0.35	39.0	5.6
rn8	211	241	23.4	4.4	28.6	0.66	0.57	0.01	0.25	38.2	3.9
	249	221	26.5	4.3	29.9	0.16	0.27	0.00	0.12	36.9	1.9
	358	232	25.8	4.3	29.3	0.31	0.38	0.03	0.00	37.2	2.6
2DH	47	260	26.7	4.2	25.2	2.57	0.38	0.11	0.04	34.9	5.9
rn4	67	249	27.9	4.2	27.8	1.36	0.22	0.06	0.03	34.9	3.6
	73	241	28.3	4.2	28.8	0.94	0.15	0.04	0.02	34.9	2.6
	95	230	28.8	4.2	29.7	0.61	0.09	0.03	0.01	34.9	1.8
2DL	52	259	26.7	4.2	25.3	2.48	0.41	0.09	0.04	34.9	5.9
rn4	61	249	27.8	4.2	27.5	1.46	0.25	0.05	0.03	34.9	3.8
	83	240	28.1	4.2	28.6	1.02	0.17	0.04	0.02	35.0	2.8
	92	230	28.7	4.2	29.6	0.63	0.10	0.02	0.01	34.9	1.8
1UHa	85	251	25.1	4.2	22.7	3.11	0.33	0.00	0.12	35.3	9.2
rn9	95	251	25.9	4.1	24.0	2.64	0.29	0.00	0.10	35.1	7.8
	108	251	26.5	4.1	25.1	2.23	0.25	0.00	0.08	35.0	6.7
	127	251	24.6	4.2	22.5	3.27	0.36	0.00	0.14	35.4	9.5
	153	230	28.1	4.1	28.3	1.05	0.11	0.00	0.04	34.8	3.5
	174	220	29.0	4.1	28.9	0.70	0.07	0.00	0.03	34.6	2.7
	200	240	26.5	4.1	24.9	2.25	0.23	0.00	0.10	35.0	6.9
	231	251	25.4	4.1	22.8	3.09	0.34	0.00	0.14	35.1	9.0
	247	251	26.6	4.1	24.6	2.37	0.26	0.00	0.10	34.9	7.1
	267	220	29.1	4.1	28.9	0.70	0.07	0.00	0.02	34.5	2.6
	302	240	26.5	4.1	25.0	2.20	0.22	0.00	0.09	35.0	6.8
1ULa	12	266	24.6	5.2	23.0	5.59	0.57	0.14	0.14	38.3	3.0
rn2	68	265	23.8	5.2	21.0	6.59	0.82	0.15	0.22	38.3	3.0

— Continued on next page —

Table C.3 — continued from previous page

Cat.	TOS h	T °C	Molar composition of reactor effluent								
			H_2 %	Ar %	CO %	CO_2 %	CH_4 %	C_2H_4 %	C_2H_6 %	He %	H_2O %
	144	256	27.6	5.2	26.9	3.91	0.49	0.11	0.13	38.3	2.5
	212	254	27.0	5.2	26.0	4.28	0.52	0.11	0.13	38.3	2.6
	263	255	26.5	5.2	25.2	4.61	0.57	0.11	0.13	38.3	2.8
	283	243	30.7	5.2	30.7	2.16	0.28	0.07	0.07	38.3	2.2
	297	277	24.0	6.2	17.3	11.14	1.70	0.22	0.50	45.2	4.3
1WLa	83	237	28.2	4.5	30.8	0.47	0.22	0.03	0.04	34.1	1.6
rn1	124	245	26.0	4.5	29.0	1.07	0.41	0.03	0.09	34.1	2.2
	171	255	23.0	4.5	26.3	2.17	0.75	0.04	0.20	34.1	2.7
	226	258	23.2	4.5	26.9	1.93	0.73	0.03	0.19	34.1	2.6
	287	256	23.7	4.5	26.8	1.93	0.74	0.03	0.17	34.1	2.6
	344	233	28.5	4.5	31.0	0.45	0.26	0.05	0.06	34.1	1.5
P1	33	260	23.6	5.1	26.2	2.71	0.20	0.04	0.03	37.5	4.7
rn2	105	260	24.6	5.1	26.7	2.83	0.29	0.06	0.06	37.5	4.1
	195	248	29.8	5.1	31.2	1.33	0.22	0.04	0.04	37.5	2.6
	269	250	30.2	5.1	31.0	1.52	0.26	0.05	0.05	37.5	2.3
	275	239	32.7	5.1	33.1	0.69	0.14	0.03	0.02	37.5	1.9
	309	271	27.4	6.0	25.3	6.51	0.99	0.10	0.26	43.9	4.3
P2	0	233	31.0	4.3	30.5	0.09	0.07	0.01	0.00	32.7	1.2
rn1	49	233	31.0	4.3	31.1	0.13	0.06	0.03	0.00	32.7	0.5
	141	242	31.0	4.3	29.9	0.51	0.13	0.03	0.02	32.7	1.0
	216	253	28.5	4.3	28.0	1.30	0.26	0.04	0.03	32.7	1.3
	265	257	27.7	4.3	27.4	1.59	0.31	0.04	0.04	32.7	1.3

APPENDIX D. AUXILIARY PARTIAL PRESSURE DATA FOR 2UH

This appendix gives auxiliary data for the partial pressure study on 2UH from FB run 10. Two-parameter joint confidence regions are given followed by a discussion of correlation coefficients and finally the high conversion data from R1 of FB run 10 on 2UH.

D.1 Representative Join Confidence Regions

The most accurate representation of the confidence region for values of E/R, A, m, and n in Equation 4.5 is a four-dimensional plot of the joint confidence regions of all variables, but such plots are difficult to produce and can be confusing. Instead, two-parameter joint confidence regions were plotted for each pair of parameters in Figures D.1 to D.6. For all of these figures, due to the nature of the calculations (varying two parameters while holding the others at their best estimates), the confidence regions are of the proper shape and magnitude, but are not centered on the best estimates of the parameters as they should be.

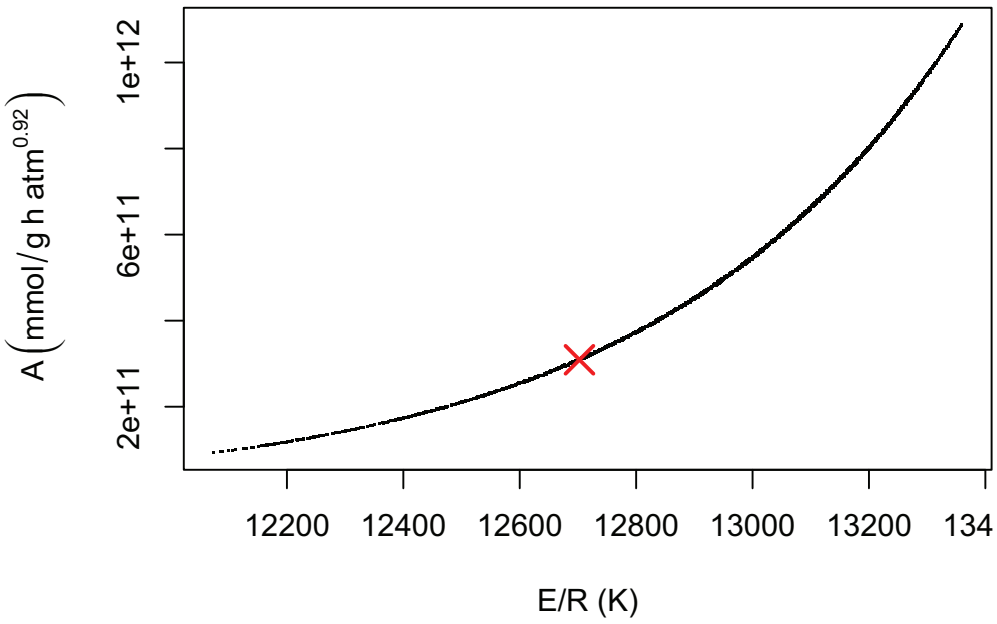

Figure D.1: Representative joint confidence region of ER and A from Equation 4.5.

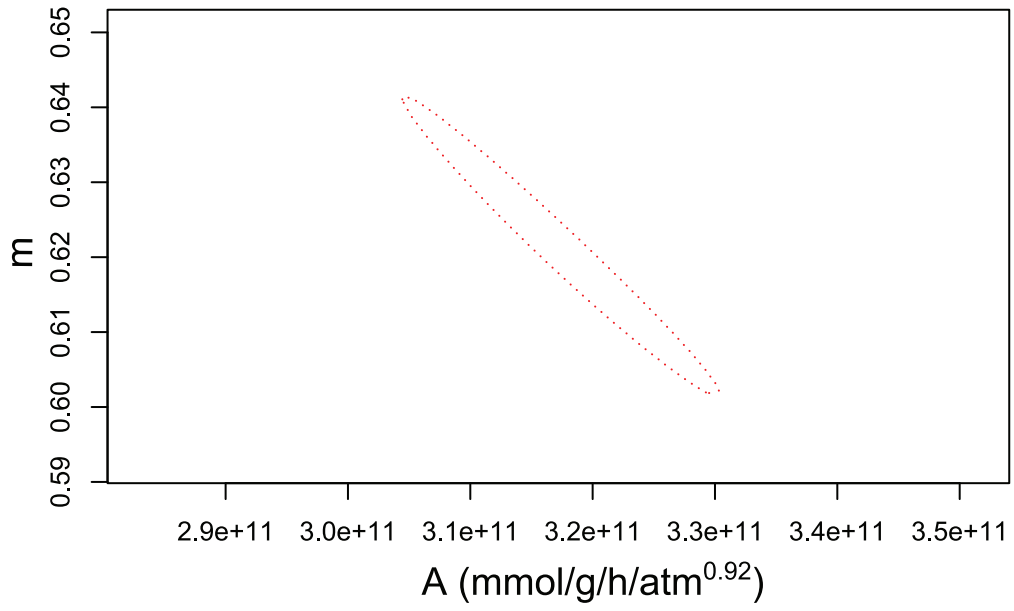

Figure D.2: Representative joint confidence region of A and m from Equation 4.5.

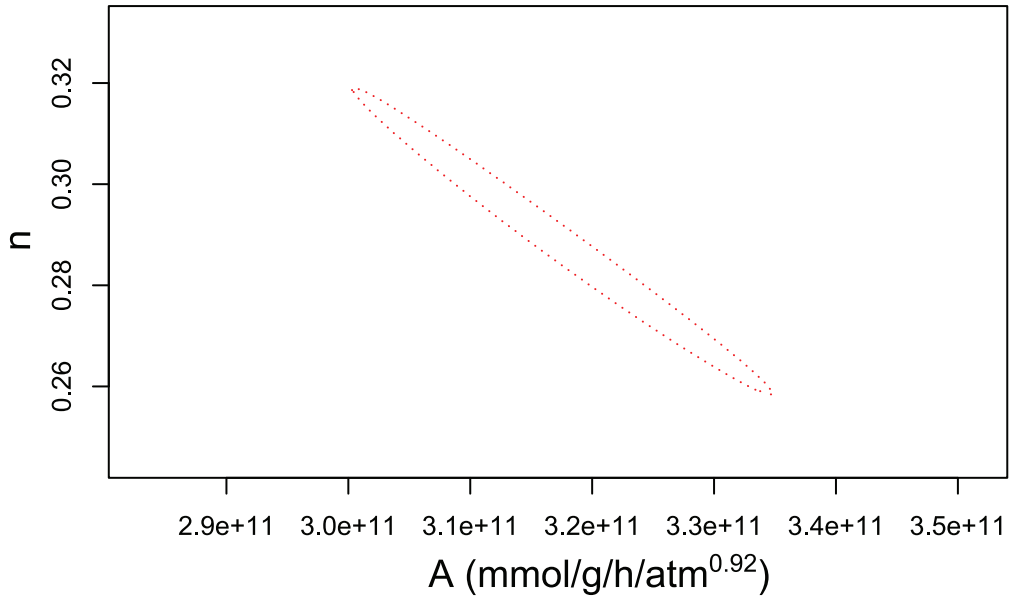

Figure D.3: Representative joint confidence region of A and n from Equation 4.5.

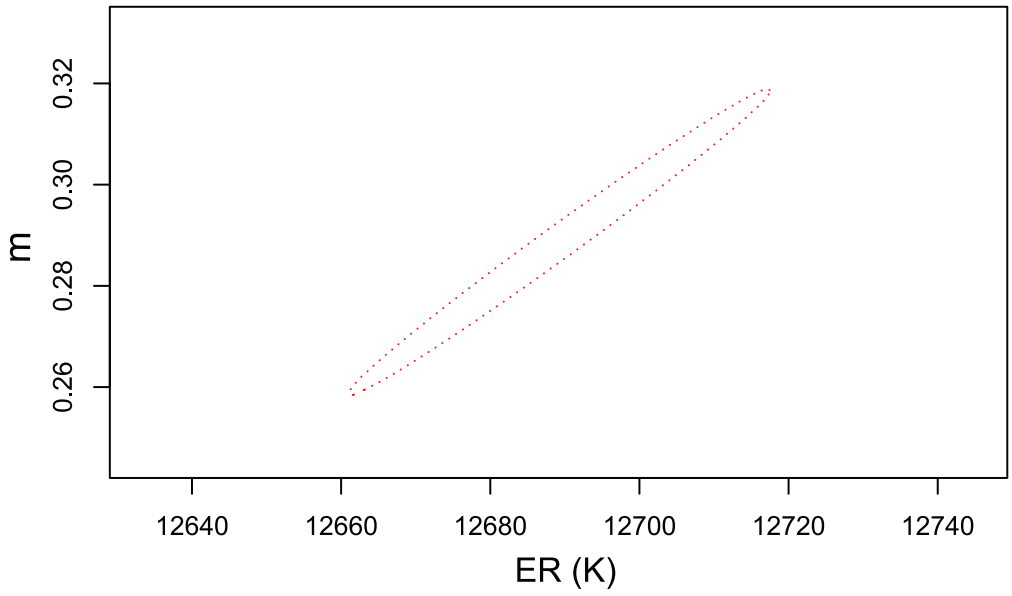

Figure D.4: Representative joint confidence region of ER and m from Equation 4.5.

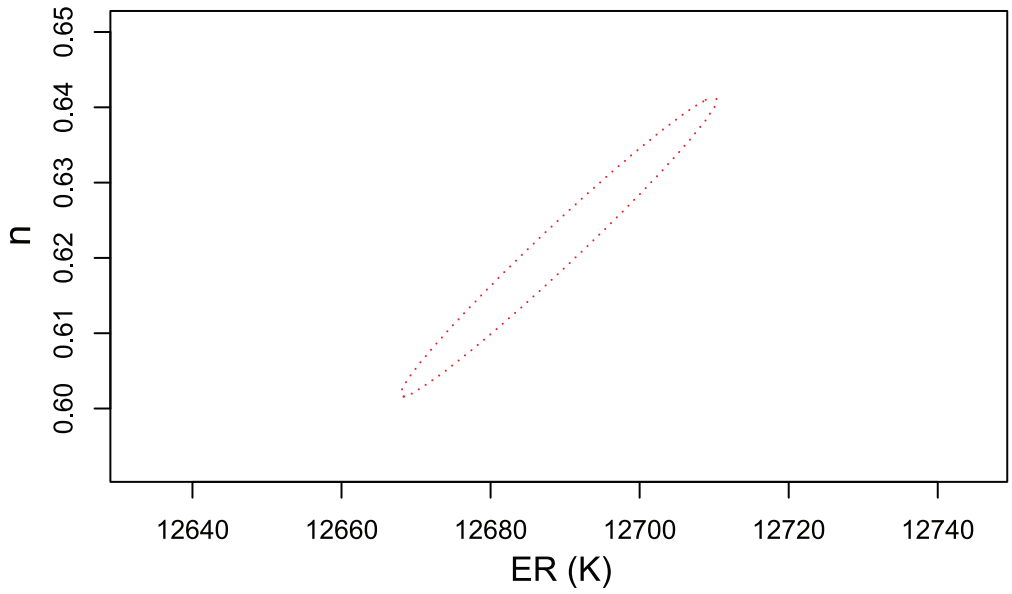

Figure D.5: Representative joint confidence region of *ER* and *n* from Equation 4.5.

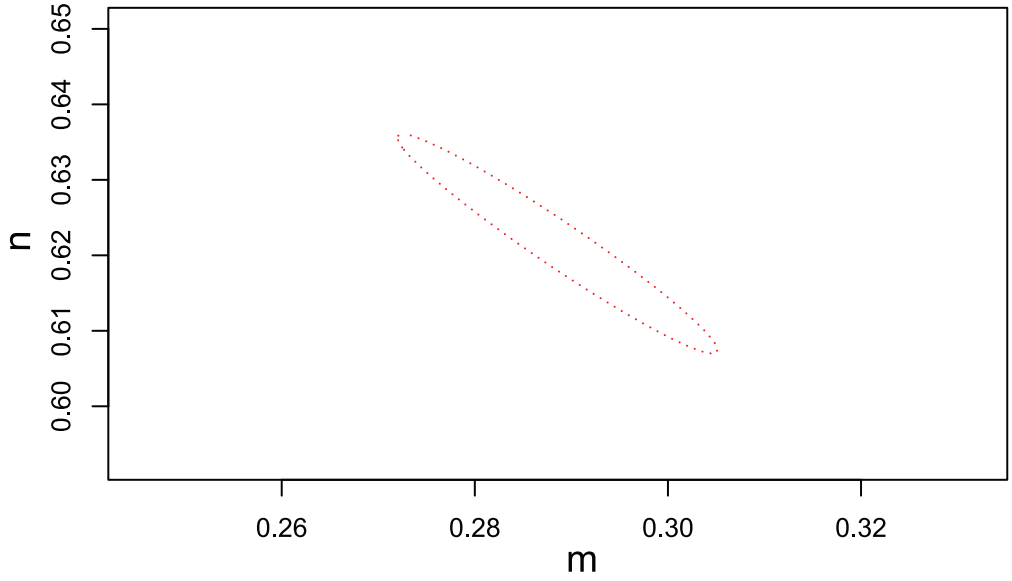

Figure D.6: Representative joint confidence region of *m* and *n* from Equation 4.5.

D.2 Discussion of Correlation Coefficients

The correlation coefficients in Table 4.12 indicate the degree of correlation between parameters. Coefficients near 0.0 indicate that the parameters are nearly completely uncorrelated while values of 1.0 of -1.0 indicate complete correlation. For negatively correlated parameters, as the value of one parameter increases, the value of the other parameter decreases. Each of the parameters is completely correlated with itself. In addition, ER and A are nearly completely correlated (-1.0) meaning that for any given value of ER, there is a very narrow range of values of A that fit the data. There is almost no correlation between m and ER and between m and A, but there is some correlation between m and n, between n a ER, and between n and A. The degree of correlation is expressed in the joint confidence region plots where in the extreme case of total correlation (ER and A) the region is almost a line (Figure D.1) rather than an ellipse (Figures D.2 to D.6). For pairs of uncorrelated parameters, one parameter of the pair can assume a wide range of values for any given value of its mate.

D.3 High Conversion Partial Pressure Data from R1 of FB run 10 on 2UH

The high conversion partial pressure data from R1 of FB run 10 on 2UH are presented in Table D.1. The table is divided between temperature experiments and partial pressure experiments.

Table D.1: Temperature and partial pressure kinetic data on 0.251 g of 2UH from R1 of FB run 10. The time on stream of the first data point for each condition is given in the first column. The table is divided between temperature and partial pressure data.

										mol% CO selectivity			
TOS	T	F^0_{H2}	F^0_{CO}	$F^{0\ a}_{inr}$	X_{CO}	X_{H_2}	$-r_{CO}$	$\overline{P_{CO}}$	$\overline{P_{H_2}}$	CO_2	CH_4	C_2H_4	C_2H_6
h	°C	mmol/h			%	%	[c]	atm	atm	%	%	%	%
206	249	41.5	42.4	50.9	21.9	18.3	37.0	6.0	6.0	32.4	5.6	5.6	7.0
232	230	41.5	42.4	50.9	8.9	10.8	15.0	6.2	6.4	30.9	4.6	6.0	4.9
267	220	41.5	42.4	50.9	5.9	6.9	10.0	6.4	6.6	26.2	3.7	5.2	4.2
280	239	41.5	42.4	50.9	14.7	13.2	24.9	6.3	6.3	31.3	4.7	5.7	5.4
292	249	41.6	42.4	50.9	22.7	19.0	38.3	6.0	6.0	32.7	5.4	5.6	6.8
314	249	41.6	42.4	50.9	22.3	19.1	37.6	6.0	6.0	33.1	5.3	5.5	6.9
528	250	51.0	52.0	62.5	13.4	12.4	27.7	6.2	6.3	33.2	4.7	6.4	5.3
547	259	64.4	65.6	78.9	15.9	14.3	41.7	6.1	6.1	33.6	5.3	5.9	5.9
363	249	9.8	13.6	9.7	69.5	56.8	37.5	4.6	5.8	33.0	4.0	4.1	6.7
391	249	9.1	12.5	16.5	63.2	55.0	31.5	3.8	4.9	35.0	4.1	4.6	6.7
404	249	47.2	23.5	10.6	46.5	21.3	43.6	11.4	4.9	30.4	7.5	4.6	11.9
427	249	9.1	12.6	16.3	57.7	29.8	29.1	4.3	5.0	33.5	4.5	4.7	7.3
448	249	20.1	10.1	33.7	52.3	24.3	21.0	6.0	2.5	32.0	7.4	4.4	11.9
468	249	9.9	13.6	9.7	65.2	30.5	35.2	5.4	5.9	31.1	4.7	3.9	7.3
495	250	47.6	23.8	10.7	41.4	18.7	39.1	11.6	5.0	31.0	7.6	4.9	11.9
512	249	21.2	10.7	35.7	46.6	20.5	19.8	6.1	2.6	32.4	7.6	4.8	12.2

[a] inerts are Ar and He

[b] averaged partial pressure in reactor

[c] rate units are $mmol_{CO}/g_{cat}/h$

APPENDIX E. AUXILIARY DATA FOR CATALYST CHARACTERIZATION

Presented here are calculations of EOR, *Disp*, and d_c, H_2 uptake scans, and the PSD code.

E.1 Example Calculations of EOR, Dispersion, and Crystallite Diameter

The following worksheet calculates extent of reduction, dispersion of iron, and iron metal crystallite diametes for the six 1S and 1D catalysts.

Molecular Weights

$MW_{Fe} := 55.85\frac{gm}{mol}$ $MW_{Cu} := 63.55\frac{gm}{mol}$ $MW_{K} := 39.10\frac{gm}{mol}$

$MW_{Si} := 28.09\frac{gm}{mol}$ $MW_{O} := 16.00\frac{gm}{mol}$

Constants

$mmol := 10^{-3}mol$ $\mu mol := 10^{-6}mol$ $mol_{Fe} := mol$ Define units used below.

$mol_{Fe3O4} := mol$ $mol_{FeO} := mol$ $mol_{O} := mol$ $mol_{Fe2O3} := mol$

$C_1 := 123$ $C_2 := 1.12$ Constants for dispersion and crystallite diameter calculations.

EOR Data from TGA for 1 Step Catalysts

$$m_{passivated} := \begin{pmatrix} 17.263 \\ 17.736 \\ 19.026 \\ 16.124 \\ 16.328 \\ 20.4769 \end{pmatrix} mg \qquad \begin{pmatrix} 1UH \\ 1WH \\ 1UL \\ 1WL \\ 1DH \\ 1DL \end{pmatrix}$$

Total mass of passivated sample.

$$m_{Dry} := \begin{pmatrix} 17.01 \\ 17.21 \\ 18.69 \\ 15.73 \\ 16.05 \\ 20.11 \end{pmatrix} mg \qquad \begin{pmatrix} 1UH \\ 1WH \\ 1UL \\ 1WL \\ 1DH \\ 1DL \end{pmatrix}$$

Mass of dry sample (100°C).

$$m_{Red} := \begin{pmatrix} 15.62 \\ 15.13 \\ 17.11 \\ 14.24 \\ 14.44 \\ 18.64 \end{pmatrix} mg \qquad \begin{pmatrix} 1UH \\ 1WH \\ 1UL \\ 1WL \\ 1DH \\ 1DL \end{pmatrix}$$

Mass of reduced sample.

$$m_{Oxi} := \begin{pmatrix} 17.36 \\ 17.81 \\ 18.86 \\ 17.2 \\ 16.77 \\ 20.87 \end{pmatrix} mg \qquad \begin{pmatrix} 1UH \\ 1WH \\ 1UL \\ 1WL \\ 1DH \\ 1DL \end{pmatrix}$$

Mass of oxidized sample post reduction.

H2 Uptake Data

$$n_{H2} := \begin{pmatrix} 159.06 \\ 202.53 \\ 146.41 \\ 130.83 \\ 199.65 \\ 272.4 \end{pmatrix} \cdot \frac{\mu mol}{gm} \qquad \begin{pmatrix} 1UH \\ 1WH \\ 1UL \\ 1WL \\ 1DH \\ 1DL \end{pmatrix}$$

Moles of H2 taken by reduced catalyst.

Passivated Catalyst Composition

$$Fe := \begin{pmatrix} 0.664 \\ 0.614 \\ 0.713 \\ 0.695 \\ 0.622 \\ 0.583 \end{pmatrix} \quad Cu := \begin{pmatrix} 0.033 \\ 0.031 \\ 0.035 \\ 0.037 \\ 0.035 \\ 0.031 \end{pmatrix} \quad Ka := \begin{pmatrix} 0.025 \\ 0.002 \\ 0.026 \\ 0.002 \\ 0.003 \\ 0.003 \end{pmatrix} \quad SiO2 := \begin{pmatrix} 0.106 \\ 0.098 \\ 0.114 \\ 0.111 \\ 0.099 \\ 0.093 \end{pmatrix}$$

Composition on a mass ratio basis. From ICP analysis of passivated catalyst.

$$O := 1 - Fe - Cu - Ka - SiO2 = \begin{pmatrix} 0.172 \\ 0.255 \\ 0.112 \\ 0.155 \\ 0.241 \\ 0.29 \end{pmatrix} \quad \begin{pmatrix} 1UH \\ 1WH \\ 1UL \\ 1WL \\ 1DH \\ 1DL \end{pmatrix}$$

Mass of oxygen in passivated catalysts determined from ICP analysis, including H2O.

Calculate EOR Based on Oxygen Uptake

$$m_{Ouptake} := m_{Oxi} - m_{Red} = \begin{pmatrix} 1.74 \\ 2.68 \\ 1.75 \\ 2.96 \\ 2.33 \\ 2.23 \end{pmatrix} \cdot mg \quad \begin{pmatrix} 1UH \\ 1WH \\ 1UL \\ 1WL \\ 1DH \\ 1DL \end{pmatrix}$$

Mass gain due to oxygenation of reduced catalyst.

$$n_{Ouptake} := \frac{m_{Ouptake}}{MW_O} = \begin{pmatrix} 0.109 \\ 0.167 \\ 0.109 \\ 0.185 \\ 0.146 \\ 0.139 \end{pmatrix} \cdot mmol \quad \begin{pmatrix} 1UH \\ 1WH \\ 1UL \\ 1WL \\ 1DH \\ 1DL \end{pmatrix}$$

Moles of atomic oxygen taken.

$$n_{Fe} := \overrightarrow{\left(\frac{Fe \cdot m_{passivated}}{MW_{Fe}} \right)} = \begin{pmatrix} 0.205 \\ 0.195 \\ 0.243 \\ 0.201 \\ 0.182 \\ 0.214 \end{pmatrix} \cdot mmol \quad \begin{pmatrix} 1UH \\ 1WH \\ 1UL \\ 1WL \\ 1DH \\ 1DL \end{pmatrix}$$

Mole of Fe in passivated sample.

$$n_{Cu} := \overrightarrow{\left(\frac{Cu \cdot m_{passivated}}{MW_{Cu}} \right)} = \begin{pmatrix} 0.009 \\ 0.009 \\ 0.01 \\ 0.009 \\ 0.009 \\ 0.01 \end{pmatrix} \cdot mmol \quad \begin{pmatrix} 1UH \\ 1WH \\ 1UL \\ 1WL \\ 1DH \\ 1DL \end{pmatrix}$$

Mole Cu in passivated sample.

$$nO_{Cu} := n_{Cu} = \begin{pmatrix} 0.009 \\ 0.009 \\ 0.01 \\ 0.009 \\ 0.009 \\ 0.01 \end{pmatrix} \cdot mmol \quad \begin{pmatrix} 1UH \\ 1WH \\ 1UL \\ 1WL \\ 1DH \\ 1DL \end{pmatrix}$$

Mole O gained in oxidizing Cu to CuO.

$$p_{Fe27guess} := \begin{pmatrix} 0.637 \\ 0.430 \\ 0.670 \\ 0.337 \\ 0.529 \\ 0.605 \end{pmatrix} \quad \begin{pmatrix} 1UH \\ 1WH \\ 1UL \\ 1WL \\ 1DH \\ 1DL \end{pmatrix} \qquad p_{Fe20} := 0.1$$

Assume Fe is present in various oxidation states after "full" reduction (0, 2+, 2.7+). Partition out fractions of Fe in each oxide, assuming the 10% FeO.

$$p_{Fe00}(p_{Fe27}) := \overrightarrow{(1 - p_{Fe27} - p_{Fe20})}$$

$$nO_{Fe3O4}(p_{Fe27}) := \left(n_{Fe} \cdot p_{Fe27} \cdot \frac{1\,mol_{Fe3O4}}{3\,mol_{Fe}} \cdot \frac{1\,mol_{O}}{2\,mol_{Fe3O4}} \right)$$

Function for mole O gained in oxidation of Fe3O4 to Fe2O3.

$$nO_{FeO} := n_{Fe} \cdot 0.1 \cdot \frac{1\,mol_{FeO}}{1\,mol_{Fe}} \cdot \frac{1\,mol_{O}}{2\,mol_{FeO}}$$

Function for mole O gained in oxidation of FeO to Fe2O3.

$$nO_{Fe}(p_{Fe27}) := \left(n_{Fe} \cdot p_{Fe00}(p_{Fe27}) \cdot \frac{3\,mol_{O}}{2\,mol_{Fe}} \right)$$

Mole O gained in oxidation of Fe to Fe2O3.

$$nO_{Total}(p_{Fe27}) := nO_{Cu} + nO_{Fe3O4}(p_{Fe27}) \ldots + nO_{FeO} + nO_{Fe}(p_{Fe27})$$

Total theoretical O gained during oxidation.

Given $\quad n_{Ouptake} = nO_{Total}(p_{Fe27guess})$

Solve block to find percentages of Fe in 2.7+ state after reduction.

$$p_{Fe27} := \text{Find}(p_{Fe27guess}) = \begin{pmatrix} 0.685 \\ 0.439 \\ 0.745 \\ 0.394 \\ 0.486 \\ 0.596 \end{pmatrix} \quad \begin{pmatrix} 1UH \\ 1WH \\ 1UL \\ 1WL \\ 1DH \\ 1DL \end{pmatrix}$$

$$EOR := p_{Fe00}(p_{Fe27}) = \begin{pmatrix} 21.5 \\ 46.1 \\ 15.5 \\ 50.6 \\ 41.4 \\ 30.4 \end{pmatrix} \cdot \% \quad \begin{pmatrix} 1UH \\ 1WH \\ 1UL \\ 1WL \\ 1DH \\ 1DL \end{pmatrix}$$

Extent of reduction to Fe metal or percent of Fe in metal state.

Calculate Dispersion and Crystallite Diameter

$$X := n_{H2} \cdot \frac{gm}{\mu mol} = \begin{pmatrix} 159 \\ 203 \\ 146 \\ 131 \\ 200 \\ 272 \end{pmatrix} \quad \begin{pmatrix} 1UH \\ 1WH \\ 1UL \\ 1WL \\ 1DH \\ 1DL \end{pmatrix}$$

H2 uptake.

$$f := EOR = \begin{pmatrix} 0.215 \\ 0.461 \\ 0.155 \\ 0.506 \\ 0.414 \\ 0.304 \end{pmatrix} \quad \begin{pmatrix} 1UH \\ 1WH \\ 1UL \\ 1WL \\ 1DH \\ 1DL \end{pmatrix}$$

Fraction of Fe in Fe0 state after reduction.

$$W := Fe \cdot 100 = \begin{pmatrix} 66.4 \\ 61.4 \\ 71.3 \\ 69.5 \\ 62.2 \\ 58.3 \end{pmatrix} \quad \begin{pmatrix} 1UH \\ 1WH \\ 1UL \\ 1WL \\ 1DH \\ 1DL \end{pmatrix}$$

Percentage of Fe in sample. Composition should be identical to the sample used in H2 uptake.

$$D := \overrightarrow{\left(\frac{C_2 \cdot X}{f \cdot W}\right)} = \begin{pmatrix} 12.5 \\ 8.0 \\ 14.8 \\ 4.2 \\ 8.7 \\ 17.2 \end{pmatrix} \quad \begin{pmatrix} 1UH \\ 1WH \\ 1UL \\ 1WL \\ 1DH \\ 1DL \end{pmatrix}$$

Percent dispersion, defined as percent of reduced Fe available for chemisorption (on surface).

$$d := \frac{C_1}{D} nm = \begin{pmatrix} 9.8 \\ 15.3 \\ 8.3 \\ 29.5 \\ 14.1 \\ 7.1 \end{pmatrix} \cdot nm \quad \begin{pmatrix} 1UH \\ 1WH \\ 1UL \\ 1WL \\ 1DH \\ 1DL \end{pmatrix}$$

Crystallite diameter based on percent of reduced Fe exposed to the surface.

E.2 Hydrogen Uptake Scans

Hydrogen chemisorption scans for the eight 1S and 2S catalysts as well as 1UHa and 1ULa are given in Figures E.1 to E.10.

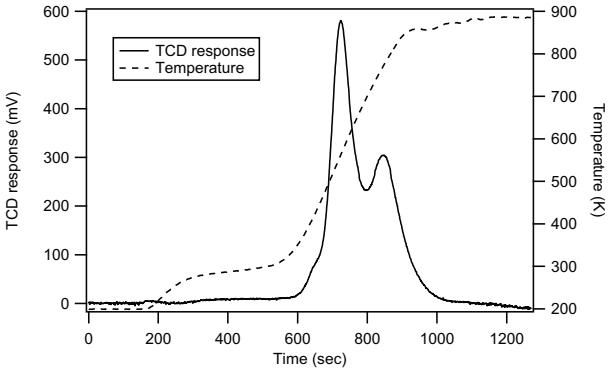

Figure E.1: Hydrogen chemisorption uptake scan of 1UH.

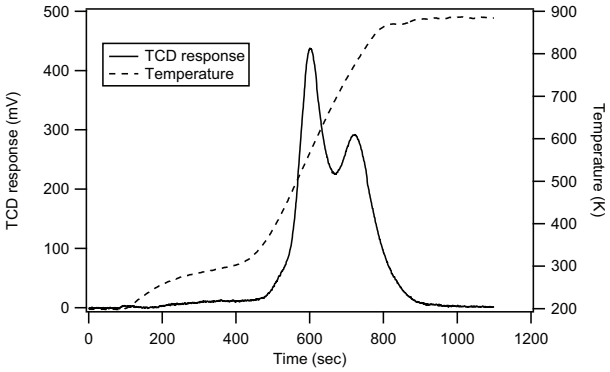

Figure E.2: Hydrogen chemisorption uptake scan of 1UL.

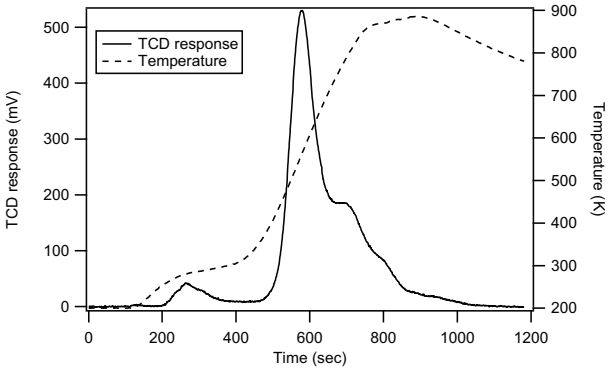

Figure E.3: Hydrogen chemisorption uptake scan of 1WH.

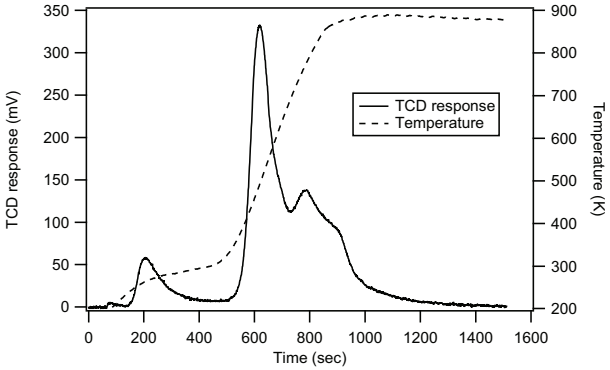

Figure E.4: Hydrogen chemisorption uptake scan of 1WL.

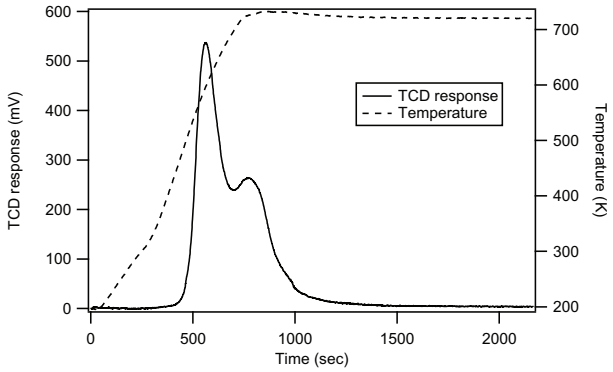

Figure E.5: Hydrogen chemisorption uptake scan of 2UH.

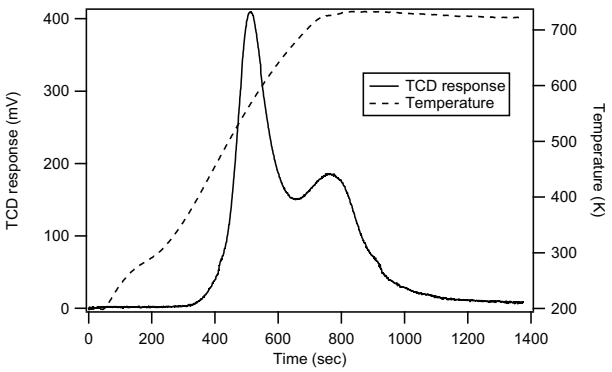

Figure E.6: Hydrogen chemisorption uptake scan of 2UL.

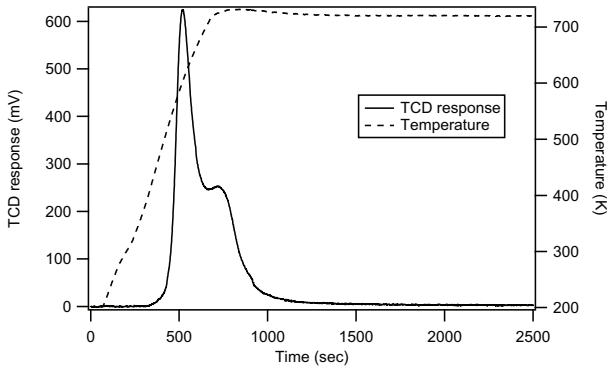

Figure E.7: Hydrogen chemisorption uptake scan of 2WH.

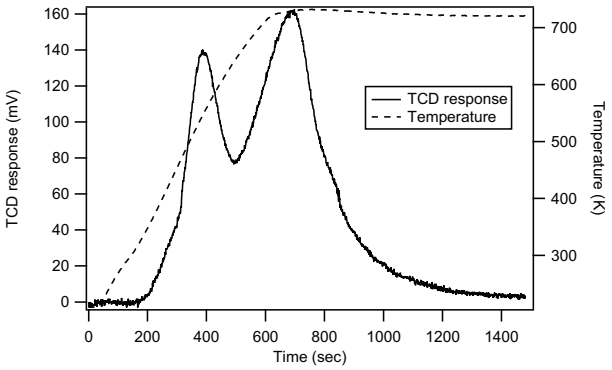

Figure E.8: Hydrogen chemisorption uptake scan of 2WL.

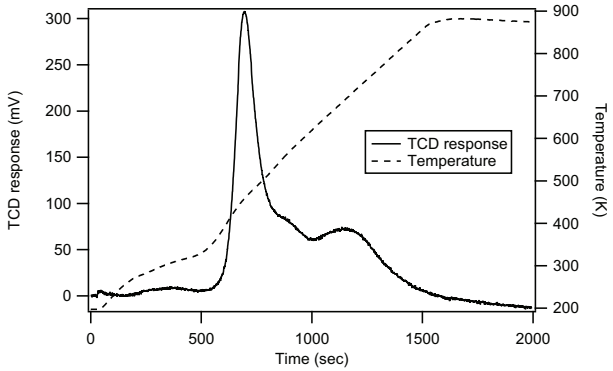

Figure E.9: Hydrogen chemisorption uptake scan of 1UHa.

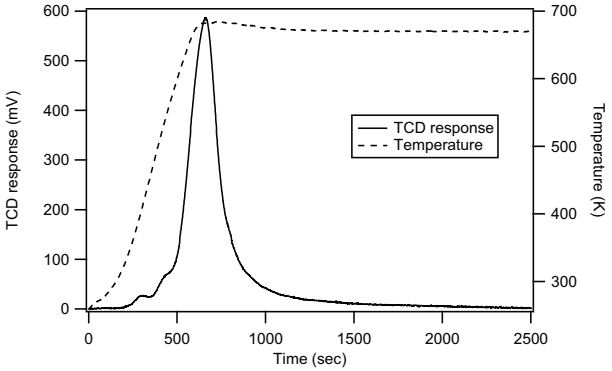

Figure E.10: Hydrogen chemisorption uptake scan of 1ULa.

E.3 Pore Size Distribution Calculator

The following code was developed in Microsoft Visual Basic Applications in Excel and calculates a pore size distribution from the desorption branch of BET isotherm data. The subroutine BETCruncher calls the subroutine fitsolver which calls the solver add-in for Excel. The outputs of the BETCruncher are put directly into the excel worksheet in cells C17 and C18 and in columns L through AJ.

```
''''''''''''''''''''''''''''''''''''''''''''''''''''''''''''''''''''''''''''
''' BETCruncher by Kyle Brunner 1 January 2012                           '''
''' Prints the formulas into the cells and sets up equalities for the    '''
''' solver to find the pore size distribution. Inputs are PP0() and Vg() '''
''' which are the arrays of BET data. The outputs are put directly into  '''
''' an Excel worksheet, specifically, the average diameter is in C17     '''
''' and the standard deviation is in C18.                                '''
''''''''''''''''''''''''''''''''''''''''''''''''''''''''''''''''''''''''''''
Public Sub BETCruncher(ByRef PP0() As Double, ByRef Vg() As Double, ByRef _
errmsg As String, ByRef errstop As Boolean, wkshtname As String)
    Dim i As Integer
    Dim j As Integer
    Dim nn As Integer
    Dim nr As Integer
    Dim adsns As Double
    Dim desns As Double
    Dim cPP0 As Integer
    Dim cVg As Integer
    Dim rk As Integer
    Dim rp As Integer
    Dim t As Integer
    Dim dt As Integer
    Dim drp As Integer
```

```
Dim rpavg As Integer
Dim Q As Integer
Dim n As Integer
Dim Vliq As Integer
Dim dVliq As Integer
Dim dVf As Integer
Dim dVk As Integer
Dim dVp As Integer
Dim dAp As Integer
Dim EdAp As Integer
Dim dVdr As Integer
Dim ravgdV As Integer
Dim lnravg As Integer
Dim dVdlnravg As Integer
Dim VDF As Integer
Dim nVDF As Integer
Dim ndVdlnravg As Integer
Dim SE As Integer
Dim DesorbRow As Double
Dim AddsDesSign As Double
Dim rmin() As Double
Dim rmax() As Double
Dim sdVp() As Double
Dim ravg() As Double
Dim xcol() As Integer
Dim ycol() As Integer
Dim srow() As Integer
Dim frow() As Integer
Dim sumravgdV As Double
Dim sumdVp As Double
```

```
Dim Ri As String
Dim Ri1 As String
Dim maxdVdlnr As Double
Dim maxlnr() As Double

''' initialize parameters
adsns = 0
desns = 0
nn = UBound(PP0) + 2 'will be the row containing the last entry

nr = 1 'number of different pore ranges to find

''' Create arrays to find the dataset to perform the calculations on
ReDim rmin(nr)
ReDim rmax(nr)
ReDim sdVp(nr)
ReDim ravg(nr)
ReDim maxlnr(nr)

''' Assign each value a column with PP0 as columns L (12) and Vg as
''' column M (13)
cPP0 = 12
cVg = 13
rk = 14
t = 15
dt = 16
rp = 17
drp = 18
rpavg = 19
Q = 20
```

```
n = 21
Vliq = 22
dVliq = 23
dVf = 24
dVk = 25
dVp = 26
dAp = 27
EdAp = 28
dVdr = 29
ravgdV = 30
lnravg = 31
dVdlnravg = 32
VDF = 33
nVDF = 34
ndVdlnravg = 35
SE = 36

''' Print equations to cells then remove the meaningless entries
''' Find the first point of the desorption leg
DesorbRow = 3
For i = 3 To nn
    Ri = "R" & i & "C"  'current row
    Ri1 = "R" & i - 1 & "C" 'previous row
    Cells(i, cPP0) = PP0(i - 2)
    Cells(i, cVg) = Vg(i - 2)
    If Cells(i, 12) > Cells(DesorbRow, 12) Then DesorbRow = i
    If i <= DesorbRow Then AddsDesSign = -1 Else AddsDesSign = 1
    Cells(i, rk) = "= -0.953 / ln(" & Ri & cPP0 & ")"
    ''' this equation for thickness seems more abundant in literature
    Cells(i, t) = "= 0.354 * (-5 / ln(" & Ri & cPP0 & ")) ^ (0.333)"
```

```
Cells(i, rp) = "=" & Ri & rk & "+" & Ri & t  'rk(i)+t(i)
''' moles = Vg / (0.082058 * 273.15)
Cells(i, n) = "=" & Ri & cVg & "/(0.082058 * 273.15)"
''' Vliquid = n * 34.68
Cells(i, Vliq) = "=" & Ri & n & "*34.68"
If i > 3 Then
    ''' t(i-1)-t(i)
    Cells(i, dt) = "=" & AddsDesSign & "*" & Ri1 & t & "-" & _
    AddsDesSign & "*" & Ri & t
    ''' rp(i-1)-rp(i)
    Cells(i, drp) = "=" & AddsDesSign & "*" & Ri1 & rp & "-" & _
    AddsDesSign & "*" & Ri & rp
    ''' (rp(i - 1) + rp(i)) / 2
    Cells(i, rpavg) = "=(" & Ri1 & rp & "+" & Ri & rp & ")/2"
    ''' Qfactor = (rpavg / (rpavg - t)) ^ 2
    Cells(i, Q) = "=(" & Ri & rpavg & "/(" & Ri & rpavg & "-" & _
    Ri & t & "))^2"
    ''' delVliq = Vliq(i - 1) - Vliq(i)
    Cells(i, dVliq) = "=" & AddsDesSign & "*" & Ri1 & Vliq & "-" _
    & AddsDesSign & "*" & Ri & Vliq
    ''' delVf = dt(i) * EdAp(i - 1)
    Cells(i, dVf) = "=" & Ri & dt & "*" & Ri1 & EdAp
    ''' delVk = dVliq - dVf
    Cells(i, dVk) = "=" & Ri & dVliq & "-" & Ri & dVf
    ''' delVp = dVk * Q
    Cells(i, dVp) = "=" & Ri & dVk & "*" & Ri & Q
    ''' delAp = 2 * dVp / rpavg
    Cells(i, dAp) = "=2*" & Ri & dVp & "/" & Ri & rpavg
    ''' SumdAp = EdAp(i - 1) + dAp(i)
    Cells(i, EdAp) = "=" & Ri1 & EdAp & "+" & Ri & dAp
```

```
        ''' delVdr = dVp / drp
        Cells(i, dVdr) = "=" & Ri & dVp & "/" & Ri & drp
        ''' rdelVm = dVm * rpavg
        Cells(i, ravgdV) = "=" & Ri & dVp & "*" & Ri & rpavg
        ''' lnravg=ln(rpavg)
        Cells(i, lnravg) = "=ln(" & Ri & rpavg & ")"
        ''' dVdrlogger = dVliq / (rpi - rp)
        Cells(i, dVdlnravg) = "=" & Ri & dVp & "/(" & AddsDesSign & _
        "*" & Ri1 & lnravg & "-" & AddsDesSign & "*" & Ri & lnravg & _
        ")"
        Cells(i, VDF) = "=1/(Sqrt(2*Pi())*R24C3*" & Ri & rpavg & _
        ")*EXP(-((ln(" & Ri & rpavg & ")-R23C3)^2)/(2*R24C3^2))"
        Cells(i, nVDF) = "=" & Ri & VDF & "*R" & nn + 3 + AddsDesSign _
        & "C" & VDF
        Cells(i, ndVdlnravg) = "=" & Ri & dVdlnravg & "*R" & nn + 3 + _
        AddsDesSign & "C" & dVdlnravg
        Cells(i, SE) = "=(" & Ri & nVDF & "-" & Ri & ndVdlnravg & ")^2"
        If Cells(i, rpavg) < 1.5 Then 'Find the last relevant data
            If i <= DesorbRow Then
                adsns = i - 1
            ElseIf desns = 0 Then
                desns = i - 1
            End If
        End If
    End If
Next i

''' correct the equations for at the adsorption/desoprtion boundary
Cells(DesorbRow + 1, dVf) = "=" & "R" & DesorbRow + 1 & "C" & dt & "*0"
Cells(DesorbRow + 1, EdAp) = "=0" & "+" & "R" & DesorbRow + 1 & "C" & _
```

```
dAp 'SumdAp = EdAp(i - 1) + dAp(i)
Cells(i, dVdlnravg) = "=" & "R" & DesorbRow & "C" & dVp & "/(0-" & _
"R" & DesorbRow & "C" & lnravg & ")"  'dVdrlogger = dVliq / (rpi - rp)

''' delete non-sensical values
For i = dVdlnravg To SE
    Cells(adsns - 1, i) = ""
    Cells(DesorbRow + 1, i) = ""
Next i

Cells(21, 3) = "=2*EXP(C23)" 'mu
Cells(22, 3) = "=2*EXP(C24)" 'sigma

''' Format labels for the output cells
Cells(nn + 1, lnravg) = "Ads Sum"
Cells(nn + 2, lnravg) = "Ads 1/Sum"
Cells(nn + 3, lnravg) = "Des Sum"
Cells(nn + 4, lnravg) = "Des 1/Sum"
Cells(nn + 1, dVdlnravg) = "=sum(R" & adsns & "C" & dVdlnravg & ":R" _
& DesorbRow & "C" & dVdlnravg & ")"
Cells(nn + 2, dVdlnravg) = "=1/R" & nn + 1 & "C" & dVdlnravg
Cells(nn + 3, dVdlnravg) = "=sum(R" & DesorbRow + 1 & "C" & dVdlnravg _
& ":R" & desns & "C" & dVdlnravg & ")"
Cells(nn + 4, dVdlnravg) = "=1/R" & nn + 3 & "C" & dVdlnravg
Cells(nn + 1, VDF) = "=sum(R" & adsns & "C" & VDF & ":R" & DesorbRow _
& "C" & VDF & ")"
Cells(nn + 2, VDF) = "=1/R" & nn + 1 & "C" & VDF
Cells(nn + 3, VDF) = "=sum(R" & DesorbRow + 1 & "C" & VDF & ":R" & _
desns & "C" & VDF & ")"
Cells(nn + 4, VDF) = "=1/R" & nn + 3 & "C" & VDF
```

```
Cells(nn + 1, nVDF) = "=sum(R" & adsns & "C" & nVDF & ":R" & _
DesorbRow & "C" & nVDF & ")"
Cells(nn + 3, nVDF) = "=sum(R" & DesorbRow & "C" & nVDF & ":R" & _
desns & "C" & nVDF & ")"
Cells(nn + 1, ndVdlnravg) = "=sum(R" & adsns & "C" & ndVdlnravg & _
":R" & DesorbRow & "C" & ndVdlnravg & ")"
Cells(nn + 3, ndVdlnravg) = "=sum(R" & DesorbRow + 1 & "C" & _
ndVdlnravg & ":R" & desns & "C" & ndVdlnravg & ")"
Cells(nn + 1, SE) = "=sum(R" & adsns & "C" & SE & ":R" & DesorbRow & _
"C" & SE & ")"
Cells(nn + 3, SE) = "=sum(R" & DesorbRow & "C" & SE & ":R" & desns & _
"C" & SE & ")"

''' delete entries outside of the mezopore range
For i = 4 To adsns - 1
    Cells(i, ravgdV) = ""
    Cells(i, lnravg) = ""
    Cells(i, dVdlnravg) = ""
    Cells(i, VDF) = ""
    Cells(i, nVDF) = ""
    Cells(i, ndVdlnravg) = ""
    Cells(i, SE) = ""
Next i
For i = desns + 1 To nn
    Cells(i, ravgdV) = ""
    Cells(i, lnravg) = ""
    Cells(i, dVdlnravg) = ""
    Cells(i, VDF) = ""
    Cells(i, nVDF) = ""
    Cells(i, ndVdlnravg) = ""
```

```
    Cells(i, SE) = ""
Next i
DoEvents

''' Add the appropriate summations
''' Find the guess values for the solver
For i = 1 To nr
    maxdVdlnr = 0
    ''' guess value for solver is the ln(r) for the max dVdlnr
    For j = rmax(i) To rmin(i)
        If Cells(j, dVdlnravg) > maxdVdlnr Then
            maxdVdlnr = Cells(j, dVdlnravg)
            maxlnr(i) = Cells(j, lnravg)
        End If
    Next j
    If i > 1 Then
        Cells(nn + 1, VDF + (i - 1) * 4) = "=1/sum(R" & rmin(i) & "C" _
        & VDF + (i - 1) * 4 & ":R" & rmax(i) & "C" & VDF + (i - 1) * _
        4 & ")"
        Cells(nn + 1, nVDF + (i - 1) * 4) = "=sum(R" & rmin(i) & "C" _
        & nVDF + (i - 1) * 4 & ":R" & rmax(i) & "C" & nVDF + (i - 1) _
        * 4 & ")"
        Cells(nn + 1, ndVdlnravg + (i - 1) * 4) = "=1/sum(R" & _
        rmin(i) & "C" & dVdlnravg & ":R" & rmax(i) & "C" & dVdlnravg _
        & ")"
        Cells(31 + i, 7) = "=sum(R" & rmin(i) & "C" & SE + (i - 1) * _
        4 & ":R" & rmax(i) & "C" & SE + (i - 1) * 4 & ")"
    End If
Next i
```

```
    ''' Now provide guess values for sigma and mu - the value for mu will
    ''' be the lnravg value of the maximum experimental value
    If Cells(23, 3) = "" Then Cells(23, 3) = maxlnr(1)
    If Cells(24, 3) = "" Then Cells(24, 3) = 0.1 'sigma

    ''' Finally, if installed, run the Solver
    If Application.AddIns("Solver Add-In").Installed = True Then
        Call fitsolver("$AJ$" & nn + 3, "$C$23:$C$24", 1, 6)
    End If

    ''' Calculate pore volume and average pore radii and report to user
    If errstop = True Then Exit For
    sumravgdV = 0
    sumdVp = 0
    For i = rmax(1) To rmin(1)
        sumravgdV = sumravgdV + Cells(i, ravgdV)
        sumdVp = sumdVp + Cells(i, dVp)
    Next i
    if sumdVp <> 0 then
        ravg(1) = sumravgdV / sumdVp
        sdVp(i) = sumdVp
        Cells(17, 3) = ravg(1) * 2
        Cells(18, 3) = "=Max(R" & DesorbRow + 1 & "C" & EdAp & ":R" & _
        desns & "C" & EdAp & ")"
        Cells(19, 3) = sdVp(1) / 1000
    Else
        Cells(17, 3) = "Divde by 0"
    End If
End Sub
''''''''''''''''''''''''''''''''''''''''''''''''''''''''''''''''''''''''''''''
```

```
’’’ END BETCruncher                                                      ’’’
’’’’’’’’’’’’’’’’’’’’’’’’’’’’’’’’’’’’’’’’’’’’’’’’’’’’’’’’’’’’’’’’’’’’’’’’’’’’

’’’’’’’’’’’’’’’’’’’’’’’’’’’’’’’’’’’’’’’’’’’’’’’’’’’’’’’’’’’’’’’’’’’’’’’’’’’’
’’’ fitsolver                                                            ’’’
’’’ Calls the solver macro add-in for Excel. ctarget is the target cell  ’’’
’’’ to set to zero. crange is the range of cells to vary. ’in theory,   ’’’
’’’ this does not require solver to be installed a priori. In practice   ’’’
’’’ the user should create a reference to the solver macro by selecting  ’’’
’’’ "References" from the "Tools" menu of the VBA window and then        ’’’
’’’ selecting the "Solver" check box and pressing "OK". This code draws  ’’’
’’’ heavily from http://peltiertech.com/Excel/SolverVBA.html 1 Jan 2012  ’’’
’’’’’’’’’’’’’’’’’’’’’’’’’’’’’’’’’’’’’’’’’’’’’’’’’’’’’’’’’’’’’’’’’’’’’’’’’’’’
Sub fitsolver(ctarget As String, crange As String, rrow As Integer, _
rcol As Integer)
    Dim Result As Integer
    Dim solverinstalled As Boolean
    Dim resulttxt As String
    Dim fontc As Integer

    ’’’ if solver installed, then solve, otherwise quit
    SolverReset
    SolverOK ctarget, 3, "0", crange
    SolverAdd crange, 3, "0.001"
    Result = SolverSolve(True)
    SolverFinish
End Sub
’’’’’’’’’’’’’’’’’’’’’’’’’’’’’’’’’’’’’’’’’’’’’’’’’’’’’’’’’’’’’’’’’’’’’’’’’’’’
’’’ END fitsolver                                                        ’’’
’’’’’’’’’’’’’’’’’’’’’’’’’’’’’’’’’’’’’’’’’’’’’’’’’’’’’’’’’’’’’’’’’’’’’’’’’’’’
```

APPENDIX F. TRICKLE FIXED-BED RECYCLE REACTOR MODEL CODE

The following code is described in Chapter 5 and was developed in Visual Basic Applications for Excel. Inputs and outputs are provided through a series of worksheets in the Excel file.

```
''''''''''''''''''''''''''''''''''''''''''''''''''''''''''''''''''''''''''''
''' Version 12.07 (July 2012)                                            '''
''' Trickle Fixed-Bed Recycle Reactor Model for the Fischer-Tropsch      '''
''' synthesis for iron and cobalt catalysts. The entry point is the      '''
''' Starter() subroutine. There are many global variables which should   '''
''' be initialized each run with a call to the Initializer() subroutine. '''
''''''''''''''''''''''''''''''''''''''''''''''''''''''''''''''''''''''''''''
Option Explicit

Public Eact As Double, Eads1 As Double, Eads2 As Double, Eads3 As Double
Public Eads4 As Double, Eads5 As Double
Public a0_conv_unit As Double, a1_conv_unit As Double
Public a2_conv_unit As Double, a3_conv_unit As Double
Public a4_conv_unit As Double
Public m1 As Double, n1 As Double, z1 As Double, z2 As Double
Public z3 As Double, z4 As Double, z5 As Double, z6 As Double, z0 As Double
Public BB As Double
Public SCH4 As Double, SC2C4 As Double, SC5plus As Double
Public SWGS As Double, SOXY As Double
Public nCORri As Double, nH2ri As Double, nCO2ri As Double
Public nH2Ori As Double, nCH4ri As Double, nC2C4ri As Double
```

```
Public nC5plusri As Double, nOXYri As Double, nN2ri As Double
Public Tin As Double, Tw As Double, act As Double, Dt As Double
Public manualhbed As Double, manualk As Double, manualdelP As Double
Public rhop As Double, order As Double, pp As Double
Public XCORi As Double, deltaH_overall As Double, dpeff As Double
Public rhob As Double, Lpeff As Double, Acrs As Double, eb As Double
Public m As Double, n As Double, H2COst As Double, cobalt As Integer
Public iron As Integer, cat As Integer, vapor As Integer, liquid As Integer
Public waterphase As Integer
Public Rg As Double, Time_converter As Double, PI As Double
Public P_converter As Double, g As Double, MWC5plus As Double
Public Vpore As Double
Public ThermalConductivityString As String, HbedString As String
Public BedVoidString As String, FrictionFactorString As String
Public stopcheck As Boolean
Public errmsg As String

Public Sub Starter()
    'Initialize results sheets
    Sheets("Inputs").Cells(26, 3) = "Running"
    Sheets("Inputs").Cells(26, 3).Font.Color = vbGreen
    DoEvents
    Sheets("Results").Range("B2:AA50000").ClearContents
    Sheets("Stream").Range("A2:S50000").ClearContents

    'Turn off automatic screen updates to increase performance time
    Application.ScreenUpdating = False
    Application.Calculation = xlCalculationManual

    'Start calculations and check for errors
```

```
    'On Error GoTo err1
    Call Calculations
    Sheets("Inputs").Cells(3, 3).Value = DateTime.Now
    Sheets("Inputs").Cells(3, 1) = _
        ActiveWorkbook.BuiltinDocumentProperties(7)

    'Report all error messages
    If errmsg = "" Then
        Sheets("Inputs").Cells(26, 3) = "Outputs"
        Sheets("Inputs").Cells(26, 3).Font.Color = vbWhite
    ElseIf stopcheck = True Then
        Sheets("inputs").Cells(26, 3) = "Calculations terminated early. " _
            & errmsg
        Sheets("Inputs").Cells(26, 3).Font.Color = vbRed
    Else
        Sheets("Inputs").Cells(26, 3) = "Calculations complete. " & errmsg
        Sheets("Inputs").Cells(26, 3).Font.Color = vbYellow
    End If
    DoEvents

    'Turn automatic screen updates back on
    Application.ScreenUpdating = True
    Application.Calculate
    Application.Calculation = xlCalculationAutomatic
    Exit Sub

    'If an error occurs, let the user know
err1:
    Sheets("Inputs").Cells(26, 3).Font.Color = vbRed
    Sheets("Inputs").Cells(26, 3) = "****ERROR**** " & errmsg
```

```
    Application.ScreenUpdating = True
    Application.Calculate
    Application.Calculation = xlCalculationAutomatic
    DoEvents
End Sub

Public Sub Calculations()
    'Result Arrays
    Dim z(20000) As Double, X(20000) As Double, T(20000) As Double
    Dim P(20000) As Double, FCO(20000) As Double, W(20000) As Double
    Dim Rateobs(20000) As Double

    'User Inputs
    Dim a0 As Double, a1 As Double, a2 As Double, a3 As Double, a4 As Double
    Dim H2COpi As Double, Ptot_in As Double, RR As Double
    Dim RRC5plus As Double, XCOf As Double, deltaz As Double, dp As Double
    Dim AR As Double, ID As Double, rho As Double
    Dim catselect As String, geometry As String
    Dim ntube As Integer

    'Vairables
    Dim U As Double, hbed As Double, ke As Double, Pr As Double
    Dim i As Integer

    'Heat of reaction variables
    Dim deltaH_r1 As Double, deltaH_r2 As Double, deltaH_r3 As Double
    Dim deltaH_r4 As Double, deltaH_r5 As Double
    Dim deltaH_r1_Tin As Double, deltaH_r2_Tin As Double
    Dim deltaH_r3_Tin As Double, deltaH_r4_Tin As Double
    Dim deltaH_r5_Tin As Double
```

```
Dim Integral_r1 As Double, Integral_r2 As Double
Dim Integral_r3 As Double, Integral_r4 As Double
Dim Integral_r5 As Double, dHfCO As Double, dHfH2 As Double
Dim dHfCO2 As Double, dHfH2O As Double, dHfCH4 As Double
Dim dHfC2C4 As Double, dHfC5plus As Double, dHfOXY As Double

'Constants
Dim Pin As Double, stot As Double, vpH2O As Double
Dim cool_duty_one_tube As Double, cool_duty_overall As Double
Dim SA As Double, sphericity As Double, MWcat As Double
Dim nCOpi As Double, nH2pi As Double, nCO2pi As Double
Dim nH2Opi As Double, nCH4pi As Double, nC2C4pi As Double
Dim nC5pluspi As Double, nN2pi As Double, ntotpi As Double
Dim ytotpi As Double, nCOpo As Double, nH2po As Double, nCO2po As Double
Dim nH2Opo As Double, nCH4po As Double, nC2C4po As Double
Dim nC5pluspo As Double, nOXYpo As Double, nN2po As Double
Dim nCOrc As Double, nH2rc As Double, nCO2rc As Double
Dim nH2Orc As Double, nCH4rc As Double, nC2C4rc As Double
Dim nC5plusrc As Double, nOXYrc As Double, nN2rc As Double
Dim nCOri As Double, manualeb As Double, updater As Integer
Dim dispersion As Variant, loading As Variant

'Initialize variables
Call initializer

'Read in User Input (Model Description)
'These are input in order of Column then by Row
'All user inputs should be collected here (one time only) and then
'used as defined variables elsewhere
'Repeatedly accessing values in cells causes the program to slow down
```

```
'significantly - avoid it at all costs
'User determines which catalyst is modeled
catselect = Sheets("Inputs").Range("C2").Text
'Moles total at process inlet (mol/s)
ntotpi = Sheets("Inputs").Range("E6").Value
'Moles CO at process inlet (mol/s) - divide by ntube in "Set Physical
'Constants" section below
nCOpi = Sheets("Inputs").Range("E7").Value
'Moles H2 at process inlet (mol/s) - divide by ntube in "Set Physical
'Constants" section below
nH2pi = Sheets("Inputs").Range("E8").Value
'Moles CO2 at process inlet (mol/s) - divide by ntube in "Set
'Physical Constants" section below
nCO2pi = Sheets("Inputs").Range("E9").Value
'Moles H2O at process inlet (mol/s) - divide by ntube in "Set
'Physical Constants" section below
nH2Opi = Sheets("Inputs").Range("E10").Value
'Moles CH4 at process inlet (mol/s) - divide by ntube in "Set
'Physical Constants" section below
nCH4pi = Sheets("Inputs").Range("E11").Value
'Moles C5H12 at process inlet (mol/s) - divide by ntube in "Set
'Physical Constants" section below
nC2C4pi = Sheets("Inputs").Range("E12").Value
'Moles Heavy Hydrocarbons  at process inlet (mol/s) - divide by ntube
'in "Set Physical Constants" section below
nC5pluspi = Sheets("Inputs").Range("E13").Value
'Moles N2 at process inlet (mol/s) - divide by ntube in "Set Physical
'Constants" section below & added to nN2pi below
nN2pi = Sheets("Inputs").Range("E14").Value
'Ratio of syngas in process
```

```
H2COpi = Sheets("Inputs").Range("D15").Value
'Reactor inlet temperature (K)
Tin = Sheets("Inputs").Range("D18").Value
'Cooling water temperature (K)
Tw = Sheets("Inputs").Range("D19").Value
'Reactor inlet pressure (atm)
Ptot_in = Sheets("Inputs").Range("D20").Value
'Recycle ratio
RR = Sheets("Inputs").Range("D21").Value
'Fraction of hydrocarbons recycled
RRC5plus = Sheets("Inputs").Range("D22").Value
'Target conversion at reactor exit
XCOf = Sheets("Inputs").Range("D23").Value
'Set friction factor correlation
FrictionFactorString = Sheets("Inputs").Range("H5").Text
'Set thermal conductivity mode
ThermalConductivityString = Sheets("Inputs").Range("H9").Text
'Set bed void fraction mode
BedVoidString = Sheets("Inputs").Range("H16").Text
'Set Bed Heat Transfer Coefficient Mode
HbedString = Sheets("Inputs").Range("H17").Text
deltaz = Sheets("Inputs").Range("I2").Value     'node step size (m)
'manual pressure drop per length (atm/m)
manualdelP = Sheets("Inputs").Range("I5").Value
ntube = Sheets("Inputs").Range("I6").Value      'number of tubes
'diameter (m) of one reactor tube
Dt = Sheets("Inputs").Range("I7").Value
order = Sheets("Inputs").Range("I8").Value      'reaction order in CO
'thermal conductivity of bed (W/m K)
manualk = Sheets("Inputs").Range("I9").Value
```

```
dp = Sheets("Inputs").Range("I10").Value        'diameter of pellet (m)
rho = Sheets("Inputs").Range("I11").Value       'bed density (kg/m^3)
geometry = Sheets("Inputs").Range("I12").Text   'Catalyst geometry
Vpore = Sheets("Inputs").Range("I13").Value     'Pore volume
AR = Sheets("Inputs").Range("I14").Value        'Aspect Ratio
'Hollow Cylinder Inner Diameter (m)
ID = Sheets("Inputs").Range("I15").Value
'manual bed void fraction value
manualeb = Sheets("Inputs").Range("I16").Value
'manual hbed value (W/mK)
manualhbed = Sheets("Inputs").Range("I17").Value
act = Sheets("Inputs").Range("I18").Value       'activity of catalyst
SCH4 = Sheets("Inputs").Range("I19").Value      'Methane selectivity
'Selectivity of hydrocarbons between C2-C7
SC2C4 = Sheets("Inputs").Range("I20").Value
'Selectivity of hydrocarbons that is above C8
SC5plus = Sheets("Inputs").Range("I21").Value
'Water-Gas Shift selectivity
SWGS = Sheets("Inputs").Range("I22").Value
'Methanol selectivity Add to interface
SOXY = Sheets("Inputs").Range("I23").Value
'rate equation constant in the numberator as turn-over frequency (1/s)
a0 = Sheets("Inputs").Range("O13").Value
'Activation energy (J/mol)
Eact = Sheets("Inputs").Range("O14").Value
'rate equation power on Pco in numberator
m1 = Sheets("Inputs").Range("O15").Value
'rate equation power on PH2 in numberator
n1 = Sheets("Inputs").Range("O16").Value
BB = Sheets("Inputs").Range("O19").Value        'Constant in denominator
```

```
'rate equation constant in the denominator (1/atm^z1)
a1 = Sheets("Inputs").Range("O21").Value
'CO heat of adsorption (J/mol)
Eads1 = Sheets("Inputs").Range("O22").Value
'rate equation Power on Pco in denomenator
z1 = Sheets("Inputs").Range("O23").Value
'rate equation constant in the denominator (1/atm^(z2+z3))
a2 = Sheets("Inputs").Range("O25").Value
'Combined CO & H2 heat of adsorption (J/mol)
Eads2 = Sheets("Inputs").Range("O26").Value
'rate equation power on Pco in denomenator
z2 = Sheets("Inputs").Range("O27").Value
'rate equation power on PH2 in denomenator
z3 = Sheets("Inputs").Range("O28").Value
'rate equation constant in the denominator (1/atm^(z4))
a3 = Sheets("Inputs").Range("O30").Value
'Combined CO & H2 heat of adsorption (J/mol)
Eads3 = Sheets("Inputs").Range("O31").Value
'rate equation power on Pco in denomenator
z4 = Sheets("Inputs").Range("O32").Value
'rate equation constant in the denominator (1/atm^(z5))
a4 = Sheets("Inputs").Range("O34").Value
'Combined CO & H2 heat of adsorption (J/mol)
Eads4 = Sheets("Inputs").Range("O35").Value
'rate equation power on Pco in denomenator
z5 = Sheets("Inputs").Range("O36").Value
'rate equation power on Pco in denomenator
z0 = Sheets("Inputs").Range("O38").Value
```

```
'For cobalt rate constant only
loading = Sheets("Inputs").Range("Q16")
'For cobalt rate constant only
dispersion = Sheets("Inputs").Range("Q19")

'Check user input mole fraction for consistency
ytotpi = (nCOpi + nH2pi + nCO2pi + nH2Opi + nCH4pi + nC2C4pi + _
    nC5pluspi + nN2pi) / ntotpi
If Abs(1# - ytotpi) > 0.000001 Then
    MsgBox "The inlet mole fractions must sum to 1 before " & _
        "proceeding", vbOKOnly, "Inlet mole fraction does not sum to 1"
    errmsg = "Inlet mole fraction does not sum to 1. "
    Exit Sub
End If

'Check user input for selectivity model
stot = SCH4 + SC2C4 + SC5plus + SWGS + SOXY
If Abs(1 - stot) > 0.000001 Then
    MsgBox "The selectivities must sum to 1 before proceding", _
        vbOKOnly, "Selectivity model does not sum to 1"
    errmsg = errmsg & "Selectivity model does not sum to 1. "
    Exit Sub
End If

'Stop calculations if values for dispersion and/or loading not specified
If Sheets("Inputs").Range("P13").Text = "mol/(mol s atm^(m+n))" And _
    (Sheets("Inputs").Range("Q16").Value = 0 Or _
    Sheets("Inputs").Range("Q19").Value = 0) Then
    MsgBox "Please specify dispersion and loading."
    errmsg = errmsg & "Dispersion and/or Loading Undefined. "
```

```
    Exit Sub
End If

'Stop Calculations if a value for thermal conductivity is not specified
If ThermalConductivityString = "Input Effective Radial Thermal " _
    & "Conductivity" And Sheets("Inputs").Range("i9").Value = 0 Then
    MsgBox "Please specify a value for Effective Radial Thermal " _
        & "Conductivity """
    errmsg = errmsg & "Thermal Conductivity Undefined. "
    Exit Sub
ElseIf ThermalConductivityString = "Input Static Thermal " _
    & "Conductivity" And Sheets("Inputs").Range("i9").Value = 0 Then
    MsgBox "Please specify a value for Static Thermal Conductivity"
    errmsg = errmsg & "Thermal Conductivity Undefined. "
    Exit Sub
End If

'Stop calculations if a value for the bed heat transfer coefficient
'is not specified
If HbedString = "Input Constant Bed Heat Transfer Coefficient" And _
    Sheets("Inputs").Range("i17").Value = 0 Then
    MsgBox "Please specify a value for bed heat transfer coefficient"
    errmsg = "Bed Heat Transfer Coefficient Undefined. "
    Exit Sub
End If

'Stop calculations if a value for pressure drop is not specified
If FrictionFactorString = "Manually Specify Pressure Drop Per Bed " _
    & "Length " And manualdelP = 0 Then
    MsgBox "Please specify a value for pressure drop per bed length"
```

```
    errmsg = errmsg & "Pressure drop not specified. "
    Exit Sub
End If

'Stop calculations if manual bed void fraction option is selected,
'but pressure drop is not specified
If BedVoidString = "Manual Bed Void Fraction" And _
    FrictionFactorString <> "Manually Specify Pressure Drop Per Bed " _
        & "Length" Then
    MsgBox "Manual bed void fraction is specified. Please select " _
        & "'Manually Specify Pressure Drop Per Bed Length' and give " _
            & "an appropriate value."
    errmsg = errmsg & "Specify manual pressure drop per bed length. "
End If

'Check tube diameter:particle diameter ratio - from Benyahia &
'O'Neill 2005 Enhanced Voidage Correlations for Packed Beds of
'Various Particle Shapes and Sizes
If Dt / dp < 1.5 Or Dt / dp > 50 Then
    If BedVoidString <> "Manual Bed Void Fraction" Then errmsg = _
        errmsg & "Warning: Dt/dp = " & Dt / dp & ", but should be " _
        & "between 1.5 and 50 for eb correlation. "
End If

'Give a warning if there is no liquid recycle - Thermal conductivity
'equation is for gas-liquid downflow
If RRC5plus = 0# Then
    errmsg = errmsg & "Warning: liquid RR = 0 may be outside of " _
        & "correlations. "
End If
```

```
'Give warning about turning off keffective if static thermal
'conductivity selected
If ThermalConductivityString = "Input Static Thermal Conductivity" _
    Then errmsg = errmsg & "Constant static thermal conductivity " _
    & "specified. "

'Give warning about turning off keffective if manual thermal
'conductivity selected
If ThermalConductivityString = "Input Effective Radial Thermal " _
    & "Conductivity" Then errmsg = errmsg & "Constant effective " _
    & "thermal conductivity specified. "

'Give warning about turning off hbed if manual hbed input selected
If HbedString = "Input Constant Bed Heat Transfer Coefficient" Then _
    errmsg = errmsg & "Constant bed heat transfer coefficient " _
    & "specified. "

'Give warning that hbed continues to use kstatic = 1.5*kliq when
'manual keffective is used
If ThermalConductivityString = "Input Effective Radial Thermal " _
    & "Conductivity" And _
    HbedString = "Use Bed Heat Transfer Coefficient Correlation" Then
    errmsg = errmsg & "Constant effective radial thermal " _
        & "conductivity specified: hbed will continue to use kstatic " _
        & "= 1.5 * kliq. "
End If

'Set catalyst and stop calculations if incorrectly specified
cobalt = 1
```

```
iron = 2
If catselect = "Cobalt" Then
    cat = cobalt
ElseIf catselect = "Iron" Then
    cat = iron
Else
    MsgBox "Invalid Choice of Catalyst. Select either Cobalt or " _
        & "Iron.", vbOKOnly, "Invalid Catalyst"
    Exit Sub
End If

'Set Constants
If cat = cobalt Then
    n = 25              'average carbon number for hydrocarbons
    MWC5plus = 0.352    'molecular weight of liquid C25H52 (kg/mol)
    MWcat = 0.05893     'molecular weight of Co (kg/mol)
ElseIf cat = iron Then
    n = 20              'average carbon number for hydrocarbons
    MWC5plus = 0.282    'molecular weight of liquid C20H42 (kg/mol)
    MWcat = 0.05585     'molecular weight of iron (kg/mol)
End If
m = 2 * n + 1           'stoichiometric H2 molecules for reaction
Rg = 8.314              'Gas constant (J/mol K) or (m^3 Pa/mol K)
g = 9.808665            'Gravitational constant (m/s^2)
PI = 3.14159265         'mmmm I like pie
P_converter = 101325    'pressure conversion factor (Pa/atm)
Time_converter = 3600   'time conversion factor (s/hr)
XCORi = (RR / (RR + 1)) * XCOf  'conversion at reactor inlet
Pin = Ptot_in * P_converter     'Pressure in SI units (Pa)
```

```
Select Case geometry
    Case Is = "trilobe"
        'effective particle diameter (m)
        dpeff = dp * (3 / 4 * AR + 9 / 16 * 3 ^ (0.5) _
            * AR / PI) ^ (1 / 3)
        'effective thickness of the catalyst layer (m)
        Lpeff = dp / 8
        'surface area (m^2)
        SA = dp ^ 2 * (PI / 4 + 3 * 3 ^ 0.5 / 16 + PI * AR)
    Case Is = "cylinder"
        'effective particle diameter (m)
        dpeff = dp * (1.5 * AR) ^ (1 / 3)
        'effective thickness of the catalyst layer (m)
        Lpeff = dp / 4
        SA = PI * (0.5 + AR) * dp ^ 2   'surface area (m^2)
    Case Is = "sphere"
        dpeff = dp              'effective particle diameter (m)
        'effective thickness of the catalyst layer (m)
        Lpeff = dp / 6
        SA = PI * dp ^ 2        'surface area (m^2)
    Case Is = "h cylinder"
        'effective particle diameter (m)
        dpeff = (1.5 * AR * (dp ^ 3 - dp * ID ^ 2)) ^ (1 / 3)
        'catalyst thickness is 1/2*(OD-ID) and L for flat plates is
        '1/2 thickness (m)
        Lpeff = (dp - ID) / 4
        'surface area (m^2)
        SA = PI * (dp ^ 2 - ID ^ 2) / 2 + PI * AR * (dp ^ 2 + dp * ID)
End Select
'sphericity is the ratio of the surface area of the effective sphere
```

```
'to the actual surface area
sphericity = PI * dpeff ^ 2 / SA
Select Case BedVoidString
    Case Is = "Bed Void Fraction Correlation"
        'bed void fraction
        eb = 0.1504 + 0.2024 / sphericity _
            + 1.0814 / (Dt / dpeff + 0.1226) ^ 2
    Case Is = "Manual Bed Void Fraction"
        eb = manualeb
        errmsg = errmsg & "Manual bed void fraction specified. "
End Select
Select Case Sheets("Inputs").Cells(11, 8).Text
    Case Is = "Bed Density"
        rhob = rho              'density of bed (kg/m^3)
        rhop = rhob / (1 - eb)  'density of catalyst bed (kg/m^3)
        Sheets("Inputs").Cells(32, 8) = "Pellet Density"
        Sheets("Inputs").Range("I32").Value = rhop
    Case Is = "Pellet Density"
        rhop = rho
        rhob = rhop * (1 - eb)
        Sheets("Inputs").Cells(32, 8) = "Bed Density"
        Sheets("Inputs").Range("I32").Value = rhob
End Select
'convert numerator pre-exponential factor to the units (mol/kgcat s
'Pa^(m+n))
If Sheets("Inputs").Range("P13").Text = "mol/(mol s atm^(m+n))" Then
    a0_conv_unit = a0 * dispersion * loading / (MWcat * P_converter ^ _
        (m1 + n1))
ElseIf Sheets("Inputs").Range("P13").Text = "mol/(kg-Cat s _
    atm^(m+n))" Then
```

```
    a0_conv_unit = a0 / (P_converter ^ (m1 + n1))
ElseIf Sheets("Inputs").Range("P13").Text = "mol/(L-reactor s _
    atm^(m+n))" Then
    a0_conv_unit = a0 / (rhob * P_converter ^ (m1 + n1))
Else
    errmsg = "Invalid Units on Kinetic Model"
    Exit Sub
End If
'convert denominator pre-exponential factor to the units (Pa^-z1)
'from (atm^-z1)
a1_conv_unit = a1 / P_converter ^ z1
'convert denominator pre-exponential factor to the units
'(Pa^-(z3+z4)) from (atm^-(z3+z4))
a2_conv_unit = a2 / P_converter ^ (z2 + z3)
'convert denominator pre-exponential factor to the units (Pa^-(z5))
'from (atm^-(z5))
a3_conv_unit = a3 / P_converter ^ z4
'convert denominator pre-exponential factor to the units (Pa^-(z6))
'from (atm^-(z6))
a4_conv_unit = a4 / P_converter ^ z5
'stoichiometric ratio of H2 to CO
H2COst = (m / n) * SC5plus + (7 / 3) * SC2C4 + 3 * SCH4 - SWGS + 2 _
    * SOXY
Acrs = (PI * Dt ^ 2) / 4        'cross sectional area of tube (m^2)
stopcheck = False

'Check void fraction correlation for sphericity component
If sphericity < 0.42 Or sphericity > 1# Then
    errmsg = errmsg & "Warning: pi*dpeff^2/SA = " & sphericity _
    & ", but 0.42 < pi*dpeff^2/SA < 1.0 for eb"
```

```
End If

'Mass Balance
'moles of CO at process inlet per tube (mol/s)
nCOpi = nCOpi / ntube
'Moles H2 at process inlet per tube (mol/s)
nH2pi = nH2pi / ntube
'Moles CO2 at process inlet per tube (mol/s)
nCO2pi = nCO2pi / ntube
'Moles H2O at process inlet per tube (mol/s)
nH2Opi = nH2Opi / ntube
'Moles CH4 at process inlet per tube (mol/s)
nCH4pi = nCH4pi / ntube
'Moles Light Hydrocarbons (pentane) at process inlet per tube (mol/s)
nC2C4pi = nC2C4pi / ntube
'Moles Heavy Hydrocarbons at process inlet per tube (mol/s)
nC5pluspi = nC5pluspi / ntube
'Moles N2 at process inlet per tube (mol/s)
nN2pi = nN2pi / ntube
'This is Levenspiel's hypothetical Fco' (moles of CO at reactor
'inlet) (mol/s)
nCORri = nCOpi * (1 + RR)
'molar flow rate of CO in process outlet per tube (mol/s)
nCOpo = nCOpi * (1 - XCOf)
' molar flow rate of H2 in process outlet per tube (mol/s)
nH2po = nH2pi - nCOpi * XCOf * H2COst
'Molar flow rate of CO2 in process outlet per tube (mol/s)
nCO2po = nCO2pi + nCOpi * XCOf * SWGS
'H2O molar flow rate in process outlet per tube (mol/s) - all H2O is
'removed
```

```
nH2Opo = nH2Opi + nCOpi * XCOf * (SCH4 + SC2C4 + SC5plus - SWGS)
'molar flow rate of CH4 in process outlet per tube (mol/s)
nCH4po = nCH4pi + nCOpi * XCOf * SCH4
'molar flow rate of light hydrocarbons (propane) in process outlet
'per tube (mol/s)
nC2C4po = nC2C4pi + nCOpi * XCOf * SC2C4 / 3
'molar flow rate of heavy hydrocarbons in process outlet per tube
'(mol/s) - only 1/3 of total liquid HC are recycled
nC5pluspo = nC5pluspi + nCOpi * XCOf * SC5plus / n
'molar flow rate of CH3OH in process outlet per tube
nOXYpo = nCOpi * XCOf * SOXY
nN2po = nN2pi                    'molar flow rate of N2 in process outlet
nCOrc = nCOpo * RR               'CO in recyle per tube (mol/s)
nH2rc = nH2po * RR               'H2 in recycle per tube (mol/s)
nCO2rc = nCO2po * RR             'CO2 recycled per tube (mol/s)
'H2O in recycle per tube (mol/s) - H2O is not recycled, so nH2Orc = 0.0
nH2Orc = 0#
nCH4rc = nCH4po * RR             'CH4 in recycle per tube (mol/s)
'gaseous hydrocarbons recycled per tube (mol/s)
nC2C4rc = nC2C4po * RR
'liquid hydrocarbons recycled per tube (mol/s)
nC5plusrc = nC5pluspo * RRC5plus
nOXYrc = nOXYpo * RR             'CH3OH in recycle per tube (mol/s)
nN2rc = nN2po * RR               'N2 in the recycle per tube (mol/s)
'molar flow rate of CO at reactor inlet per tube (mol/s)
nCOri = nCOpi + nCOrc
'molar flow rate of H2 at reactor inlet per tube (mol/s)
nH2ri = nH2pi + nH2rc
'molar flow rate of CO2 at reactor inlet per tube (mol/s)
nCO2ri = nCO2pi + nCO2rc
```

```
'molar flow rate of H2O at reactor inlet per tube (mol/s)
nH2Ori = nH2Opi + nH2Orc
'molar flow rate of CH4 at reactor inlet per tube (mol/s)
nCH4ri = nCH4pi + nCH4rc
'molar flow rate of C2C4 at reactor inlet per tube (mol/s)
nC2C4ri = nC2C4pi + nC2C4rc
'molar flow rate of C5plus at reactor inlet per tube (mol/s)
nC5plusri = nC5pluspi + nC5plusrc
'molar flow rate of CH3OH at reactor inlet per tube (mol/s)
nOXYri = nOXYrc
'molar flow rate of N2 at reactor inlet per tube (mol/s)
nN2ri = nN2pi + nN2rc

'Compute the heat of reaction for the reactions at reactor inlet
'temperature given the heat of reactions at 298K
'On 5 September 2008 KMB did VLE calculation for Base Case reactor
'exit species showing 0.008 mole fraction of total water is liquid.
'Water molar fraction of the liquid phase is about 0.11.
'Based on VLE, all calculations asume water is entirely in vapor phase
'IG Heat of formation for CO at 298K J/mol
dHfCO = -110530#
'IG Heat of formation for H2 at 298K J/mol
dHfH2 = 0#
'IG Heat of formation for CO2 at 298K J/mol
dHfCO2 = -393510#
'IG Heat of formation for H2O at 298K J/mol
dHfH2O = -241814#
'IG Heat of formation for CH4 at 298K J/mol
dHfCH4 = -74520#
'IG Heat of formation for Propane at 298K J/mol
```

```
dHfC2C4 = -104680#
'IG Heat of formation for CH3OH as 298K J/mol
dHfOXY = -200940#
If cat = cobalt Then
    'Heat of formation of liquid C25H52 J/mol
    dHfC5plus = -560700# - HvapC5plus(cat)
ElseIf cat = iron Then
    'Heat of formation of liquid C20H42 J/mol
    dHfC5plus = -456460# - HvapC5plus(cat)
End If
'Heat of reaction at 298K per mole CO for methanation (J/mol CO)
deltaH_r1 = dHfCH4 + dHfH2O - dHfCO - dHfH2 * 3
'Heat of reaction at 298K per mole CO for propane (J/mol CO)
deltaH_r2 = dHfC2C4 / 3 + dHfH2O - dHfCO - dHfH2 * 7 / 3
'Heat of reaction at 298K per mole CO for heavy hydrocarbons (J/mol CO)
deltaH_r3 = dHfC5plus / n + dHfH2O - dHfCO - dHfH2 * m / n
'Heat of reaction at 298K per mole CO for WGS (J/mol CO)
deltaH_r4 = dHfCO2 + dHfH2 - dHfCO - dHfH2O
'Heat of reaction at 298K per mole CO for Methanol (J/mol CO)
deltaH_r5 = dHfOXY - dHfCO - dHfH2 * 2
Call Simpson(Integral_r1, Integral_r2, Integral_r3, Integral_r4, _
    Integral_r5)
'heat of reaction for methane reaction at inlet temperature
deltaH_r1_Tin = deltaH_r1 + Integral_r1
'heat of reaction for pentane reaction at inlet temperature
deltaH_r2_Tin = deltaH_r2 + Integral_r2
'heat of reaction for heavy hydrocarbons reaction at inlet tmperature
deltaH_r3_Tin = deltaH_r3 + Integral_r3
'heat of reaction for WGS reaction at inlet temperature
deltaH_r4_Tin = deltaH_r4 + Integral_r4
```

```
'heat of reaction for Methanol reaction at inlet temperature
deltaH_r5_Tin = deltaH_r5 + Integral_r5
'overall heat of reaction at inlet temperature
deltaH_overall = deltaH_r1_Tin * SCH4 + deltaH_r2_Tin * SC2C4 + _
    deltaH_r3_Tin * SC5plus + deltaH_r4_Tin * SWGS + deltaH_r5_Tin * _
    SOXY

'Report calculated values
Sheets("Inputs").Range("I31").Value = eb
Sheets("Inputs").Range("I34").Value = dpeff
'Sheets("Inputs").Range("I34").Value = Lpeff
Sheets("Inputs").Range("I36").Value = n
Sheets("Inputs").Range("I37").Value = rhoC5plus(cat, 298.15)
Sheets("Inputs").Range("I39").Value = deltaH_r1 / 1000
Sheets("Inputs").Range("I40").Value = deltaH_r2 / 1000
Sheets("Inputs").Range("I41").Value = deltaH_r3 / 1000
Sheets("Inputs").Range("I42").Value = deltaH_r4 / 1000
Sheets("Inputs").Range("I43").Value = deltaH_r5 / 1000

'Set initial conditions
T(0) = Tin
P(0) = Pin
z(0) = 0
X(0) = XCORi
W(0) = 0
FCO(0) = nCOri
Rateobs(0) = eta(X(0), T(0), P(0)) * intrinsic_rate(X(0), T(0), P(0))
cool_duty_one_tube = 0
cool_duty_overall = 0
i = 0
```

```
'update the worsheet every 200 nodes - OLD:
'WorksheetFunction.Ceiling(0.5 / deltaz, 1)
updater = 200

'Perform calculations
While X(i) <= XCOf
    'Calculate complex relationships once for current node
    Pr = Prxt(X(i), T(i))
    hbed = hb(X(i), T(i), P(i), Pr)
    ke = keffective(X(i), T(i), P(i))
    U = Uoverall(hbed, ke) 'overall heat transfer coefficient (W/m^2 K)

    'Record properties of the current node in "Results" sheet
    Sheets("Results").Cells(2 + i, 2) = i
    Sheets("Results").Cells(2 + i, 3) = z(i)
    Sheets("Results").Cells(2 + i, 4) = X(i)
    Sheets("Results").Cells(2 + i, 5) = T(i)
    Sheets("Results").Cells(2 + i, 6) = P(i) / P_converter
    Sheets("Results").Cells(2 + i, 7) = FCO(i)
    Sheets("Results").Cells(2 + i, 8) = intrinsic_rate(X(i), T(i), P(i))
    Sheets("Results").Cells(2 + i, 9) = W(i)
    Sheets("Results").Cells(2 + i, 10) = Re_gas(X(i), T(i), P(i))
    Sheets("Results").Cells(2 + i, 11) = u_gas(X(i), T(i), P(i))
    Sheets("Results").Cells(2 + i, 12) = U
    Sheets("Results").Cells(2 + i, 13) = MWl(X(i))
    Sheets("Results").Cells(2 + i, 14) = cool_duty_one_tube
    Sheets("Results").Cells(2 + i, 15) = cool_duty_overall
    Sheets("Results").Cells(2 + i, 16) = ke
    Sheets("Results").Cells(2 + i, 17) = hbed
```

```
Sheets("Results").Cells(2 + i, 18) = cp_gas(X(i), T(i))
Sheets("Results").Cells(2 + i, 19) = eta(X(i), T(i), P(i))
Sheets("Results").Cells(2 + i, 20) = cp_mean(X(i), T(i))
Sheets("Results").Cells(2 + i, 21) = Pr
Sheets("Results").Cells(2 + i, 22) = 1.5 * k_liq(X(i), T(i))
Sheets("Results").Cells(2 + i, 23) = (0.009623 _
    * (dpeff * 1000) ^ 2 - 0.09228 * dpeff * 1000 + 0.5089) _
    * Go_gas(X(i), T(i), P(i)) * cp_gas(X(i), T(i)) _
    * dpeff / MWg(X(i))
Sheets("Results").Cells(2 + i, 24) = abl(X(i), T(i), P(i)) _
    * Go_liquid(X(i), T(i), P(i)) * cp_liq(X(i), T(i)) * dpeff _
    / MWl(X(i))
Sheets("Results").Cells(2 + i, 25) = 10.21 * 1.5 _
    * k_liq(X(i), T(i)) / (Dt ^ (4 / 3))
Sheets("Results").Cells(2 + i, 26) = 0.033 * Pr _
    * Re_gas(X(i), T(i), P(i)) * k_gas(X(i), T(i)) / dpeff
Sheets("Results").Cells(2 + i, 27) = Deff(T(i))

'Record properties of current node to "Stream" sheet
Sheets("Stream").Cells(2 + i, 1) = X(i)
Sheets("Stream").Cells(2 + i, 2) = nCO(X(i)) * ntube
Sheets("Stream").Cells(2 + i, 3) = nH2(X(i)) * ntube
Sheets("Stream").Cells(2 + i, 4) = nCO2(X(i)) * ntube
Sheets("Stream").Cells(2 + i, 5) = nH2O(X(i)) * ntube
Sheets("Stream").Cells(2 + i, 6) = nCH4(X(i)) * ntube
Sheets("Stream").Cells(2 + i, 7) = nC2C4(X(i)) * ntube
Sheets("Stream").Cells(2 + i, 8) = nC5plus(X(i)) * ntube
Sheets("Stream").Cells(2 + i, 9) = nOXY(X(i)) * ntube
Sheets("Stream").Cells(2 + i, 10) = nN2ri * ntube
Sheets("Stream").Cells(2 + i, 11) = ntotal(X(i)) * ntube
```

```
Sheets("Stream").Cells(2 + i, 13) = zCO(X(i))
Sheets("Stream").Cells(2 + i, 14) = zH2(X(i))
Sheets("Stream").Cells(2 + i, 15) = zCO2(X(i))
Sheets("Stream").Cells(2 + i, 16) = zH2O(X(i))
Sheets("Stream").Cells(2 + i, 17) = zCH4(X(i))
Sheets("Stream").Cells(2 + i, 18) = zC2C4(X(i))
Sheets("Stream").Cells(2 + i, 19) = zC5plus(X(i))
Sheets("Stream").Cells(2 + i, 20) = zOXY(X(i))
Sheets("Stream").Cells(2 + i, 21) = zN2(X(i))

'Predict conversion, temperature, and pressure at next node
Call RK4(z, X, T, P, deltaz, i)

If stopcheck = False Then
    'Predict the observed rate at next node
    Rateobs(i + 1) = eta(X(i + 1), T(i + 1), P(i + 1)) * _
        intrinsic_rate(X(i + 1), T(i + 1), P(i + 1))

    'Compute weight of catalyst
    W(i + 1) = W(i) + nCORri * (X(i + 1) - X(i)) / Rateobs(i + 1)

    'Compute molar flow rate of CO at the next node
    FCO(i + 1) = nCORri * (1 - X(i + 1))

    'Compute cooling duty
    'for one tube
    cool_duty_one_tube = Acrs * (-4 * U / Dt) * (T(i + 1) - Tw) * _
        deltaz
    cool_duty_overall = cool_duty_one_tube * ntube   'for all tubes
```

```
            'Update the screen at appropriate intervals
            If i Mod updater = 0 Then 'update the worksheet
                Application.ScreenUpdating = True
                Application.Calculate
                DoEvents
                Application.ScreenUpdating = False
            End If
        Else
            Exit Sub
        End If

        i = i + 1
        If i > UBound(z) Then
            errmsg = errmsg & "Exceeded the limit of nodes in the reactor."
            Exit Sub
        End If
    Wend
End Sub

Public Sub RK4(ByRef z() As Double, ByRef X() As Double, ByRef T() As _
    Double, ByRef P() As Double, deltaz As Double, i As Integer)
    'Fouth order Runge-Kutta method solves the mass, energy and momentum
    'balance equations
    Dim kX1 As Double, kT1 As Double, kP1 As Double
    Dim kX2 As Double, kT2 As Double, kP2 As Double
    Dim kX3 As Double, kT3 As Double, kP3 As Double
    Dim kX4 As Double, kT4 As Double, kP4 As Double

    If stopcheck = False Then kX1 = deltaz * fx(X(i), T(i), P(i))
    If stopcheck = False Then kT1 = deltaz * fT(X(i), T(i), P(i))
```

```
    If stopcheck = False Then kP1 = deltaz * fP(X(i), T(i), P(i))
    If stopcheck = False Then kX2 = deltaz * fx(X(i) + kX1 / 2, T(i) + _
        kT1 / 2, P(i) + kP1 / 2)
    If stopcheck = False Then kT2 = deltaz * fT(X(i) + kX1 / 2, T(i) + _
        kT1 / 2, P(i) + kP1 / 2)
    If stopcheck = False Then kP2 = deltaz * fP(X(i) + kX1 / 2, T(i) + _
        kT1 / 2, P(i) + kP1 / 2)
    If stopcheck = False Then kX3 = deltaz * fx(X(i) + kX2 / 2, T(i) + _
        kT2 / 2, P(i) + kP2 / 2)
    If stopcheck = False Then kT3 = deltaz * fT(X(i) + kX2 / 2, T(i) + _
        kT2 / 2, P(i) + kP2 / 2)
    If stopcheck = False Then kP3 = deltaz * fP(X(i) + kX2 / 2, T(i) + _
        kT2 / 2, P(i) + kP2 / 2)
    If stopcheck = False Then kX4 = deltaz * fx(X(i) + kX3, T(i) + kT3, _
        P(i) + kP3)
    If stopcheck = False Then kT4 = deltaz * fT(X(i) + kX3, T(i) + kT3, _
        P(i) + kP3)
    If stopcheck = False Then kP4 = deltaz * fP(X(i) + kX3, T(i) + kT3, _
        P(i) + kP3)
    If stopcheck = False Then X(i + 1) = X(i) + (kX1 + 2 * kX2 + 2 * kX3 _
        + kX4) / 6
    If stopcheck = False Then T(i + 1) = T(i) + (kT1 + 2 * kT2 + 2 * kT3 _
        + kT4) / 6
    If stopcheck = False Then P(i + 1) = P(i) + (kP1 + 2 * kP2 + 2 * kP3 _
        + kP4) / 6
    If stopcheck = False Then z(i + 1) = z(i) + deltaz
End Sub

Public Sub TPErrCatcher(xT, xP)
    'critical temperature of C20 wax (see rhoC5plus function)
```

```
    If xT > 768 Then
        stopcheck = True
        errmsg = "Temperature increased above 768 K limit. " & errmsg
    End If
    If xP < 1000 Then
        stopcheck = True
        errmsg = "Pressure dropped below 1000 Pa. " & errmsg
    End If
End Sub

Public Function fx(xx As Double, xT As Double, xP As Double) As Double
    'Evaluates the mass balace differential equation given in Davis and
    'Davis p.320
    Call TPErrCatcher(xT, xP)
    If stopcheck = False Then fx = (Acrs * rhob * eta(xx, xT, xP) * _
        intrinsic_rate(xx, xT, xP)) / nCORri
End Function

Public Function fT(xx As Double, xT As Double, xP As Double) As Double
    'Evaluates the energy balance differential equation given in Davis
    'and Davis p.320
    'Both liquid and gas phases must be accounted for in the energy balance
    Dim U As Double

    Call TPErrCatcher(xT, xP)
    If stopcheck = False Then
        'overall heat transfer coefficient (W/m^2 K)
        U = Uoverall(hb(xx, xT, xP, Prxt(xx, xT)), keffective(xx, xT, xP))
        fT = (-deltaH_overall * rhob * eta(xx, xT, xP) * _
            intrinsic_rate(xx, xT, xP) - 4 * U * (xT - Tw) / Dt) / _
```

```
            (u_sf(xx, xT, xP) * rho_gas(xx, xT, xP) * cp_gas(xx, xT) / _
            MWg(xx) + u_liquid(xx, xT) * rho_liquid(xx, xT) * cp_liq(xx, _
            xT) / MWl(xx))
    End If
End Function

Public Function fP(xx As Double, xT As Double, xP As Double) As Double
    'Evaluates the momentum balance differential equation for trickle
    'fixed bed reactors
    'Given in Fremont and Bischoff p. 403 & 622 with friction factors
    'from various sources
    Dim es As Double, eGw As Double, Re As Double
    Dim dGw As Double, vl As Double, eL As Double
    Dim PI As Double

    Call TPErrCatcher(xT, xP)
    If stopcheck = False Then
        PI = WorksheetFunction.PI
        If stopcheck = False Then Re = Re_gas(xx, xT, xP)
        es = 0.035  'static bed void space (liquid holdup)
        eGw = eb - es 'void fraction of wet particle
        eL = (mu_liquid(xx, xT) * u_liquid(xx, xT) / (dpeff ^ 2 * g * _
            rho_liquid(xx, xT))) ^ (1 / 3)
        'Determine which equation to use
        'dGw equations account for pressure drop (Pa/m) of gas
        Select Case FrictionFactorString
            Case Is = "Use Tallmadge Friction Factor Equation"
                'Tallmadge equation
                'Tallmadge equation
                dGw = ((1 - eGw) / eGw ^ 3) * (150 * (1 - eGw) / Re + 4.2 _
```

```
            * ((1 - eGw) / Re) ^ (1 / 6)) * Go_gas(xx, xT, xP) ^ _
            2 / (rho_gas(xx, xT, xP) * dpeff)
        Case Is = "Use Mehta-Hawley Friction Factor Equation"
            'Mehta-Hawley equation
            'Davis & Davis
            dGw = ((1 - eGw) / eGw ^ 3) * (((1 + 2 * dpeff / (3 * (1 _
            - eGw) * Dt)) ^ 2) * (1.75 / (1 + 2 * dpeff / (3 * (1 _
            - eGw) * Dt)) + 150 * (1 - eGw) / Re)) * Go_gas(xx, _
            xT, xP) ^ 2 / (rho_gas(xx, xT, xP) * dpeff)
        Case Is = "Use Ergun Friction Factor Equation"
            'Ergun equation
            'Ergun
            dGw = ((1 - eGw) / eGw ^ 3) * (150 * (1 - eGw) / Re + _
            1.75) * Go_gas(xx, xT, xP) ^ 2 / (rho_gas(xx, xT, xP) _
            * dpeff)
        Case Is = "Use Tallmadge-Liu Friction Factor Equation"
            'Tallmadge-Liu combined friction factor equation
            'Tallmadge-Liu equation
            dGw = ((1 - eGw) / eGw ^ 3) * (116.8 * (1 - eGw) / Re * _
            (1 + PI * dpeff / (6 * Dt * (1 - eGw))) ^ 2 + 4.48 * _
            ((1 - eGw) / Re) ^ (1 / 6) * (1 - PI ^ 2 * dpeff / _
            (24 * Dt) * (1 - 0.5 * dpeff / Dt))) * Go_gas(xx, xT, _
            xP) ^ 2 / (rho_gas(xx, xT, xP) * dpeff)
        Case Is = "Manually Specify Pressure Drop Per Bed Length"
            'user specifies delP/L in atm/m, so convert to Pa/m
            dGw = manualdelP * 101325
    End Select
    'corrects gas pressure drop for liquid holdup
    fP = -(dGw / (1 - eL / eb) ^ 3) + rho_gas(xx, xT, xP) * g
End If
```

```
End Function

Public Function intrinsic_rate(xx As Double, xT As Double, xP As Double) _
    As Double
    'Calculates the intrinsic rate multiplied by the activity of the
    'catalyst (mol/kg s)
    Dim top As Double, bottom As Double
    Dim b1 As Double, b2 As Double, b3 As Double, rCO As Double
    Dim b4 As Double

    'units of (mol/kg s Pa^(m1+n1))
    top = a0_conv_unit * Exp(-Eact / (Rg * xT)) * PCO(xx, xP) ^ (m1) * _
        PH2(xx, xP) ^ (n1)
    'First term in denomenator
    b1 = a1_conv_unit * Exp(-Eads1 / (Rg * xT)) * PCO(xx, xP) ^ z1
    'second term in denomenator
    b2 = a2_conv_unit * Exp(-Eads2 / (Rg * xT)) * PCO(xx, xP) ^ z2 * _
        PH2(xx, xP) ^ z3
    'third term in denomenator
    b3 = a3_conv_unit * Exp(-Eads3 / (Rg * xT)) * PH2O(xx, xP) ^ z4
    'fourth term in denomenator
    b4 = a4_conv_unit * Exp(-Eads4 / (Rg * xT)) * PCO2(xx, xP) ^ z5
    bottom = (BB + b1 + b2 + b3 + b4) ^ z0
    rCO = top / bottom
    intrinsic_rate = rCO * act   'intrinsic rate will be in (mol/kg s)
End Function

Public Function eta(xx As Double, xT As Double, xP As Double) As Double
    'Calculates the effectiveness factor, assuming nth order reaction
```

```
    Dim phi As Double, tanh_phi As Double, k_intrinsic As Double, PCO As _
        Double

    'since nth order
    k_intrinsic = intrinsic_rate(xx, xT, xP) / CCO(xx, xT, xP) ^ order
    'theile modulus for nth order reaction
    phi = Lpeff * ((k_intrinsic * rhop * (order + 1) * CCO(xx, xT, xP) ^ _
        order) / (2 * Deff(xT) * CCO(xx, xT, xP))) ^ 0.5
    tanh_phi = sinh(phi) / cosh(phi)
    eta = tanh_phi / phi
End Function

'consider feeding in the weights that are found earlier for C5plus
'instead of calculating the MW
Public Function Deff(xT As Double)
    Dim MWH2 As Double, MWCO As Double, sigmaH2 As Double
    Dim sigmaCO As Double, tortuosity As Double, cn As Single, V As Double
    Dim Diffusivity As Double, BinaryDiffusivity As Double
    Dim KnudsenDiffusivity As Double

    pp = rhop * Vpore / 1000
    'outputs pellet porosity to the results
    Sheets("Inputs").Range("I33").Value = pp
    'References to Erkey refer to the article "A correlation for
    'predicting diffusion coefficients in alkanes"
    'found on page 681 of The Canadian Journal of Chemical Engineering
    'Volume 68, Issue 4, 1990
    'Define Constants
    MWH2 = 2.0158 'gm/mol
    MWCO = 28.011 'gm/mol
```

```
    'molecular diameter for Hydrogen is the Leonard-Jones sigma given by
    'Hirschfelder et al. cited by Erkey. The CO diameter was calculated
    'from Bondi's method as cited by Erkey
    sigmaH2 = 2.92 'Angstrom hard sphere diameter
    sigmaCO = 3.72 'Angstrom
    'fairly standard value. This could be a possible user input
    tortuosity = 3.5
    'The average carbon number is 25 for a Cobalt catalyst and 20 for an
    'Iron catalyst
    If cat = 1 Then
        'The molar volume is needed and can be found by taking one over
        'the density defined by DIPPR105
        V = 1 / DIPPR105(0.14071, 0.22812, 812, 0.28571, xT) 'm^3/kmol
        BinaryDiffusivity = DAB(sigmaCO, MWCO, 25, xT, V)
        KnudsenDiffusivity = Dk(xT, MWCO, 0.00000001)
        'Resistance sum of binary and Knudsen diffusions
        Diffusivity = 1 / ((1 / BinaryDiffusivity) + (1 / _
            KnudsenDiffusivity))
        'effective diffusivity
        Deff = Diffusivity * pp / tortuosity 'm^2/s
    ElseIf cat = 2 Then
        V = 1 / DIPPR105(0.18166, 0.23351, 768, 0.28571, xT) 'm^3/kmol
        BinaryDiffusivity = DAB(sigmaCO, MWCO, 20, xT, V)
        KnudsenDiffusivity = Dk(xT, MWCO, 0.00000001)
        Diffusivity = 1 / ((1 / BinaryDiffusivity) + (1 / _
            KnudsenDiffusivity))
        Deff = Diffusivity * pp / tortuosity
    End If
End Function
```

```
Function DAB(sigma1 As Double, MW1 As Double, cn As Single, xT As Double, _
    V As Double)
    Dim sigmaHC As Double, MWHC As Double, beta As Double, b As Double, _
        Vo As Double, VD As Double
    'Hard sphere diameter of any hydrocarbon, where cn is the carbon
    'number. Erkey Table 2.
    sigmaHC = (21.82 + 32.44 * cn) ^ (1 / 3)
    'Molecular Weight of any hydrocarbon, where cn is the carbon number.
    'Erkey Table 2.
    MWHC = (14.027 * cn + 2.016)
    'beta is defined in Erkey equation 6, but the constants are given in 9
    beta = 94.5 / (((MW1) ^ (0.239)) * (MWHC ^ (0.781)) * ((sigma1 * _
        sigmaHC) ^ (1.134)))
    'Equation 8 of Erkey
    b = 1.206 + 0.0632 * (sigma1 / sigmaHC)
    'Equation 7 of Erkey
    Vo = (6.022 * 10 ^ 23 * ((sigmaHC * 1 * 10 ^ -10) ^ 3)) / Sqr(2)
    'defined by Erkey 7
    VD = b * Vo * 1000000
    'Erkey Equation 9 is the general correlation for diffusivities in
    'hydrocarbon waxes
    DAB = beta * (V * 1000 - VD) * (xT ^ 0.5) / 1000000000 'm^2/s
End Function

Function Dk(xT, MW1, dpore)
    'Knudsen diffusivity
    Dk = dpore * 100 * 4850 * ((xT / MW1) ^ (1 / 2)) / 10000 'm^2/s
End Function

Public Function Uoverall(hbed As Double, ke As Double) As Double
```

```
    'Calculates the overall heat transfer coefficient (W/m^2 K)
    Uoverall = 1 / ((1 / hbed) + (Dt / 8 / ke))
End Function

Public Function keffective(xx As Double, xT As Double, xP As Double) As _
    Double
    'Calculates the effective radial thermal conductivity for packed beds
    'with gas-liquid downflow (W/m K)
    'Given by Matsuura (1980)
    Dim abg As Double
    'If the user elects to use the standard Thermal conductivity equation
    'this is used. If they instead give a static conductivity the
    'correlation is changed accordingly. If the user specifies an
    'effective thermoconductivity the entire correlation is overridden.
    'constant for thermal conductivity of gas
    abg = 0.009623 * (dpeff * 1000) ^ 2 - 0.09228 * dpeff * 1000 + 0.5089
    Select Case ThermalConductivityString
        Case Is = "Use Thermal Conductivity Correlation"
            keffective = 1.5 * k_liq(xx, xT) + abg * Go_gas(xx, xT, xP) * _
                cp_gas(xx, xT) * dpeff / MWg(xx) + abl(xx, xT, xP) * _
                Go_liquid(xx, xT, xP) * cp_liq(xx, xT) * dpeff / MWl(xx)
        Case Is = "Input Static Thermal Conductivity"
            keffective = manualk + abg * Go_gas(xx, xT, xP) * cp_gas(xx, _
                xT) * dpeff / MWg(xx) + abl(xx, xT, xP) * Go_liquid(xx, _
                xT, xP) * cp_liq(xx, xT) * dpeff / MWl(xx)
        Case Is = "Input Effective Radial Thermal Conductivity"
            keffective = manualk
    End Select
End Function
```

```
Public Function abl(xx As Double, xT As Double, xP As Double) As Double
    'alpha beta liquid term for keffective correlation
    abl = 0.167 * (1 + 0.0134 * Re_gas(xx, xT, xP))
End Function

Public Function hb(xx As Double, xT As Double, xP As Double, Pr As _
    Double) As Double
    '04/25/2012 optional switch allows user to determine which method he
    'prefers
    'If the heat transfer correlation is selected the user defined
    'thermal conduction will be used. If a constant heat transfer
    'coefficient is specified this will be used.
    Select Case HbedString
        Case Is = "Use Bed Heat Transfer Coefficient Correlation"
            Select Case ThermalConductivityString
                Case Is = "Use Thermal Conductivity Correlation"
                    '11/15/2010 changed kstatic to 1.5*k_liq to agree
                    'with Matsuura keffective static term
                    hb = (k_gas(xx, xT) / dpeff) * ((1.5 * k_liq(xx, xT) _
                        * 10.21 / Dt ^ (4 / 3)) * (dpeff / k_gas(xx, xT)) _
                        + 0.033 * Pr * Re_gas(xx, xT, xP))
                Case Is = "Input Static Thermal Conductivity"
                    'Calculates the bed heat transfer coeficient (W/m^2
                    'K) Froment & Bischoff p.404, 486
                    hb = (k_gas(xx, xT) / dpeff) * ((manualk * 10.21 / Dt _
                        ^ (4 / 3)) * (dpeff / k_gas(xx, xT)) + 0.033 * Pr _
                        * Re_gas(xx, xT, xP))
                Case Is = "Input Effective Radial Thermal Conductivity"
                    hb = (k_gas(xx, xT) / dpeff) * ((1.5 * k_liq(xx, xT) _
                        * 10.21 / Dt ^ (4 / 3)) * (dpeff / k_gas(xx, xT)) _
```

```
                        + 0.033 * Pr * Re_gas(xx, xT, xP))
            End Select
        Case Is = "Input Constant Bed Heat Transfer Coefficient"
            hb = manualhbed
    End Select
End Function

Public Function Prxt(xx As Double, xT As Double) As Double
    'Calculates Prandlt number = Cpgas*mutot/(MWg*kgas)
    Prxt = cp_gas(xx, xT) * mu_gas(xx, xT) / (MWg(xx) * k_gas(xx, xT))
    'Prxt = 0.7
End Function

Public Function Re_gas(xx As Double, xT As Double, xP As Double) As Double
    'Calculates Reynolds number for gas based on superficial velocity,
    'not actual fluid velocity
    'Reynolds number for gas stream
    Re_gas = Go_gas(xx, xT, xP) * dpeff / mu_gas(xx, xT)
End Function

Public Function Re_liquid(xx As Double, xT As Double, xP As Double) _
    As Double
    'Calculates Reynolds number for liquid based on superficial velocity,
    'not actual fluid velocity
    'Reynolds number for liquid at inlet
    Re_liquid = Go_liquid(xx, xT, xP) * dpeff / muC5plus(xT)
End Function

Public Function Go_gas(xx As Double, xT As Double, xP As Double) As Double
    'Calculates gas mass flux (kg/m^2 s)
```

```
    Go_gas = u_sf(xx, xT, xP) * rho_gas(xx, xT, xP)
End Function

Public Function Go_liquid(xx As Double, xT As Double, xP As Double) _
    As Double
    'Calculates liquid mass flux (kg/m^2 s)
    Go_liquid = u_liquid(xx, xT) * rho_liquid(xx, xT)
End Function

Public Function u_liquid(xx As Double, xT As Double) As Double
    'Calculates the superficial liquid velocity (m/s)
    u_liquid = MWl(xx) * nliq(xx) / (rho_liquid(xx, xT) * Acrs)
End Function

Public Function u_sf(xx As Double, xT As Double, xP As Double) As Double
    'Calculates the superficial gas velocity (m/s)
    u_sf = ngas(xx) * Rg * xT / (xP * Acrs)
End Function

Public Function u_gas(xx As Double, xT As Double, xP As Double) As Double
    'Calculates the actual gas velocity (m/s) (not used in code as of
    '10/2008)
    u_gas = u_sf(xx, xT, xP) / eb
End Function

Public Function rho_gas(xx As Double, xT As Double, xP As Double) As Double
    'Calculates gas density (kg/m^3)
    rho_gas = MWg(xx) * xP / (Rg * xT)
End Function
```

```
Public Function rho_C5plus(xT As Double) As Double
    'Calculates density of liquid HC from DIPPR equations (kg/m^3)
    'NOTE: original DIPPR equation gives density in kmol/m^3
    'originally, this value was assumed to be constant 800 kg/m^3
    If cat = cobalt Then    'density of liquid C25H52 (kg/m^3)
        rho_C5plus = MWC5plus * 1000 * 0.14071 / 0.22812 ^ (1 + (1 - xT / _
            812#) ^ 0.28571)
    ElseIf cat = iron Then  'density of liquid C20H42 (kg/m^3)
        rho_C5plus = MWC5plus * 1000 * 0.18166 / 0.23351 ^ (1 + (1 - xT / _
            768#) ^ 0.28571)
    End If
End Function

Public Function rho_liquid(xx As Double, xT As Double) As Double
    'Calculates the liquid density (kg/m^3)
    rho_liquid = rho_C5plus(xT)
End Function

Public Function Dcp_r1(xT As Double) As Double
    'Calculates delta Cp of methane reaction per mole of CO (J/mol K)
    Dcp_r1 = -cpCO(xT) - 3 * cpH2(xT) + cpCH4(xT) + cpH2O(xT)
End Function

Public Function Dcp_r2(xT As Double) As Double
    'Calculates delta Cp of propane reaction per mole of CO (J/mol K)
    Dcp_r2 = -cpCO(xT) - (7 / 3) * cpH2(xT) + (1 / 3) * cpC2C4(xT) + _
        cpH2O(xT)
End Function

Public Function Dcp_r3(xT As Double) As Double
```

```
    'Calculates delta Cp of C5plus reaction per mole of CO (J/mol K)
    Dcp_r3 = -cpCO(xT) - (m / n) * cpH2(xT) + (1 / n) * cpC5plus(xT) + _
        cpH2O(xT)
End Function

Public Function Dcp_r4(xT As Double) As Double
    'Calculates delta Cp of WGS reaction per mole of CO (J/mol K)
    Dcp_r4 = -cpCO(xT) - cpH2O(xT) + cpCO2(xT) + cpH2(xT)
End Function

Public Function Dcp_r5(xT As Double) As Double
    'Calculates delta Cp of Methanol reaction per mole of CO (J/mol K)
    Dcp_r5 = -cpCO(xT) - 2 * cpH2(xT) + cpOXY(xT)
End Function

Public Sub Simpson(ByRef Integral_r1 As Double, ByRef Integral_r2 As _
    Double, ByRef Integral_r3 As Double, ByRef Integral_r4 As Double, _
    ByRef Integral_r5 As Double)
    'Evaluates integrals numerically based on simpson's 1/3 rule.
    'Calculates heat of reaction at inlet temperature.
    Dim nsteps As Integer, ii As Integer, n_int As Integer
    Dim int_step As Double
    Dim sum2_r1 As Double, sum4_r1 As Double, sum2_r2 As Double, sum4_r2 _
        As Double, sum2_r3 As Double, sum4_r3 As Double
    Dim sum2_r4 As Double, sum4_r4 As Double, sum2_r5 As Double, sum4_r5 _
        As Double

    int_step = 0.1  'integration step size
    n_int = ((Tin - 298) / int_step) + 1
    nsteps = Int(n_int)
```

```
sum2_r1 = 0
sum4_r1 = 0
sum2_r2 = 0
sum4_r2 = 0
sum2_r3 = 0
sum4_r3 = 0
sum2_r4 = 0
sum4_r4 = 0
sum2_r5 = 0
sum4_r5 = 0
For ii = 3 To nsteps - 1 Step 2
    sum2_r1 = sum2_r1 + Dcp_r1(298 + int_step * (ii - 1))
    sum2_r2 = sum2_r2 + Dcp_r2(298 + int_step * (ii - 1))
    sum2_r3 = sum2_r3 + Dcp_r3(298 + int_step * (ii - 1))
    sum2_r4 = sum2_r4 + Dcp_r4(298 + int_step * (ii - 1))
    sum2_r5 = sum2_r5 + Dcp_r5(298 + int_step * (ii - 1))
Next ii
For ii = 2 To nsteps - 1 Step 2
    sum4_r1 = sum4_r1 + Dcp_r1(298 + int_step * (ii - 1))
    sum4_r2 = sum4_r2 + Dcp_r2(298 + int_step * (ii - 1))
    sum4_r3 = sum4_r3 + Dcp_r3(298 + int_step * (ii - 1))
    sum4_r4 = sum4_r4 + Dcp_r4(298 + int_step * (ii - 1))
    sum4_r5 = sum4_r5 + Dcp_r5(298 + int_step * (ii - 1))
Next ii
'integral of delta cp from 298K to inlet temperature for reaction 1
Integral_r1 = int_step * (Dcp_r1(298) + 2 * sum2_r1 + 4 * sum4_r1 + _
    Dcp_r1(Tin)) / 3
'integral of delta cp from 298K to inlet temperature for reaction 2
Integral_r2 = int_step * (Dcp_r2(298) + 2 * sum2_r2 + 4 * sum4_r2 + _
    Dcp_r2(Tin)) / 3
```

```
    'integral of delta cp from 298K to inlet temperature for reaction 3
    Integral_r3 = int_step * (Dcp_r3(298) + 2 * sum2_r3 + 4 * sum4_r3 + _
        Dcp_r3(Tin)) / 3
    'integral of delta cp from 298K to inlet temperature for reaction 4
    Integral_r4 = int_step * (Dcp_r4(298) + 2 * sum2_r4 + 4 * sum4_r4 + _
        Dcp_r4(Tin)) / 3
    'integral of delta cp from 298K to inlet temperature for reaction 5
    Integral_r5 = int_step * (Dcp_r5(298) + 2 * sum2_r5 + 4 * sum4_r5 + _
        Dcp_r5(Tin)) / 3
End Sub

Public Function cosh(xT As Double) As Double
    'Calculates hyperbolic cos
    'cosh = (Exp(xT) + Exp(-xT)) / 2
    cosh = WorksheetFunction.cosh(xT)
End Function

Public Function sinh(xT As Double) As Double
    'Calculates hyperbolic sin
    'sinh = (Exp(xT) - Exp(-xT)) / 2
    sinh = WorksheetFunction.sinh(xT)
End Function

Public Function CCO(xx As Double, xT As Double, xP As Double) As Double
    'Calculates the concentration of CO (mol/m^3)
    CCO = PCO(xx, xP) / (Rg * xT)
End Function

Public Function PCO(xx As Double, xP As Double) As Double
    'Calculates the partial pressure of CO (Pa)
```

```
    PCO = xP * nCO(xx) / ngas(xx) 'partial pressure of CO
End Function

Public Function PH2(xx As Double, xP As Double) As Double
    'Calculates the partial pressure of H2 (Pa)
    PH2 = xP * nH2(xx) / ngas(xx)
End Function

Public Function PH2O(xx As Double, xP As Double) As Double
    'Calculates the partial pressure of H2 (Pa)
    PH2O = xP * nH2O(xx) / ngas(xx)
End Function

Public Function PCO2(xx As Double, xP As Double) As Double
    'Calculates the partial pressure of H2 (Pa)
    PCO2 = xP * nCO2(xx) / ngas(xx)
End Function

Public Function cpCO(xT As Double) As Double
    'Calculates heat capacity of CO in (J/mol*K) as a function of
    'temperature from DIPPR
    cpCO = DIPPR107(29100, 8773, 3090, 8460, 1540, xT) / 1000
End Function

Public Function cpH2(xT As Double) As Double
    'Calculates heat capacity of H2 in (J/mol*K) as a function of
    'temperature from DIPPR
    cpH2 = DIPPR107(27600, 9560, 2470, 3760, 568, xT) / 1000
End Function
```

```
Public Function cpCO2(xT As Double) As Double
    'Calculates heat capacity of CO2 in (J/mol*K) as a function of
    'temperature from DIPPR
    cpCO2 = DIPPR107(29370, 34540, 1428, 26400, 588, xT) / 1000
End Function

Public Function cpH2O(xT As Double) As Double
    'Calculates heat capacity of H2O in (J/mol*K) as a function of
    'temperature from DIPPR
    cpH2O = DIPPR107(33400, 26800, 2610, 8900, 1170, xT) / 1000
End Function

Public Function cpCH4(xT As Double) As Double
    'Calculates heat capacity of CH4 in (J/mol*K) as a function of
    'temperature from DIPPR
    cpCH4 = DIPPR107(33300, 79900, 2090, 41600, 992, xT) / 1000
End Function

Public Function cpC2C4(xT As Double) As Double
    'Calculates heat capacity of C3H8 in (J/mol*K) as a function of
    'temperature from DIPPR
    cpC2C4 = DIPPR107(51920, 192450, 1626.5, 116800, 723.6, xT) / 1000
End Function

Public Function cpC5plus(xT As Double) As Double
    'Calculates heat capacity of liquid C5plus in (J/mol*K) as a function
    'of temperature from DIPPR
    If cat = cobalt Then
        'Heat capacity of C25H52
        cpC5plus = DIPPR100(534660#, 693.87, 0.45205, 0#, 0#, xT) / 1000
```

```
    ElseIf cat = iron Then
        'Heat capacity of C20H42
        cpC5plus = DIPPR100(352720#, 807.32, 0.2122, 0#, 0#, xT) / 1000
    End If
End Function

Public Function cpOXY(xT As Double)
    'Calculates heat capacity of xoygenates in (J/mol*K) as a function of
    'temperature from DIPPR
    cpOXY = DIPPR107(39252, 87900, 1916.5, 53654, 896.7, xT) / 1000
End Function

Public Function cpN2(xT As Double) As Double
    'Calculates heat capacity of N2 in (J/mol*K) as a function of
    'temperature from DIPPR
    cpN2 = DIPPR107(29105#, 8614.9, 1701.6, 103.47, 909.79, xT) / 1000
End Function

Public Function cp_gas(xx As Double, xT As Double) As Double
    'Calcualtes the heat capacity (J/mol K) of gas weighted by mole fraction
    cp_gas = (nCO(xx) * cpCO(xT) + nH2(xx) * cpH2(xT) + nH2O(xx) * _
        cpH2O(xT) + nCO2(xx) * cpCO2(xT) + nCH4(xx) * cpCH4(xT) + _
        nC2C4(xx) * cpC2C4(xT) + nOXY(xx) * cpOXY(xT) + nN2ri * cpN2(xT)) _
        / ngas(xx)
End Function

Public Function cp_liq(xx As Double, xT As Double) As Double
    'Calculates the heat capacity (J/mol K) of liquid weighted by mole
    'fraction
    cp_liq = cpC5plus(xT)
```

```
End Function

Public Function cp_mean(xx As Double, xT As Double) As Double
    'Calculates the mean heat capacity of ALL species in the reactor
    'relative to that of CO (J/molCO K) (Not used as of 10/2008)
    cp_mean = (nCO(xx) * cpCO(xT) + nH2(xx) * cpH2(xT) + nCO2(xx) * _
        cpCO2(xT) + nH2O(xx) * cpH2O(xT) + nCH4(xx) * cpCH4(xT) + _
        nC2C4(xx) * cpC2C4(xT) + nC5plus(xx) * cpC5plus(xT) + nOXY(xx) * _
        cpOXY(xT) + nN2ri * cpN2(xT)) / nCO(xx)
End Function

Public Function kCO(xT As Double) As Double
    'Calculates the thermal conductivity of CO in (W/m*K) as a function
    'of temperature from DIPPR
    kCO = DIPPR102(0.000599, 0.686, 57.1, 502, xT)
End Function

Public Function kH2(xT As Double) As Double
    'Calculates the thermal conductivity of H2 in (W/m*K) as a function
    'of temperature from DIPPR
    kH2 = DIPPR102(0.00265, 0.745, 12, 0, xT)
End Function

Public Function kCO2(xT As Double) As Double
    'Calculates the thermal conductivity of CO2 in (W/m*K) as a function
    'of temperature from DIPPR
    kCO2 = DIPPR102(3.69, -0.3838, 964#, 1860000#, xT)
End Function

Public Function kH2O(xT As Double) As Double
```

```
    'Calculates the thermal conductivity of H2O in (W/m*K) as a function
    'of temperature from DIPPR
    kH2O = DIPPR102(0.00216, 0.768, 3940, -445000, xT)
End Function

Public Function kCH4(xT As Double) As Double
    'Calculates the thermal conductivity of CH4 in (W/m*K) as a function
    'of temperature from DIPPR
    kCH4 = DIPPR102(6330, 0.43, 770000000, -38700000000#, xT)
End Function

Public Function kC2C4(xT As Double) As Double
    'Calculates the thermal conductivity of C3H8 in (W/m*K) as a function
    'of temperature from DIPPR
    kC2C4 = DIPPR102(-1.12, 0.10972, -9834.6, -7535800, xT)
End Function

Public Function kC5plus(xT As Double) As Double
    'Calculates the liquid thermal conductivity of C5plus in (W/m*K) as a
    'function of temperature from DIPPR
    If cat = cobalt Then
        'Thermal Conductivity of C25H52
        kC5plus = DIPPR100(0.2209, -0.00020554, 0#, 0#, 0#, xT)
    ElseIf cat = iron Then
        'Thermal Conductivity of C20H42
        kC5plus = DIPPR100(0.2178, -0.0002233, 0#, 0#, 0#, xT)
    End If
End Function
Public Function kOXY(xT As Double)
    'Calculates the thermal conductivity of oxygenates as a function of
```

```
    'temperature (K) in (W/m*K)
    kOXY = DIPPR102(5.7992 * 10 ^ -7, 1.7862, 0, 0, xT)
End Function

Public Function kN2(xT As Double) As Double
    'Calculates the thermal conductivity of N2 (W/m*K) as a function of
    'Temperature from DIPPR
    kN2 = DIPPR102(0.00033143, 0.7722, 16.323, 373.72, xT)
End Function

Public Function k_gas(xx As Double, xT As Double) As Double
    'Calculates the thermal conductivity of gas (W/m*K) weighted by mole
    'fraction
    k_gas = (nCO(xx) * kCO(xT) + nH2(xx) * kH2(xT) + nCO2(xx) * kCO2(xT) _
        + nH2O(xx) * kH2O(xT) + nCH4(xx) * kCH4(xT) + nC2C4(xx) * _
        kC2C4(xT) + nOXY(xx) * kOXY(xT) + nN2ri * kN2(xT)) / ngas(xx)
End Function

Public Function k_liq(xx As Double, xT As Double) As Double
    'Calculates the thermal conductivity of liquid (W/m K) weighted by
    'mole fraction
    k_liq = kC5plus(xT)
End Function

Public Function k_tot(xx As Double, xT As Double) As Double
    'Calculates the total thermal conductivity (W/m^2K) weighted by mole
    'fraction
    k_tot = (nCO(xx) * kCO(xT) + nH2(xx) * kH2(xT) + nH2O(xx) * kH2O(xT) _
        + nCO2(xx) * kCO2(xT) + nCH4(xx) * kCH4(xT) + nC2C4(xx) * _
        kC2C4(xT) + nC5plus(xx) * kC5plus(xT) + nOXY(xx) * kOXY(xT) + _
```

```
        nN2ri * kN2(xT)) / ntotal(xx)
End Function

Public Function muCO(xT As Double) As Double
    'Calculates the viscosity of CO (Pa-s) as a fuction of temperature
    'from DIPPR
    muCO = DIPPR102(0.00000111, 0.534, 97.4, 0, xT)
End Function

Public Function muH2(xT As Double) As Double
    'Calculates the viscosity of H2 (Pa-s) as a fuction of temperature
    'from DIPPR
    muH2 = DIPPR102(0.00000018, 0.685, -0.56, 140, xT)
End Function

Public Function muH2O(xT As Double) As Double
    'Calculates the viscosity of H2O (Pa-s) as a fuction of temperature
    'from DIPPR
    muH2O = DIPPR102(0.0000000117, 1.11, 0, 0, xT)
End Function

Public Function muCO2(xT As Double) As Double
    'Calculates the viscosity of CO2 (Pa-s) as a fuction of temperature
    'from DIPPR
    muCO2 = DIPPR102(0.000002148, 0.46, 290, 0, xT)
End Function

Public Function muCH4(xT As Double) As Double
    'Calculates the viscosity of CH4 (Pa-s) as a fuction of temperature
    'from DIPPR
```

```
    muCH4 = DIPPR102(0.000000525, 0.59, 106, 0, xT)
End Function

Public Function muC2C4(xT As Double) As Double
    'Calculates the viscosity of C3H8 (Pa-s) as a fuction of temperature
    'from DIPPR
    muC2C4 = DIPPR102(0.000000049054, 0.90125, 0, 0, xT)
End Function

Public Function muC5plus(xT As Double) As Double
    'Calculates the viscosity of liquid C5plus (Pa-s) as a fuction of
    'temperature  from DIPPR
    If cat = cobalt Then
        'viscosity of C25H52
        muC5plus = DIPPR101(-11.456, 2012.7, 0.00021696, 0#, 0#, xT)
    ElseIf cat = iron Then
        'viscosity of C20H42
        muC5plus = DIPPR101(-18.315, 2283.5, 0.95485, 0#, 0#, xT)
    End If
End Function
Public Function muOXY(xT As Double) As Double
    'Calculates the viscosity of oxygenates (Pa-s) as a function of
    'temperature (K) from DIPPR
    muOXY = DIPPR102(0.00000030663, 0.69655, 205, 0, xT)
End Function

Public Function muN2(xT As Double) As Double
    'Calculates the viscosity of N2 (Pa*s) as a function of temperature
    muN2 = DIPPR102(0.00000065592, 0.6081, 54.714, 0, xT)
End Function
```

```
Public Function mu_gas(xx As Double, xT As Double) As Double
    'Calculates the gas viscosity weighted by mole fraction (Pa * s)
    mu_gas = (nCO(xx) * muCO(xT) + nH2(xx) * muH2(xT) + nH2O(xx) * _
        muH2O(xT) + nCO2(xx) * muCO2(xT) + nCH4(xx) * muCH4(xT) + _
        nC2C4(xx) * muC2C4(xT) + nOXY(xx) * muOXY(xT) + nN2ri * muN2(xT)) _
        / ngas(xx)
End Function

Public Function mu_liquid(xx As Double, xT As Double) As Double
    'Calculates the liquid viscosity weighted by mole fraction (Pa * s)
    mu_liquid = muC5plus(xT)
End Function

Public Function MWg(xx As Double) As Double
    'Calculates molecular weight of gas
    Dim MW1 As Double, Mw2 As Double
    MW1 = (nCO(xx) * 0.028 + nH2(xx) * 0.002 + nH2O(xx) * 0.018) / ngas(xx)
    Mw2 = (nCH4(xx) * 0.016 + nCO2(xx) * 0.044 + nC2C4(xx) * 0.044 + _
        nOXY(xx) * 0.032 + nN2ri * 0.028) / ngas(xx)
    MWg = (MW1 + Mw2)
End Function

Public Function MWl(xx As Double) As Double
    'Calculates molecular weight of liquid
    MWl = MWC5plus
End Function

Private Function nCO(xx As Double) As Double
    'Calculates CO molar flow rate as a function of conversion
```

```
    nCO = nCORri * (1 - xx)
End Function

Public Function nH2(xx As Double) As Double
    'Calculates the molar flow rate (mole/s) of H2 as a function of CO
    'conversion
    nH2 = nH2ri - nCORri * H2COst * (xx - XCORi)
End Function

Public Function nCO2(xx As Double) As Double
    'Calculates the molar flow rate (mole/s) of CO2 as a function of CO
    'conversion
    nCO2 = nCO2ri + nCORri * SWGS * (xx - XCORi)
End Function

Public Function nH2O(xx As Double) As Double
    'Calculates the molar flow rate (mole/s) of H2O as a function of CO
    'conversion
    nH2O = nH2Ori + nCORri * (SC5plus + SC2C4 + SCH4 - SWGS) * (xx - XCORi)
End Function

Public Function nCH4(xx As Double) As Double
    'Calculates the molar flow rate (mole/s) of CH4 as a function of CO
    'conversion
    nCH4 = nCH4ri + nCORri * SCH4 * (xx - XCORi)
End Function

Public Function nC2C4(xx As Double) As Double
    'Calculates the molar flow rate (mole/s) of C2C4 as a function of CO
    'conversion
```

```
    nC2C4 = nC2C4ri + nCORri * SC2C4 * (xx - XCORi) / 3
End Function

Public Function nC5plus(xx As Double) As Double
    'Calculates the molar flow rate (mole/s) of C5plus as a function of
    'CO conversion
    nC5plus = nC5plusri + nCORri * SC5plus * (xx - XCORi) / n
End Function
Public Function nOXY(xx As Double) As Double
    'Calculates the molar flow rate (mole/s) of CH3OH as a function of CO
    'conversion
    nOXY = nOXYri + nCORri * SOXY * (xx - XCORi)
End Function

Public Function ngas(xx As Double) As Double
    'Calculates the gas molar flow rate in the reactor as a function of
    'CO conversion (mol/s)
    ngas = nCO(xx) + nH2(xx) + nH2O(xx) + nCO2(xx) + nCH4(xx) + nC2C4(xx) _
        + nOXY(xx) + nN2ri
End Function

Public Function nliq(xx As Double) As Double
    'Calculates the molar flow rate of liquid(mol/s)
    nliq = nC5plus(xx)
End Function

Public Function ntotal(xx As Double) As Double
    'Calculates the total molar flow rate in the reactor as a function of
    'CO conversion (mol/s)
    ntotal = nCO(xx) + nH2(xx) + nH2O(xx) + nCO2(xx) + nCH4(xx) + _
```

```
        nC2C4(xx) + nC5plus(xx) + nOXY(xx) + nN2ri
End Function

Public Function zCO(xx As Double) As Double
    'Calculates the total mole faction of CO as a function of conversion
    zCO = nCO(xx) / ntotal(xx)
End Function

Public Function zH2(xx As Double) As Double
    'Calculates the total mole faction of H2 as a function of conversion
    zH2 = nH2(xx) / ntotal(xx)
End Function

Public Function zH2O(xx As Double) As Double
    'Calculates the total mole faction of H2O as a function of conversion
    zH2O = nH2O(xx) / ntotal(xx)
End Function

Public Function zCH4(xx As Double) As Double
    'Calculates the total mole faction of CH4 as a function of conversion
    zCH4 = nCH4(xx) / ntotal(xx)
End Function

Public Function zCO2(xx As Double) As Double
    'Calculates the total mole fraction of CO2 as a function of conversion
    zCO2 = nCO2(xx) / ntotal(xx)
End Function

Public Function zC2C4(xx As Double) As Double
    'Calculates the total mole faction of C2C4 as a function of conversion
```

```
    zC2C4 = nC2C4(xx) / ntotal(xx)
End Function

Public Function zC5plus(xx As Double) As Double
    'Calculates the total mole faction of C5plus as a function of conversion
    zC5plus = nC5plus(xx) / ntotal(xx)
End Function
Public Function zOXY(xx As Double) As Double
    'Calculates the total mole faction of CH3OH as a function of conversion
    zOXY = nOXY(xx) / ntotal(xx)
End Function

Public Function zN2(xx As Double) As Double
    'Calculates the total mole fraction of N2 as a function of conversion
    zN2 = nN2ri / ntotal(xx)
End Function

Public Function HvapC5plus(catalyst As Integer) As Double
    'Calculates the heat of vaporization of C5plus using DIPPR equations
    '(J/mol)
    'Used in calculating the Heat of formation of C5plus
    Dim expnt As Double, Tc As Double, Ts As Double
    'Standard temperature for this equation is 298K
    Ts = 298
    If catalyst = cobalt Then
        Tc = 812                'Critical Temperature of C25H52
        HvapC5plus = DIPPR106(160760000#, 0.61375, 0.27889, -0.47511, 0#, _
            Ts / Tc) / 1000
    ElseIf catalyst = iron Then
        Tc = 768                'Critical temperature of C20H42
```

```
        HvapC5plus = DIPPR106(128600000#, 0.50351, 0.32986, -0.42184, 0#, _
            Ts / Tc) / 1000
    End If
End Function

Public Function rhoC5plus(catalyst As Integer, xT As Double) As Double
    'Calculates the liquid density of C5plus using the DIPPR equation
    '(kg/m^3)
    'Used in calculating catalyst productivity
    If catalyst = cobalt Then
        rhoC5plus = DIPPR105(0.14071, 0.22812, 812, 0.28571, xT)
    ElseIf catalyst = iron Then
        rhoC5plus = DIPPR105(0.18166, 0.23351, 768, 0.28571, xT)
    End If
    rhoC5plus = rhoC5plus * 1000 * MWC5plus
End Function

Function DIPPR100(A As Double, b As Double, C As Double, D As Double, E _
    As Double, xT As Double)
    'Input termperature in K
    'Used for thermal conductivity of liquids (W/m*K), heat capacity of
    'liquids (J/kmol*K)
    DIPPR100 = A + b * xT + C * xT ^ 2 + D * xT ^ 3 + E * xT ^ 4
End Function

Function DIPPR101(A As Double, b As Double, C As Double, D As Double, E _
    As Double, xT As Double)
    'Input temperature in K
    'Used for viscosity of liquids (Pa*s), vapor pressure (Pa)
    'NOTE: in VBA, Log() is the natural logrithm function [ln()]
```

```
    DIPPR101 = Exp(A + b / xT + C * Log(xT) + D * xT ^ E)
End Function

Function DIPPR102(A As Double, b As Double, C As Double, D As Double, xT _
    As Double)
    'Input temperature in K
    'Used for thermal conductivity of vapors (W/m*K), viscosity of vapors
    '(Pa*s)
    DIPPR102 = A * xT ^ b / (1 + C / xT + D / xT ^ 2)
End Function

Function DIPPR105(A As Double, b As Double, C As Double, D As Double, xT _
    As Double)
    'Input temperature in K
    'Used for liquid density of hydrocarbons (kmol/m^3)
    DIPPR105 = A / b ^ (1 + (1 - xT / C) ^ D)
End Function

Function DIPPR106(A As Double, b As Double, C As Double, D As Double, E _
    As Double, Tr As Double)
    'Input temperature in K
    'Used for heat of vaporization (J/kmol)
    Dim expnt As Double
    expnt = b + C * Tr + D * Tr ^ 2# + E * Tr ^ 3#
    DIPPR106 = (A * (1 - Tr) ^ expnt)
End Function

Function DIPPR107(A As Double, b As Double, C As Double, D As Double, E _
    As Double, xT As Double)
    'Input temperature in K
```

```
    'Used for heat capacity of vapors (J/kmol*K)
    DIPPR107 = (A + b * ((C / xT) / sinh(C / xT)) ^ 2 + D * ((E / xT) / _
        cosh(E / xT)) ^ 2)
End Function

Public Function initializer()
    'Clears all global variables of previous values
    'Global variables retain their values until the Excel sheet is closed
    nCORri = 0#
    m = 0#
    n = 0#
    Eact = 0#
    Eads1 = 0#
    Eads2 = 0#
    Eads3 = 0#
    Eads4 = 0#
    Eads5 = 0#
    a0_conv_unit = 0#
    a1_conv_unit = 0#
    a2_conv_unit = 0#
    a3_conv_unit = 0#
    a4_conv_unit = 0#
    m1 = 0#
    n1 = 0#
    BB = 0#
    z1 = 0#
    z2 = 0#
    z3 = 0#
    z4 = 0#
    z5 = 0#
```

```
z6 = 0#
z0 = 0#
XCORi = 0#
H2COst = 0#
SCH4 = 0#
SC2C4 = 0#
SC5plus = 0#
SWGS = 0#
SOXY = 0#
nH2ri = 0#
nCO2ri = 0#
nH2Ori = 0#
nCH4ri = 0#
nC2C4ri = 0#
nC5plusri = 0#
nOXYri = 0#
nN2ri = 0#
dpeff = 0#
Rg = 0#
act = 0#
eb = 0#
Dt = 0#
Lpeff = 0#
Acrs = 0#
Tin = 0#
manualk = 0#
Time_converter = 0#
MWC5plus = 0#
cobalt = 0
iron = 0
```

```
    cat = 0
    vapor = 0
    liquid = 0
    waterphase = 0
    PI = 0#
    P_converter = 0#
    g = 0#
    deltaH_overall = 0#
    rhob = 0#
    Tw = 0#
    order = 0#
    pp = 0#
    rhop = 0#
    stopcheck = False
    errmsg = ""
End Function

Public Sub DLoader()
    'Loads based case depending on catalyst selection
    Dim catselect As String
    Dim i As Integer, j As Integer, rw As Integer, cl As Integer
    Dim done As Boolean

    i = 0
    j = 0
    'User determines which catalyst is modeled
    catselect = Sheets("Inputs").Range("C2").Text
    If catselect = "Cobalt" Then
        j = 2
    ElseIf catselect = "Iron" Then
```

```
        j = 3
    Else
        MsgBox "Invalid Catalyst selection. Please select either Cobalt " _
            & "or Iron.", vbOKOnly, "Invalid Catalyst"
        Exit Sub
    End If

    'Copy Base Case Values to User Input Fields
    i = 2
    done = False
    Do Until done = True
        rw = Sheets("Base Cases").Cells(i, 4)
        cl = Sheets("Base Cases").Cells(i, 5)
        Sheets("Inputs").Cells(rw, cl) = Sheets("Base Cases").Cells(i, j)
        i = i + 1
        If Sheets("Base Cases").Cells(i, 1) = "" Then done = True
    Loop
End Sub

Public Sub Terminator()
    'Calls for calculations to end prematurely
    stopcheck = True
    errmsg = "Stopped by user. " & errmsg
    DoEvents
End Sub
```